

15c  
18-67-41

6-78-69-41 • DECEMBER 1969

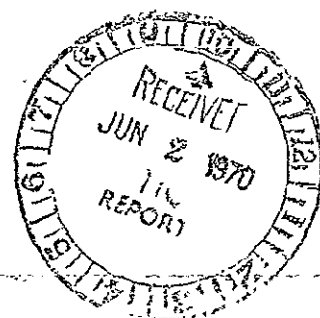
6-78-69-41

STEEF LISTED

# LIMITATIONS IN THERMAL MODELING

LMISC LIBRARY INVENTORY - PALO ALTO

Return to LMISC Library. Do not destroy  
or transmit to another person or office.



FACILITY FORM 602

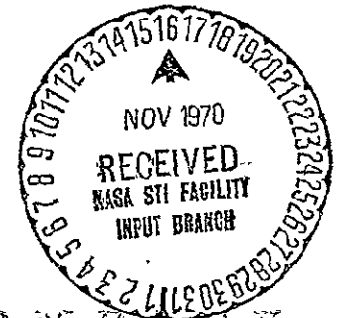
N71-10429  
(ACCESSION NUMBER)

245  
(PAGES)

CR#102566  
(NASA CR OR TMX OR AD NUMBER)

(THRU)  
G3  
(CODE)  
33  
(CATEGORY)

*Lockheed*



MISSILES & SPACE COMPANY

A GROUP DIVISION OF LOCKHEED AIRCRAFT CORPORATION

SUNNYVALE, CALIFORNIA

Reproduced by  
NATIONAL TECHNICAL  
INFORMATION SERVICE  
Springfield, Va. 22151

LIMITATIONS IN THERMAL MODELING

Technical Summary Report  
for Period  
6 June 1967 to 8 December 1969

6-78-69-41

December 1969

by

R. E. Rolling  
D. O. Murray  
K. N. Marshall

LMSC LIBRARY INVENTORY - PALO ALTO  
Return to LMSC Library. Do not destroy  
or transmit to another person or office.

Aerospace Sciences Laboratory  
Lockheed Palo Alto Research Laboratory  
LOCKHEED MISSILES & SPACE COMPANY  
A Group Division of Lockheed Aircraft Corporation  
Palo Alto, California 94304

PRECEDING PAGE BLANK NOT FILMED

## FOREWORD

This report was prepared by the Lockheed Palo Alto Research Laboratory of Lockheed Missiles & Space Company, for George C. Marshall Space Flight Center of the National Aeronautics and Space Administration. The work was performed under Contract NAS 8-21153 and was administered by the Space Sciences Laboratory of Marshall Space Flight Center, with Mr. B. P. Jones as contract officer's technical representative.

The Technical Summary Report describes work performed from 6 June 1967 to 8 December 1969.

# CONTENTS

Section		Page
1	INTRODUCTION	1
2	MODELING CRITERIA	4
	2.1 Temperature Dependence of Properties	6
3	TYPICAL SPACECRAFT	10
4	THERMOPHYSICAL PROPERTIES OF MATERIALS	22
	4.1 Thermophysical Property Data	22
	4.2 Temperature Coefficients	28
	4.3 Material and Temperature Preservation Modeling	33
	4.3.1 Temperature Preservation With Constant Thermophysical Properties	33
	4.3.2 Temperature Preservation With Power Function Dependence of Thermophysical Properties	37
	4.3.3 Temperature Preservation With Linear Dependence of Thermophysical Properties	38
	4.3.4 Materials Preservation and Nontemperature Dependence of Properties	39
	4.3.5 Materials Preservation With Thermally Dependent Properties	42
	4.3.6 Summary of Materials Problems	46
5	MODELING OF SIMPLE SYSTEMS	49
6	MODELING OF COMPLETE SYSTEMS	63
	6.1 Solar Probe Model	64
	6.1.1 Steady State Assumption	69
	6.1.2 Temperature Preservation	69
	6.1.3 Pioneer Model Laws	70
	6.1.4 Structural Members	71



Section		Page
	6.1.5 Multilayer Insulation	72
	6.1.6 Model Performance	72
	6.2 Orbiting Telescope Model	76
	6.2.1 Telescope Model	79
	6.2.2 Primary Mirror Model Design	81
	6.2.3 Secondary Support Rod Model Design	84
	6.2.4 Telescope Model Multilayer Insulation	85
	6.2.5 Complete Telescope Model	89
	6.2.6 Summary of Telescope Model Study	93
	6.3 Twenty-Foot-Diameter Unfurlable Antenna	94
	6.4 Summary of Complete System Modeling	102
7	LIMITATIONS IN MODELING MULTILAYER INSULATION	104
	7.1 Introduction	104
	7.2 Multilayer Insulation Modeling at Elevated Temperature ( $T^* > 1$ )	106
	7.2.1 Material Preservation at Elevated Temperature	109
	7.2.2 Transient Modeling	113
	7.2.3 Modeling of MLI With Undistorted Thickness	116
	7.3 Elevated Temperature Experiments With MLI	118
	7.4 Temperature Preservation	129
	7.5 Temperature Preservation Experiments	133
	7.5.1 Multilayer Insulation Test Articles	134
	7.5.2 Test Procedures	136
	7.5.3 Test Results	137
	7.6 Conclusions	143
8	SPECIAL COMPONENTS	145
	8.1 Joint Scale Modeling Criteria	149
9	CONCLUSIONS	153
10	REFERENCES	157

Appendix		Page
A	SOURCES OF INFORMATION FOR REVIEW OF SPACE- CRAFT DESIGNS	160
B	THERMOPHYSICAL PROPERTIES	167

## ILLUSTRATIONS

Figure		Page
1	Range of Thermal Conductivity for Various Materials at Room Temperature	24
2	Range of Specific Heat for Various Materials at Room Temperature	24
3	Range of $\rho C_p$ for Various Materials at Room Temperature	25
4	Range of $\rho C_p K$ for Various Materials at Room Temperature	26
5	Range of $\rho C_p / K$ for Various Materials at Room Temperature	26
6	Heat Flow in the Longitudinal and Circumferential Directions	36
7	Influence of Scale Ratio Selection on Temperature Ratio	40
8	Influence of Scale Ratio Selection on Time Scale	40
9	Exact and Approximate Forms of the Radiation Coefficient	55
10	Maximum and Minimum Temperature of the Front Surface of a Rotating Thick Plate in Space	59
11	Regions of $F_o$ and $\phi$ for Isothermal Conditions in a Rotating Thick Flat Plate	60
12	Proposed Configuration of Advanced Pioneer Solar Probe Spacecraft	65
13	1/2 Scale Thermal Model of Pioneer Solar Probe Spacecraft	73
14	Schematic of 2-m Telescope Conceptual Design	77
15	1/6.43 Scale Model of 2-m Optical System	83
16	Comparison of 36 and 27 Layer Multilayer Insulation Performance	87
17	Thermal Conductivity of Two Insulation Models	87
18	Assembled 2-m Telescope 1/6.43 Scale Model Ready for Test	90
19	Transient Thermal Behavior Predicted for Telescope Tube Interior at Section B	91

Figure		Page
20	Transient Thermal Behavior Predicted for Interior of Telescope Tube at Section D	91
21	Model Predictions for Temperatures of Regions Surrounding Primary Mirror	91
22	Total Deformations of Secondary Support Rods on the 1/6.43 Scale Model	93
23	Prototype Configuration of Unfurlable Antenna	95
24	One-Dimensinal Test Arrangement	119
25	Insulation Thermal Conductivities for the Full Scale	120
26	Insulation Thermal Conductivities for the Full and Half Scale	122
27	Correlation of Internal Temperature for One-Dimensional Heat Flow	123
28	Transient Temperatures; Section A Cycled and Top Exterior of Sections B, C, and D Subjected to Average Heat Flux	125
29	Transient Temperatures; Section A Cycled and Top Exterior of Sections B, C, and D Subjected to Average Heat Flux	126
30	Prototype Insulation Test Article	135
31	One-Half and One-Quarter Scale Insulation Test Articles	135
32	Insulation Conductivity Variation With Temperature	138
33	Two-Dimensional Heat Flow Variation With Scaling Ratio	140
34	One-Dimensional Cooling Data	141
35	Two-Dimensional Cooling Data	142
36	Geometry for Clausings Relation	147

## TABLES

Table		Page
1	Spacecraft Designs Reviewed	12
2	Typical Spacecraft Materials and General Usage	16
3	Coefficients for Thermal Conductivity Defining Temperature Dependence Characteristics	29
4	Coefficients for Specific Heat Defining Temperature Dependence Characteristics	31
5	Predicted Solar Probe Prototype Temperatures	67
6	Model Test Results for Solar Probe	74
7	Energy Distribution of Tungsten Source	75
8	Effective $\alpha/\epsilon$ of Major Sections for Various Sources	76
9	Properties of Quartz and Pyrex	82
10	Material Properties at Room Temperature	100
11	Length and Thickness Ratios for Thickness Distortion	101
12	Comparison of Measured and Calculated Thermal Conductivity Model Ratios (K*)	121
13	Modeling Results for Section A Cycled and Top Exterior at Constant Heat Flux	127
14	Steady State Data	137
15	Two-Dimensional Steady State Data	139
16	One-Dimensional Transient Data	141
17	Transient Data Comparison	142

## Section 1

### INTRODUCTION

This report covers work performed during an analytical and experimental study of the possible limitations existent in utilizing small-scale models for determination of spacecraft thermal behavior. The work was supported by the Space Sciences Laboratory, Marshall Space Flight Center, National Aeronautics and Space Administration, Huntsville, Alabama.

It was recognized at the inception of the study effort that to uncover all possible limitations in the use of spacecraft thermal models would be an impossible undertaking since there is little doubt that there are as many difficulties associated with the design of accurate thermal models as there are with complete thermal design of space hardware. Associated with each spacecraft design is a potential limitation in scale factor, experimental accuracy, accuracy in model design, etc. While it would be possible to set forth a long list of potential limitations based upon the design of particular spacecraft, it is improbable that such a listing would be of material assistance to an investigator faced with the decision to undertake a modeling program. Therefore, this study was directed toward uncovering and clarifying the broad limitations existent in thermal model studies so that the results could be used as a guide for the uninitiated model designer. In this sense, each of the sections treats individual problem areas of thermal modeling.

Presentation of the model criteria in Section 2 has been included under the assumption that many readers have not previously been exposed to the similarity requirements. The criteria cover the general case where neither temperature nor materials preservation are used, and also cover each of these special approaches.

Sections 3 and 4 deal with the problems of selecting materials for a thermal model. The review of spacecraft designs completed for preparation of Section 3 furnished a list of materials in common use on spacecraft and led to a search and compilation of thermophysical properties data including changes of properties with temperature. The results of the materials survey and problems associated with materials selection are discussed in Section 4 and materials property data presented in detail in Appendix B.

It is recognized that a complete spacecraft presents the model investigator with a very complex thermal system when viewed in totality. However, any complete system can be broken down into subsystems and individual components so that a satisfactory modeling approach can be selected for the less complex units. Section 5 considers modeling of simple systems such as flat plates, cylinders and spheres which have thermal behavior representative of the individual components. Consideration of these simple systems points out some of the simplifications that can be used on each component to achieve a satisfactory overall design.

Section 6 presents the approaches used to model three separate spacecraft systems. The systems discussed are a solar probe, large aperture telescope, and large diameter unfurlable antenna. Through consideration of the model approaches used and data obtained, it is hoped that the reader will gain insight into both the utility and shortcomings of thermal model studies. In all three systems it was necessary to distort thermal paths and use materials which were not in strict compliance with the model criteria. However, a review of the model test results shows that in spite of failure to maintain a precise thermal model design, the objectives of the study efforts were met.

The special problems arising in modeling of joints and multilayer insulation systems are covered in Sections 7 and 8. Multilayer insulation systems are being used to achieve near adiabatic boundary conditions for temperatures from 10 to 600°K and pose considerable difficulty to the model designer. The systems in current use

utilize a wide variety of reflecting surfaces both with and without spacer material. are assembled in various layer densities, and may vary from 9 to 90 layers in a single blanket. It is obvious that no single approach can be suggested for simulation of this wide variety of insulation systems. However, through completion of a thorough model study on a single system, it is possible to demonstrate potential techniques for modeling other multilayer systems. Such a study was performed on a system composed of aluminized Mylar spaced with Dexiglas and a complete description of the methods used and results of that study are presented in Section 7.

The information presented in this report is intended to provide the reader with sufficient knowledge to judge on the merits of undertaking a small-scale model study for experimental verification of prototype thermal behavior. As the title "Limitations in Thermal Similitude" implies, a concerted effort has been made to point out the major difficulties in pursuing a model study. As a result, many considerations contained in this report are negative in nature and may leave the reader with the impression that the limitations inherent in model studies rule out the possibility of obtaining accurate thermal predictions from a small-scale model. The authors recognize the possibility of creating a negative viewpoint and state that within their experience the use of thermal models has been most valuable. The models of the solar probe and telescope described in Section 6 proved invaluable in demonstrating thermal performance, in providing experience on prototype materials and construction techniques, and in proving out techniques for thermal testing of the flight hardware. These models were designed, constructed, and tested for one-half the cost of the preliminary thermal analyses of the prototype. The limitations and difficulties pointed out in the following sections were present and considered during these studies; however, the problems were not sufficiently serious to detract from the successful implementation of the model studies.

In brief, the following report is intended to provide information on the limitations of thermal similitude so that the model investigator gives each source of difficulty careful consideration. The contents are not intended to place limits on the utility of using thermal models.



## Section 2

### MODELING CRITERIA

Design of small-scale models for thermal studies of spacecraft requires that certain specific criteria be followed in order that the model thermal behavior will be representative of the prototype. The derivation of criteria for thermal modeling in the radiation-conduction coupled space environment has been presented by numerous authors. (See, for example, Refs. 1, 2, 3, 4.) In view of the general availability of these presentations, the derivations will not be repeated here. A somewhat general derivation of the thermal modeling criteria, derived from consideration of a differential equation describing energy transfer in an atmosphere free environment, results in the following statement (Ref. 1):

$$\frac{\rho^* V^* C^* T^*}{\theta^*} = A_I^* I^* = Q^* = \frac{K^* A_n^* T^*}{L^*} = A_i^* T^{*4} \quad (2.1)$$

The starred quantities are ratios of properties between the model and prototype at each geometrically similar point. Thus,  $T^* = T_m/T_p$  for similar points on the model and prototype. The symbols used are defined as

- $\rho^* = \rho_m/\rho_p$  = density ratio
- $C^* = C_m/C_p$  = specific heat ratio
- $V^* = V_m/V_p$  = volume ratio
- $\theta^* = \theta_m/\theta_p$  = time ratio
- $K^* = K_m/K_p$  = thermal conductivity ratio
- $L^* = L_m/L_p$  = length ratio
- $A_I^* = A_{I_m}/A_{I_p}$  = ratio of areas receiving radiation from external sources
- $A_n^* = A_{n_m}/A_{n_p}$  = ratio of areas perpendicular to conductivity path
- $A_i^* = A_{i_m}/A_{i_p}$  = ratio of areas involved in radiant interchange between vehicle components and to space

$$\begin{aligned}
 T^* &= T_m/T_p && \text{absolute temperature ratio} \\
 Q^* &= Q_m/Q_p && \text{ratio of rate of internal energy dissipation within the model} \\
 &&& \text{and prototype} \\
 I^* &= I_m/I_p && \text{intensity ratio of external sources of radiant energy}
 \end{aligned}$$

Equation (2.1) can be rearranged to provide any desired form as long as the indicated idealities remain satisfied at all geometrical locations and at all temperature levels.

In deriving the form presented in Eq. (2.1), the following assumptions were used and must be satisfied:

- (1) Complex radiation shape factors must be identical for the model and prototype. This requires that comparable surfaces have the same thermal radiation properties.
- (2) The property ratios, i.e.,  $C^*$ ,  $K^*$ ,  $\rho^*$ ,  $A^*$ , etc., are single valued under all operating conditions for all geometrically similar locations.
- (3) Geometric identity is required if point-by-point similarity is to be achieved.

When these assumptions are met, and the model designed so that the identities in Eq. (2.1) are satisfied for all elements of the model, the model will theoretically provide a precise indication of prototype steady state and transient behavior. For cases where transients are not involved, the term containing the specific heat and time ratios need not be considered.

Deviation from compliance with the foregoing three assumptions is sometimes necessary during practical application of thermal modeling. Many times the selected scale ratio requires that some of the minor heat-flow paths be distorted to properly model more important regions. The extent to which noncompliance with exact modeling can be carried depends upon each particular situation and must be evaluated in terms of the effects of the resulting distortion on the primary objectives of the program. The effects of deviating from strict compliance with the modeling laws and associated assumptions are discussed later in this report.

## 2.1 TEMPERATURE DEPENDENCE OF PROPERTIES

In actuality, both thermal conductivity ( $K$ ) and specific heat ( $C_p$ ) for most materials vary with temperature. If  $K$  and  $C_p$  are strong functions of temperature in the prototype, then their temperature dependence must be properly scaled in the model. Errors caused by overlooking such effects are covered in principle by Chao (Ref. 2) where the temperature dependence of thermal conductivity and specific heat are considered.

The analysis presented by Chao assumes simple power law functions for both  $K$  and  $C_p$ . Under this assumption, which is reasonable over a limited temperature range, properties are given by

$$\begin{aligned} K &= \bar{K} T^a \\ C_p &= \bar{C} T^b \end{aligned} \quad (2.2)$$

The property ratios then become

$$\bar{K}^* = \frac{\bar{K}_m T_m^{a_m}}{\bar{K}_p T_p^{a_p}} = \bar{K}^* T^{*a_m} T_p^{(a_m - a_p)} \quad (2.3)$$

$$C^* = \frac{\bar{C}_m T_m^{b_m}}{\bar{C}_p T_p^{b_p}} = \bar{C}^* T^{*b_m} T_p^{(b_m - b_p)} \quad (2.4)$$

Substitution of these results in Eq. (2.1) gives a more explicit set of model criteria that includes the assumed variation in temperature of Eq. (2.2)

$$\frac{\rho^* V^* \bar{C}^* T^{*(1+b_m)} T_p^{(b_m - b_p)}}{\theta^*} = A_I^* I^* = Q^* = \frac{\bar{K}^* A_n^* T^{*(1+a_m)} T_p^{(a_m - a_p)}}{L^*} = A_i^* T^{*4} \quad (2.5)$$

A basic requirement for similarity between model and prototype is that the dimensionless ratios of properties remain constant throughout for all thermal levels of the two systems. From Eq. (2.5) it may be seen that this is possible only for the case where  $a_m = a_p$  and  $b_m = b_p$ . If these equalities are not met, strict similarity will not be achieved. Assuming that materials are available which satisfy the equalities and dropping the subscripts for model and prototype gives for Eq. (2.5)

$$\frac{\rho^* V^* \bar{C}^* T^{*(1+b)}}{\theta^*} = A^* T^* = Q^* = \frac{\bar{K}^* A_n^* T^{*(1+a)}}{L^*} = A_i^* T^{*4} \quad (2.6)$$

This result shows that the temperature ratio between model and prototype is influenced as a power function by thermal changes in material properties. The potential for locating modeling materials where  $a_m = a_p$  and  $b_m = b_p$  is further discussed in subsection 4.3.

A major effort during the present program was that of surveying the literature and compiling a comprehensive list of the thermophysical properties of typical spacecraft and modeling materials. A part of this activity was directed toward finding information showing the temperature dependence of a select number of the more commonly used materials. The results show that many materials do not have a power function dependence on temperature and that they are better characterized over a large temperature range by a linear relationship of the form

$$K = \bar{K}_0 (1 + \beta_0 T)$$

$$C_p = \bar{C}_0 (1 + \alpha_0 T)$$

Modeling criteria to incorporate linear temperature dependence of properties were derived using the approach described in Ref. 1. A differential equation describing the thermal system is written in terms of first the prototype and then the model. Dimensionless ratios (e. g.,  $\bar{C}_0^* = \bar{C}_{0_m} / \bar{C}_{0_p}$ ,  $\alpha_0^* = \alpha_{0_m} / \alpha_{0_p}$ ,  $\bar{K}_0^* = \bar{K}_{0_m} / \bar{K}_{0_p}$ ,  $\beta_0^* = \beta_{0_m} / \beta_{0_p}$ ,  $T^* = T_m / T_p$ , etc.) describing the relation between the model and

prototype parameters are introduced into differential equation providing the following identities:

$$\frac{\rho^* V^* \bar{C}_o^* T^*}{\theta^*} = \frac{\rho^* V^* \bar{C}_o^* \alpha_o^* T^{*2}}{\theta^*} = A_I^* T^* = Q^* = \frac{\bar{K}_o^* A_n^* T^*}{L^*} = \frac{\bar{K}_o^* A_n^* \beta_o^* T^{*2}}{L^*} = A_i^* T^{*4} \quad (2.7)$$

From these identities it is easily seen that equality of all terms requires that

$$\alpha_o^* T^* = \beta_o^* T^* = 1 \quad (2.8)$$

or

$$\alpha_o^* = \beta_o^* = 1/T^* \quad (2.9)$$

The restrictions placed on model design by Eq. (2.9) are severe in the sense that, for the general case, the ratio between the model and prototype temperature coefficients must correspond to the inverse of the temperature ratio. It is highly improbable that a prototype constructed of a variety of materials could be exactly modeled under these restrictions on the choice of model material thermal properties. This observation is substantiated by the data presented in Tables 4-1 and 4-2 and in Appendix B where very few materials can be selected to give  $\alpha_o^* = \beta_o^* = 1/T^*$  at a given value of  $T^*$ . For thermal conditions in the prototype with a strong dependence on changes in thermal properties, it is possible that the model temperature ratio  $T^*$  may have to be selected with sole consideration given to the values of  $\alpha_o$  and  $\beta_o$ , rather than to the choice of a convenient temperature and time scale for the test.

Equation (2.9) shows that, for a precise thermal model, the use of identical materials in model and prototype to provide  $\alpha_o^* = \beta_o^* = 1$  requires that  $T^* = 1$ . The first, fourth, and sixth terms in Eq. (2.7) then give

$$\frac{V^*}{\theta^*} = \frac{A_n^*}{L^*} = A_i^* \quad (2.10)$$

which can be satisfied only by severe geometric distortion of conducting paths and radiating areas or by the use of  $L^* = 1$ , which results in construction of a full-scale thermal test object rather than a small-scale model.

The material presented in this section provides the uninitiated with the general model criteria that must be satisfied to construct an exact thermal scale model of a prototype system operating in space. In presenting the criteria, a few difficulties have been introduced for purposes of establishing the broad limitations existing in the model approach. For situations where material properties can be assumed constant, the model design depends primarily on the selection of a model scale temperature, or properties ratio which can be satisfied throughout the model. The selection of a maximum scale ratio is frequently dictated by considerations of test facility size while the minimum scale ratio is limited by ease of manufacturing the smaller components, structural rigidity, and frequently the time ratio  $\theta^*$ .

For cases where temperature-dependent material properties of the prototype must be accounted for in the model, the selection of scale ratios is considerably more complex. Assuming either a linear or power law dependence for the prototype leads to model criteria that are severely restrictive in terms of material selection. It is unlikely that a model design of all prototype components could be achieved under these conditions without the use of geometric distortion as a means for additional control of conducting paths.

### Section 3

#### TYPICAL SPACECRAFT

The previous section has presented the criteria applicable to spacecraft thermal modeling and includes an indication of the general areas where difficulty may be experienced. Limitations are anticipated in selection of a suitable length ratio, time ratio, temperature ratio, and materials properties ratio.

The major problems involved in modeling one spacecraft may be entirely different from those experienced in completing a similar study on a different system. This is to be expected since each thermal design is in itself a unique solution to a given set of requirements. In spite of the variety of spacecraft thermal designs, it may be postulated that trends have been established in overcoming thermal and structural problems. Manufacturers frequently tend toward the use of aluminum and magnesium for skins and supporting structure due to their favorable strength-to-weight ratio. Honeycomb with facing sheets is receiving increasing use as a skin and mounting platform material due to its excellent rigidity and light weight. Stainless steel is used for secondary support structure, tubing, and fittings where the lighter or lower temperature metals are unsatisfactory. Each of these materials lends itself to a different solution in terms of modeling considerations.

Overall size of the prototype may well place limits on the scale ratio used. A vehicle 1 m in diameter and 2-m long would be most difficult to model at less than 1/2 scale since major components become too small to control both thermally and structurally. On the other hand, a vehicle 3-m diameter by 10-m long may necessitate a very small scale ratio to permit testing in a reasonably sized chamber.

To gain some specific knowledge of the variety of limitations that may exist in thermal model studies, it became necessary to review a number of spacecraft thermal

designs. Through completion of the review, and presentation of the findings, it was hoped that general problem areas could be defined and treated in terms of their effect on experimental model studies. The required review was completed on 25 separate spacecraft. In some cases a great deal of detail was available with respect to geometry and materials while in others only cursory information was received from the program office.

All material received was carefully reviewed and a compilation of spacecraft geometry and size made. In addition, a listing of materials was compiled for purposes of determining general usage for spacecraft application. The sources of all information are indicated in Appendix A.

The programs reviewed are indicated in Table 1 where the name, sponsor, mission, general shape, and size are indicated. The sizes and shapes of space vehicles are highly variable and include cylinders, spheres, triangles, truncated cones, flat octagons, and others. None of the shapes used pose a particular problem to the model designer though some are such that limits will be imposed on test facilities. Some of the vehicles are simply shaped spheres and cylinders, have a minimum of appendages causing shadowing, and are spin stabilized. These represent the least difficult problem in space simulation since the solar source used need not have a high degree of collimation or uniformity. Other vehicles incorporate a variety of complex shapes and contain numerous solar cell panels, antenna, and other appendages that shadow the solar vector and also cause interreflections. Modeling of these vehicles would necessitate use of a facility having excellent collimation, uniformity, and spectral content in the solar simulator.

Vehicle sizes span a wide range. Some can be enclosed within a 1 cubic meter volume while others would require an enclosure of  $10^5$  cubic meters. The manned past Apollo experiments fall into the larger category while unmanned experiments are generally smaller and more compact. Once again there is no apparent limitation associated with vehicle size except that scale ratios for the smaller vehicles would be held near unity and for the larger vehicles a scale ratio compatible with test



Table 1  
SPACECRAFT DESIGNS REVIEWED

Spacecraft	Sponsor	Mission	External Shape of Main Body	Appendages	Approximate Sizes
Apollo Applications Program	NASA	Manned, earth orbital; multiple phase mission includes rendezvous and docking, orbital laboratory workshop, and solar observations with ATM	—	—	Total envelope 38 × 11 × 22 m including solar cell panels
AAP Cluster					
Multiple Docking Adapter			Cylindrical with one end a truncated cone	—	Cylinder 2.92-m dia × 5.28-m long, truncated cone 2.92-m dia × 0.81-m long × 0.96-m dia
Apollo Telescope			Octagonal outside with concentric cylinder inside Some external tube structure forming triangular framework	4 solar panels	Octagonal of 3.66 m across × 3.05-m high; cylinder ~2.13-m dia × 3.36-m long, tubular framework extends ~1.07 m out from each of four sides, four solar panels 2.6 × 15.2 m extending outward from body-like flower petals
Orbital Workshop			Cylindrical	2 solar panels	6.62-m dia × 15.2-m long, two solar panels each 5.35 × 8.85 m
Airlock Module			Truncated cone	—	6.62-m dia × 2.92-m dia × 1.37-m long
Laboratory Module			Cylindrical with rectangular portions	—	2.44 × 3.66 m
Solar Array System			Rectangular		Dimensions given above
OGO (Orbiting Geophysical Observatory)	NASA	Unmanned, earth orbital; multi-experiment spacecraft to study particles, fields, and sources of energy in earth's atmosphere and cislunar space	Parallelepiped	2 solar panels; 11 other major appendages	Satellite fully deployed 18-m long × 6.1 m across, parallelepiped 0.79 × 0.81 × 1.83 m; solar panels each ~2.44-m long × 1.83 m across; two booms 6.7-m long; four booms 1.83-m long
OAO (Orbiting Astronomical Observatory)	NASA	Unmanned, earth orbital, optical observation and mapping	Octagonal	4 solar panels; 2 large booms; sun shades; several small items	Spacecraft is 5.5-m long × 4.94-m wide with sun shades extended, octagonal 2.96-m long × 20.4 m across flats, solar panels each approx 1.22 × 1.37 m
AOSO (Advanced Orbiting Solar Observatory)	NASA	Unmanned, earth orbital, solar physics experiments	Cylindrical	8 solar panels	Spacecraft 3.05 m long × 6.6 m dia with solar panels deployed one cylinder 2.56 m long × 1.22 dia, second cylinder 0.46 m long × 1.4 m dia; solar panels each 2.56 × 0.76 m
GEOS (Geodetic Satellite)	NASA	Unmanned, earth orbital; study earth's magnetic field and provide data for worldwide geodetic reference guide	Octagonal; truncated octagonal cone, spherical antenna dome	—	Spacecraft 1.02 m long × 1.14 m across

Table 1 (Cont.)

Spacecraft	Sponsor	Mission	External Shape of Main Body	Appendages	Approximate Sizes
ATS (Applications Technology Satellite)	NASA	Unmanned synchronous orbit; to develop concepts in the application of space technology to communication, meteorology, navigation, and earth resources management	Parabolic antenna of cylindrical experiment package	2 solar panels	Parabolic antenna 9.15 m dia; central structure, equipment experiment packages 1.4 m dia $\times$ 7.2 m long; solar panels extend beyond outer edge of parabolic antenna
P-11	USAF	Unmanned, earth orbital, multi-purpose host satellite launched from another orbiting vehicle	Modified octagon	Small booms	Spacecraft 0.92 m $\times$ 0.92 m $\times$ 0.31 m deep
Nimbus	NASA	Unmanned, earth orbital; weather spacecraft for R&D tests of new sensors, subsystems, and system configurations	Dumbbell with lower cylindrical section and upper hexagonal section	2 solar panels	Spacecraft 2.96 m tall $\times$ 3.4 m across with solar panels deployed; lower cylinder 1.4 m dia
Multi-purpose Communications Satellite	Comsat Corp.	Unmanned, earth orbital, communications	Cylindrical and triangular box	Large solar cell panels, several antennas	Various spacecraft sizes depending on configuration selected, ranging from approx. 13.7 m $\times$ 9.15 m; antenna sizes vary from 9.15-m dia to 1.52 m $\times$ 0.92 m, main body approx. 3.36-m long $\times$ 1.83 m across
Pioneer VI and VII	NASA	Unmanned, interplanetary to study interplanetary phenomena	Cylindrical	2 antennas and 3 booms	Cylindrical section 0.94-m dia $\times$ 0.92-m high, top antenna 1.32-m long; 3 booms 1.63-m long
Mariner Mars Orbiter	NASA	Unmanned, interplanetary Mars orbital	Various configurations proposed	Solar panels and antennas	Spacecraft envelope approx. 4.9 m dia $\times$ 3.36-m high
Orbital Tanker	NASA	Unmanned, earth orbital; delivery of cryogenic propellants into orbit	Various configurations proposed, conical, cylindrical	--	Conical 1: base 10 m dia $\times$ 13.7 m high; Conical 2: base 10 m dia $\times$ 20 m high, Cylindrical, 10 m dia $\times$ 27 m long
OTES (Optical Technology Experiment System)	NASA	Manned, earth orbital; observations of spacial bodies	Cylindrical (two-meter concept)	Solar panels and antenna	Telescope barrel, 2.6 m dia $\times$ 12 m long; Manned section, 3.05 m dia $\times$ 1.83 m high; System diameter with solar panels deployed: 11.3 m dia
AGENA	USAF	Unmanned, upper stage booster and earth orbital, various USAF and NASA Scientific Missions	Cylindrical	Antenna and solar panels	Cylinder 1.52 m dia $\times$ 5.5 m long
Multipurpose Space Exploration Spacecraft	LOCKHEED	Unmanned; interplanetary; no specific mission defined, proposed for scientific exploration of entire solar system	Solar reflector parabolic shaped		Spacecraft 31 m dia $\times$ 17 m high

Table 1 (Cont.)

Spacecraft	Sponsor	Mission	External Shape of Main Body	Appendages	Approximate Sizes
Surveyor	NASA	Unmanned, lunar lander, studies of lunar surface of Apollo	Triangular	Solar panels and antenna	Spacecraft 3.05 m high $\times$ 4.27 m across extended legs
Mariner	NASA	Unmanned, interplanetary, studies of planet features, primarily Mars and Venus	Octagonal	Solar panels and antennas	Octagon 1.3 m across $\times$ 0.51 m high; spacecraft in flight 5.5 m across solar panels $\times$ 2.9 m high
Voyager (Lockheed Proposed Configuration)	NASA	Unmanned, interplanetary; orbit Mars and land instrument package	Conical in part	Antennas	Main body 3.66 m dia $\times$ 6.1 m long, high gain (circular) antenna extends 3.66 m beyond main body of craft on one side, medium gain antenna extends $\sim$ 2.1 m beyond spacecraft on the other side
Explorers	NASA	Unmanned, earth orbital and interplanetary, diverse variety of space missions	Various shapes depending on mission	Antenna, booms, solar panels	Various sizes, however, in general relatively small (i.e., 0.915 m dia; 0.46 m octagon, etc.). Some have solar panels that extend beyond main body making total spacecraft envelope longer
Lunar Orbiter	NASA	Unmanned, lunar; photographing of lunar surface	Somewhat resembles truncated cone	4 solar panels; booms, antennas	Spacecraft 1.68 m $\times$ 5.65 m across
Ranger	NASA	Unmanned, lunar hard landing, photography of lunar surface	Conical structure mounted on hexagonal bus	2 solar panels; antennas	Spacecraft 4.6 m span across solar panels, 3.2 m high
ESRO II (European Space Research Organization)	EUROPE	Unmanned, earth orbital, study of cosmic rays and solar astronomy	Cylindrical	Antennas	Cylinder 0.76 m dia $\times$ $\sim$ 9.2 m long
San Marco	ITALY	Unmanned, earth orbital; upper atmospheric studies	Spherical	Antenna	Sphere 0.66 m dia
U.K. 3	UNITED KINGDOM	Unmanned, earth orbital; variety of experiments to study global atmospheric noise, galactic radio noise, electron density, etc.	Cylindrical	Solar panels, antennas	Cylinder 7 m dia $\times$ 1.22 m high; spacecraft 3.2 m across $\times$ 1.83 m high

facility size would be necessary. Problems associated with manufacture of miniature items limit to some extent the scale ratio for small vehicles. The minimum scale ratio for modeling of the larger items will be limited by satisfactory maintenance of thermal properties for conducting paths and insulations. Previous experience at LMSC on actual models indicates a lower limit for  $L^*$  on the order of  $1/7$ th, though this is not necessarily a fixed value.

Given that adequate space simulation facilities are available wherein a  $1/7$ th scale or larger model can be tested, then it becomes apparent that the most dominant problems facing the model investigator lie in the area of materials selection. The spacecraft design review revealed that an extremely wide variety of materials are used for spacecraft construction. A complete listing of materials used in the 25 programs studied was compiled during this study and required many pages of single-spaced entries. It is doubtful that its inclusion herein would serve a useful purpose. However, it is of interest to consider the materials receiving most common usage and their most frequent application.

Table 2 presents a summary of the materials observed to be most frequently utilized. The listing shows that a wide variety of metallic and nonmetallic materials are in use on spacecraft. It also shows that no single material is commonly employed to accomplish a given task. Skins are made from various aluminum alloys, magnesium alloys, stainless steels, and berylliums. Support structure and fasteners are also made from a variety of metals and nonmetals. The wide variety of materials used leads to the need for individual treatment of each modeling problem and the fact that a material may or may not be found that satisfies the model criteria.

Table 2

## TYPICAL SPACECRAFT MATERIALS AND GENERAL USAGE

<u>Materials</u>	<u>Typical Uses</u>
<u>Aluminum</u>	
1100	Solar cell substrate, thermal control louvers
2014	Skins, primary and secondary support structure, honeycomb facing
2024	Skins, primary and secondary support structure, antennas, shields, honeycomb core and facing
2219	Skins, primary and secondary support structure, propellant tanks, pressure vessels
2319	Skins, pressure vessels
3003	Skins, honeycomb core and facing
5052	Primary and secondary support structure, antennas, honeycomb core and facing
6061	Primary and secondary support structure, antennas, booms
7039	Tank structure
7075	Skins, primary and secondary support structure, honeycomb core and facing
7079	Skins, primary support structure, propellant tanks, pressure vessels, solar cell array support structure
7106	Propellant tank
7178	Honeycomb facing
356	Casting material, secondary support structure
<u>Magnesium</u>	
AZ-31B	Skins, primary and secondary supporting structure, variety of uses for special ports
HK-31A	Skins, primary and secondary support structure, solar cell arrays structure
HM-21A	Skin, primary and secondary support structure
HM-31A	Extrusions, primary and secondary support structure
ZK-60A	Extrusions, forgings, primary and secondary support structure

Table 2 (Cont.)

<u>Material</u>	<u>Typical Uses</u>
ZK-62A	Castings, primary and secondary support structure
AZ-80	Primary support structure
<u>Magnesium-Lithium</u>	
LA141A	Primary and secondary support structure
<u>Stainless Steel</u>	
A286	Primary and secondary support structure, tubing fittings
304	Secondary support structure
321	Skin, primary and secondary support structure, tubing, fittings
347	Tubing, fittings, fuel tanks
17-7PH	Honeycomb core and facing for skin structure
PH14-8Mo	Honeycomb core and facing for skin structure
Maraging Steel (19 Ni)	Special parts
PH15-17Mo	Special parts
<u>Beryllium</u>	
Commercially Pure	Skins, primary support structure
Be-Cu Alloy	Secondary support structure
Lockalloy (62%, 38% Al)	Skins, primary and secondary support structure
<u>Titanium</u>	
6 Al-4V	Primary and secondary support structure, fuel tanks, pressure vessels
8 Al-1Mo-1V	Primary support structure, fuel tanks, insulation penetration supports
5 Al-2.5 Sn	Fuel tanks, pressure vessels
13V-11Cr-3Al	Shock absorber tubes
<u>Honeycomb</u>	
Aluminum Core and Facing	Skins, primary and secondary support structure
Aluminum Core, Titanium Facing	Skins, primary and secondary support structure
Aluminum Core, Magifacing	Skins, primary and secondary support structure

Table 2 (Cont.)

<u>Material</u>	<u>Typical Uses</u>
Aluminum Core, Fiber glas Facing	Skins, primary and secondary support structure
Magnesium Core and Facing	Skins, primary and secondary support structure
Stainless Steel Core and Facing	Skins, primary and secondary support structure
Fiberglas Core and Facing	Skins, primary and secondary support structure
Fiberglas Core, Nylon Facing	Skins, primary and secondary support structure
Nylon-phenolic Honey- comb Core, Fiber- glas Facing	Skins, primary and secondary support structure
Plastic Core and Facing	Skins, primary and secondary support structure
<u>Insulation and Miscellaneous Materials</u>	
Nylon	Secondary support structure, netting, thermal insulator
Teflon	Secondary support structure, thermal insulator, multi- layer blanket
Foam (Various Types)	Thermal insulation
Fiberglas (Various Types)	Secondary support structure, thermal insulation, honeycomb
Multilayer insulation (Various forms)	Thermal insulation (high performance)
Mylar-alum composite	Primary and secondary support structure
Textolite	Thermal insulation
Rexolite	Thermal insulation
Mo filled Nylon	Solar panel hinges
Silicone Rubber	Cushioning material
Bakelite	Battery case

Thermal designers are increasing their reliance on multilayer insulation to provide thermal isolation of internal components from the external environment. Here again, no single multilayer system is preferred with the trend being to design the insulation to meet the needs of each individual requirement. The various types used on the spacecraft studied included: crinkled aluminized Mylar, crinkled aluminum foil spaced with glass-fiber paper, aluminized Kapton (H-film) spaced with glass-fiber paper, single-side aluminized Mylar, embossed aluminized Mylar, double aluminized Mylar spaced with glass paper, aluminized Mylar spaced with Teflon, and aluminized Mylar spaced with Dacron. These systems were designed using from 5 layers per blanket to 90 layers per blanket and at unspecified layer densities.

It is immediately apparent that no single modeling approach or material exists for application to the wide variety of multilayer insulation blankets. Each problem will require design of a special model blanket and, where the model design is critically dependent on conductivity, confirming laboratory measurements are necessary. The possible procedures for modeling of the multilayer systems are treated in more detail in Section 7.

Modeling of thermal control surfaces also poses a problem in the design of a model. Spectrally selective white paints, pure metallic surfaces, anodized surfaces, second surface mirrors, and solar cells with filters are examples of materials used whose surface absorptance is a strong function of the spectral content of incident energy. The model must duplicate the surface absorptance and infrared emittance properties to maintain the required equality of complex shape factors ( $\mathcal{F}^* = 1$ ) and thereby attain the required component thermal levels. This is most easily achieved using the same surface coatings and surface geometry. In some cases, an accurate duplication of surface coating properties may be difficult to achieve since the spacecraft manufacturer may use a coating process that is unavailable to the model manufacturer. It has also been observed that batch to batch differences in paint formulations often exceed acceptable tolerances in terms of solar absorptance and infrared emittance. However, the fact that these difficulties are overcome in manufacture of the prototype suggests that satisfactory procedures exist for duplication of coatings on the model.



As was the case for multilayer insulation, it will be necessary to perform laboratory measurements on the model surfaces to assure that the desired reflectance absorptance, emittance, and transmittance properties have been attained.

Numerous other special purpose materials are also in wide use in spacecraft construction. The list includes a variety of glasses for viewing ports, solar cell cover slides, visible and infrared optics, and also for structural elements. Various types of Teflon, plastics, epoxies, impregnated glass fabrics, laminates of Mylar and aluminum foil, laminates of epoxies and fiberglass, and composites of plastics and aluminum in honeycombs are found in current use. These kinds of materials pose difficulties in that their thermal properties tend to be nonreproducible since manufacturing processes are variable. Here again, the model designer must carefully evaluate the use of these materials in terms of their impact on vehicle thermal behavior and seek individual solutions to simulation of that behavior. Both analytical and experimental tools must be available so that confirmation of satisfactory model material properties is possible.

The review of spacecraft designs completed during this program provided a vast amount of information on current practice in spacecraft thermal design. This information was compiled and given careful study in terms of the problems associated with the design and testing of thermal models. The results of this study failed to reveal any unique limitation existent in thermal modeling of the systems studied. Vehicle size and shape in combination with test facility capabilities will influence both the selection of scale ratio and the degree of geometric identity between prototype and model. No limiting scale ratio was suggested by the information reviewed though the larger vehicles would have to be reduced by approximately 1/5th to fit in most available test facilities. Previous modeling programs completed in this laboratory disclosed that accurate design, construction, and testing of a model at less than 1/6th scale is possible though considerably more difficult than at a larger scale ratio. The difficulties are associated with manufacturing tolerances, maintenance of required path conductances, particularly where thermal isolation is desired for prototype components, and in inclusion of real sized instrumentation on components without influencing the thermal environment of the component being measured.

In addition, as the scale ratio is reduced to lower values it becomes increasingly difficult to select materials which suit the model criteria and geometric distortion of conducting elements becomes mandatory. This experience suggests that proposals for modeling at less than 1/6th scale should receive careful review before their implementation.

The review further indicated that standardization of material usage is completely nonexistent which increases the model investigators materials selection problems. Thermophysical properties of the materials are frequently not specified or the reported properties are in variance with values reported in current literature. Needed information must then be sought out or confirmed prior to model design. The following section considers the materials related problems in more detail.

## Section 4

### THERMOPHYSICAL PROPERTIES OF MATERIALS

The conclusions reached in Section 3 point to the fact that model design is strongly dependent on the availability of materials having thermophysical properties compatible with the model criteria. This section considers the materials selection problem in more detail and includes a listing of materials and their properties for quick reference during initial stages of model design. Consideration is given to the materials problems associated with temperature preservation and materials preservation models.

The performance of any materials property survey requires the completion of an extensive search of available literature from which the required data are compiled. During this process it was found that for many materials the values reported by separate investigators were in considerable disagreement and that most sources leave out statements of accuracy based on measurement procedures. Wide tolerances were especially encountered for thermal conductivity data where alloying and heat treating can have gross effects. Disagreement also exists in changes of properties with temperature, particularly at temperatures below earth ambient. The differences observed frequently required that judgment be exercised in including or rejecting certain data and also that averaging be employed. Therefore, while the data reported are considered the best available for initiation of model design, the reader is cautioned that values given may not be an accurate representation for a specific sample.

#### 4.1 THERMOPHYSICAL PROPERTY DATA

The data required for model design include density ( $\rho$ ), thermal conductivity ( $K$ ), specific heat ( $C_p$ ), thermal diffusivity ( $\alpha$ ), and thermal expansion coefficient (designated herein as  $\sigma$ ). Values for these properties at room temperature are given in

Appendix B, Table B-1, for many of the materials in current use on spacecraft as determined by completion of the survey presented in Section 3. The listed properties are also useful for selection of materials to be used in model design since the list includes most available structural materials.

The data presented cover a wide range of values which vary from material to material and vary considerably for alloys of the same basic material. The variation of alloys is greatest in terms of thermal conductivity. The alloys have sufficient variation of  $K$  that for steady state modeling, it is entirely possible that an aluminum alloy could be used to model another aluminum alloy for moderate length scale ratios. For example, for temperature preservation modeling (i.e.,  $K^* = L^*$ ), 2020-TO aluminum can be used to model 1100-H14 aluminum for an  $L^* = 1.05/2.20 \approx 0.48$  or 2020-TO can be used to model 6061-TO for an  $L^* = 1.05/1.71 = 0.615$ . A similar situation exists with the magnesium and stainless steel alloys.

The general variation of material properties tabulated in Table B-1 is presented in chart form on Figs. 1 and 2. The thermal conductivity and specific heat are shown here for the major categories of materials. This form of data presentation permits a rough initial selection of model materials following which the more accurate tabular values can be used.

Figure 1 shows the large range of  $K$  covered by presently used materials and shows that, except for the middle region (0.017 to 0.07 W/cm-°K), a material can be found to meet most modeling needs. For modeling of aluminum it is possible to obtain a  $K^*$  anywhere from 1 to 1/25th using metals. Much lower values could be obtained substituting honeycomb materials for the aluminum. Modeling of the nonmetallics, except for Fiberglas which has wide variations, appears more difficult than for metals since the range spanned is not as great.

Figure 2 presents the variations observed in specific heat. The range spanned here is roughly 1 order of magnitude in contrast to the 3 orders of magnitude for conductivity. From this observation it can be inferred that transient modeling, where the

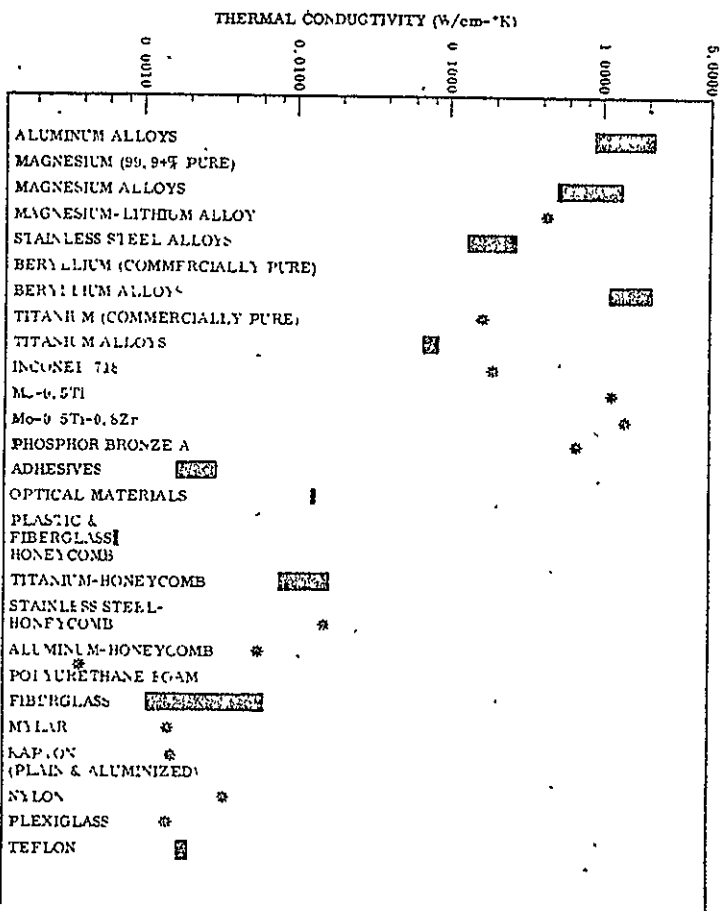


Fig. 1 Range of Thermal Conductivity for Various Materials at Room Temperature

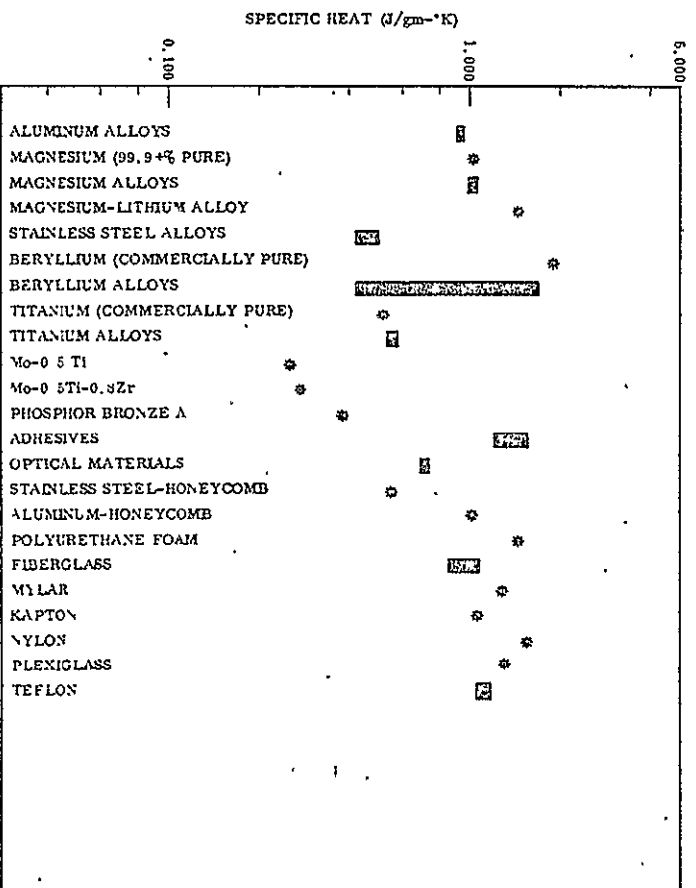


Fig. 2 Range of Specific Heat for Various Materials at Room Temperature

term  $\rho^*V^*C_p^*T^*/\theta^*$  is important, may be more difficult than steady state due to difficulties in selecting a required  $\rho^*C_p^*$ . Where the model design is limited to such a selection, the inference is correct. The difficulty is more apparent when the values of  $\rho^*C_p^*$  are considered as shown in Fig. 3. As shown on that figure, the value of  $\rho C_p$  varies over a very limited range at  $3.0 \pm 1.5 \text{ J/cm}^3\text{-}^\circ\text{K}$ . The model designer is therefore limited to a very narrow region of  $\rho^*C_p^*$  which poses design difficulties in transient studies. Figure 4 and 5 present additional information on  $\rho C_p K$  and  $\rho C_p/K$  for use in model material selection.

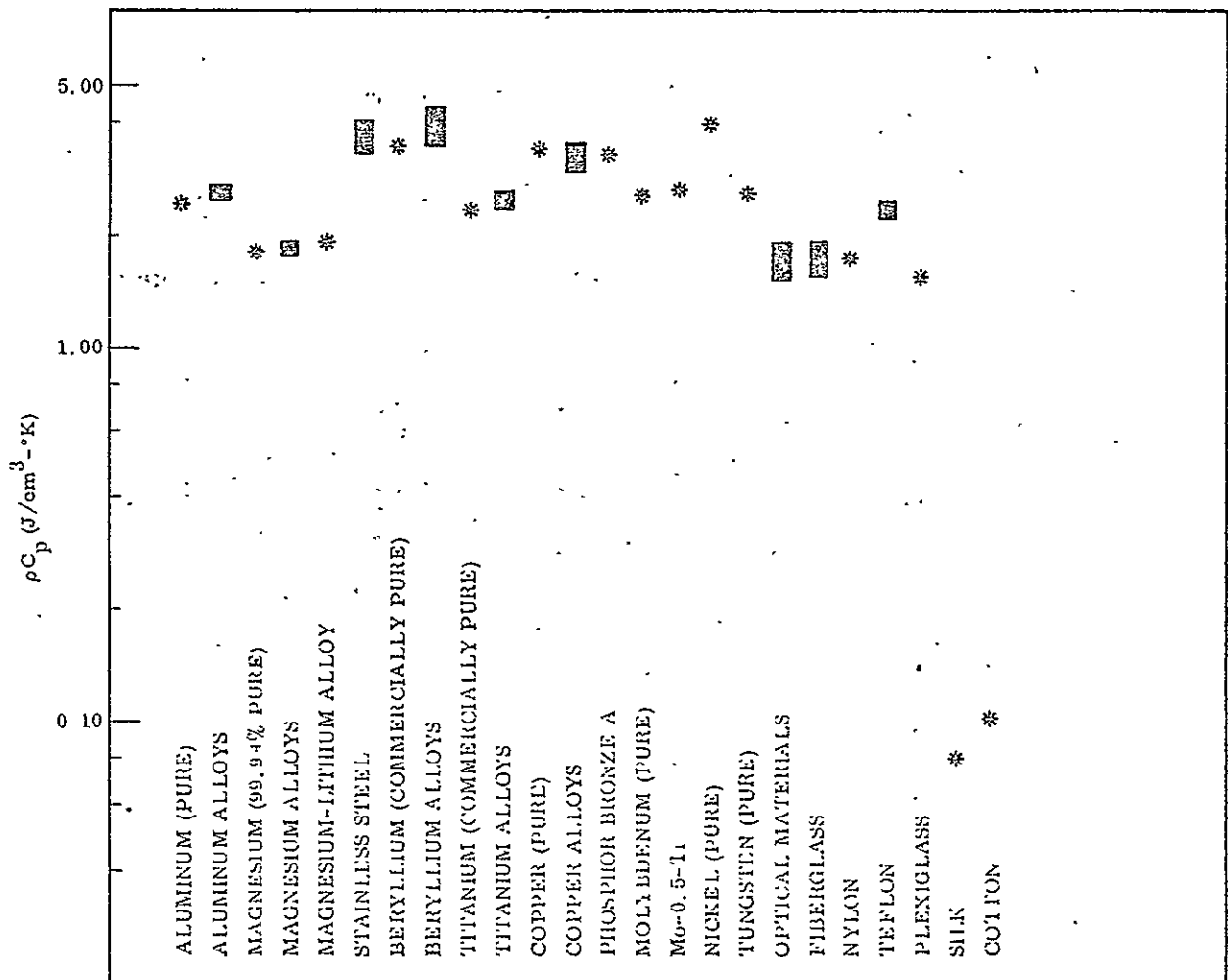


Fig. 3 Range of  $\rho C_p$  for Various Materials at Room Temperature

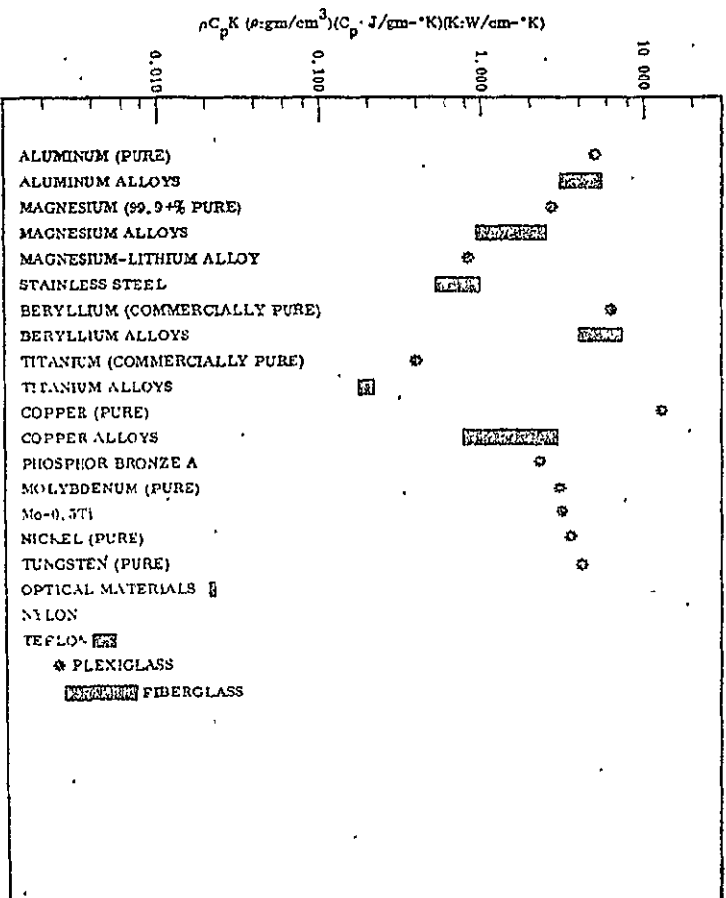


Fig. 4 Range of  $\rho C_p K$  for Various Materials at Room Temperature

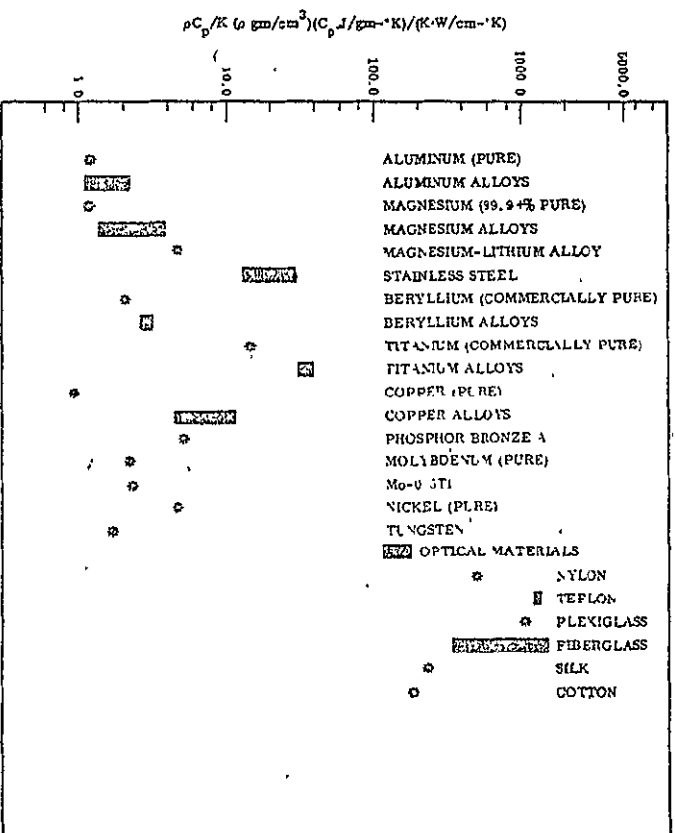


Fig. 5 Range of  $\rho C_p / K$  for Various Materials at Room Temperature

As shown in Section 2, the variation of thermophysical properties with temperature is also of concern when highest model accuracy is desired. Therefore, it was of major interest to gather together data on temperature dependence and include this as part of the study effort. The results of the data gathering effort are presented in graphical form in Appendix B, Figs. B-1 through B-40.

The curves of conductivity and specific heat show that these properties can vary over a wide range and emphasize the importance of considering this thermal influence when designing a model. Unfortunately, the temperature dependence data for all prototype materials are not always available; therefore, special property measurements or extrapolation of existing data are sometimes necessary to construct a reliable thermal model.

As stated in Section 3, many materials used in spacecraft design are not shown in Table B-1. Those not shown include a wide variety of adhesives, thermal control coatings, special laminated composites, Fiberglas and Fabriglass, optical materials, corrugated structures, and special types of honeycomb. It was virtually impossible in this work to include representative data on this wide variety of materials. For data on adhesives and optical materials, the designer is referred to various data publications issued by specific manufacturers. Radiative properties of typical thermal control coatings may be found in Ref. 5.

A wide variety of multilayer insulation was found to be used in spacecraft thermal control. Table B-2 (Appendix B) presents the effective thermal conductivity as a function of layer density and boundary temperatures for a number of the more commonly used systems. Other property data may be found for some of the component parts in Table B-1 and for various others in Ref. 6. Section 7 of this report also gives experimental values of conductivity for the commonly used blanket of double aluminized Mylar with glass-paper spacer material. In selecting property values from the literature for multilayer insulation, the model designer should keep in mind that the thermal conductivity is greatly influenced by both hot and cold



boundary temperatures, by the number of insulation layers, layer density, penetrations, edge effects, and changes in bulk temperature of the blanket. It should also be noted that at the present time there is a paucity of conductivity data for many of the multilayer insulation systems for other than low temperature boundary conditions.

#### 4.2 TEMPERATURE COEFFICIENTS

For most materials used in spacecraft and modeling design, the temperature dependence can be represented over certain temperature ranges by either an exponential or linear function. In most cases, one function or the other better represents the behavior; however, for some materials either can be used over a limited temperature range.

In Section 2, thermal modeling criteria were presented for three separate cases of temperature dependence of thermophysical properties. They consisted of:

- Properties constant with temperature [Eq. (2.1)]
- Properties varying as a power function of temperature [Eq. (2.6)]
- Properties varying as a linear function of temperature [Eq. (2.7)]

The coefficients  $a$ ,  $b$ ,  $\bar{K}$ ,  $\bar{C}$ ,  $\alpha_0$ ,  $\beta_0$ ,  $\bar{K}_0$ , and  $\bar{C}_0$  for these three cases were determined for the materials plotted in Figs. B-1 through B-40 and are presented in Tables 3 and 4. Log plots of properties of materials are given in Figs. B-41 through B-54 to further demonstrate their thermal behavior.

The coefficients presented in the tables were calculated using the method of selected points and the graphical results in which two points are selected that best approximate a representative straight line. The two coordinated points are used for solution of the equations and determination of the required coefficients. For this program, simple computer programs were written for solving the necessary two simultaneous equations. In view of the procedure used, the results reported in Tables 3 and 4 represent the authors' best interpretation of approximate straight line functions. Variations in coefficient values can occur as a result of differences in judgment or with differences in temperature range requirements for a particular program.

Table 3  
COEFFICIENTS FOR THERMAL CONDUCTIVITY DEFINING TEMPERATURE  
DEPENDENCE CHARACTERISTICS

Material	Type of Function	Temperature Range (°K)		a	$\bar{K}$ (W/cm-°K)	$-\beta_0$ (°K <sup>-1</sup> )	$\bar{K}_0$ (W/cm-°K)	Constant
		From	To					
Aluminum								
2024-T4	Power	110	535	0.555	0.053	—	—	—
5052-T0	Linear	260	320	—	—	$-5.81 \times 10^{-3}$	-1.86	—
	Linear	320	380	—	—	$-8.68 \times 10^{-3}$	-0.883	—
6061-T0	Power	260	380	1.83	$3.88 \times 10^{-5}$	—	—	—
	Power	60	300	0.431	0.147	—	—	—
7075-T6	Power	300	500	0.254	0.404	—	—	—
	Power	150	550	0.535	0.060	—	—	—
Magnesium								
AZ-31B-0	Power	120	580	0.587	0.027	—	—	—
AZ-31B-H24								
HK-31A-T0	Power	295	540	0.261	0.236	—	—	—
HK-31A-T6	Power	295	540	0.369	0.113	—	—	—
HK-31A-H24	Power	295	540	0.206	0.351	—	—	—
HK-31A-T0	Linear	295	540	—	—	$9.33 \times 10^{-4}$	0.824	—
HK-31A-T6	Linear	295	540	—	—	$5.26 \times 10^{-3}$	0.359	—
HK-31A-H24	Linear	295	540	—	—	$2.45 \times 10^{-4}$	1.13	—
HM-21A	Power	295	535	0.054	1.01	—	—	—
	Linear	297	542	—	—	$1.59 \times 10^{-4}$	1.30	—
Stainless Steel								
304	Power	80	930	0.415	0.014	—	—	—
347(a)	Linear	110	1560	—	—	$1.40 \times 10^{-3}$	$9.88 \times 10^{-2}$	—
347(b)								
347(b)	Linear	12	50	1.25	$4.53 \times 10^{-4}$	—	—	—
347(b)	Linear	50	80	0.665	$4.43 \times 10^{-3}$	—	—	—
347(b)	Linear	80	300	0.472	0.010	—	—	—
Beryllium								
Comm. Pure(c)	Linear	255	700	—	—	$-6.17 \times 10^{-4}$	2.21	—
Comm. Pure(c)	Linear	700	1300	—	—	$-5.57 \times 10^{-4}$	2.04	—
Comm. Pure(d)	Linear	100	200	—	—	$2.98 \times 10^{-4}$	0.795	—
Comm. Pure(d)	Linear	200	500	—	—	$6.56 \times 10^{-3}$	0.544	—
Comm. Pure(d)	Power	100	200	0.272	0.296	—	—	—
Comm. Pure(d)	Power	200	500	0.630	0.045	—	—	—
Comm. Pure(e)	Linear	250	700	—	—	$-4.49 \times 10^{-4}$	1.44	—
Comm. Pure(e)	Constant	700	850	—	—	—	—	0.999
Comm. Pure(e)	Power	250	700	-0.225	4.50	—	—	—
Lockalloy (62% Be, 38% Al)	Power	300	815	-0.475	32.4	—	—	—
(a) From Ref. 2, Appendix B								
(b) From Ref. 6, Appendix B								
(c) From Ref. 1, Appendix B								
(d) From Ref. 6, Appendix B								
(e) From Ref. 3, Appendix B								

Table 3 (Cont.)

Material	Type of Function	Temperature Range (°K)		a	$\bar{K}$ (W/cm-°K)	$\beta_o$ (°K <sup>-1</sup> )	$\bar{K}_o$ (W/cm-°K)	Constant
		From	To					
Titanium								
6Al-4V(f)	Linear	310	1140	—	—	$5.71 \times 10^{-3}$	$2.33 \times 10^{-2}$	—
6Al-4V(g)	Power	15	100	0.968	$5.13 \times 10^{-4}$	—	—	—
6Al-4V(g)	Power	100	300	0.514	$4.02 \times 10^{-3}$	—	—	—
Fused Silica								
Corning 7940	Power	70	150	0.635	$4.09 \times 10^{-4}$	—	—	—
	Power	150	1150	0.110	$8.34 \times 10^{-3}$	—	—	—
Polyurethane Foam								
(h)	Power	300	335	0.727	$8.93 \times 10^{-6}$	—	—	—
(i)	Power	240	410	1.25	$2.91 \times 10^{-7}$	—	—	—
(j)	Power	315	370	1.76	$9.97 \times 10^{-9}$	—	—	—
Fiberglas								
Fig. 19	Power	225	450	0.522	$3.24 \times 10^{-4}$	—	—	—
"	Power	450	530	-0.862	1.54	—	—	—
"	Power	530	660	0.543	$2.28 \times 10^{-4}$	—	—	—
⊥	Power	230	280	0.717	$8.58 \times 10^{-5}$	—	—	—
⊥	Power	280	365	-0.258	0.021	—	—	—
⊥	Power	365	670	-0.412	$3.94 \times 10^{-4}$	—	—	—
Fiberglas								
Fig. 20	Linear	230	475	—	—	0.489	$2.25 \times 10^{-4}$	—
Mylar	Power	90	250	0.207	$4.74 \times 10^{-4}$	—	—	—
	Constant	250	333	—	—	—	—	$1.49 \times 10^{-3}$
Kapton	Power	300	390	0.166	$6.17 \times 10^{-4}$	—	—	—
Fused Quartz	Power	50	150	0.945	$8.50 \times 10^{-5}$	—	—	—
	Power	150	400	0.505	$7.67 \times 10^{-4}$	—	—	—
	Linear	400	750	—	—	$3.72 \times 10^{-4}$	$1.39 \times 10^{-2}$	—
	Power	750	1100	1.92	$5.5 \times 10^{-8}$	—	—	—
Honeycomb A	Linear	102	233	—	—	$1.76 \times 10^{-2}$	$2.74 \times 10^{-3}$	—
Honeycomb B	Linear	92	245	—	—	$1.11 \times 10^{-3}$	$1.04 \times 10^{-2}$	—
Honeycomb C	Linear	225	427	—	—	$5.01 \times 10^{-3}$	$7.67 \times 10^{-3}$	—
Honeycomb D	Linear	285	370	—	—	$7.94 \times 10^{-3}$	$2.91 \times 10^{-3}$	—
Honeycomb E	Linear	225	450	—	—	0.68	$2.86 \times 10^{-5}$	—
Honeycomb E	Linear	450	600	—	—	$-8.95 \times 10^{-3}$	$-2.32 \times 10^{-3}$	—
Honeycomb F	Linear	227	420	—	—	$9.15 \times 10^{-3}$	$4.25 \times 10^{-4}$	—
Nylon	Power	10	50	0.599	0.024	—	—	—
	Power	50	100	0.390	0.054	—	—	—
	Power	100	300	0.107	0.195	—	—	—
	Linear	10	50	—	—	$-3.21 \times 10^{-3}$	$-4.68 \times 10^{-3}$	—
Teflon (PTFE)	Linear	285	590	—	—	$-7.45 \times 10^{-4}$	$-6.07 \times 10^{-4}$	—
Teflon (TFE)	Power	3	10	0.386	$1.8 \times 10^{-4}$	—	—	—
	Power	10	100	0.297	$6.31 \times 10^{-4}$	—	—	—
	Power	100	330	0.041	$1.98 \times 10^{-3}$	—	—	—
	Linear	3	10	—	—	$6.24 \times 10^{-2}$	$6.18 \times 10^{-2}$	—
	Linear	125	330	—	—	$4.26 \times 10^{-3}$	$1.18 \times 10^{-2}$	—
(f) From Ref. 1, Appendix B								
(g) From Ref. 8, Appendix B								
(h) From Ref. 16, Appendix B								
(i) From Ref. 15, Appendix B								
(j) From Ref. 17, Appendix B								

Table 4  
COEFFICIENTS FOR SPECIFIC HEAT DEFINING TEMPERATURE  
DEPENDENCE CHARACTERISTICS

Material	Type of Function	Temperature Range (°K)		$\bar{C}$ (J/gm-°K)		$\alpha_o$ (°K <sup>-1</sup> )	$\bar{C}_o$ (J/gm-°K)	Constant (J/gm-°K)
		From	To	b				
Aluminum								
2024-T0	Power	150	540	0.318	0.145	-	-	-
2024-T4	Power	67	400	0.422	0.077	-	-	-
	Linear	400	600	-	-	$5.733 \times 10^{-4}$	0.764	-
	Linear	600	730	-	-	$4.736 \times 10^{-3}$	0.268	-
6061-T6	Power	145	300	0.353	0.012	-	-	-
	Constant	300	550	-	-	-	-	0.092
7075-T0	Power	145	200	0.560	0.037	-	-	-
	Power	200	500	0.489	0.048	-	-	-
7075-T6(a)	Power	145	700	0.353	0.111	-	-	-
	Power	250	600	0.312	0.141	-	-	-
Magnesium								
AZ-31B(b)	Power	117	410	0.288	0.192	-	-	-
	Power	410	600	0.184	0.358	-	-	-
AZ-31B(c)	Power	420	760	0.382	0.111	-	-	-
HK-31A	Linear	310	550	-	-	$4.31 \times 10^{-4}$	0.914	-
	Linear	550	750	-	-	$1.53 \times 10^{-3}$	0.617	-
HM-1A	Power	300	535	0.190	0.344	-	-	-
	Linear	300	535	-	-	$5.95 \times 10^{-4}$	0.863	-
Stainless Steel								
347	Power	55	400	0.310	0.076	-	-	-
	Linear	350	1530	-	-	$4.88 \times 10^{-4}$	0.410	-
Beryllium	Power	150	300	2.314	$3.42 \times 10^{-6}$	-	-	-
	Power	300	450	0.544	0.086	-	-	-
	Linear	450	1530	-	-	$5.79 \times 10^{-4}$	1.91	-
Lockalloy (62% Be, 38% Al)	Power	300	500	0.482	0.109	-	-	-
	Power	500	850	0.181	0.707	-	-	-
Titanium (6Al-4V-0)	Power	22	60	3.08	$4.76 \times 10^{-7}$	-	-	-
	Linear	60	100	-	-	$-5.12 \times 10^{-2}$	$-7.17 \times 10^{-2}$	-
	Power	100	1150	0.415	0.048	-	-	-
	Linear	225	800	-	-	$5.21 \times 10^{-4}$	0.469	-
Fused Silica (Corning 7940)	Power	125	400	0.828	$6.58 \times 10^{-3}$	-	-	-
	Power	400	1600	0.256	0.199	-	-	-
Honeycomb								
A	Linear	220	550	-	-	$7.35 \times 10^{-2}$	$4.66 \times 10^{-2}$	-
A	Power	220	550	0.968	$4.31 \times 10^{-3}$	-	-	-
B	Constant	225	580	-	-	-	-	1.18
C	Constant	220	615	-	-	-	-	1.07
D	Constant	200	620	-	-	-	-	0.545
Nylon	Linear	235	460	-	-	$-1.26 \times 10^{-2}$	-0.567	-
Teflon (TFE)(d)	Power	10	300	0.949	$4.73 \times 10^{-3}$	-	-	-
	Power	300	400	0.266	0.221	-	-	-
	Linear	10	300	-	-	$9.1 \times 10^{-3}$	$3.7 \times 10^{-2}$	-
	Linear	300	400	-	-	$1.04 \times 10^{-3}$	0.770	-

Table 4 (Cont.)

Material	Type of Function	Temperature Range (°K)		$\bar{b}$ (J/gm-°K)		$\alpha_o$ (°K <sup>-1</sup> )	$\bar{C}_o$ (J/gm-°K)	Constant (J/gm-°K)
		From	To					
Teflon (TPE)(e)	Power	300	525	0.309	0.167	-	-	-
	Linear	300	525	-	-	$1.18 \times 10^{-3}$	0.722	-
Polyurethane Foam								
Type A	Linear	240	495	-	-	0.015	0.263	-
Type B	Linear	297	422	-	-	$-1.25 \times 10^{-3}$	2.96	-
Type C	Constant	300	422	-	-	-	-	1.72
Type D	Constant	300	422	-	-	-	-	1.675
Glass Fabric Reinforced Polyester								
Type A	Linear	310	550	-	-	-0.64	$-5.0 \times 10^{-3}$	-
Type B	Constant	290	610	-	-	-	-	1.157
Type C	Power	300	570	-0.0702	1.43	-	-	-
Glass Fiber Reinforced Epoxy								
Type A	Power	233	555	0.698	0.016	-	-	-
	Linear	233	555	-	-	$7.07 \times 10^{-3}$	0.278	-
Type B	Power	235	350	0.162	0.429	-	-	-
	Linear	350	500	-	-	$5.59 \times 10^{-3}$	0.376	-
Resin Cements								
A	Linear	307	342	-	-	$1.45 \times 10^{-2}$	-0.419	-
A'	Linear	315	333	-	-	$-1.49 \times 10^{-2}$	0.235	-
B	Linear	297	342	-	-	-0.167	$-2.71 \times 10^{-2}$	-
B'	Linear	315	333	-	-	$-1.28 \times 10^{-2}$	-0.435	-
Mylar	Linear	0	295	-	-	0.118	0.038	-
	Power	10	295	0.964	$5.88 \times 10^{-3}$	-	-	-
(a) From Ref. 1, Appendix B								
(b) From Ref. 1, Appendix B								
(c) From Ref. 1, Appendix B								
(d) From Ref. 12, Appendix B								
(e) From Ref. 20, Appendix B								

The temperature ranges used to compute the coefficients are given in the tables along with the assumed linear or power function dependence. For some materials, coefficients were calculated over a given temperature range for both linear and power dependence.

#### 4.3 MATERIAL AND TEMPERATURE PRESERVATION MODELING

Considerable attention has been given in previous literature to the use of either "Temperature Preservation" or "Material Preservation" techniques. These are, as the terminology implies, models that are designed to identically duplicate the temperature of the prototype or that are constructed from materials identical to those of the prototype. There are certain practical advantages to be gained in selecting one or the other of these approaches in designing a model. While experience has shown that the design of a model using preservation of either materials or temperature is frequently not possible and that a more general approach is necessary, these preservation techniques will be considered as a starting point for discussion of potential limitations in modeling of spacecraft.

##### 4.3.1 Temperature Preservation With Constant Thermophysical Properties

As shown in Section 2, the general criteria for thermal scale modeling can be stated as

$$\frac{\rho^* V^* C^* T^*}{\theta^*} = A_I^* I^* = Q^* = \frac{K^* A_n^* T^*}{L^*} = A_i^* T^*$$

In cases where temperature preservation is desired in the model, the temperature ratio  $T^*$  is specified as unity and the modeling criteria become:

$$\frac{\rho^* V^* C^*}{\theta^*} = A_I^* I^* = Q^* = \frac{K^* A_n^*}{L^*} = A_i^* \quad (4.1)$$

For conformance with geometric similarity  $A_n^* = A_1^* = A_I^* = L^{*2}$  and  $V^* = L^{*3}$  Eq. (4.1) becomes:

$$\frac{\rho^* L^* C^*}{\theta^*} = I^* = \frac{Q^*}{L^{*2}} = \frac{K^*}{L^*} = 1 \quad (4.2)$$

From this reduced form, the following relations are obtained for this case:

$$K^* = L^* \quad (4.3)$$

$$\left( \frac{\rho^* C^*}{K^*} \right) L^{*2} = \rho^* C^* L^* = \rho^* C^* K^* \quad (4.4)$$

This result shows that steady state modeling requires the selection of model materials whose thermal conductivities are less than those of the prototype in accordance with the chosen length ratio. For small length ratios, this is often a severe limitation, especially in modeling components where poor thermal conductors are used in the prototype. For example, let us assume that a Fiberglass or reinforced plastic honeycomb is being used for a spacecraft skin or instrument supporting panel. Referring to Fig. 1 (or Table B-1 in Appendix B), the thermal conductivities of these materials are found to be in the range of 0.00069 W/cm-°K at room temperature. Scanning the list for materials having lower conductivities, it is seen that only one, polyurethane foam, is lower with a K of 0.0004 W/cm-°K. For strict geometric identity, the overall scale factor  $L^*$  is limited to a value greater than  $L^* = K^* = 0.004/0.00069 = 0.58$  or not quite a half-scale model. Assuming that this  $L^*$  ratio was satisfactory for the model as a whole, it is doubtful that the foam would be used as a substitute for honeycomb because of its strength characteristics. Table B-2 (Appendix B) shows that multilayer insulation systems have thermal conductivities perpendicular to the layers lower than Fiberglass honeycomb by 3 orders of magnitude. However, for most applications, modeling honeycomb using multilayer insulation is totally impractical due to the nonload bearing capabilities of multilayer insulation. The only case where such a scheme might be practical is where only one dimensional heat flow was of concern and no loading was required for the multilayer blanket.

For modeling of metals, the materials problem is less difficult since some scale factors might present limitations whereas others would not. Take, for example, the typical case of an 0.060-in. thick 2024-T4 aluminum skin with a conductivity of 1.2 W/cm-°K. Steady state modeling with a length scale ratio down to 0.11 (i. e., about 1/10) is possible using 321 stainless steel with a thickness of 0.0066 in. However, this exact thickness of stainless steel may be difficult to procure as off-the-shelf material in the width sizes required for the model. Considering the same aluminum skin and an  $L^* = 1/2$ , a material with a  $K = (1/2) (1.21) = 0.605$  W/cm-°K would have to be located. Searching Table B-1 for a suitable material, it is found that none of the materials meet the exact requirements; however, some of the magnesium alloys come close with conductivities of 0.502 and 0.76 W/cm-°K. Therefore, a small compromise in  $L^*$  can be made to allow selection of a material and with strict geometrical similarity.

When the temperature preservation model must also serve for prediction of transient behavior, the model design is additionally complicated by the necessity for maintaining a proper time ratio as given by  $\theta^* = \rho^* C^* L^*$  [Eq. (4.4)]. This ratio assures an equal time constant for all elements and is set to some degree by selection of materials for maintenance of required path conductances. Complete satisfaction of Eqs. (4.3) and (4.4) under transient conditions with temperature preservation can present some difficulties for the designer. Using the previous example of 0.060-in. thick 2024-T4 aluminum skin being modeled with AZ31B-H24 magnesium to give  $K^* = L^* = 0.76/1.2 = 0.627$ , it is found that  $\theta^* = \rho^* L^* C^* = 0.444$  for strict geometric similarity. Now suppose the prototype also utilizes HM21A-T8 for various portions of the internal primary supporting structure. This material has a  $K$  of 1.37 W/cm-°K; therefore, to model it properly, a material with a  $K = (1.37) (0.627) = 0.86$  must be found. Searching the list of Table B-1, it is seen that only one material, 2020-T4 or T6 aluminum comes close to satisfying the requirements of  $K^*$ . Using these materials and calculating the corresponding  $\theta^*$ , we get  $\theta^* = \rho^* L^* C^* = (1.52) (0.627) (0.875) = 0.835$ , where a value of 0.92 J/gm-°K was assumed for the specific heat of 2020-T4 aluminum. This value of  $\theta^*$  fails to match the skin required value of  $\theta^* = 0.444$ .



This leads to consideration of distortion of the conductive heat flow path in order to meet the modeling criteria. For metallic components such as skin structure or supporting structure, thermal gradients across the material thickness are generally small. Under these conditions the important heat flow paths to model are those in the longitudinal or circumferential directions. Separating the thickness dimension from the other length dimensions shown in Fig. 6, the criteria for the case of  $T^* = 1$  become

$$\frac{K^* L^* t^*}{L^*} = L^{*2}$$

or

$$K^* = \left( \frac{L^*}{t^*} \right) L^* \quad (4.5)$$

and

$$\theta^* = \rho^* C^* t^* \quad (4.6)$$

where  $t^*$  is the thickness ratio,  $A_n^* = L^* t^*$  and  $A_i^* = L^{*2}$ .

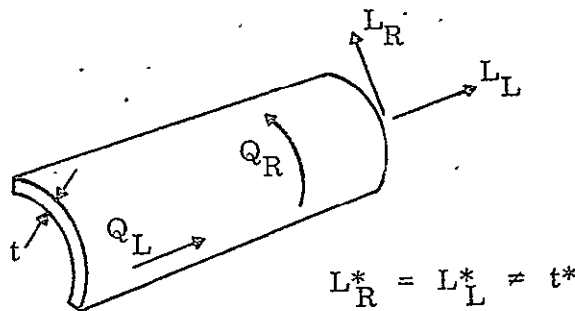


Fig. 6 Heat Flow in the Longitudinal and Circumferential Directions

In Eq. (4.5), distortion of  $t^*$  from the geometrical similar case of  $t^* = L^*$  introduces an additional variable in the relationship between  $K^*$  and  $L^*$  and allows more freedom

in design of the modeled element. To satisfy Eq. (4.6), requires that  $\theta^* = \rho^* C^* t^*$  be the same for all materials. Manipulation of  $t^*$  from pure geometrical identity gives more flexibility in meeting the  $\theta^*$  requirement. Of course, the  $t^*$  values in Eqs. (4.5) and (4.6) must be the same for any one specific material being modeled.

When distortion techniques are employed, the important external radiating areas  $A_i$  and  $A_j$  must be modeled according to  $L^{*2}$ .

In cases where two- and three-dimensional heat flows are important, distortion of the conduction heat flow path cannot be done without distortion of the point-to-point temperature identity between the model and prototype. Sometimes the three-dimensional heat flow can be approximated satisfactorily by constructing composites of different materials or by "slitting" as suggested by S. Katzoff (Ref. 7) to modify the conduction path.

#### 4.3.2 Temperature Preservation With Power Function Dependence of Thermophysical Properties

Where properties can be represented by  $K = \bar{K} T^a$  and  $C_p = \bar{C} T^b$ , and  $T^* = 1$ , the model criteria are

$$\frac{\rho^* V^* \bar{C}^* T_p^{(b_m - b_p)}}{\theta^*} = A_i^* I^* = Q^* = \frac{\bar{K}^* A_n^* T_p^{(a_m - a_p)}}{L^*} = A_i^* \quad (4.7)$$

The fundamental requirement of pointwise similarity between model and prototype through maintenance of single valued ratios of properties, temperatures, and heat rates necessitates elimination of dependence on the prototype temperatures. This can be achieved only by selection of materials having  $a_m = a_p$ . When this is achieved, and geometric similarity maintained, the model criteria become

$$\frac{\rho^* L^* \bar{C}^*}{\theta^*} = I^* = \frac{Q^*}{L^{*2}} = \frac{\bar{K}^*}{L^*} = 1 \quad (4.8)$$

Satisfying the criteria of  $\bar{K}^* = L^*$  concurrently with  $\theta^* = \rho^* \bar{C}^* L^*$  for the case of transient heat flow for all components in the design is again very challenging.

Taking, for example, the case of a 2024-T4 aluminum prototype skin and considering a 1/2 scale model, the  $\bar{K}_p$  from Table 3 is found to be 0.053 over the temperature range of 110 to 535°K, which means that a material with a  $\bar{K}_m = \bar{K}_p K^* = (0.053) \times (0.5) = 0.0265$  must be located to satisfy the model laws. Scanning the table we find that AZ-31B-0 magnesium with a  $\bar{K} = 0.027$  is the only material that comes close to meeting the requirements for the temperature range of interest. However, the criteria  $a_m = a_p$  and  $b_m = b_p$  must also be satisfied. From Tables 3 and 4 we find that  $a_p = 0.555$  (for 2024-T4 Al),  $a_m = 0.587$  (for AZ-31B Mag),  $b_p = 0.422$  and  $b_m = 0.288$ . Therefore, the required equality is closely approximated for a steady state model with a slight mismatch occurring in the b exponents which influences the transient condition. Thus, this modeling situation was satisfied with the temperature behavior of magnesium modeling that of the aluminum for a length scale ratio of 0.5. Similar matches may or may not be found for other materials used in the prototype and the difficulty of complete model design rapidly increases as more prototype materials are encountered.

#### 4.3.3 Temperature Preservation With Linear Dependence of Thermophysical Properties

In this case, the thermal properties are expressed in the form  $K = \bar{K}_0(1 + \beta_0 T)$  and  $C_p = \bar{C}_0(1 + \alpha_0 T)$ . Derivation of model criteria, with  $T^* = 1$  gives:

$$\frac{\rho^* V^* \bar{C}_0^*}{\theta^*} = \frac{\rho^* V^* \bar{C}_0^* \alpha_0^*}{\theta^*} = A^* I^* = Q^* = \frac{\bar{K}_0^* A^*}{L^*} = \frac{\bar{K}_0^* A^* \beta_0^*}{L^*} = A_j^* \quad (4.9)$$

Again for geometric similarity  $V^* = L^{*3}$  and  $A^* = L^{*2}$  giving

$$\frac{\rho^* L^* \bar{C}_0^*}{\theta^*} = \frac{\rho^* L^* \bar{C}_0^* \alpha_0^*}{\theta^*} = I^* = \frac{Q^*}{L^{*2}} = \frac{\bar{K}_0^*}{L^*} = \frac{\bar{K}_0^* \beta_0^*}{L^*} = 1 \quad (4.10)$$

This result, similar to that for a power function temperature dependence, necessitates selection of materials with  $\alpha_o^* = \beta_o^* = 1$  to obtain equality of the various terms. This requires materials to be selected with  $\alpha_{om} = \alpha_{op}$  and  $\beta_{om} = \beta_{op}$  and introduces the same difficulties as those associated with  $a_m = a_p$  and  $b_m = b_p$ . A scan of properties given in Tables 3 and 4 immediately demonstrates that the few materials having equal coefficients considerably limits the investigator.

#### 4.3.4 Materials Preservation and Nontemperature Dependence of Properties

The modeling with materials preservation under the assumption of nontemperature dependence of properties,  $\rho^*$ ,  $C^*$ , and  $K^*$  are equal to unity and the modeling criteria become

$$\frac{V^*T^*}{\theta^*} = A_I^*I^* = Q^* = \frac{A_n^*T^*}{L^*} = A_i^*T^{*4} \quad (4.11)$$

For geometric similarity,  $A_n^* = A_i^* = A_I^* = L^{*2}$  and  $V^* = L^{*3}$  and the following relations are obtained:

$$T^* = \left(\frac{1}{L^*}\right)^{1/3} \quad (4.12)$$

$$\theta^* = L^{*2} \quad (4.13)$$

For Eq. (4.12) it can be seen that  $T^*$  increases as the length scale ratio decreases. This eventually leads to a limiting condition when the length scale ratio has decreased to the point where the maximum operating temperature for any of the model materials has been reached. The relationships between  $T^*$  and  $L^*$  from Eq. (4.12) and  $\theta^*$  and  $L^*$  from Eq. (4.13) are shown plotted in Figs. 7 and 8, respectively. For a 1/4 scale materials preservation model,  $T^* = 1.59$  which means that a spacecraft operating at 294°K (70°F) would be modeled at  $T_m = 1.59 (294) = 467^\circ\text{K} (380^\circ\text{F})$ . This temperature would not be too severe for most materials; however, some problems would

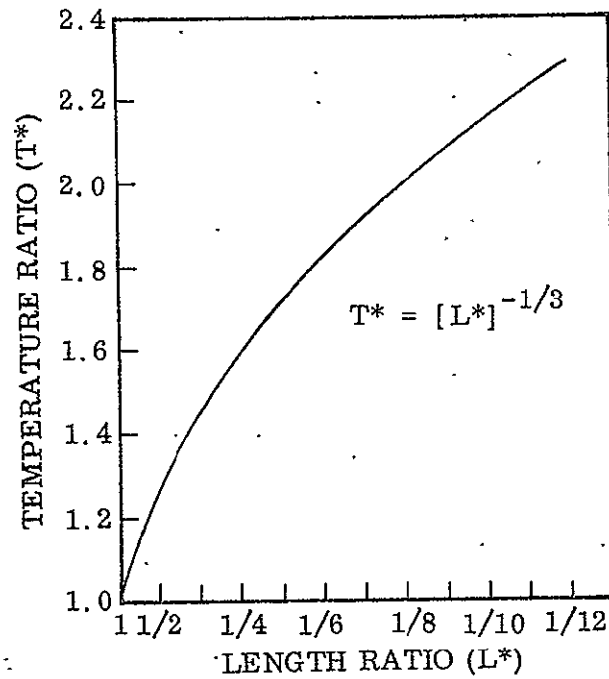


Fig. 7 Influence of Scale Ratio Selection on Temperature Ratio

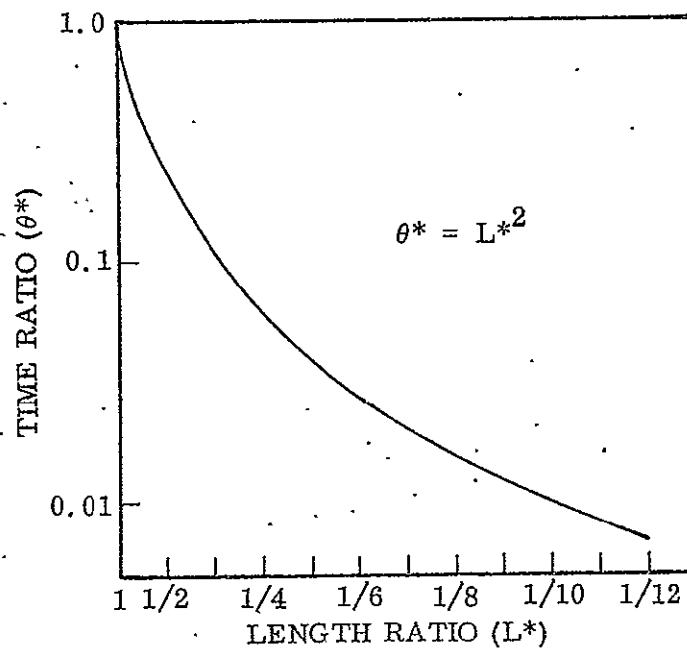


Fig. 8 Influence of Scale Ratio Selection on Time Scale

begin to occur with aluminized Mylar and some of the insulating materials such as nylon. For a 1/10 scale model,  $T^* = 2.16$  and the average model temperature becomes  $T_m = 2.16 (294) = 635^\circ\text{K} (685^\circ\text{F})$ . This level eliminates the use of most nonmetallic materials including many of the widely used thermal control paints.

Additional problems arise in the elevated temperature model since the incident energy rate per unit area, given by  $I^*$ , must be increased by sizeable amounts. Equation (4.11) gives the ratio of incident energy as  $I^* = T^{*4} = (1/L^*)^{4/3}$ . For the 1/4th scale model, this gives  $I^* = (1.59)^4 = 6.4$ , and for the 1/10th scale model  $I^* = (2.16)^4 = 21.7$ . These high levels of incident flux required by the model rule out the use of this procedure on systems that require collimated solar energy for proper simulation. Current simulators are seldom designed for flux levels above two suns and are totally incapable of 22 suns over a reasonably sized test volume. Assuming an upper limit of two suns for an available solar simulator leads to a limiting scale ratio of  $L^* = (I/T^*)^{3/4} = 1/1.68$  using materials preservation. Of course, where the test boundary conditions can be provided without solar simulation the limiting scale ratio can be further reduced. Two programs described in Section 6 have utilized procedures wherein solar simulation was not required at high flux ratios allowing a materials preservation model at an  $L^* = 1/6.43$ .

From Fig. 8 it can be seen that a 1/10 scale model would require a time scale ratio of 1/100. This is beyond the useful limit for modeling of near-earth orbital vehicles since the orbital transient for the model would have to be run in less than 60 sec.

As was the case for a temperature preservation model, it is possible in some cases to introduce geometrical distortion to reduce the problems encountered. Considering once again that we can neglect gradients through skins and other regions constructed of thin material, it is possible to state the model criteria as

$$T^* = (t^*/L^*)^{1/3} \cdot (1/L^*)^{1/3} \quad (4.14)$$

$$\theta^* = L^{*2} \quad (4.15)$$

These forms were derived assuming  $A_1^* = A_i^* = L^{*2}$  and  $A_n^* = L^* t^*$ . The form in Eq. (4.14) shows that distortion of the thickness ratio  $t^*$ , toward lower value, i. e.,  $t^* < L^*$ , reduces the thermal level of the model. For example, if  $L^* = 1/2$  and  $t^* = 1/4$  then  $T^* = 1$ . This is the so-called case of concurrent materials and temperature preservation modeling; however, this terminology is misleading since the system is not a point by point similar model due to the distortion required. It may appear surprising that distortion reduces  $T^*$  but has no apparent influence on the time scale  $\theta^*$ . This comes about through the ratio of energy storage capacity to the rate of energy absorption and/or internal dissipation.

Considering the internal dissipation rate, we find

$$Q^* = t^* T^* = t^* (t^*/L^*)^{1/3} (1/L^*)^{1/3}$$

Thus, as  $t^*$  is reduced to lower  $T^*$ , it is also necessary to further reduce  $Q^*$  to compensate for the time constant and maintain it at  $\theta^* = L^{*2}$ . Likewise, external energy levels must be reduced according to  $I^* = (t^*/L^{*2})^{4/3}$  instead of  $I^* = (1/L^*)^{4/3}$  as for the undistorted case.

In all cases where geometric distortion is employed to reduce temperatures and flux ratios, it is necessary to give careful consideration to the influence of distortion on the temperature field and heat flow path being studied. The distortion assumes a two-dimensional temperature field and maintenance of radiation shape factors. Where distortion changes these fundamental assumptions to the extent that the temperature and heat flow fields of the model no longer maintain similarity, then the model quite obviously will serve no useful purpose.

#### 4.3.5 Materials Preservation With Thermally Dependent Properties

The need for geometric distortion of the materials preservation model has been related to the necessity for reducing temperatures in the model to reasonable levels. This necessity is made even clearer by considering the fundamental properties of

materials. Materials preservation assumes that the model has preserved the thermo-physical properties of the prototype since identical materials are used. In addition, the method generally requires that the model temperature be elevated ( $T^* = L^{*-1/3}$ ). The need for a  $T^* \neq 1$ , except for distorted models, results in a change of thermal properties which in itself degrades model accuracy. This influence is more readily seen by writing the materials preservation criteria with temperature-dependent properties.

For power function dependence of properties, assuming that  $\bar{K}^* = \bar{C}^* = 1$ ,  $b_m = b_p$  and  $a_m = a_p$  (reasonable assumptions for considerable changes in temperature), the model criteria are

$$\frac{\rho^* V^* T^* (1 + b)}{\theta^*} = A^* I^* = Q^* \frac{A_n^* T^* (1 + a)}{L^*} = A_i^* T^{*4} \quad (4.16)$$

Solution of the above terms with strict geometric similarity gives

$$T^* = L^{*(1/a - 3)}$$

$$\theta^* = L^{*2} L^{*\left(\frac{b-a}{a-3}\right)}$$

The dependence of  $T^*$  and  $\theta^*$  on the absolute values of  $a$  and  $b$  introduces a considerable limitation. The fundamental precept leading to model design is that all components of the model have the same temperature and time scales relative to the prototype. Yet the above result indicates that this can be achieved only for cases where all prototype materials have identical values of  $a$  and  $b$ . The low potential for such fortuitous circumstances may be rapidly evaluated by scanning the values given in Table 4. Identical values for both constants in different materials or even for different alloys is extremely rare.



As one would expect, similar results are obtained in considering thermal properties with linear temperature dependence. Assuming for materials preservation that  $\bar{K}_o^* = \bar{C}_o^* = 1$ , Eq. (2.7) gives

$$\frac{\rho^* V^* T^*}{\theta^*} = \frac{\rho^* V^* \alpha_o^* T^{*2}}{\theta^*} = A_I^* T^* = Q^* = \frac{A_n^* T^*}{L^*} = \frac{A_n^* \beta_o^* T^{*2}}{L^{*2}} = A_i^* T^{*4}$$

Quite obviously equality of the above terms requires

$$\alpha_o^* T^* = \beta_o^* T^* = 1$$

$$\alpha_o^* = \beta_o^* = 1/T^*$$

However, for materials preservation  $\alpha_o^* = \beta_o^* = 1$  which gives  $T^* = 1$ , and through further manipulation  $L^* = 1$  follows. Thus, a material preservation approach apparently requires that a full-scale thermal system be constructed. The indication obtained by considering a linear temperature dependence differs little from that obtained using a power law temperature dependence where only for  $L^* = T^* = 1$  can the influence of the constants  $a$  and  $b$  be completely eliminated.

When thermal changes of materials properties are introduced into the model criteria, we find that an accurate model exists only for the case of  $T^* = L^* = 1$ , which is a full-scale system. This apparent limitation in using the materials preservation technique is a serious one since material properties vary as a function of temperature for nearly all known structural materials. The assumption of materials preservation is obviously negated through thermally induced properties variations.

In a practical sense it becomes apparent that prior to excluding the feasibility of using a materials preservation model it is necessary to evaluate changes in overall thermal behavior due to thermally induced property changes. For example, the heat conduction in an insulated rod is given by

$$Q = -K A_n \frac{dT}{dx}$$

When  $K = \bar{K}_0 (1 + \beta_0 T)$  the equation becomes

$$Q = -\bar{K}_0 A_n (1 + \beta_0 T) \frac{dT}{dx}$$

and integration between the limits  $x_1$ ,  $x_2$ , and  $T_1$ ,  $T_2$ , gives

$$Q = K A_n \left[ 1 + (T_1 + T_2) \beta_0 / 2 \right] \frac{T_1 - T_2}{x_2 - x_1}$$

The model laws derived from this result are

$$Q^* = \frac{\bar{K}^* A_n^* T^*}{x^*} = \frac{\beta_0^* \bar{K}^* A_n^* T^{*2}}{x^*}$$

Thus, we see by inspection of the derived model laws that equality requires

$$\beta_0^* T^* = 1,$$

and with  $\beta_0^* = 1$  (materials preservation) we must model to  $T^* = 1$ . However, the question must be asked as to the importance of the  $\beta_0$  influence in the model and prototype. If  $(T_1 + T_2) \beta_0 / 2 \ll 1$ , then the model conditions dictated by inclusion of  $\beta_0$  may be neglected. For aluminum at an average temperature of 300°K, Table 3 gives  $\beta_0 = -5.81 \times 10^{-3}$ . At an average temperature of 300°K,  $(T_1 + T_2) \beta_0 / 2 = -1.74$ . For these values  $\beta_0$  can not be neglected. However, for HM-21A Magnesium,  $\beta_0 = 1.59 \times 10^{-4}$ ,  $(T_1 + T_2) \beta_0 / 2 = 0.047$ , and thermal property changes could be a minor effect on overall performance.

It becomes apparent that the decision to pursue a materials presentation model should be based upon an analysis of the prototype system to determine the sensitivity of prototype thermal behavior to changes in properties. For a steady state system, the analysis should evaluate the relative importance of radiation and conduction in

establishing component thermal levels. If thermal radiation dominates the distribution of energy, then variations in conductivity will be of minor importance. For transient systems, the importance of heat capacity and changes in  $C_p$  should also be investigated. The results of such an analysis on the prototype may well show that an accurate materials preservation model is both a feasible and practical tool for a detailed experimental study of the prototype system.

#### 4.3.6 Summary of Materials Problems

The material presented in this section has shown that a wide variety of common and special materials are in current use on spacecraft. The wide variety of material and applications will introduce considerable difficulties to the model designer. The relation of materials properties selection to a model design has been presented and discussed in terms of the generally apparent limitations. The difficulties in the materials preservation and temperature preservation approaches have also been introduced and related to materials properties.

Upon consideration of the contents of this section, one must conclude that a major general limitation in thermal modeling is that of materials availability. Conductivities of structural materials cover a range of nearly 4 orders of magnitude. Metals are grouped in the range 0.10 to 2.0 W/cm-°K and nonmetals from 0.001 to 0.01 W/cm-°K.

From 0.01 to 0.1 W/cm-°K, it is necessary to fabricate composites or laminates since materials are not generally available with conductivities in this range. Therefore, to model a low conductivity metal with  $T^* = 1$  ( $K^* \approx L^*$ ) becomes difficult for  $L^*$  less than 1/2. Likewise, modeling of the low conductivity materials is a problem since they are chosen for inherently low values of  $K$  and a less conductive system is unavailable.

The transient model presents similar difficulties in materials selection since  $\rho C_p$  must also be considered. The range of  $\rho C_p$  for all materials is quite small as

shown by Fig. 3. The total range for available materials is from 1.5 to 4.4 J/cm<sup>3</sup>-°K which means that control of the time constant  $\theta^*$  is limited in terms of  $\rho C_p$  alone. For temperature preservation  $T^* = 1$ ,  $K^* = L^*$ , and the time ratio is given by  $\theta^* = \rho^* C_p^* L^* = \rho^* C_p^* K^*$ . Figure 4 was compiled to demonstrate the values of  $\rho C_p K$  for materials both as an aid in materials selection and to show that most materials are again grouped near the higher values. A considerable lack of materials are found for  $0.007 < \rho C_p K < 0.5$  which causes material substitution difficulties when prototype materials are on either edge of this range. Likewise, the inverse thermal diffusivity  $\rho C_p / K$  has been plotted in Fig. 5 to aid in materials selection. This property is represented over a wide range by the available materials though there are definite lower and upper limits where a selection to fit a model design may not be available.

The discussion of temperature dependence of materials properties, and the data presented on thermal coefficients, demonstrates the very real problems associated with modeling over a wide temperature range. The model criteria for a materials substitution model require matching of the thermal coefficients. This restriction considerably narrows the field of available model materials since  $K^*$ ,  $\rho^*$ , and  $C_p^*$  are usually tied down by the selection of  $T^*$  and  $L^*$ . For a materials preservation model, the criteria state that an accurate solution exists only for  $T^* = L^* - 1$  since no changes in properties can exist between the model and prototype. In view of this finding, it is apparent that materials preservation models should first receive careful analytical study to determine whether material property changes will seriously degrade model performance.

In addition to model design difficulties associated with materials selection and matching of temperature coefficients, there exists the problem of ascertaining the actual properties of materials used on the model. Manufacturers information on thermal conductivity, density, and specific heat is usually limited to room temperature values and of questionable accuracy in terms of batch-to-batch variations. Alloying and heat treating of metals causes wide variations in thermal conductivity. For nonmetals variations in chemical composition, density, and process temperature can occur that change

the thermal conductivity and make manufacturers data unreliable. At low temperatures there is a general lack of accurate data on thermal properties of common materials since manufacturers and users are not commonly involved in low temperature applications. In view of the difficulties faced by the investigator in obtaining accurate data, he must have available the necessary apparatus for determination of the thermophysical properties of materials used in model design. Checks must be made on quoted values of thermal conductivity, specific heat, density, spectral reflectance, and absorptance in the incident energy spectrum, and infrared emittance and reflectance in the spectrum associated with model temperature. Only through performance of such measurements can model properties be as well known as those prescribed for the prototype.

## Section 5

### MODELING OF SIMPLE SYSTEMS

Some insight to delineation of the limitations existent in attempting to accurately model complex spacecraft systems can be gained through consideration of the thermal behavior of simple geometries. For example, the one-dimensional steady state heat conduction through an infinitely wide plane homogeneous plate is described by the relation

$$Q = -kA \frac{T_1 - T_2}{x_1 - x_2} \quad (5.1)$$

for which the similarity criteria are

$$Q^* = \frac{k^* A^* T}{X^*} = k^* L^* T^* \quad (5.2)$$

It is easily seen, from either Eq. (5.1) or (5.2), that temperature preservation in the model will be obtained, i.e.,  $T^* = 1$ , if  $k^* L^* = Q^*$ .

That is, as long as the plate thickness of the model is chosen so that  $(x_1 - x_2)_m = (x_1 - x_2)_p Q_m k_p / Q_p K_m$  or heat rates through the model are controlled according to

$$Q_m = Q_p \frac{k_m (x_1 - x_2)_m}{k_p (x_1 - x_2)_p}$$

then the prototype conditions are strictly preserved. This flat plate problem is extremely simple and has few difficulties that lead to a limitation in the modeling approach. It is necessary to select materials with accurately known properties and thicknesses, and to measure or control heat rates with reasonable precision to obtain

excellent model results. Geometrical distortion of the model is entirely permissible for the flat plate one-dimensional heat flow.

For thick-walled hollow cylindrical and spherical shapes, the modeling approach becomes more complex. The energy transfer per unit length through the walls of an infinite cylinder is given by

$$Q/L = -2\pi k \frac{t_1 - t_2}{\ln r_1/r_2} \quad \text{with diagram of a thick-walled cylinder showing inner radius } r_1 \text{ and outer radius } r_2 \text{ and temperatures } t_1 \text{ and } t_2 \text{ at the inner and outer surfaces respectively.} \quad (5.3)$$

and the temperature field by

$$t = \frac{(t_1 - t_3) \ln r}{\ln r_1/r_2} + \frac{t_2 \ln r_1 - t_1 \ln r_2}{\ln r_1/r_2} \quad (5.4)$$

A derivation of the similarity criteria from these equations shows that the temperature field is preserved only if  $\ln(r_1^*/r_2^*) = 0$ , i.e.,  $r_1^* = r_2^*$ . Thus, a geometrically identical model must be constructed and the ratios of temperatures at identical locations will be given by

$$T^* = Q^*/k^*L^*$$

The geometrical identity introduced by the cylindrical shape leads to a considerable restriction of acceptable length ratios which can be accommodated using available materials. This results in a practical limitation of the modeling approach since cylindrical construction materials normally come in standard wall thicknesses which, in many cases, may not provide an exact match to the desired length ratio of a complex model. Jacob (Ref. 8) has replaced Eq. (5.3) by the form

$$Q = \frac{1}{\phi} k A \frac{t_1 - t_2}{\ln r_2/r_1} \quad (5.5)$$

so that a direct comparison could be made with the solution for a flat plate as given by Eq. (5.1). In this form

$$A_n = L\pi (r_1 + r_2) \quad (5.6)$$

a mean area, and

$$\phi = \frac{1}{2} \frac{(r_2/r_1) + 1}{(r_2/r_1) - 1} \ln (r_2/r_1) \quad (5.7)$$

a shape factor whose value reflects the departure of energy transfer through a cylinder from that through a flat plate. Values of the shape factor are given by Jacob as

$r_2/r_1$	1.0	1.1	1.2	1.3	1.4	1.5	2.0	4.0
$\phi$	1.000	1.001	1.003	1.006	1.010	1.014	0.140	1.155

These numerical values show that a thick-walled cylinder whose ratio of outer to inner diameter is less than 1.4 has a temperature field and energy transfer rate within 1% of that of a flat plate of equivalent mean area. Therefore, for a prototype with  $0 < r_2/r_1 \leq 1.4$ , it is apparent that geometric distortion of the cylinder wall thickness is allowable in design of a small-scale model. Removal of the restriction  $r_1^* = r_2^*$  makes the model design considerably less difficult since selection of wall thickness can be combined with model conductivity.

The difficulty of modeling a hollow sphere is similar to that encountered with the long cylinder. For a hollow sphere with inner diameter  $r_1$  and outer diameter  $r_2$ , the temperature  $t$  at radius  $r$  is given by

$$t = \frac{(t_1 - t_2)}{\left(\frac{1}{r_1} - \frac{1}{r_2}\right)} + \frac{(t_2/r_1 - t_1/r_2)}{(1/r_1 - 1/r_2)} \quad (5.8)$$



and

$$Q = 4\pi k \frac{t_1 - t_2}{(1/r_1 - 1/r_2)} = 4\pi k \frac{t - t_2}{(1/r - 1/r_2)} \quad (5.9)$$

The derivation of model criteria from these equations gives

$$r_1^*/r_2^* = 1 \quad (5.10)$$

and

$$\phi^* = k^*T^*r_1^* = k^*T^*r_2^* \quad (5.11)$$

both of which must be satisfied. As for the cylinder, these criteria demand exact geometrical similarity for preservation of the temperature field. The simplification of Eq. (5.5) can again be made for the sphere where

$$A = 4\pi \left( \frac{r_1 + r_2}{2} \right)^2 \quad (5.12)$$

and

$$\phi = 1/2 + r_1/4r_2 + r_2/4r_1 \quad (5.13)$$

Values of  $\phi$  for various ratios of  $r_1/r_2$  are

$r_2/r_1$	1.0	1.1	1.2	2.0
$\phi$	1.000	1.002	1.008	1.125

These values show that a thick-walled sphere can be distorted in thickness for  $0 < r_2/r_1 < 1.2$  since the departure from a simple flat plate solution is less than 1% for values in this range.

The results for the flat plate, cylinder, and sphere are useful in determining the need for geometrical identity between the model and prototype under steady state conditions. For most structures used in spacecraft where these shapes are employed, the radius ratios fall well below a value of  $r_2/r_1 < 1.2$  within which range the wall thicknesses can be distorted. For radius ratios above 1.4 for the cylinder and 1.2 for the sphere, it becomes necessary to design the model more carefully to assure compliance of the thermal system with the model criteria. Under these conditions the model designer will be considerably more limited in selection of length, property, or temperature ratios due to the unavailability of material sizes which match his design approach.

The solutions describe the temperature field in simple systems whose boundary temperatures are fixed and known. In most cases, these boundary temperatures are functions of the radiative or convective boundary conditions whose influence must be considered in deriving the model criteria.

Infinite and semi-infinite flat plates, infinite cylinders, and spheres have been thoroughly analyzed for solution of numerous conduction and conduction-convection heat transfer problems. The solutions to these problems have frequently been presented in generalized forms in terms of the nondimensional Biot, Fourier, Reynolds, Prandtl, and Nusselt numbers whose values are a measure of the thermal similarity existing in geometrically similar systems. Unfortunately, only a few generalized solutions have been presented for the radiation-conduction environment which fact is primarily due to the nonlinear dependence on temperature of radiant heat transfer and the necessity to solve most of these problems using thermal analyzer computer programs. However, under conditions where the thermal environment surrounding the system of interest permits linearization of the fourth power temperature dependence of the net radiant interchange, then it is possible to define a radiation coefficient and utilize the generalized forms presented for convection-conduction coupled systems.

The net energy transfer rate between opposed black surfaces at temperatures  $T_1$  and  $T_2$  ( $T_1 > T_2$ ) is given by the fourth power law as  $Q/A = \sigma(T_1^4 - T_2^4)$ . Since

$$\sigma(T_1^4 - T_2^4) = \sigma(T_1^3 + T_1^2 T_2 + T_1 T_2^2 + T_2^3) (T_1 - T_2)$$

a definition for  $h_r$ , the radiation coefficient, is  $h_r = \sigma(T_1^3 + T_1^2 T_2 + T_1 T_2^2 + T_2^3)$ . Using the radiation coefficient permits computation in the form  $q/A = h_r(T_1 - T_2)$  which, given that  $h_r$  is essentially constant, linearizes the temperature dependence and considerably simplifies the solutions of many radiant heat transfer problems.

Numerical values for  $h_r$  are more conveniently presented in the form

$$\frac{h_r}{\sigma T_1^3} = 1 + x + x^2 + x^3 \quad (5.14)$$

where

$$x = \frac{T_2}{T_1}$$

or, since the equation is symmetric in  $T_1$  and  $T_2$ ,

$$\frac{h_r}{\sigma T_2^3} = 1 + x + x^2 + x^3 \quad (5.15)$$

where

$$x = \frac{T_1}{T_2}$$

Equations (5.14) and (5.15) are shown graphically in Fig. 9. A frequently used approximation for the above defined  $h_r$  is  $h_r' = 4\sigma T_{av}^3$  where  $T_{av}$  is the average

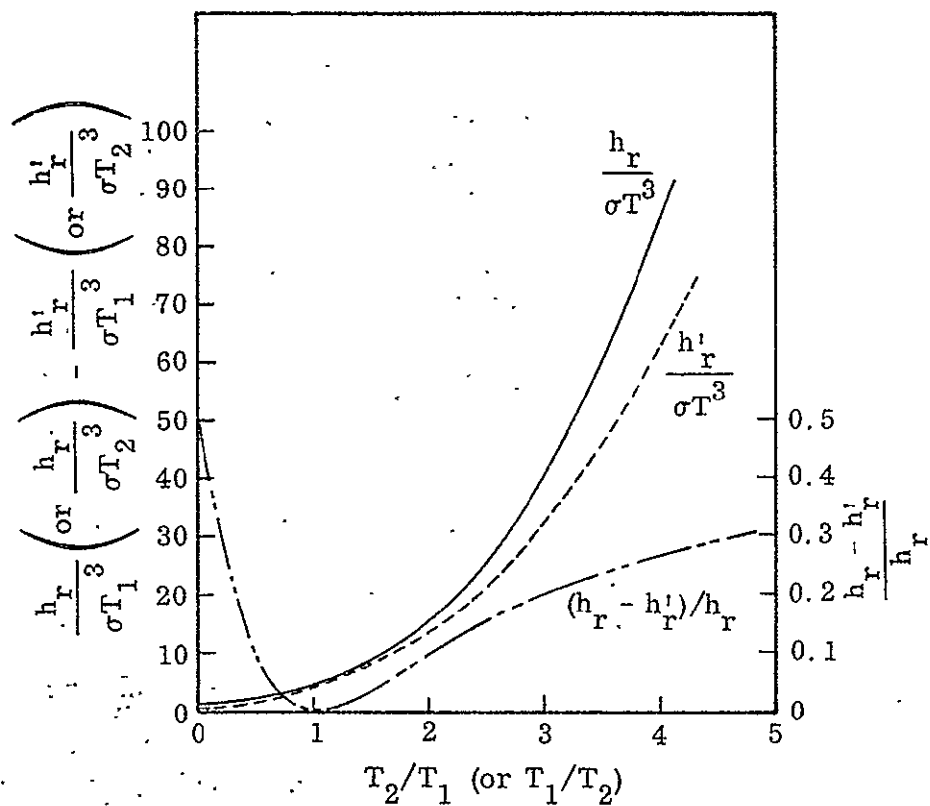


Fig. 9 Exact and Approximate Forms of the Radiation Coefficient

temperature given by  $T_{av} = (T_1 + T_2)/2$ . Using this form gives

$$\frac{h_r}{\sigma T_1^3} = \frac{1}{2} (1 + 3x + 3x^2 + x^3) \quad (5.16)$$

where

$$x = \frac{T_2}{T_1}$$

and

$$\frac{h'_r}{\sigma T_2^3} = \frac{1}{2} (1 + 3x + 3x^2 + x^3) \quad (5.17)$$

where

$$x = \frac{T_1}{T_2}$$

This relation is also plotted in Fig. 9 along with the error,  $(h_r - h'_r)/h_r$ , incurred through its use. For the range  $0.80 < (T_2/T_1) < 1.20$ , the error in using the approximate form is on the order of 1% while for  $0.64 < (T_1/T_2) < 1.60$  it is no greater than 5%.

The majority of solutions to heat conduction problems with convection heating or cooling assume that the surface heat transfer coefficient is constant. This assumption is reasonable for many situations where average convection heat transfer coefficients are defined in terms of Reynolds, Grashof, and Prandtl numbers characterizing the system. The use of an average coefficient is also appropriate for many radiation problems where the surrounds may be considered as equivalent to a blackbody at fixed temperature  $T_s$ , and the body of interest has limited variations in time or space about some mean temperature  $T_1$ . In this case  $q = h_r (T_1 - T_s)$  and  $h_r$  is assigned a value at the mean surface temperature. The relative variation of  $h_r$  [with temperature  $T_1$  by differentiation of Eq. (5.15)] is given by

$$\frac{\Delta h_r}{h_r} = \frac{x + 2x^2 + 3x^3}{1 + x + x^2 + x^3} \frac{\Delta T_1}{T_1} ; \quad x = \frac{T_1}{T_s}$$

and, where the approximate form is used, by

$$\frac{\Delta h'_r}{h'_r} = \frac{3x + 6x^2 + 3x^3}{1 + 3x + 3x^2 + x^3} \frac{\Delta T_1}{T_1} ; \quad x = \frac{T_1}{T_s}$$

A few selected numerical values for these equations are as follows:

$T_1/T_s$	$\Delta h_r/h_r$	$\Delta h'_r/h'_r$
0	0	0
0.2	0.24 $\Delta T_1/T_1$	0.5 $\Delta T_1/T_1$
0.5	0.73 $\Delta T_1/T_1$	1.0 $\Delta T_1/T_1$
0.7	1.07 $\Delta T_1/T_1$	1.24 $\Delta T_1/T_1$
1.0	1.5 $\Delta T_1/T_1$	1.5 $\Delta T_1/T_1$
2.0	2.27 $\Delta T_1/T_1$	2.0 $\Delta T_1/T_1$
5.0	2.76 $\Delta T_1/T_1$	2.5 $\Delta T_1/T_1$
10	2.89 $\Delta T_1/T_1$	2.73 $\Delta T_1/T_1$
00	3 $\Delta T_1/T_1$	3 $\Delta T_1/T_1$

The indicated values may be used as a measure of the error involved in assuming a constant heat transfer coefficient. The error is frequently negligible for the temperature ranges and heat transfer rates associated with spacecraft hardware.

The purpose of the preceding discussion of a radiation coefficient is to provide a foundation for the use of previously established solutions for simple systems in a convection-conduction environment as a guide in estimating behavior for similar geometries in a radiation-conduction environment. The purpose of establishing prototype thermal behavior using an average heat transfer coefficient is not to obtain an accurate measure of energy rates or thermal levels, but rather to gain insight into the limitations that may exist in constructing a thermal model of the system. For example, solutions for the time-temperature histories of flat plates, cylinders, and spheres are available in generalized form in terms of the Fourier numbers  $(\alpha\theta/\ell^2)$ , Biot number  $(h\ell/k)$ , and position ratio  $(x/\ell)$ . The variables used in these dimensionless ratios are:  $\alpha = k/\rho C$  = thermal diffusivity,  $\theta$  = time,  $\ell$  = characteristic thickness or length,  $k$  = thermal conductivity,  $h$  = surface heat transfer coefficient, and  $x$  = distance from zero reference in direction of  $\ell$ . These solutions are in chart form (Heisler, Groeber, Gurney-Lurie charts) and cover a wide variety of problems. By reference to charts for the case of a flat plate with heat transfer at one surface

and the other insulated, it is immediately apparent that for  $k/h\ell > 100$  ( $\alpha/\ell^2 > 0.2$ ),  $\ell$  = plate thickness, the plate may be considered as isothermal since the external resistance to heat flow overshadows the internal resistance. For this case, the plate temperature is a function of the product  $(h\ell/k)(\alpha\theta/\ell^2) = \theta h/\rho C\ell$ . For the radiant environment  $h$  is proportional to  $\sigma T^3$ , giving  $\theta h/\rho C\ell = \theta\sigma T^3/\rho C\ell > (1/100) \times (0.2) = 1/500$ , as a value below which the plate may be considered as isothermal. The same conclusion can be drawn for isothermal temperature in the solid infinite cylinder and solid sphere where  $\ell$  is replaced by the radius  $r$ . For times and properties which fall outside of the range  $k/h\ell > 100$  and  $\alpha\theta/\ell^2 > 0.2$ , it is necessary to consult the charts to determine the extent of temperature differences caused by a transient condition.

The validity of the above interpretations is borne out by the investigation of Harris (Ref. 9) wherein he considered the temperature history of a rotating flat plate in space with one surface exposed to the space environment and the other adiabatic. A fourth power radiation boundary condition was used for the emitting exposed surface which was irradiated by and absorbing solar energy during each half-cycle of rotation. Energy was absorbed during the first half-cycle with no illumination during the second half. The analyses assumed adiabatic edges for the plate and solved the one-dimensional heat transfer equation to obtain temperature histories during rotation for the front and back plate surfaces. The solution was numerical using a digital computer.

The solutions obtained for front and back temperature histories were presented in terms of  $F_o = \alpha\theta_p/\ell^2$  ( $\theta_p$  = period of rotation),  $\phi = \rho\ell C/\sigma\epsilon T_{av}^3$  ( $\epsilon$  = surface emittance,  $T_{av}$  = average surface temperature based upon thermal equilibrium with the average solar irradiance for one complete cycle), and  $n = \theta/\theta_p$  (the relative time from the beginning of a cycle). Two summary figures presented by the author are of particular value for purposes of this discussion. The first, which presents the maximum and minimum temperatures of the front surface during a complete cycle, is shown in Fig. 10.

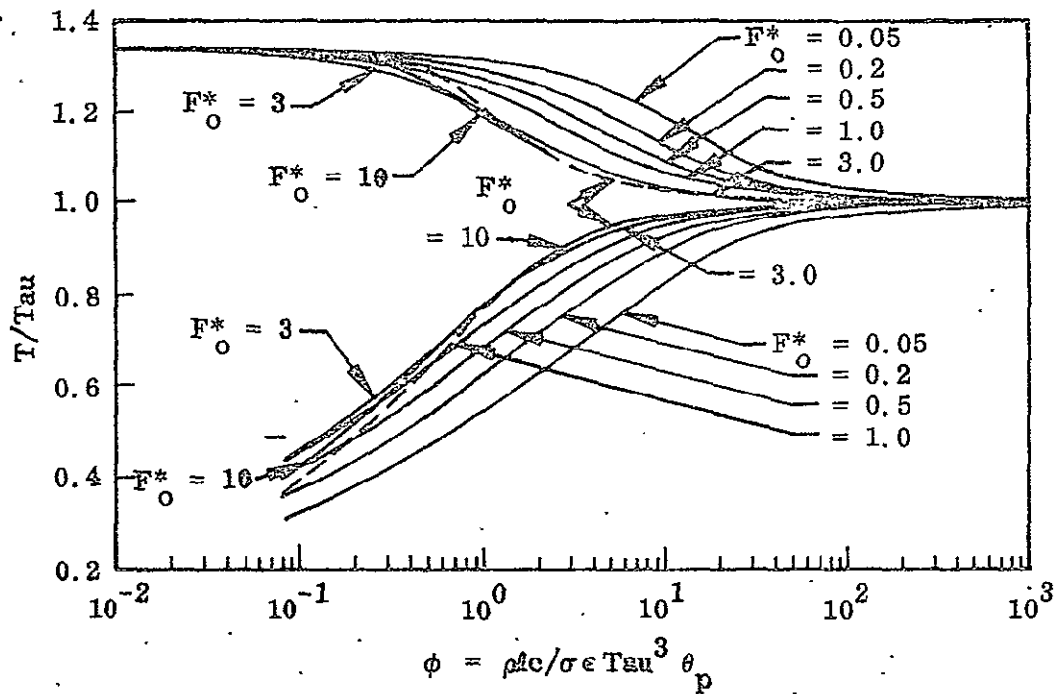


Fig. 10 Maximum and Minimum Temperature of the Front Surface of a Rotating Thick Plate in Space

Some general observations may be drawn from the figure that are useful in considering model design. For values of  $\phi < 0.1$ , the front surface of the plate will reach the same maximum regardless of the value of  $F_O = \alpha \theta_p / l^2$ . This region corresponds to low volume heat capacity per unit area combined with a long period of rotation so that the front surface is in equilibrium with the solar input. The minimum temperature will, of course, depend on the modified Fourier number  $F_O$  since stored energy must be conducted to the surface and emitted to space. For  $F_O > 10$ , the maxima and minima front surface temperatures approach those for  $F_O = \infty$ . This indicates that the designer has considerable freedom in his approach to modeling prototypes with large  $F_O$  if the transient front surface temperature is of primary interest. For  $\phi > 10^2$ , the front surface temperature is nearly invariant over a complete cycle. The region corresponds, for the steady periodic case, with the previously determined value of  $\rho Cl / \sigma T \theta = 500$  for isothermal conditions as determined from Heisler charts for a flat plate with a sudden change in surface temperature.



The second summary figure compiled by Harris is shown in Fig. 11. Here, the author presented regions of  $F_o$  and  $\phi$  within which the front and back surfaces were nearly identical throughout each cycle. Thus, for the values, shown, the plate may be considered as isothermal within 1/2, 1, or 2%. The range of  $F_o$  and  $\phi$  covered by the figure covers maximum amplitude steady-periodic response ( $F_o > 10^3$ ) through steady-state equilibrium where  $T = T_{av}$  ( $\phi > 10^3$ ).

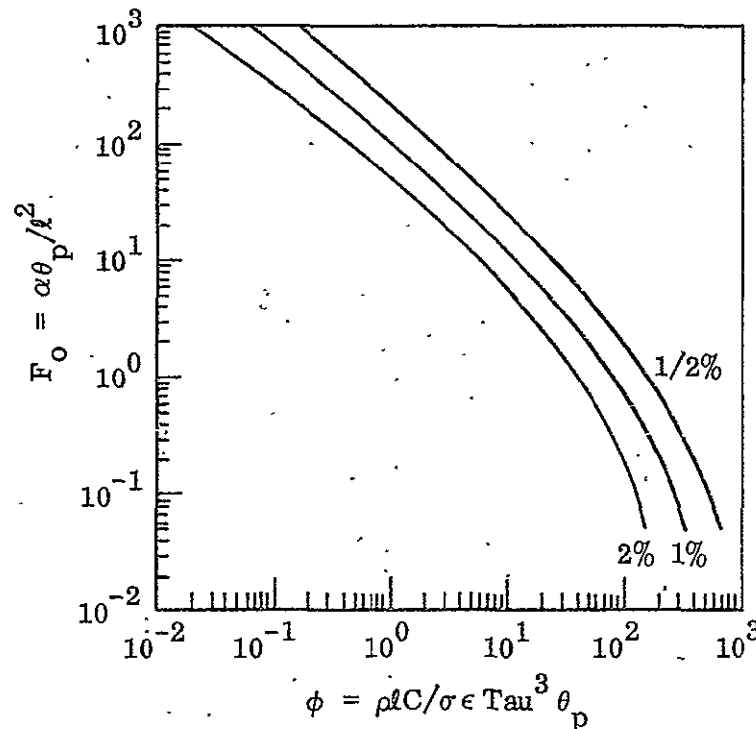


Fig. 11 Regions of  $F_o$  and  $\phi$  for Isothermal Conditions in a Rotating Thick Flat Plate

Of particular interest to the model designer is that the 1% isothermal condition is achieved throughout the range of interest for  $\phi F_o = k / \sigma \epsilon T_{av}^3 l > 10^2$ . Once again this corresponds with the findings obtained for flat plates, cylinders, and spheres by inspection of Heisler charts. This value of  $\phi F_o > 10^2$  is, in a sense, a limiting

condition for conducting a model investigation under transient or steady-periodic conditions. If the prototype object provides a  $\phi F_o > 10^2$ , then it is apparent that the model design can be relaxed in terms of geometric identity since temperature differences in thickness are not a governing parameter in overall thermal performance. However, for prototype objects having  $\phi F_o < 10^2$ , it is necessary that the model preserve all prototype properties so that the thermal gradient and front-to-back phase differences match the prototype. Where both the front-to-back gradient and phase must be preserved, it will be found that model design is considerably more difficult.

Most spacecraft components exposed to the external space environment are constructed of sufficiently thin, high conductivity material to fall in the high range of  $F_o$  and  $F_o \phi$ . For example, a spacecraft skin or other enclosure constructed of aluminum and having  $\epsilon = 1$ ,  $k = 1.76 \text{ J/sec cm}^{-1}\text{K}$ ,  $\rho = 2.8 \text{ gm/cm}^3$ ,  $C = 0.837 \text{ J/gm}^{-1}\text{K}$ ,  $\ell = 0.127 \text{ cm}$  (50 mil), and an operating temperature near  $300^\circ\text{K}$  gives

$$F_o = \frac{k \theta_p}{\rho C \ell^2} = 4.65 \theta_p \quad (\theta_p \text{ in sec})$$

$$F_o \phi = \frac{k}{\sigma \epsilon T_{av}^3 \ell} = 0.904 \times 10^4$$

For this material and thickness it is apparent that it may be assumed isothermal through its thickness. Also, since  $\phi \cong (2 \times 10^3)/\theta_p$ , it will exhibit nearly steady state behavior at  $T = T_{av}$  for periods of input flux variation on the order of 10 sec and maximum steady-periodic fluctuations for periods in excess of  $2 \times 10^4 \text{ sec}$  ( $\approx 5.5 \text{ hr}$ ). Since the value of  $F_o \phi$  is an order of magnitude greater than required for isothermal conditions, it is possible to distort the model from strict compliance with the model criteria. This is allowable as long as  $F_o \phi$  remains greater than  $10^3$ . However, consideration must also be given to the model time ratio so that proper values of  $F_o$  and  $\phi$  are separately attained to properly match the steady state or steady-periodic behavior.

Many other examples can be presented using the guidelines presented by Heisler charts, the referenced work of Harris, or similar parametric studies of simple systems. Each example will demonstrate the regions of prototype design, material properties, and environmental conditions where considerable freedom exists in model design or conversely where strict compliance with the model laws is essential. A reasonable estimate of the limiting parameters must be established by the investigator for each case in order to establish the required accuracy of model construction and test operation.

## Section 6

### MODELING OF COMPLETE SYSTEMS

The feasibility of designing and testing a thermal model of a complete spacecraft has been demonstrated through completion of such work on the Mariner IV vehicle (Ref. 10). The model built for that work was 1/2 scale and was complete in all thermally important details with the prototype system. The results obtained from tests on the Mariner II model were, for the most part, within  $\pm 5^{\circ}\text{K}$  of results obtained during thermal testing of the flight hardware, although a temperature difference as large as  $30^{\circ}\text{K}$  was observed for one component.

While the Mariner IV model is presently the only known attempt at modeling a complete vehicle, which fact considerably limits the broad conclusion to be drawn from that work, other experimental evidence is available to substantiate that scale model studies can provide meaningful results. References 11 to 13 report experimental results on modeling of complex configurations under transient conditions; Ref. 14 reports modeling of a spin stabilized solar probe; and Ref. 15 considers the thermal and structural modeling of a large space telescope. A study of results obtained from these later investigations leads to the conclusion that reasonably simple models can provide excellent indications of prototype performance. The later studies did not include comparisons to either flight performance or space chamber tests of a prototype since they were completed on the basis of information available during conceptual design stages. However, comparisons to analytical predictions obtained from computer-analyzer programs were made and these led to quite useful conclusions with regard to the fundamental design approach, the need for improvement of the computer model, and to the need for modification of the experimental small-scale model.

These studies are specifically referred to here since they will be discussed in detail in this section. Readers interested in obtaining a more complete coverage of the literature will find numerous works referenced and discussed in Refs. 16 and 17.

The limitations encountered in modeling complete systems are as many and varied as the systems themselves. Limits exist in the selection of an acceptable length ratio due either to prototype or test facility size. Model designs are limited by the availability of materials that meet the requirements imposed by selected values of  $\rho^*$ ,  $C^*$ , and  $k^*$  and by the accuracy of available materials property data. The experimental results are limited in accuracy by inherent errors in procedure and instrumentation, which errors are either magnified or reduced through the temperature ( $T^*$ ) and time ( $\theta^*$ ) scales employed.

It is not possible to provide a simple statement that sets forth the absolute limits existent in using thermal modeling procedures for all varieties of complex spacecraft. Such limits vary as a function of spacecraft size, geometry, and thermal design. For example, the problems associated with small-scale modeling of a spacecraft having major outer dimensions on the order of 2 m may well be associated with the need for high precision in manufacture of subcomponents to accurately preserve radiation view factors and path conductances at their required values. On the other hand, the major limitation in modeling a larger vehicle, with outer dimensions on the order of 30 m, may be in obtaining materials that have a low thermal conductivity and that also preserve the necessary ratios of  $\rho^*$  and  $C^*$  to match the overall  $\theta^*$ . The following paragraphs present examples of model studies on complex systems to further illustrate the limitations imposed by prototype characteristics.

## 6.1 SOLAR PROBE MODEL

Under a separate program, a study was performed to establish the test techniques applicable to thermal qualification testing of an advanced Pioneer Solar Probe (Ref. 18). The vehicle would extend space exploration to within 0.2 A. U. of the sun where the outer skin would experience 25 solar constants. Since the mission extended from 1 to 0.2 A. U. (1 to 25 solar constants) the vehicle design required use of the most advanced thermal control techniques available making a thorough thermal qualification test mandatory.

The conceptual spacecraft configuration is shown in Fig. 12. The main body of the spacecraft is 0.91 m in diameter and approximately 0.91-m high with an antenna reflector and dipole extending approximately 1.32 m above the top of the vehicle. The external surface of the upper solar cell array is covered with a mosaic of filtered silicon solar cells and optical solar reflector (OSR) thermal control surface. The surface of the lower solar cell array is covered entirely with solar cells which are protected by a variable aperture heat shield that is programed to allow a maximum solar cell temperature of 366°K. The viewing band is entirely covered with OSR and has twelve penetrations of various sizes and shapes that provide experiment apertures and sun sensor and boom mountings. All apertures are covered with a layer of aluminized polyimide film with the exception of two which are open. The experiment booms are entirely coated with OSR.

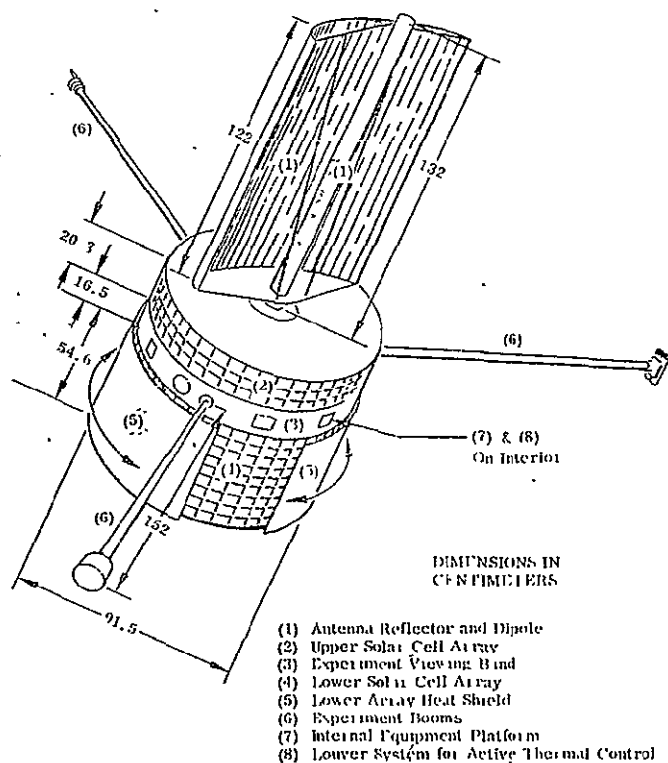


Fig. 12 Proposed Configuration of Advanced Pioneer Solar Probe Spacecraft

The spacecraft is spin stabilized at 60-rpm; however, both the antenna reflector and lower array heat shield are despun and remain fixed with respect to the solar vector. The external surface of the heat shield is coated with OSR, while the inner surface that faces the lower array is aluminized to provide for minimum thermal coupling with the main body. The antenna reflector has OSR on the convex surface and white thermal control paint on the concave surface.

All interior surfaces are thermally isolated from the exterior by high-performance multilayer insulation attached to the skin inner surfaces. Additional isolation from exterior surfaces was obtained using insulating spacers located between all internal to external structural attachment points. Heat leaks through the insulation and 50 W of internal power are radiated to space by an active louver system located directly below the equipment platform. The louvers are designed to maintain equipment platform temperatures at near-earth ambient levels ( $272^{\circ}$  to  $305^{\circ}\text{K}$ ) throughout the entire mission.

A thermal-analyzer computer program was established on the basis of available preliminary design information and was used to predict prototype performance during one solar orbit. The results obtained forecast that the basic design would function satisfactorily, although maximum temperatures would, in some cases, closely approach maximum allowable limits for the materials used. Predicted minimum (at 1 A. U.) and maximum (at 0.2 A. U.) temperatures for several locations are given in Table 5.

Several approaches were considered as having potential for provision of required levels of energy during thermal testing of the spacecraft. Sources considered were carbon arcs, xenon compact arcs, filtered xenon compact arcs, and high intensity quartz-enclosed tungsten filament lamps.

Table 5  
PREDICTED SOLAR PROBE PROTOTYPE TEMPERATURES

Component	Temperature (°K)	
	Minimum (1 A. U.)	Maximum (0.2 A. U.)
Antenna Reflector	233	519
Upper Solar Cell Array	284	636
Experiment Viewing Band	144	304
Lower Solar Cell Array	336	360
Experiment Booms	182	333
Internal Equipment Platform	284	293

Additional computations were made to determine prototype temperatures under exposure to these sources in order to establish the thermal errors caused by the spectral mismatch between each source and the solar energy spectral distribution. The results of the computations showed that use of a collimated source of filtered xenon energy would result in the least thermal error, while tungsten lamps would result in the greatest error. Unfortunately, thermal simulation of the mission would require, at the minimum, a 1.5-m diameter beam with intensities from 1 to 25 solar constants which exceeds the state-of-the-art in simulator designs using either compact xenon or carbon arc sources. The development of such a source for the test effort would obviously be extremely expensive.

Further studies of the utilization of tungsten lamp energy were deemed desirable to establish the feasibility of utilizing this form of incident energy in combination with a normalization of test results to solar energy through use of a highly refined thermal-analyzer computer program. Such a procedure had the potential of thermally exercising the flight hardware through prescribed limits (i. e. , go-no-go quality assurance testing) and at the same time of proving the validity of analytical predictions. To establish the validity of this approach, the study program undertook the design and construction of a thermal scale model and the establishment of a thermal analyzer



program for prediction of model behavior. The model was then to be tested using a 1 solar constant carbon-arc simulator and various arrays of high intensity tungsten filament lamps using incident fluxes equivalent to 1 to 25 suns.

In view of the intent of the program, i. e., to investigate test procedures, it was not considered necessary to construct a model with geometric identity in all details and with strict compliance with the model laws. To undertake that task would have required an increase in scope of the program to include the development of a more exact thermal analyzer program, additional prototype thermal design, and a complete thermal test effort. Since such a study exceeded the available funding level, it was decided to construct a geometrically similar 1/2 scale system whose thermal performance, though not identical to the prototype, would be equally as sensitive to external thermal inputs with surface solar absorptance and infrared emittance properties distributed in the same manner as for the prototype.

Model design was accomplished under the following ground rules:

- (1) Steady state conditions could be assumed due to the use of a high spin rate.
- (2) Temperatures for the model should be of the same as those of the spacecraft.
- (3) The design of the model should comply insofar as possible with the model laws for steady-state conditions given by

$$A_i^* I^* = Q^* \frac{K^* A_n^* T^*}{x} = A_i^* T^{*4} \quad (6.1)$$

- (4) Major thermal paths should model, as closely as possible, those used in the thermal analyzer program to describe the prototype configuration.
- (5) External surfaces should have the same thermal sensitivity to external source spectral variations as the spacecraft.
- (6) The size of the model should be approximately one-half that of the spacecraft for compliance with the test chamber capacity.
- (7) The same thickness and layer density of multilayer insulation would be utilized.

The advantages and limitations of each of these ground rules were carefully considered and will be reviewed herein for purposes of demonstrating the adequacy of the approach.

#### 6.1.1 Steady State Assumption

Computations were performed on the prototype concept to establish surface temperature transients during one revolution of the spin-stabilized spacecraft at 0.2 A. U. from the sun. At this orbital position, the lower solar array shield is nearly closed and the upper solar array is subjected to a maximum variation in input flux. Results obtained from the computations indicated that steady-periodic transients in skin temperature would be less than  $1^{\circ}\text{C}$ , and that periodic inputs from the booms and antenna were negligible. These findings permitted use of the steady state modeling criteria given by Eq. (6.1). The use of steady-state criteria considerably simplified model design though model rotation was still necessary to obtain the proper distribution of surface irradiance.

#### 6.1.2 Temperature Preservation

Numerous approaches could have been used in modeling the Pioneer vehicle to obtain information on its thermal performance. A model could have been constructed with  $T^* < 1$  and  $I^* < 1$  to reduce required levels of incident flux and associated temperatures. The actual values of  $T^*$  and  $I^*$  would, of course, depend upon the selected value of  $L^*$  and the availability of materials with the required thermal conductivities. In lieu of this approach, a decision was made to pursue a design and  $T^* = 1$  for purposes of gaining additional knowledge on the behavior of construction, insulation, and surface coating materials at the highest test temperatures. Thus, the use of  $T^* = 1$  was not selected on the basis of modeling considerations but rather on the desire to obtain additional information from the model that was not directly related to the thermal test requirements.

### 6.1.3 Pioneer Model Laws

For steady-state conditions with  $T^* = 1$ , the model criteria of Eq. (6.1) become

$$A_i^* I^* = Q^* \frac{K^* A_n^*}{X^*} = A_i^* \quad (6.2)$$

For regions where geometry can be preserved, i. e.,  $X^{*2} = L^{*2} = A_i^* = A_n^*$ , then

$$I^* = \frac{Q^*}{L^{*2}} = \frac{K^*}{L^*} = 1 \quad (6.3)$$

A main requirement of the model is that it preserve the proper relationships between externally absorbed energy, surface emission, and internal energy dissipation so that surface temperatures of the model properly scale those of the prototype. For temperature preservation, it is seen by inspection of Eq. (6.2) that proper scaling, i. e.,  $T^* = 1$ , requires that  $Q^*/A_i^* = A_i^* I^*/A_i^* = 1$ . Considering that  $A_i^* = A_n^* = L^{*2}$  for external surfaces, it is required that internal energy dissipation be modeled to give  $Q_m = Q_p (L_m/L_p)^2$  and that absorbed external flux be controlled to give  $I_m = I_p$  (absorbed). A design to meet the criteria  $Q_m = Q_p (L_m/L_p)^2$  was easily achieved by use of resistance heaters placed inside of boxes which were in turn firmly attached to the instrument platform. The energy dissipation of the heaters was controlled and continuously monitored to guarantee proper simulation.

Control of absorptance on external surfaces was considerably more difficult and is representative of the limitations encountered in model design. The prototype, as shown by Fig. 12, has three separate zones with distinctly different solar absorptance properties. The upper solar cell array consisted of both solar cells and OSR (second surface silvered mirrors) to provide an overall ratio of solar absorptance to infrared emittance ( $\alpha_s/\epsilon$ ) of 0.45. The viewing band was all OSR with experiment openings, both open and closed, to give an overall  $\alpha_s/\epsilon = 0.10$ . The lower array was all solar cells giving an overall  $\alpha_s/\epsilon = 0.84$ . To properly duplicate these values on the model, on both a total and spectral basis, would have required the use of identical materials in the

proportion of surface coverage. While this requirement presented no difficulties in fabrication or assembly, it was deemed undesirable in terms of the materials cost for solar cells. Thus, the availability and cost of surface materials became a major limitation in pursuing the design of an exact model of the solar probe. The use of alternate materials with different spectral properties would obviously result in a modification of thermal performance since the sources to be used during test, i. e., a carbon arc and tungsten filament lamps, have quite different spectral emission properties. However, this undesirable variance from the model criteria was deemed acceptable for the program as long as the detailed thermal analyzer program could be used to interpret model performance in terms of actual prototype performance. Therefore, the model surfaces were coated with combinations of OSR and black paint in proportions that preserved the ratio of  $\alpha_s/c$  for each section while not separately preserving  $\alpha_s$  and  $\epsilon$ . The computer analyzer program was altered accordingly to comply with the model boundary conditions.

#### 6.1.4 Structural Members

Design of the internal structure of the model was accomplished in strict compliance with the model criteria using a scale ratio  $L^* = 1/2$ . Conductive paths were controlled in geometry and materials properties to give  $K \cdot A_n^*/X^* = (L^*)^2$ . The design of brackets, boom attachments, and other conductive members required materials substitution and geometric distortion to meet the existent criteria.

The external skin of the prototype consisted of honeycomb materials whose thermal conductivity properties could not be properly modeled at 1/2 scale using a homogeneous material. However, computations showed that the skin served only as a structural mounting surface for the solar cells and OSR and played a negligible role in distributing energy around or through the inner boundary composed of multilayer insulation. This permitted use of a stainless steel skin (0.030-cm thick) that was broken into four major sections to preserve isolation of the separate surface zones being studied. This approach was permissible only because of the high resistance of multilayer insulation

in the perpendicular direction in combination with the rapid spin rate of the satellite which provided uniform circumferential temperatures. In the absence of either of these prototype conditions, the model skin would have to strictly comply with the model criteria requiring the use of special honeycomb materials.

#### 6.1.5 Multilayer Insulation

Compliance with the model laws requires that thermal conductivities be reduced according to  $K^* = X^* = 1/2$  (for  $T^* = 1$ ). With multilayer insulation, these are difficult criteria to meet since the material is nonhomogeneous, requiring control of both the perpendicular and parallel thermal conductivity, and is nonreproducible in the sense that identical insulation wraps may differ by a factor of 2 in thermal conductivity. In addition, most prototype designs strive for the minimum conductivity possible with a given number of layers making it difficult to further reduce the conductivity for a small-scale model. These difficulties were recognized during study of the solar probe and were clarified by use of the computer analyzer program using various values of conductivity for the multilayer insulation. The computations revealed that increasing the wrap thermal conductivity from the prototype design value of  $8.6 \times 10^{-6}$  W/cm-°K ( $5 \times 10^{-4}$  Btu/hr-ft-°R) to  $1 \times 10^{-4}$  W/cm-°K ( $5.8 \times 10^{-3}$  Btu/hr-ft-°R) would not result in a noticeable increase of internal temperatures or decrease of external surface temperatures. This finding confirmed that energy entering the internal region from booms, support brackets, and instrument ports was dominant over that passing through the insulation blankets and permitted a relaxing of the model criteria calling for an insulation with  $K_m = 1/2 k_p$ . Therefore, the model was constructed using an insulation identical to that of the prototype which allowed direct observation of its thermal performance and of its stability under the high temperatures to be experienced by the prototype.

#### 6.1.6 Model Performance

The completed 1/2 scale thermal model is shown in Fig. 13. The model was tested at 1.04 solar constants of carbon arc energy and at 0.9, 1.12, 4.92, and 9.0 solar constants of tungsten lamp energy. A test was not made above 9 suns of tungsten

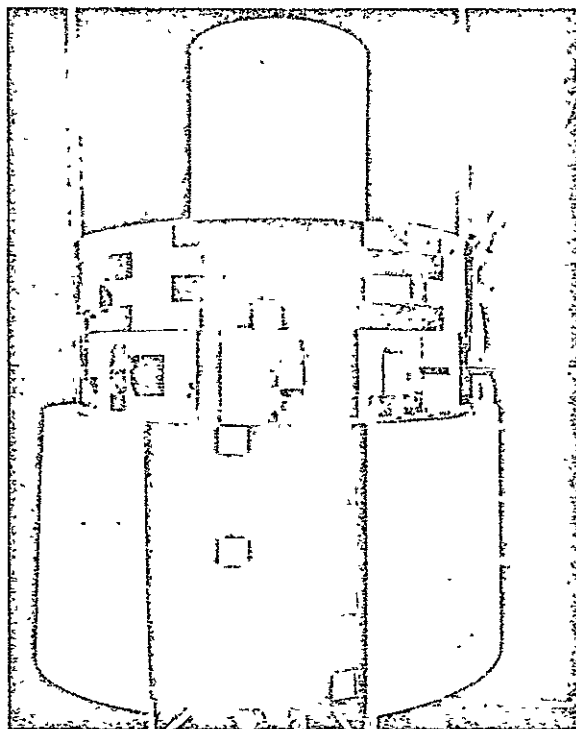


Fig. 13 1/2 Scale Thermal Model of Pioneer  
Solar Probe Spacecraft

energy due to excessive skin temperatures due to higher than expected surface absorptances for tungsten lamp energy. Some tests were performed using a lamp array of 28 lamps and some with an array of 6 lamps to observe changes due to filament temperatures. A brief summary of thermal tests using the model is presented in Table 6.

The computed values were determined from the thermal analyzer program using model design and test boundary conditions. As can be seen by inspection of the data, the tungsten filament lamps resulted in higher than anticipated surface temperatures which led to high internal temperatures. Studies following completion of the test program showed that the higher temperatures were caused by higher than anticipated

Table 6

MODEL TEST RESULTS FOR SOLAR PROBE  
(Temperature °K)

Source	Solar	Carbon Arc	Tungsten	Solar	Tungsten	Tungsten	Solar	Tungsten
Intensity Solar Constants	1.04	1.04	0.90	4.92	4.92	4.22	9.0	9.0
Number of Lamps			28		28	6		28
Internal Power Watts	29.5	29.5	29.5	30	30	30	6	6
Approach	Computed	Test	Test	Computed	Test	Test	Computed	Test
Location								
Upper Solar Cell Array, Outside Surface	246	260	282	359	416	387	418	482
Upper Solar Cell Array, Inside Insulation	268	271	285	314	338	330	337	374
Viewing Band, Outside Surface	204	230	278	257	386	336	288	434
Viewing Band, Inside Insulation Surface	270	274	286	279	333	325	266	364
Lower Solar Cell Array upper section, Outside Surface	332	336	324	360	361	364	360	370
Lower Solar Cell Array upper section, Inside Insulation	255	255	251	266	272	276	254	288
Experiment Booms	218	239	277	354	376	344	277	430
Equipment Platform	278	278	282	283	298	300	261	310

lamp emission at wavelengths beyond  $5\mu$ . The existence of considerable energy at the lower wavelengths results in an increase in  $\alpha/\epsilon$  for the OSR surfaces. Tests were made on the lamp arrangement using a thermopile detector, both with and without a quartz filter, roughly to evaluate the energy distribution of the source. Table 7 presents the results obtained.

Table 7  
ENERGY DISTRIBUTION OF TUNGSTEN SOURCE

Source Condition	Lamp Voltage	Percent Energy	
		Below $5\mu$	Above $5\mu$
Tungsten, 28 lamps			
0.90 sun	10.3	16	84
4.92 suns	40	42	58
9.0 suns	63	47	53
Tungsten, 6 lamps			
1.12 suns	34	51	49
4.22 suns	115	62	38

The source data presented in Table 8 in combination with the model test results allowed the computation of the effective  $\alpha/\epsilon$  ratio for each of the three major sections. The results of the computation are given in Table 8.

The data obtained from model tests, lamp calibration, and the computer analyzer proved of considerable value in recommending the source conditions necessary for testing of the flight hardware. The fact that an exact model could not be constructed due to funding and material limitations did not detract from the overall worth of the study since model results were referenced back to the prototype using the computer analysis. The combination of a test model and computer model proved most advantageous for completion of the program objectives in spite of the many areas where the model criteria were not satisfied.



Table 8

EFFECTIVE  $\alpha/\epsilon$  OF MAJOR SECTIONS FOR VARIOUS SOURCES

Source Condition	Upper Array	Viewing Band	Lower Array
Solar	0.45	0.10	0.84
Carbon Arc	0.45	0.10	0.84
28 Lamp Tungsten			
10.3 V	0.92	0.87	1.0
40 V	0.79	0.64	0.99
63 V	0.76	0.58	0.98
6 Lamp Tungsten			
34 V	0.74	0.56	0.99
115 V	0.66	0.43	0.98

## 6.2 ORBITING TELESCOPE MODEL

The second complete system which serves to demonstrate the modeling approach is that of a large aperture orbiting telescope. The program of interest was the performance of a preliminary thermal study on the conceptual design of a 2-m aperture reflective telescope in synchronous orbit (Refs. 15 and 19).

The 2-m telescope prototype configuration used for this study is shown schematically in Fig. 14. The overall length of the telescope tube is 12 m with an aperture of 2.38 m in diameter. The telescope consists of a 2-m-diameter active optical segment primary mirror arranged in a hexagonal array of three regular hexagonal segments.

The arrangement provides a Cassegranian f/3 parabolic reflector optical system. The secondary optic is mounted on a supporting structure at a distance of approximately 4.76 m from the primary and is maintained at that distance by three quartz spacer rods which are erected after achieving orbit and furnish the required structural support during the orbital mission. The telescope barrel consists of five multilayer insulated aluminum honeycomb cylinders and one plastic honeycomb cylinder at the barrel opening. Each cylinder collapses over the adjacent cylinder toward the primary mirror

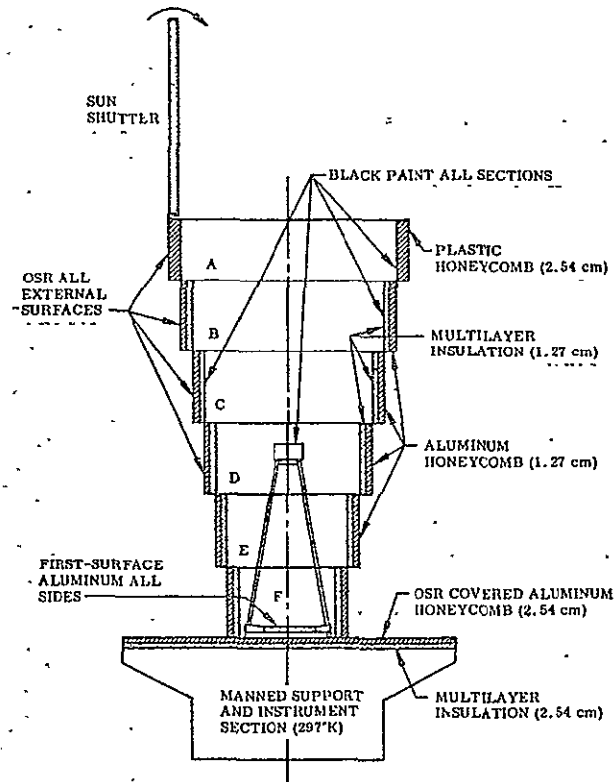


Fig. 14 Schematic of 2-m Telescope Conceptual Design

to minimize volume during the launch phase. After injection into a 24-hr synchronous orbit, the telescope is erected and placed into operation by a crew of astronauts who dock with the telescope's manned support section utilizing a LEM vehicle.

Optimum thermal-optical performance of the telescope requires minimal thermal gradients in the optics, particularly in the primary mirror segments, elimination of thermal transients imposed by the varying thermal inputs during orbit, and an average steady-state temperature near the inversion point of the thermal expansion of fused quartz which is in the range of 150°K.

Preliminary thermal design studies resulted in a thermal design that could provide near-optimal thermal conditions through utilization of passive thermal control techniques in combination with an active sun shutter at the telescope tube opening. The shutter would control the amount of direct solar illumination of the telescope

interior. The analysis completed in support of thermal design showed that use of the following materials and thermal control surfaces would be required to achieve the program objectives.

- ⊙ Plastic honeycomb, 2.54-cm thick, for the front cylindrical section.
- ⊙ Aluminum honeycomb, 1.27-cm thick, for the other five cylindrical sections which are also insulated on the interior with 1.27 cm of high performance mulilayer insulation.
- ⊙ An optical solar reflector thermal control surface material, having a solar absorptance of 0.05 and infrared emittance of 0.80, for all exterior surfaces of the telescope tube and mounting platform.
- ⊙ A highly diffuse optical black paint coating for all interior surfaces except for the primary mirror and a band on the surrounding telescope tube immediately adjacent to it, surfaces of the primary mirror mounting platform, and the reflecting surface of the secondary mirror.
- ⊙ First surface aluminum coating for all interior surfaces not coated with the black paint.

The proposed mission for the telescope anticipates operation of the system in both an earth-oriented and a space-oriented configuration. These orientations result in entirely different thermal responses due to the differences in solar illumination of the exterior and interior surfaces and operation or lack of operation of the sun shutter.

The model study was again initiated by establishing a complete thermal analyses of the conceptual prototype system. A thermal-analyzer computer program was formulated on the basis of prototype properties and used to provide information on heat flow rates, temperatures, surface absorptances and, through variation of material parameters, an indication of the design sensitivity to changes in material thermal properties. The results of this study were used as major source of information for model design. It should be emphasized that the computer model contained numerous assumptions on the conductance of joints and structural attachments, on the influence of multilayer

insulation edges, and on the temperature dependence of thermophysical properties. These influences would be observable in the model by comparison with the computer results.

The overall results obtained from the analytical studies showed that the primary mirror would be nearly uniform in temperature at 175°K and undergo less than 1°K transients. The analysis also showed that the secondary mirror support rods could be expected to have a considerable temperature difference from end to end (~25°K) and to experience considerable transients (~±7°K). Finally, the analysis showed that the multilayer insulation would provide a nearly adiabatic wall with respect to energy entering the tube aperture and would effectively damp out external surface temperature transients. These three operating conditions were used as primary guidelines during design of the telescope model.

#### 6.2.1 Telescope Model

It was desirable that the model not only provide a direct indication of thermal performance but also, where possible, of the influence of thermal performance on optical performance. To meet both objectives requires concurrent satisfaction of both thermal and structural similarity criteria. The thermal modeling criteria are, as previously stated,

$$\frac{\rho^* V^* C^* T^*}{\theta^*} = A_I^* I^* = Q^* \frac{K^* A_n^* T^*}{X^*} A_i^* T^{*4}$$

The criteria for structural modeling can be derived in generalized form from a force balance on an elemental volume with applied forces and moments or from a particular

case wherein a force balance is performed on a specific structural member. The resulting criteria using either procedure are:

<u>Effect</u>	<u>Scaling Law</u>
Forces	$F^* = \sigma^* L^{*2} = E^* L^{*2} \gamma^* (\Delta T)^*$
Moments	$M^* = \sigma^* L^{*3} = E^* L^{*3} \gamma^* (\Delta T)^*$
Linear Distortions	$y^* = e^* L^* = L^* \gamma^* (\Delta T)^*$
Angular Distortions	$\phi^* = \tau^* L^* = (\gamma^* L^* / E^*) = L^* \gamma^* (\Delta T)^*$

In the above equations,  $\sigma$  is normal stress,  $e$  is strain,  $\tau$  is shear stress,  $E$  is the modulus of elasticity, and  $\gamma$  is the coefficient of thermal expansion. The laws are derived under the assumption that materials are functioning in the elastic region so that distortions are linearly proportional to forces, moments, and thermal effects.

While it was desirable to determine directly from model measurements the influence of thermal effects on optical performance of the primary mirror, it became apparent from the analytical results that this would be very difficult using either mechanical or strain gage measurement techniques. The prototype primary mirror was expected to experience an overall change in temperature of  $\pm 1^\circ\text{K}$  during each orbit with temperature differences from edge to center of less than  $1/2^\circ\text{K}$ . At  $175^\circ\text{K}$ , the coefficient of thermal expansion for quartz is approximately  $2 \times 10^{-7} \text{ }^\circ\text{K}^{-1}$ . Therefore, total dimensional changes in the prototype mirror would be on the order of  $0.2 \mu \text{ in./in.}$  This value lies below the sensitivity of normal strain measurement techniques. In the model, the measurement would be even more difficult since its size, as dictated by the available 8-ft diameter test chamber, would have to be on the order of  $1/6$ th that of the prototype. Dimensional considerations of this type are indicative of the inherent limitations in concurrent thermal and structural modeling of optical systems.

In each modeling problem it is necessary to initially establish the ratios of  $T^*$ ,  $\theta^*$ , and  $L^*$  that will be used throughout the model design. In most cases this initial selection of ratios is determined on the basis of an analytical prototype thermal performance study. Results of the study provide needed information on thermal levels

and, through parametric studies, on the sensitivity of major components to changes in properties and boundary conditions. For the telescope it was apparent from the analytical work that the model temperature would have to be elevated above that of the prototype to properly model external surface temperatures. External surface temperatures on the prototype were predicted to be as low as 75°K during earth shadowing with a high near 200°K under direct solar irradiation. The liquid nitrogen cooled walls of the test chamber have an operational temperature of 82°K which exceeds the predicted prototype skin temperatures. To achieve satisfactory modeling conditions it is necessary that the temperature ratio used in design of the model be on the order of 1.5 so that chamber background thermal levels will not influence model test performance.

A second consideration in selecting model ratios for the telescope is the time ratio involved. For the telescope prototype, the steady-periodic period in synchronous orbit would be 24 hr. It was desirable to accelerate this period as much as possible to avoid 24-hr continuous operation of the test facility while awaiting steady-periodic conditions. Acceleration of the test model period to no more than 2 hr was considered appropriate in terms of the necessary test conditions.

Having established the desired range of scale ratios (i.e.,  $T^* \geq 1.5$ ,  $\theta^* \leq 1/12$ ,  $L^* \approx 1/6$ ), it becomes a matter of successive approximations in preliminary design of each major component to permit selection of a final set of scaling ratios that can be achieved throughout the model design. For the telescope, it was found that a model design for the primary mirror had the least flexibility. Therefore, its design led to establishment of scale ratios for the remaining elements.

### 6.2.2 Primary Mirror Model Design

A number of approaches were considered for modeling of the three segment, quartz primary mirror within the limits of reasonable operating temperatures, length ratios, time constants, and ease of fabrication. Consideration was given to the use of both plastics and metals for purposes of obtaining a sufficiently high value of  $\gamma^*$ , the

ratio of thermal expansivities, to permit direct strain measurements. However, the thermal conductivities of these materials exceeded allowable lower and upper limits of  $K^*$  that could be used in combination with the necessary scale ratio (less than  $1/5$  to fit in the test chamber) and maximum temperature ratio (no greater than 2). This can be seen by consideration of the steady-state criteria,  $K^*A_n^*T^*/x^* = A_i^*T^{*4}$ . For identical geometry, as required for proper figuring of the mirror,  $A_n^* = A_i^*$  and the relation reduces to  $K^* = L^*T^{*3}$ . With the allowable span of length and temperature ratios (i. e.,  $1/7 < L^* < 1/5$  and  $1.5 < T^* < 2$ ), the selection of materials is limited to  $0.48 < K^* < 1.5$ . Unfortunately, neither metals nor plastics have properties which would provide ratios within this range, and therefore the selection was limited to glass. A study of thermophysical properties of glasses, followed by numerous mirror designs, indicated that Pyrex was the best material for construction of the primary mirror. A comparison of some of the properties of fused quartz (Corning 7940) at  $175^\circ\text{K}$  and of Pyrex at room temperature, the region of operation of the model, is presented in Table 9.

Table 9  
PROPERTIES OF QUARTZ AND PYREX

	Quartz ( $175^\circ\text{K}$ )	Pyrex ( $293^\circ\text{K}$ )
Thermal Conductivity ( $\text{W}/^\circ\text{K}\text{-m}$ )	$1.12 \times 10^{-2}$	$1.13 \times 10^{-2}$
Specific Heat ( $\text{J/g-}^\circ\text{K}$ )	0.464	0.690
Density ( $\text{gm/cm}^3$ )	2.3	2.45
Thermal Expansion Coefficient ( $\text{cm/cm-}^\circ\text{K}$ ) $\approx 2 \times 10^{-7}$		$3.77 \times 10^{-6}$
$K^*$		1.008
$C_p^*$		1.5
$\rho^*$		1.06

In addition to considerations of test chamber size, selection of the length scale ratio was based upon the practical consideration that considerable reduction in cost could be achieved by the purchase of glass blanks for the primary mirror as off-the-shelf

items. These considerations led to selection of a scale ratio  $L^* = 1/6.43$ . For this length ratio, and the use of Pyrex, the ratios preserving the influences of radiation and conduction in Eq. (6.2) yields the following for identical geometry:

$$T^* = (K^*/L^*)^{1/3} = [(1.008)(6.43)] = 1.86$$

$$\theta^* = \rho^* C^* L^{*2} / K^* = (1.06)(1.5) / (6.43)^2 (1.008) = 1/26$$

These ratios were quite satisfactory in terms of being easily attainable during laboratory testing of the model. The temperature ratio of 1.86 raised the model temperature from the prototype level of 175 to 326°K, a range easily produced in the liquid nitrogen shrouded test chamber. The time ratio of 1/26 reduced the 24-hr orbital period of the prototype to approximately 55 min for the model and allowed acceleration of the test program. Figure 15 presents a photograph showing the primary mirror, secondary optics, and support rods.

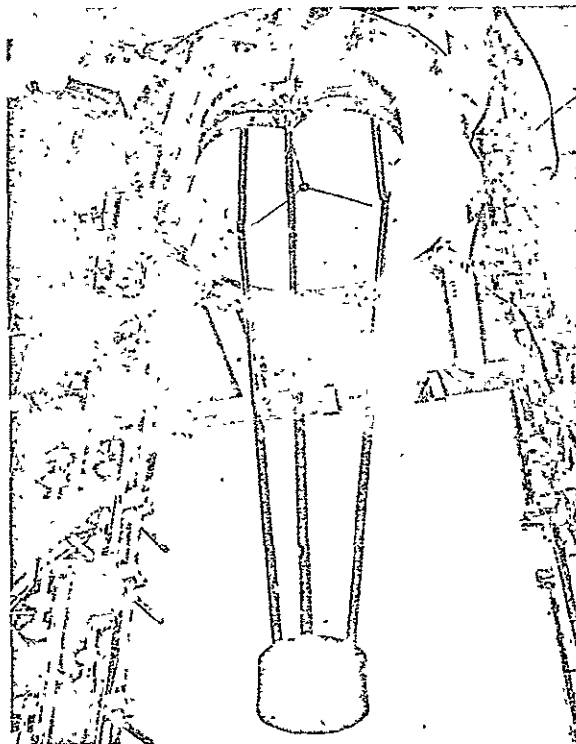


Fig. 15 1/6.43 Scale Model of 2-m Optical System



### 6.2.3 Secondary Support Rod Model Design

While direct measurement of thermal distortions on the model of the primary mirror was not possible, such was not the case for the secondary support rods. Analytical predictions indicated cyclic thermal changes for the rods on the order of  $\pm 25^\circ\text{K}$  with a temperature difference between the rod ends on the order of  $30^\circ\text{K}$ . This magnitude of thermal variations coupled with the overall rod length permitted a model design that included direct measurement of rod elongation.

Since the design required conformance to the primary mirror ratios  $T^* = 1.86$  and  $\theta^* = 1/26$ , material properties and available sizes were sought which provided these values. Thin wall stainless steel and titanium tubes were considered along with five varieties of laboratory glassware. During this selection process, the thermal effects of required instrumentation leads and black surface coatings as required by the prototype were accounted for. The best match to the requirements was obtained with Pyrex tubing with an outside diameter of 12 mm and an inside diameter of 10 mm, and a 2-mil coating of black silicone thermal control paint. Each of the three support tubes was instrumented with four equally spaced thermocouples and a pair of unbonded strain gages. The pair of gages provided two legs of a Wheatstone bridge for measurement of the total expansion of the tubes. While the tube dimensions were carefully selected to meet the thermal modeling requirements, the design obviously failed to meet the structural modeling criteria given previously since geometric identity is not provided in the model. The use of 12-mm-diameter tubing results in severe geometric distortion of the prototype except for length dimensions. For this reason, the relation between forces, moments, and thermal stresses was not preserved in the model. However, since the support rod system was not constrained at both ends, thermal stresses in the rods did not introduce forces or moments into the support system. Under these conditions, geometrical distortion was allowable and rod elongation was related only to the thermal expansion characteristics. The elongation ratio for the rods is given by

$$y^* = L^* \gamma^* (\Delta T)^* = \gamma^* (1/6.43)(1.86) = \gamma^*/3.46$$

Taking a coefficient of thermal expansion for Pyrex equal to  $3.77 \times 10^{-6}$  cm/cm-°K for the temperature range of 294 and 422°K and an expansion coefficient for fused silica of  $2 \times 10^{-7}$  cm/cm-°K for the prototype operating temperatures gives  $y^* = \gamma^*/3.46 = 5.45$ .

#### 6.2.4 Telescope Model Multilayer Insulation

The problems of modeling the multilayer insulated telescope tube were significant since the tube supported large circumferential thermal gradients and experienced a considerable thermal transient during its earth-oriented orbit. In view of the importance of the tube insulation in providing an adiabatic wall, an experimental program was undertaken to develop criteria for modeling the insulation and honeycomb skin system at an elevated temperature ratio.

Insulation tests were designed to investigate the possibility of using a materials preservation approach and a  $T^* > 1$  in design of the 1/6.43 telescope model. For most solid materials, thermal conductivity does not vary with changes in the length of the heat flow path. This is not the case for multilayer insulation where, in addition to being temperature dependent, the thermal conductivity is also dependent upon the number of layers in the wrap and upon the wrap density. Consequently, reducing insulation thickness according to the specified length scale-ratio can cause sizable changes in thermal conductivity.

The insulation studies involved the design, construction, and testing of two insulation models having similar thermal behavior. The larger of the two models was 76 cm in diameter and 186-cm long. The smaller model was geometrically identical to the larger and was designed to be a half-scale thermal model of the larger system. Its diameter was similar in size to that planned for the 1/6.43 scale thermal model. The size and configuration of the insulation models were chosen on the basis of test chamber size and a desire to duplicate the difficulties associated with fabrication of the insulation required for the prototype telescope and the telescope thermal model. Temperature conditions for the insulation models were scaled relative to the prototype

system, with the temperature ratios ( $T^*$ ) for the full- and half-scale models being 1.44 and 1.82, respectively.

Characteristics of the multilayer insulation for the larger insulation model were identical to those planned for the prototype telescope. The insulation consisted of 36 alternate layers of double aluminized Mylar and glass-fiber paper. This gave a blanket thickness of approximately 1.27 cm with a layer density of 28.3 layers/cm, which in terms of insulation performance gives a minimum effective thermal conductivity (or optimum heat flux per unit thickness) for the boundary temperatures of interest to the prototype. The results obtained from tests of the large wrap were compared to analytical predictions and then extrapolated to higher thermal levels for application to the 1/2-scale smaller insulation model.

The model criteria for materials preservation are that  $\rho^*$ ,  $C_p^*$ , and  $K^*$  be equal to unity giving  $T^* = (1/x^*)^{1/3}$ , where  $x^*$  is the insulation thickness ratio. For identical geometry,  $x^* = L^*$  and the 1/2-scale insulation model would use 18 layers of insulation. However, the increase in model temperature ( $T^* = 1.26$ ) results in a lower wrap conductivity so that  $K_m \neq K_p$  (i. e.,  $K^* \neq 1$ ). This change in material properties requires that the approach used preserve the relation  $K^*/x^* = 2$  through distortion of insulation thickness. Following this procedure resulted in selection of a 27-layer wrap for the smaller insulation model.

Test results obtained from the 36 layer and 27 layer wraps are presented in Figs. 16 and 17. Figure 16 presents the total heat input to the models as a function of hot boundary temperature. In this figure the 1/2 size (27 layer) results have been referred to the 36 layer system through the model ratios  $T_m = (1/1.26)T_p$  and  $Q_m = (1.59)Q$ .

The test results presented in Fig. 17 show the thermal conductivity of the two wraps as a function of the radiation potential  $\sigma(T_h + T_c)(T_h^2 + T_c^2)$  where  $T_h$  and  $T_c$  are the hot and cold boundary temperatures, respectively. These results have not been normalized through the model laws.

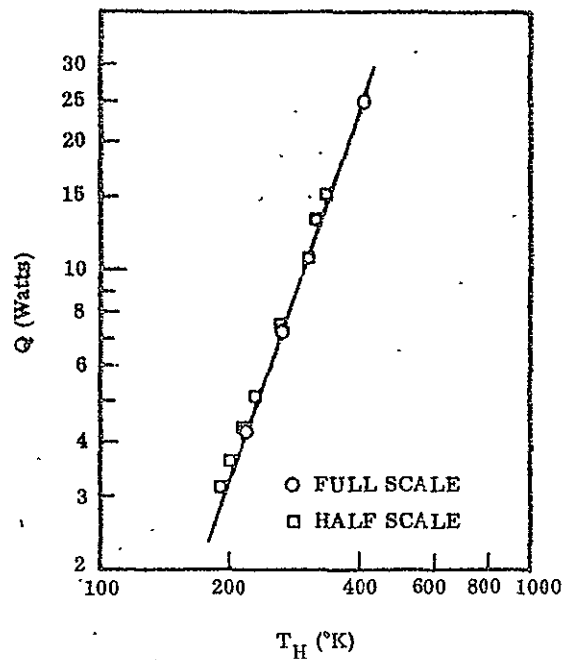


Fig. 16 Comparison of 36 and 27 Layer Multilayer Insulation Performance

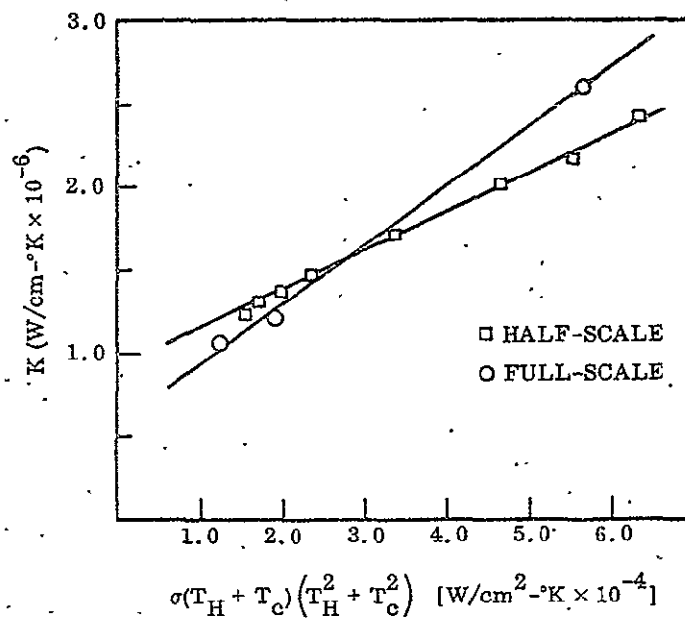


Fig. 17 Thermal Conductivity of Two Insulation Models

The performance of the full- and half-scale insulation wraps proved that the material could be modeled and provided the data required for design of the 1/6.43 scale model wrap of the prototype telescope.

For the telescope tube, it was of primary importance to model the insulation in such a manner that average model interior temperature would provide reasonable predictions of prototype conditions. The predictions obtained from the thermal analyzer program indicated that the average temperature of the telescope interior would not be strongly dependent on changes in insulation conductivity for approximately one order magnitude about the assumed value of  $4.8 \times 10^{-5}$  W/°K-m. This range of freedom permitted design of the model wrap to be based on the average temperatures predicted for the prototype and avoided the necessity to design for either maximum or minimum values. The prototype mean temperature selected for use in design of the model wrap was 122°K, corresponding to a model mean temperature of 227°K.

The model wrap was based upon the use of identical materials and the properties determined from the insulation experiments. The previous choice of  $L^* = 1/6.43$  and  $T^* = 1.86$  required that the perpendicular conductivity model according to  $K^*/x^* = 6.43$ , where  $x^*$  is the ratio of insulation thickness for identical wrap densities. The closest approach to meeting these requirements was a 13-layer wrap with an expected  $K^* = 2.36$  at the selected average temperature. Thus,  $x^* = 13/36 = 1/2.78$  and  $K^*/x^* = 6.56$  instead of the required 6.43.

It is apparent that the dependence of  $K^*$  on  $x^*$ , such that a specific thickness must be chosen to meet a specific  $K_m$  at a single temperature, allows adjustment of  $\theta^*$  only through changes in  $\rho$  and  $C$  on the model. However, since identical materials are used in the model and prototype, the wrap itself cannot be varied to provide the necessary adjustments. In addition, for the insulation it was determined that the temperature dependence of  $C$  results in  $C^* = 1.88$ , thus

$$\theta^* = \rho^* C^* L^* x^* = 1/9.35$$

rather than 1/26 as required. The large value of  $\theta^*$  for the insulation alone led to the necessity of considering the elimination of an external skin on the model and lumping the heat capacity of skin and insulation together. With this approach, the ratio of total heat capacitance becomes

$$(\rho^*V^*C^*)_{\text{total}} = \frac{(\rho_m V_m C_m)_{\text{insul}}}{(\rho_p V_p C_p)_{\text{skin}} + (\rho_p V_p C_p)_{\text{insul}}}$$

For the prototype properties, computation yields  $(\rho^*V^*C^*)_{\text{total}} = L^*/3.58$  and  $\theta^* = 1/23$ . This value is more in line with the required time constant and was used for the model.

Darkening of the tube interior was necessary and required the use of a 2-mil coating of black Thermatrol whose capacitance, when added to the insulation, resulted in an increase of the time ratio to  $\theta^* = 1/17.8$ .

The final design of the model insulation provided an overall skin system whose performance was expected to adequately simulate that of the telescope tube. While the distribution of heat capacitance was not identical to the prototype, this fact in itself would not alter the transient response. The most serious alteration of the transient behavior would be expected to be due to the differences in temperature dependence of specific heat and thermal conductivity for the model and prototype systems.

#### 6.2.5 Complete Telescope Model

The completed model consisted of the primary mirror, secondary mirror and support rods, manned section interface mounting platform, five multilayer insulated tube sections, one noninsulated front tube section, and a manually controlled sun shutter. Energy was supplied to outer boundaries of the model with separately programmed tungsten filament lamps that maintained surface temperatures at levels prescribed by the prototype thermal predictions. The assembled test model and lamp bank are shown in Fig. 18.

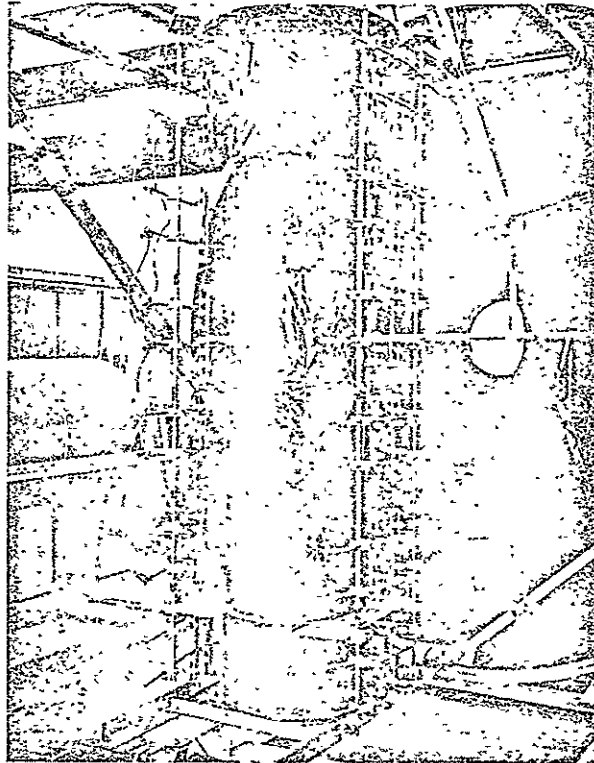


Fig. 18 Assembled 2-m Telescope 1/6.43 Scale  
Model Ready for Test

Typical results obtained after steady-periodic conditions were achieved are presented in Figs. 19 to 21. Figure 19 compares analytical and model predictions for the interior temperatures of Section B, the first insulated section near the barrel opening. The model predictions indicate an overall lower average temperature for Section B as well as a faster response of the surface to opening and closing of the sun shade. The more rapid response of the model surface was anticipated in view of the gross nature of the thermal analyser program where only two nodes were used to model the tube wall which consisted of 1.27-cm multilayer insulation and 1.27-cm of aluminum honeycomb. Such a simplified mathematical model would not result in an accurate prediction of interior surface temperatures for the first surface layer of insulation. No satisfactory explanation was found for the overall lower temperature of the test model predictions, indicating the need for a more thorough analysis of the energy transfer mechanisms in this region.

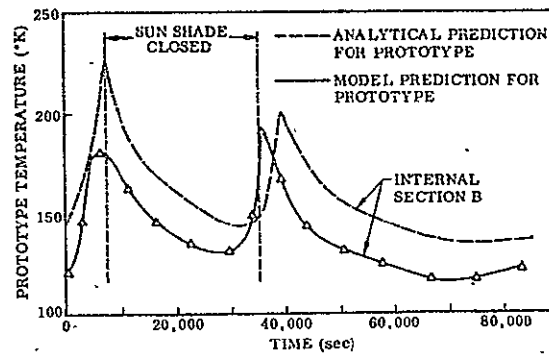


Fig. 19 Transient Thermal Behavior Predicted for Telescope Tube Interior at Section B

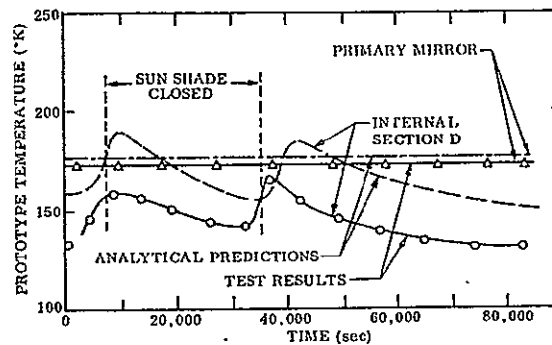


Fig. 20 Transient Thermal Behavior Predicted for Interior of Telescope Tube at Section D

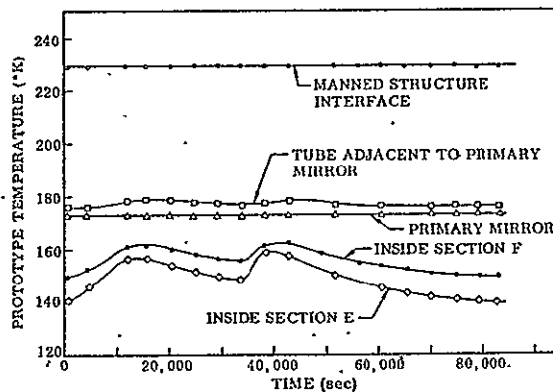


Fig. 21 Model Predictions for Temperatures of Regions Surrounding Primary Mirror



Figure 20 shows a comparison of test results and analytical predictions for Section D, the midpoint of the barrel, where the average of internal temperatures predicted by the test model are again low and the response to transient inputs more rapid than the analytical forecast. A comparison is also presented for the primary mirror temperature where close agreement was obtained with the analysis. Figure 21 shows the temperatures predicted by the test model for regions surrounding the primary mirror. These results clearly demonstrate the thermal stability of the mirror as related to its environment.

Temperatures on the prototype primary mirror were predicted from the test results and model ratios to be constant with time to within  $\pm 0.5^\circ\text{K}$ . Front-to-back temperature difference predictions indicated less than  $\pm 0.4^\circ\text{K}$  and edge-to-edge temperature differences were less than  $0.15^\circ\text{K}$ . These values fall well within the design goals of the prototype and confirm that the techniques selected for mounting the primary mirror to the manned interface structure were adequate in providing the required thermal isolation.

From the results obtained on the model, a maximum change in rod length for the prototype during its orbital transient was predicted, and a corresponding change in optical path between the primary mirror and exit optics was determined. The exact measurements of thermal expansion of the rods using strain gages were compared to computed values calculated from the temperature data and expansion coefficients. The results of the measurements are shown in Fig. 22. Exact agreement between the measured and computed values was not obtained. This was due to the fact that temperatures were known at only four locations on the rods requiring a gross estimate of the temperature distribution at the hot end. The results were satisfactory, however, in showing the feasibility of modeling the linear deformation of the quartz support rod members. As previously mentioned, structural modeling on the primary mirror was not attempted due to the very much lower deformations anticipated for the mirror sections.

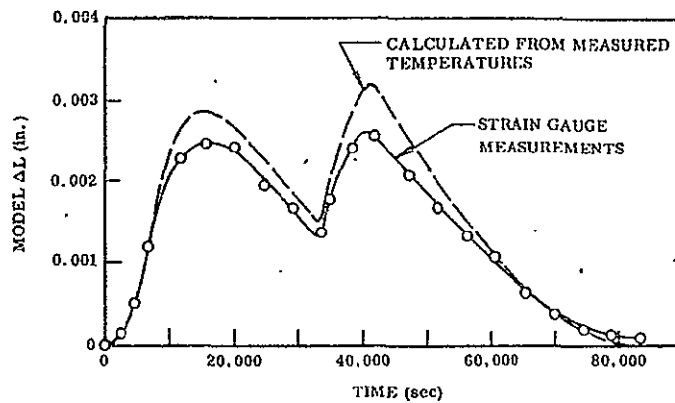


Fig. 22 Total Deformations of Secondary Support Rods on the 1/6.43 Scale Model

The data obtained on thermal deformations of the rods permitted predictions of changes in optical path length of the prototype system and showed that compensation by adjustment of the primary mirror mount was entirely possible.

#### 6.2.6 Summary of Telescope Model Study

The study completed on the telescope model provides several examples of both the advantages and limitations existent in using the model approach. The advantages of the method for this study were several. The model provided a direct indication that the overall approach used in thermal design was satisfactory. Thermal transients and gradients in the primary mirror fell below minimum acceptable levels. It was determined that average internal temperatures for the earth-oriented condition were established for the most part by sun shutter operating schedules rather than by the absolute performance of the tube insulation. Significant differences were observed between the analytical and experimental predictions for temperature distribution inside the tube which indicated the need for improvement of the analytical model for this region. Determinations of this type, during early stages, permit timely concentration of effort on clarification of performance uncertainties well before hardware design. The ability to run the tests at an elevated temperature and at an accelerated time scale was a very significant advantage over prototype test efforts.

The limitations observed during the study included difficulties in conforming strictly to the model criteria for several important regions. The secondary support rods were modeled in accordance with the thermal criteria; however, the structural criteria could not be satisfied. Noncompliance to the structural criteria was necessitated by the need for stiffer members in the model than those provided by the scale ratio  $L^* = 1/6.43$ .

Exact modeling of the multilayer insulated tube sections was not possible due to lack of appropriate materials to duplicate the insulation and honeycomb skin conductivities, and an inability to model the distribution of heat capacitance as found in the prototype. These difficulties were solved in a satisfactory manner for the telescope system. However, it is doubtful that the model design approach used would be satisfactory for a system whose thermal behavior was entirely dependent on the insulation properties.

Exact modeling of the primary mirror supporting structure was not possible due simply to a lack of design information on the prototype system. This led to the choice of a support system with maximum thermal isolation of the mirror from the mounting structure. The low conductance achieved may not be entirely representative of the prototype.

Advantages and limitations similar to those existent in the telescope model program will be found in nearly all hardware studies. Their influence on the value of the results must be evaluated on the basis of a careful analyses of the prototype and model designs for each specific thermal system.

### 6.3 TWENTY-FOOT-DIAMETER UNFURLABLE ANTENNA

The third and last complete system to be considered in this report consists of an orbiting 20-ft-diameter unfurlable antenna where thermal deformations of the parabolic shape are of prime concern.

A schematic of the system under consideration is shown in Fig. 23. The antenna extends from flexible mountings on the outer surface of the cylindrical spacecraft which houses necessary electronic components to perform the flight mission. The required parabolic shape is provided by flexible ribs that furnish support for a metallic coated loosely woven cloth which serves as the reflecting surface. Prior to launch, the supporting ribs are wrapped around the spacecraft and locked in that position. When orbit is achieved the locking mechanism is released and the ribs unfurl to provide the necessary antenna shape.

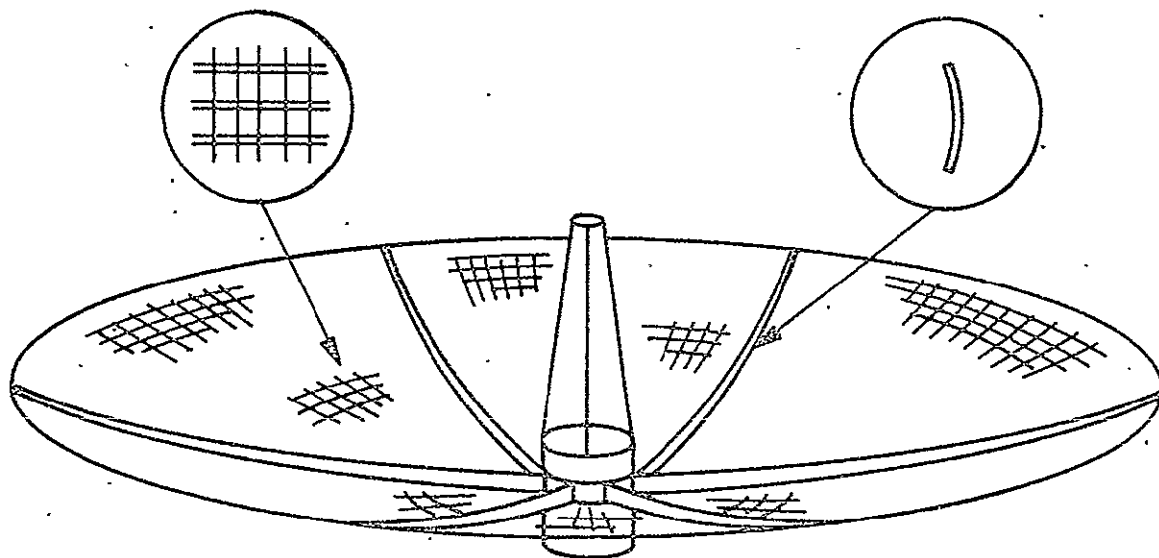


Fig. 23 Prototype Configuration of Unfurlable Antenna

The nylon cloth consists of woven threads which are coated with a thin metallic overcoating to provide desirable electrical properties and then again overcoated with a dielectric to obtain an acceptably high infrared emittance. The cloth weave is non-uniform with roughly twice as many threads running in one direction as there are in the other. This is shown by the enlarged view in Fig. 22. Each thread has a diameter of approximately 0.025 cm with an average spacing between threads of 0.18 cm. The weave provides a normal transmittance of incident energy equal to 67%.

The supporting ribs have a slight curvature to provide the necessary spring action and final rigidity and become smaller in height as they extend farther from the central vehicle. Their thickness is constant at 0.317 cm.

During early design stages, it became apparent that a thermal acceptance test of the system would be desirable so that thermal deformations of the antenna could be measured and the influence on antenna electrical performance evaluated. However, the overall vehicle size exceeded that of available test facilities which led to a study to determine the feasibility of modeling the system at roughly one-half scale. The objective of the model would be to provide data on the antenna and cloth thermal and structural behavior. Thermal modeling of the central satellite vehicle was excluded from the scope.

The major difficulty in modeling of the antenna is associated with the thermal and structural properties of the woven cloth. The cloth is a nonuniform weave resulting in variable structural properties in the X and Y directions. Laboratory measurements also disclosed that the coefficient of thermal expansion of the cloth is a strong function of temperature and both positive and negative coefficients were observed over the temperature range of interest (165 to 360°K).

Recalling that the structural modeling criteria are given by

$$\begin{array}{ll} \text{Forces} & F^* = \sigma^* L^{*2} = E^* L^{*2} \gamma^* (\Delta T)^* \\ \text{Moments} & M^* = \sigma^* L^{*3} = E^* \gamma L^{*3} \alpha^* (\Delta T)^* \\ \text{Distortions} & y^* = e^* L^* = L^* \gamma^* (\Delta T)^* \end{array}$$

The thermal criteria are, as before

$$A_I^* T^* = Q^* = \frac{K^* A^* T^*}{L^*} = A_I^* T^{*4}$$

Preservation of forces, moments, and distortions in the antenna requires that a specific, single valued, ratio of  $E^*\gamma^*$  be obtained under all operating conditions. To achieve this objective for a material whose thermal and structural properties are completely nonlinear becomes a major limitation in pursuit of a modeling program. The purpose of the remaining discussion in this section is to consider procedures which potentially circumvent the limitations imposed by the antenna cloth.

A cursory examination of the properties of woven fabrics leads directly to the conclusion that materials are not available that would provide a constant  $E^*\gamma^*$  over the temperature range of interest. Likewise, fabricating a "model" of the cloth using a different weave holds little promise unless a sizeable program is devoted to the development effort. Under these conditions it becomes necessary to use the same cloth in the model as is used in the prototype and also a  $T^* = 1$  which guarantees preservation of the required thermal-structural properties.

With  $T^* = 1$  and identical cloth in the model, the thermal model criteria, based upon cloth properties, become

$$A^*T^* = Q^* = \frac{1}{L^*} = 1$$

Quite obviously, the resulting  $L^* = 1$  dictates a full-scale thermal model which fails to circumvent the problem of test facility size.

An evaluation of the above result requires that one review the procedures used to derive the general modeling criteria. As previously mentioned, the criteria may be based either upon dimensional considerations applicable to the dominant heat transfer mechanisms existent in the radiation conduction coupled spacecraft system, or upon a specific equation resulting from an energy balance on a given system. Either approach should result in identical modeling criteria.

For the specific case at hand, i. e., the thermal behavior of the cloth, an energy balance on a single strand was established and included terms for solar absorption

and infrared emission on the outer surface and a term for conduction along the thread. Internal energy dissipation was not included. Because of the complex nature of the doubly overcoated thread, each of which contains roughly 20 strands, an exact analytical determination of the relative importance of internal conduction and external radiation in setting the temperature distribution along the thread length was not obtained. However, the results of hand computations coupled with laboratory measurements indicated that conduction along the threads was of secondary importance when compared to radiative equilibrium of the outer surface. It was observed experimentally that illumination of a circular area of antenna cloth within a simulated space environment resulted in heating of the spot, but that areas removed from the spot by 5 to 10 thread diameters experienced a negligible increase in temperature. These observations permit the assumption, for purposes of designing a model, that point to point temperatures in the cloth are set entirely by radiation equilibrium with the surroundings and that thermal conductivity can be neglected. Therefore, the thermal model criteria for the cloth become  $A_i^* I^* = A_i^* T^{*4}$ , and with  $T^* = 1$ ,  $A_i^* = A_i^*$ . The previous assumptions of identical surface properties in the model and prototype still apply. These criteria may be satisfied by use of the same cloth in the model as that used in the prototype.

Use of the same cloth in the model and prototype gives  $E^* = 1$ ,  $\gamma^* = 1$ , and with  $T^* = 1$ , as desired for the test, the model criteria become:

For the cloth

$$T^* = (\Delta T)^* = E^* = L^* = \alpha^* = F^* = 1$$

$$A_i^* = A_i^*$$

For all remaining components

$$T^* = (\Delta T)^* = \alpha^* = F^* = I^* = 1$$

$$\frac{\rho^* C^* V^*}{\theta^*} = Q^* = A_i^* = \frac{K^* A_n^*}{L^*} = A_i^*$$

$$F^* = E^* L^{*2} = 1 \quad ; \quad E^* = \left( \frac{1}{L^*} \right)^2$$

$$M^* = E^* L^{*3} \gamma^* \quad ; \quad M^* = L^*$$

$$y^* = L^*$$

The thermal and structural properties of the ribs must be in accord with the above criteria.

The first modeling approach to attempt in any program is to establish a design where identical geometry can be used in the model and prototype. This is of particular importance where both thermal and structural properties are to be studied since conducting paths and strength properties are both of importance. For the ribs, preservation of geometry with  $F^* = I^* = T^* = 1$  gives  $A_n^* = A_i^* = A_l^* = L^{*2}$ . The material must, for roughly a one-half scale model, then conform to  $K^* \approx 1/2, E^* \approx 4$ .

A survey of solid materials was performed in search of properties which would satisfy these values at the model temperature. Table 10 presents a partial list of the materials reviewed and covers the full range of properties studied at room temperature.

The summary provided in Table 10, which spans nearly the full range of available material properties, clearly indicates that no material has both the conductivity and stiffness required for solution of the problem. For example, while ingot iron (available in sheet form) and phosphor bronze provide a  $K^*$  near 0.5, their  $E^*$  is far removed from the necessary value of 4. Additionally, only a few materials have an  $\gamma^*$  that approaches unity. The largest thermal expansion coefficient found for any metal having a low thermal conductivity was 0.91, that of a iron base alloy (W545). However, its  $E^*$  and  $K^*$  are not acceptable. The remaining materials surveyed led to the conclusion that a nondistorted, geometrically identical thermal-structural model could not be designed from commonly available material.



Table 10  
MATERIAL PROPERTIES AT ROOM TEMPERATURE

Type	K (W/cm-°K)	K*	E $\times 10^6$ (Newtone/M <sup>2</sup> )	E*	$\alpha$ (°K) <sup>-1</sup>	$\alpha^*$
7075 Al	1.21	1	$6.9 \times 10^4$	1	$21.2 \times 10^{-6}$	1
Ingot Iron	0.66	0.54	$20.6 \times 10^4$	2.8	$12.2 \times 10^{-6}$	0.58
Low Carbon Steel	0.47	0.39	$20.7 \times 10^4$	2.9	$15.1 \times 10^{-6}$	0.71
Iron Base (Cr-Ni)16-25-6	0.26	0.21	$19.5 \times 10^4$	2.7	$16.9 \times 10^{-6}$	0.80
Iron Base (Cr-Ni)W545	0.18	0.15	$19.6 \times 10^4$	2.7	$19.2 \times 10^{-6}$	0.91
Stainless Steel 304	0.16	0.13	$19.3 \times 10^4$	2.7	$17.3 \times 10^{-6}$	0.81
Cobalt Base Alloy Haynes 25 L-605	0.23	0.19	$23.4 \times 10^4$	3.3	$16.9 \times 10^{-6}$	0.79
Phosphor Bronze 521	0.62	0.52	$11.0 \times 10^4$	1.5	$18.2 \times 10^{-6}$	0.86

That no single material conforms to the model design is not unusual considering the restrictions already placed on the model. In fact, when more than one scale ratio is fixed because of scale size, materials limitations, or some other requirement, it is the exception rather than the rule that geometric identity can be maintained.

The apparent lack of a suitable material for maintenance of geometrical identity forces the designer to consider geometrical distortion to satisfy certain of the model criteria. For the antenna ribs it is necessary that the model preserve stiffness, elongation, solar absorptance and infrared emittance to provide the necessary similarity of thermal distortions. Since the ribs are long, slender, of uniform thickness, attribute their rigidity mainly to the curved cross-section, and have negligible thermal gradients through the thickness, it is a possibility that similarity could be obtained through geometrical distortion of thickness. Assuming that thickness distortion is allowable, it is possible to pursue a design where the rib thickness does not conform to  $L^*$  while the overall design provides proper values for  $F^*$  and  $K^*A_n^*$ . Representing the rib thickness by  $t$  and its cross-sectional area by  $A_n$  gives

$$A_n^* = L^*t^*$$

where the rib major dimensions are still represented by  $L^*$ , i. e., they are not distorted. The thermal modeling criteria for the ribs may now be written as

$$Q^* = A_I^* = \frac{K^* A_n^*}{L^*} = A_i^*$$

$$Q^* = L^{*2} = \frac{k^* L^* t^*}{L^*} = L^{*2}$$

which gives

$$t^* = L^{*2}/K^*$$

The structural criteria become

$$F^* = E^* L^* = E^* L^* t^* = 1$$

$$t^* = 1/E^* L^*$$

These results show that a length ratio for the model will depend upon the thermal and structural properties of the material used. Solving the two independent relations for  $L^*$  gives  $L^* = [K^*/E^*]^{1/3}$ . Table 11 presents computed length and thickness ratios for a variety of potential modeling materials.

Table 11  
LENGTH AND THICKNESS RATIOS FOR THICKNESS DISTORTION  
(All Properties at Room Temperature)

Material Type	$K^*$	$E^*$	$L^*$	$t^*$	$\alpha^*$
Phosphor Bronze	0.515	1.54	1/1.44	0.935	0.855
Magnesium AZ 61 A-F	0.486	0.625	1/1.08	1.73	1.19
Nickel Base Alloy U500	0.202	3.0	1/2.46	0.82	0.830
304 Stainless Steel	0.134	2.69	1/2.72	1.01	0.814
Iron Base (Cr-Ni) Alloy W545	0.153	2.73	1/2.62	0.96	0.907

Of the materials listed in Table 11, the best solution appears to be obtainable using the iron base alloy (W545) which gives an  $L^* = 1/2.62$ ,  $\alpha \cdot t^* = 0.96$ , and an  $\alpha^* = 0.907$ . The greatest drawback here is that  $\gamma^*$  is 10% too low; however, as was previously indicated, none of the high strength materials have an  $\alpha$  as large as aluminum. The  $t^*$  of 0.96 would allow use of the same gage materials for the model while  $T^* = F^* = 1$  are also obtained. The measured distortions of the model would be in accordance with  $L^* = 1/2.62$ .

An actual model of the unfurlable antenna was not designed, constructed, and tested. Therefore, test data are not available for inclusion in this report. The program planned for the model study called for considerable additional analytical work to be performed to assure that the suggested thickness distortion was thermally and structurally allowable. The variation of  $K^*$  and  $\gamma^*$  with temperature from 100 to  $-300^\circ\text{F}$  was to be established either from the literature or by direct laboratory measurement. It is entirely possible that changes in thermophysical properties over this range could seriously degrade model performance. Additional work was planned to confirm the assumption that thermal conductance in the antenna cloth could be neglected in modeling the system.

It is obvious that the deviations taken from the model criteria would result in less than an exact simulation of prototype behavior. However, the test effort on a model of the system could be used as a basis for confirming the accuracy of analytical predictions and thereby establish the confidence required for prototype design.

#### 6.4 SUMMARY OF COMPLETE SYSTEM MODELING

There are many other complete systems that could be used as further examples of the problems associated with modeling of complete systems. The three described by this report were included since all required information was available to the investigator. They provide typical examples of some of the limitations existent in modeling of complex systems and offer examples of satisfactory methods for achieving a realistic thermal model. Other prototype systems have been studied and reported in the

literature, and demonstrate other sources of difficulty. Since each separate spacecraft design has unique features, it is obvious that no general solutions can be offered for accomplishment of model studies. What is important to note is that possibilities frequently exist for achieving a model design using geometric distortion, materials substitution, temperature ratios other than unity, and compressed or expanded time scales. These methods are best utilized in conjunction with a thorough thermal analysis so that the sensitivity of prototype thermal behavior to changes in design parameters can be properly evaluated.

The combined analytical and experimental programs used for study of the solar probe and large aperture telescope serve as examples of programs where limits imposed by the prototype were successfully overcome so that a meaningful model test could be completed. Results obtained from the test programs provided a realistic base for evaluation of the prototype designs and also clarified the accuracy of analytical predictions. Following completion of the programs, it was possible to suggest prototype design changes and changes in analytical procedures with an attendant increase in confidence that the final prototype thermal designs would be successful.

## Section 7

### LIMITATIONS IN MODELING MULTILAYER INSULATION

#### 7.1 INTRODUCTION

Multilayer insulation as commonly used in the aerospace industry is constructed of a number of layers of highly reflective radiation shields with or without an interposed low-conductivity spacer material. Mylar of 0.25-mil thickness which has been aluminized on both sides to approximately 500 Å thickness is a common reflective shield. Spacer materials vary from none (in which case the reflective layer is mechanically deformed from perfect smoothness in order to lower conductive heat transfer) to a variety of low-conductivity materials (nylon, polyurethane, glass fibers) in a variety of forms (foams, nets, fiber mats). The properties of these multilayer composite insulations vary a great deal as can be observed in Table B-2. The dominant characteristic of all multilayer systems is the very low effective thermal conductivities ( $\sim 10^{-7}$  W/cm<sup>2</sup> K) which are attainable for one-dimensional heat flow perpendicular to the insulation layers.

The temperature dependence of all MLI systems precludes exact reduced scale modeling of MLI with the approach commonly referred to as "temperature preservation" in which  $T^* = 1$  and prototype materials are replaced in the model by materials with conductivities reduced according to  $K^* = L^*$ . Attempts to model according to the "materials preservation" scheme ( $T^* > 1$ ) will also be limited by the strong temperature dependence of the heat transfer properties of the MLI. Consequently, the construction of a thermal model for even the simplest of insulated systems involves distortion of the temperature field from that of an exact model. Insight into applications where approximations of prototype conditions may lead to serious errors and procedures to minimize these errors, as well as some recent experiment results, are discussed in succeeding sections.

The investigation of spacecraft summarized in Section 3 disclosed that application of high performance insulation could be broken down into two broad categories. Type I, where it is used as a "relatively adiabatic" barrier to direct radiation entering a temperature controlled area; and Type II, where it is used as a carefully designed minimum heat transfer insulation system. The most common application is Type I, where the MLI is installed around an instrument package which has a close thermal connection to other actively and/or passively controlled components of the vehicle. In these situations, the MLI provides a low-weight, economical, and reliable means of eliminating a variable and unwanted thermal load to a thermally sensitive area of the vehicle. The thermal performance of the prototype MLI for Type I applications is generally less than that anticipated on the basis of published one-dimensional values. This situation arises wherever the insulation system has a large number of "penetrations" (e.g., relatively high conductivity supports and wires) passing through the insulation blanket.

It has been shown analytically (Ref. 20) and experimentally that penetrations and other edge effects will degrade one-dimensional insulation performance significantly. Partly because of degradation and partly because of low weight per layer, the prototype insulations for Type I applications are overdesigned to the point where an order-of-magnitude increase in the insulation effective conductivity yields relatively minor perturbations in the temperature level of the package.

The construction of moderately reduced scale thermal models for Type I applications can be accomplished without a great deal of attention to accurate modeling of the MLI thermal properties. In practice (Refs. 14 and 15), the model insulation is commonly furnished with a distorted thickness so that the one-dimensional heat flow perpendicular to the insulation layers is in accordance with the modeling criteria. This is done as a rough approximation with the knowledge that the two-dimensional heat flow and time constants of the insulation will be seriously distorted.

In the case of Type II applications, a more exact modeling is required because the absolute properties of the insulation and heat flow paths are of prime importance.

One important example of this situation is the application of MLI to containers for long-term cryogenic storage wherein an accurate prediction of boiloff rate is crucial to sizing the prototype. Here the insulation is installed in large area blankets with precautions taken to thermally isolate penetrations from the insulation. One-dimensional heat flow is purposely achieved through careful design of the prototype for these cases giving the appearance that modeling would be straightforward. However, since material preservation is absolutely required and temperature preservation is also desirable (due to the strong temperature dependence of MLI heat transfer at these temperatures), modeling would seem impossible. In practice (Ref. 21), the problem of modeling the Type II system is approached using identical materials and temperatures, and with insulation discontinuities (joints, penetrations) scaled to the area. The largest question arising in the procedure is to what extent the two-dimensional heat flow fails to follow an area ratio assumption. This question is usually answered with the aid of thermal network calculations which may or may not (due in large extent to unknown variables and ungovernable parameters) be susceptible to extrapolation to prototype sizes. One important parameter that is seldom mentioned in connection with such problems is that of constructing and installing MLI systems with any high degree of reproducibility.

Further discussion of the Type II case will be given in the next section in which the modeling criteria are developed. For Type I applications, the same modeling procedures should be followed when feasible, although the experimental effort required to develop an accurate insulation blanket may be considerably shortened by relying on published MLI data.

## 7.2 MULTILAYER INSULATION MODELING AT ELEVATED TEMPERATURE ( $T^* > 1$ )

For very low temperatures in the prototype, it is frequently advantageous to work with elevated model temperatures. When MLI is an important thermal component, such modeling requires an accurate knowledge of the temperature-dependent properties of the prototype insulation. A relationship has been developed and successfully

employed to correlate experimental data on one-dimensional MLI heat flux and boundary temperatures (Ref. 22), and is given by:

$$Q/A = B(T_H + T_C) \frac{(T_H - T_C)}{t} + \frac{C}{tN} (T_H^{4.67} - T_C^{4.67}) \quad (7.1)$$

Where  $T_H$  and  $T_C$  are the hot and cold boundary temperatures,  $N$  is the number of layers per unit thickness, and  $t$  is the insulation thickness. The coefficients  $B$  and  $C$  relate to solid conduction and radiation heat transfer in the insulation and are temperature independent. The solid conduction coefficient is dependent on the layer density (the conduction is essentially controlled by interface contact resistance between layers) and is determined by fitting Eq. (7.1) to experimental data. The coefficient  $C$  can be evaluated from basic optical properties of the components of the MLI. The appearance of temperature to the 4.67 power is a result of the temperature dependence of the reflective shield emissivity. In many cases, experimental data can be satisfactorily fitted by Eq. (7.1) with the radiation term in the form  $T_H^4 - T_C^4$  where  $C$  is treated as a free parameter to accommodate a slowly varying emissivity.

Although it is not possible to explicitly define a thermal conductivity for MLI due to its discontinuous properties, it is useful for understanding of the modeling approach to make use of an effective thermal conductivity concept. This may be defined by dividing Eq. (7.1) through by  $(T_H - T_C)/t$ . This conductivity can then be used to characterize the insulation overall performance based on boundary temperatures.

The effective conductivity is given by

$$K_I = B(T_H + T_C) + \frac{C}{N} \frac{(T_H^{4.67} - T_C^{4.67})}{(T_H - T_C)} \quad (7.2)$$

Using this definition the heat flux is

$$Q = K_I A \frac{(T_H - T_C)}{t} \quad (7.3)$$



As shown by Eq. (7.1), the conductance of MLI depends not only on material properties but also on spacing of the layers. At wide spacings, where the layers are not in contact, the conductivity is totally a function of thermal radiation transfer through the multiple layers. As the blanket is made thinner, solid conduction begins to increase the conductivity until at high layer densities (i.e., approximately 40 layers/cm) the conduction is dominant in determining the insulation properties.

Heat flow in a direction parallel to the insulation layers is governed by a thermal conductivity which is typically two to three orders of magnitude higher than the conductivity normal to the insulation layers. The parallel conductivity is generally constant above room temperature for MLI systems employing a spacer material and exhibits a linear temperature dependence down to cryogenic temperatures (Ref. 23). Since conductance along the layers degrades the one-dimensional properties, insulation systems designed for maximum efficiency are constructed with barriers to minimize parallel heat transfer. A first approximation to MLI modeling is therefore taken as the preservation of heat transfer in the normal direction. Once this is accomplished, the effect of distortion on heat flow in the parallel direction can be evaluated quantitatively from the modeling criteria.

Recent measurements on an aluminized mylar-silk net MLI system, using a fixed number of layers at various densities, show the increase in heat flux as layer spacing is decreased. The measurements were made using fixed boundary temperatures of 278° K and 80° K. Results for zero spacing were obtained by extrapolation from the lowest density used.

Heat Flux Density (Q/A) for Various Layer Densities in MLI  
(aluminized mylar-silk net)

Layer Density Layers/cm	Layer Density Layers/in.	Heat Flux Density W/M <sup>2</sup>
0	0	$1.64 \times 10^{-1}$
16	40	$3.36 \times 10^{-1}$
24	60	$6.76 \times 10^{-1}$
31	80	$12.0 \times 10^{-1}$
39	100	$18.9 \times 10^{-1}$
55	140	$35.2 \times 10^{-1}$

Assuming that the radiation term in Eq. (7.1) accounts for the heat flux at zero layers per cm, it is seen that the conduction term becomes of equal importance for a spacing as low as 16 layers/cm. At 31 layers/cm, the conduction begins to dominate the system. It is of interest to note that most wraps in current use utilize densities on the order of 30 layers/cm.

### 7.2.1 Material Preservation at Elevated Temperature

The basic criteria for constructing a complete system thermal model are given by:

$$\frac{\rho^* V^* C^* T^*}{\theta^*} = \frac{K^* A_n^* T^*}{L^*} = A_i^* T^{*4} = Q^* \quad (7.4)$$

where the nomenclature is as defined in section 2.1. Thus, to model a prototype for which radiation and solid conduction are intercoupled, it is necessary that

$$K^* = \frac{A_i^*}{A_n^*} L^* T^{*3} \quad (7.5)$$

in order to preserve the temperature field. If geometric identity is maintained (i.e.,  $A_i^* = L^{*2}$ , etc.) then all conductivities must be in the ratio

$$K^* = L^* T^{*3} \quad (7.6)$$

With materials preservation,  $K^* = 1$ , and the temperature ratio is given by

$$T^{*3} = \frac{1}{L^*} \quad (7.7)$$

However, this immediately becomes an approximation due to the temperature dependence of the conductivities of all materials used in the prototype.

As shown by Eq. (7.1), the MLI conductivity is strongly temperature dependent. Therefore, errors can be quite significant for even slightly reduced materials preservation scale models operated at elevated temperatures. To circumvent increases in thermal conductivity due to an increase in temperature, it is possible to distort the wrap thickness so that  $t^* > L^*$  with  $T^*$  maintained at the proper value for the inner and outer boundaries only.

An estimate of the distortion required can be gained through use of Eq. (7.1). From that equation the model criteria for MLI are given by:

$$Q^* = \frac{A^* B^* T^{*2}}{t^*} = \frac{C^* A^* T^{*4.67}}{t^* N^*} \quad (7.8)$$

Using a materials preservation approach, it is assumed that the model wrap will be constructed using the same materials as the prototype (gives  $C^* = 1$ ), and layer density and compressive load will be the same ( $B^* = N^* = 1$ ). However, the number of layers and thickness will not be identical to the prototype ( $t^* \neq 1$ ). Using this assumed approach on the model gives

$$Q^* = \frac{A^* T^{*2}}{t^*} = \frac{A^* T^{*4.67}}{t^*} \quad (7.9)$$

This relation can be satisfied only for  $T^* = 1$  indicating that an elevated temperature model cannot be achieved for a wrap where conduction and radiation are of equal importance. The data presented above show that this condition is present for layer densities in the range  $0 < N \leq 24$  layers/cm. For densities greater than the upper limit it is apparent that conduction dominates the behavior and as an approximation the radiation term in Eq. (7.1) can be ignored for formulation of model criteria. For the the higher layer densities, the model criteria for the insulation become

$$Q^* = \frac{A^* T^{*2}}{t^*} \quad (7.10)$$

Recalling that the criteria for the remaining components with  $K^* = 1$  are

$$Q^* = \frac{A_n^* T^*}{L^*} = A_i^* T^{*4}$$

gives

$$\frac{A^* T^{*2}}{t^*} = \frac{A_n^* T^*}{L^*}$$

Since for the perpendicular direction  $A_n^* = A^* = L^{*2}$  and the model is designed to conform to  $T^* = (1/L^*)^{1/3}$ , we find

$$t^* = T^* L^* = (1/L^*)^{1/3} L^* = L^{*2/3} \quad (7.11)$$

Thus, on the basis of a conduction dominated MLI system, it is found that the number of layers or conversely the insulation thickness should be modeled to two-thirds of the overall scaling ratio for a materials preservation model. For example, if a materials preservation model were designed to a scale ratio of  $L^* = 1/2$  and the prototype contained a 36 layer wrap of MLI then the model wrap would have  $t^* = (1/2)^{2/3} = 0.63$  and consist of 22 layers. This example is discussed in more detail in section 7.3 where tests were performed to establish the validity of this approach.

If an MLI system is employed in which the solid conduction term of Eq. (7.1) is small, the  $K^*$  ratio would increase faster than  $T^{*3}$ . The model criteria for this case are according to Eq. (7.1) given by

$$Q^* = \frac{C^* A^* T^{*4.67}}{t^* N^*} \quad (7.12)$$

Once again, this ratio must be the same as the conductive ratio for all other portions of the spacecraft. Therefore, we must preserve

$$\frac{C^* A^* T^{*4.67}}{t^* N^*} = \frac{K_n^* A_n^* T^*}{L^*} = A_i^* T^{*4} \quad (7.13)$$

As before we assume that  $C^* = N^* = K^* = 1$ ,  $A^* = A_n^* = A_i^*$  for the perpendicular direction, and that the temperature ratio is given by  $T^* = (1/L^*)^{1/3}$ . This gives for the thickness ratio

$$t^* = (1/L^*)^{0.22} \quad (7.14)$$

This result indicates that the model would require an insulation with a  $t^* > 1$  for  $L^* < 1$ . This situation is not the usual one since most wrap densities are not in the very loose regime where radiation dominates.

Prototypes for which the assumption of one-dimensional flow is invalid, or at best is a poor approximation, can still be adequately modeled according to the preceding methods. Whether the model will be seriously in error will depend on a combination of the scale ratio, the temperature dependence of the particular MLI, the type of use for the MLI (see section 7.1), and the nature and size of the temperature gradients in the MLI. An exact evaluation of the errors introduced by MLI thickness distortion can often only be answered with the help of a complete thermal network analysis or subsidiary experimentation.

In general, the necessity to use  $t^* > L^*$  will serve to increase the heat transfer in the parallel direction. If the insulation temperature levels are essentially fixed by external conditions or insignificantly perturbed by the nonmodeled parallel heat transfer, then the conductive heat transfer in the parallel direction,  $Q_p^*$ , is modeled according to

$$Q_p^* = \frac{t^*}{L^*} Q^* \quad (7.15)$$

where  $Q^*$  is the normal  $L^{*2/3}$  scale ratio for materials preservation heat transfer for all other components of the model.  $K_p^*$  has been taken as unity although it has a slight temperature dependence (Ref. 23). This enhanced heat transfer in the parallel direction (over and above that called for by the modeling criteria) will result in an increased heat transfer in the normal direction due to degradation of  $K_I$  of the model in the vicinity of penetrations. On the other hand, it will have a small effect on the normal heat transfer when it arises from gradients along the boundary layers of insulation. The latter case is presented in the discussion of recent experimental work in section 7.3.

A commonly occurring prototype configuration is an MLI blanket attached to thin supporting skin. The skin may be treated as isothermal in the normal direction and in most cases will have a much higher conductance than the insulation in the parallel direction. Thus, the insulation dominates the heat transfer in the normal direction and the skin dominates the heat transfer in the parallel direction. In this case, the model will be accurate, particularly if the MLI boundary not in contact with the skin is not subject to highly asymmetric heat loads and can therefore be taken as fairly isothermal. Even for the cases in which the surface has sizeable temperature gradients, the model will produce good results for the total heat transfer through the insulation.

For completeness, it is convenient at this point to mention the availability of distortion of the skin. This is necessary in problems dealing with highly elevated model temperatures in order to allow for the temperature dependence of the skin material. or in other cases it is simply convenient to use a substitute skin material prescribed by

$$K_s^* t_s = L^* \quad (7.16)$$

### 7.2.2 Transient Modeling

From Eq. (7.4), the time scale ratio for the condition  $T^{*3} = 1/L^*$  is given by

$$\theta^* = \frac{\rho^* V^* C^*}{L^*} \quad (7.17)$$

which reduces to

$$\theta^* = L^{*2} \quad (7.18)$$

for identical thermal properties and geometry. If the one-dimensional steady state model is employed for the MLI, it will operate with a time-scale ratio of

$$\theta_I^* = C_I^* \left( \frac{t^*}{L^*} \right) \theta^* \quad (7.19)$$

For moderately elevated temperatures,  $C^* \approx 1$  and the time constant of the insulation is lengthened by the thickness distortion parameter  $t^*/L^*$ .

Equation (7.19) can be rewritten in terms of the MLI thermal properties as

$$\theta_I^* = C_I^* K_I^* \theta^* \quad (7.20)$$

As both  $C_I$  and  $K_I$  increase with increasing temperature ( $C_I$  having a weaker temperature dependence),  $\theta_I^*/\theta^*$  will increase with decreasing scale ratio or increasing  $T^*$ . Thus, transient behavior of a MLI model will be considerably distorted from the remainder of the model. This may not be a serious detriment to the model when the one-dimensional steady state performance is modeled correctly and sets the average hot and cold boundary temperatures and the MLI transient is small compared with other transients in the system. This is often the case where the MLI is supported by a thin skin. The skin can be taken as a lumped heat capacitance, and in most cases will have a heat capacity per unit area many times that of the entire thickness of the insulation. Under these circumstances, large cyclical heat fluxes on the outside layer of insulation will result in only minor temperature excursions from the average at the inner skin.

It is sometimes feasible in dealing with simple systems that can be modeled for material preservation steady state conditions to allow the transient response to follow  $\theta_I^*$  of the insulation. Thus, for a MLI and supporting skin combination for which the skin may be treated as isothermal, requiring  $\theta_s^* = \theta_I^*$  yields

$$\frac{\rho_s^* C_s^* V_s^*}{L^*} = C_I^* K_I^* L^{*2} \quad (7.21)$$

or

$$\rho_s^* C_s^* = C_I^* K_I^* \quad (7.22)$$

Since the quantity on the right side of Eq. (7.22) increases rapidly with increasing temperature, the modeling will require a material substitution. Alternately, the skin thickness may be distorted so that Eq. (7.21) yields

$$\rho_s^* C_s^* \left( \frac{t_s}{L^*} \right) = C_I^* K_I^* \quad (7.23)$$

Here the same skin material can be used and the thickness distortion may allow for any temperature dependence of the skin specific heat.

A second application can arise wherein the steady state model is accomplished for the above system with the skin distorted according to Eq. (7.16) to preserve parallel gradients in the skin. In this case, the time scale ratio for heat flow in the normal direction (for which the skin is isothermal) and for heat flow in the parallel direction are both given

$$\theta_s^* = \rho_s^* C_s^* L^{*2} \left( \frac{t_s^*}{L^*} \right) \quad (7.24)$$



Requiring the transient response of the skin in the parallel direction and of the MLI in the normal direction to be equal results in

$$\frac{\rho_s^* C_s^*}{K_s^*} = C_I^* K_I^* \quad (7.25)$$

The MLI experiment described in Section 7.3 gives values of  $C_I^* K_I^*$  of 1.7 for a half-scale model. Although Eq. (7.25) appears restrictive in selection of a substitute material for the model, the tables of Section 3 show that the condition can be satisfied in many cases. A high-conductivity alloy of aluminum or stainless steel could be modeled with a lower conductivity alloy of the same type. With a scale ratio as high as 1/6.5 and  $C_I^* K_I^* = 4.5$ , suitable substitutions appear feasible.

### 7.2.3 Modeling of MLI with Undistorted Thickness

Multilayer insulation may be modeled with no distortion of the insulation thickness from the length scale ratio by using Eq. (7.3) to define a length scale ratio in terms of the MLI parameters:

$$L^* = \frac{K_I^*}{T^*{}^3} = f(t_p, t_n) \quad (7.26)$$

When the insulation has a small solid conduction term and the prototype temperatures are high,  $K_I^*$  may change with temperature at a rate higher than  $T^*{}^3$ . In such cases, reduced scale modeling is not possible. With most insulations this will not be the case, although the model based upon MLI properties will have a higher  $T^*$  for a given  $L^*$  when compared with the usual material preservation modeling approach.

Other materials of the prototype must be modeled with substitute materials with conductivities increased in proportion to that of the insulation:

$$K^* = K_I^* \quad (7.27)$$

Alternatively, the steady state model may employ distortions to match conductances where allowable.

The MLI transient response will scale as

$$\theta_I^* = \frac{\rho_I^* C_I^*}{K_I^*} L^{*2} \quad (7.28)$$

and since the temperature dependence of  $\rho_I C_I$  is considerably less than that of the conductivity, the insulation time scale ratio is reduced below the material preservation value of  $L^{*2}$ . To model the transient response throughout the system in accordance with the insulation transient requires that the substitute materials comply with

$$\frac{\rho^* C^*}{K^*} = \frac{\rho_I^* C_I^*}{K_I^*} \quad (7.29)$$

This condition is sufficient for modeling only when the condition of Eq. (7.28) is immaterial (e.g., the material can be assumed isothermal). since otherwise both  $K^*$  and  $\rho^* C^*$  must scale as their insulation counterparts. Thus, the conditions imposed on the substitute materials are very restrictive and the modeling would require the use of some type of distortion such as was discussed under material preservation modeling.

As an example of the application of this modeling, an extrapolation of the conductivity data reviewed in section 7.3 will be utilized. Prototype insulation hot and cold boundary temperatures of 350 and 250° K are assumed. If the model temperatures are elevated by  $T^* = 1.26$ , the resultant  $K_I^* = 1.62$  gives  $L^* = 1/1.23$  by Eq. (7.26). If the prototype temperatures are doubled (giving  $T_H = 700^\circ \text{K}$  the maximum permissible insulation test temperature), the calculation results in  $L^* = 5.76/8 = 1/1.39$ . For this insulation and example prototype, the modeling is severely limited in available length scale ratio. This situation would improve for lower prototype temperatures.

and for the telescope model discussed in section 7.3 a value of  $\epsilon^* = 1/6.43$  was possible. Another application could exist in cryogenic storage situations except for the limitations discussed in section 7.5. Also, this modeling is limited to cases in which the prototype insulation temperatures can be fairly well defined beforehand.

### 7.3 ELEVATED TEMPERATURE EXPERIMENTS WITH MLI

In this section, a review of the experimental results of material preservation modeling of MLI will be presented. These experiments are reported in more detail in Ref. 15 and a portion of the program described therein was to establish the feasibility of constructing thermal and structural models of large-aperture space telescopes. Completion of the program required definition of the one-dimensional MLI heat transfer characteristics of the insulated system and tests to confirm the behavior of the insulation under the modeling concepts developed under this contract and previously presented in section 7.2.

The insulation investigated consisted of 36 layers of alternate sheets of 0.0064-mm-thick (1/4 mil) double aluminized Mylar and glass-fiber paper (Dexiglas\*). The insulation thickness was controlled to approximately 1.27 cm, with a resultant nominal layer density of 28.3 layers/cm. This insulation was attached to a stainless steel skin using Teflon buttons on 15.2-cm centers. These buttons consist of a thin Teflon thread (0.081-cm in diameter) holding together two thin Teflon disks. The length of the thread establishes a maximum insulation density, the density between buttons being in general slightly less.

The configuration used to determine the one-dimensional heat flow characteristics of the insulation is shown in the sketch of Fig. 24. The insulation was wrapped internal to the stainless steel (0.064-cm) cylinders in three sections with two butt joints and two corner joints. (The edges of the latter were protected from direct radiation heat inputs by the interposition of Dexiglas insulation.) Insulated end plates covered the

---

\*C. H. Dexter and Sons Paper Co.

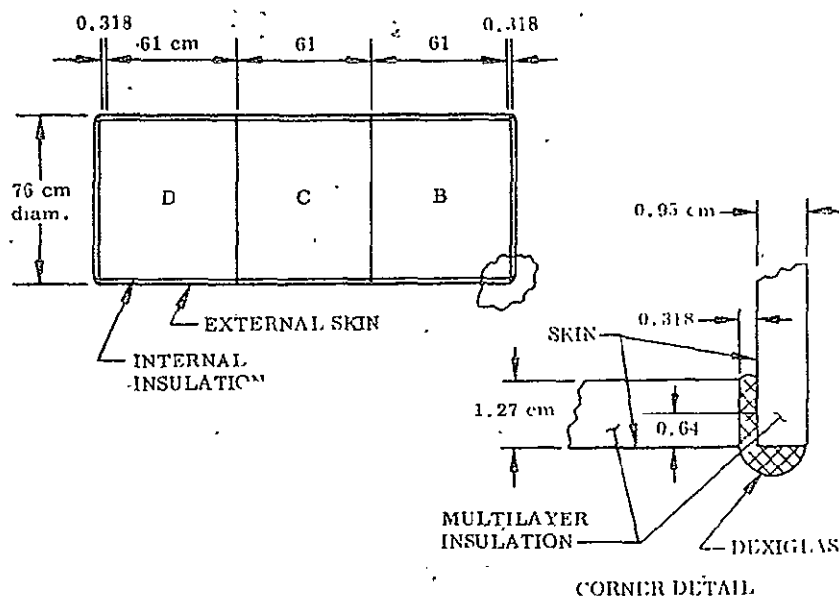


Fig. 24 One-Dimensional Test Arrangement

ends of the cylinders, giving a closed insulation system. All surfaces interior and exterior were painted with a high-emissivity ( $\epsilon \sim 0.92$ ) black paint.

The testing of the insulation systems was performed in a vacuum chamber with liquid nitrogen cooled walls. The interior of the cylinder was operated at various uniform hot boundary temperatures by an internal heat source. This source consisted of several tungsten filament lamps, with the heat input to the system determined from a measure of the power input to the lamps.

A half-scale model of the prototype shell was constructed with scaling according to material preservation. The insulation installed on this shell was designed according to the one-dimensional heat flow results of the full-scale tests and the criterion of section 7.2.

Three sets of steady-state temperature data were obtained for the full-scale insulation and used to define a linear relationship between the experimental conductivity and the radiative potential:

$$P = \sigma(T_C + T_H) / (T_C^2 + T_H^2)$$

The data are shown in the plot of Fig. 25 along with a calculated conductivity curve based on calorimeter data (Ref. 6). The calculated curve is representative of an insulation with no buttons or joints and a carefully established one-dimensional heat flow. The approximately three-fold higher conductivity of the test insulation is not unexpected; such findings are normal for this material.

Values of  $K^*$  were calculated from this curve and are presented in Table 12, where the primed variables refer to the half-scale model. In this calculation,  $T'_H = 1.26 T_H$  and the  $T_C$  values are assumed unchanged as they are closely coupled to the unscaled liquid nitrogen wall. This was acceptable since small changes in  $T_C$  do not have a large effect on the value of  $P$  or  $K$ . Over the full scaling range of the experimental data ( $T_H = 220^\circ K$  and  $T_H = 335^\circ K$ , giving the maximum  $T_H = 422^\circ K$ ), the variation in  $K^*$  is 20 percent. The full-scale point chosen for modeling was taken as

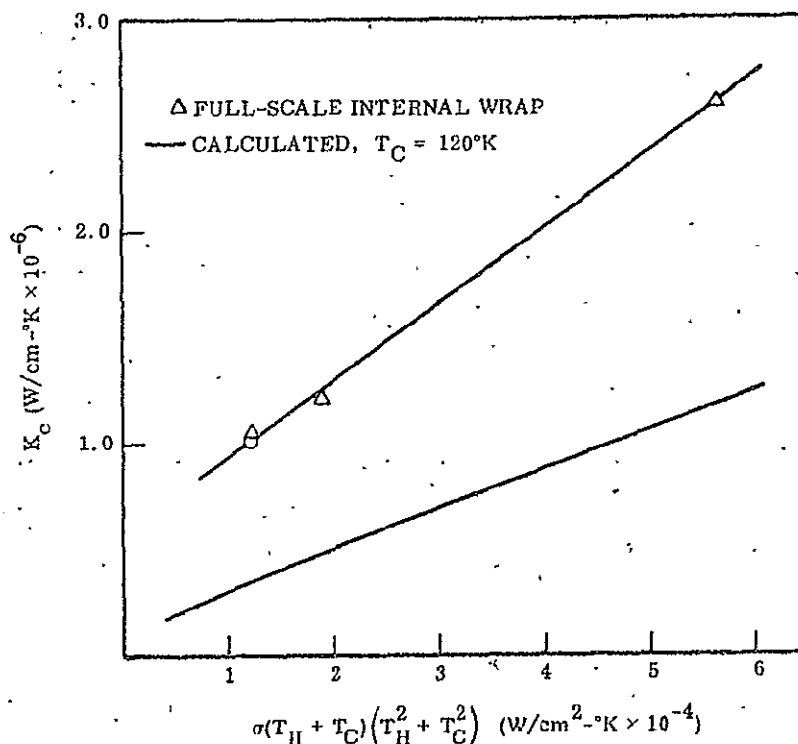


Fig. 25 Insulation Thermal Conductivities for the Full-Scale

Table 12  
COMPARISON OF MEASURED AND CALCULATED THERMAL  
CONDUCTIVITY MODEL RATIOS ( $K^*$ )

$T_C$ (° K)	$T_H$ (° K)	$T'_H$ (° K)	$P$ (W/cm <sup>2</sup> -° K $\times 10^{-4}$ )	$P'$ (W/cm <sup>2</sup> -° K $\times 10^{-4}$ )	$K^*_{\text{meas}}$	$K^*_{\text{calc}}$
120	220	277	1.21	2.05	1.30	1.46
121	270	340	1.94	3.41	1.42	1.57
125	335	422	3.34	6.01	1.54	1.68

270° K, with a resultant  $K^* = 1.42$ . From Eq. (7.2),  $t^* = L^*K^* = 0.71$ . The number of layers  $N'$  for the model is determined from a constant layer density condition as

$$\begin{aligned} N' &= Nt^* \\ &= (36)(0.71) \\ &= 25.6 \end{aligned}$$

The actual insulation for the half-scale model was taken as 27 layers,  $t^* = 0.75$ . This overdesign was used to permit adjustment of the insulation by removal of layers rather than adding. The 27-layer wrap corresponds to a  $K^* = 1.50$  and represents an exact result for  $T_H = 315^\circ \text{K}$ ,  $T'_H = 397^\circ \text{K}$ , and  $P = 2.86 \times 10^{-4}$ .

The experimentally determined conductivities are presented in Fig. 26. The half-scale data exhibit very nearly the same slope as the calculated curve, and a fairly good correlation can be obtained by increasing the solid conduction term of Eq. (7.1) by a factor of 5.5. In comparing the two sets of experimental data, it can be ascertained that the half-scale results exhibit a slightly higher solid conduction component and a smaller radiation heat-transfer component. The former could easily result from a slightly compressed insulation in the half-scale case or could reflect the increased conduction via the unscaled Teflon buttons. The lower radiative heat transfer

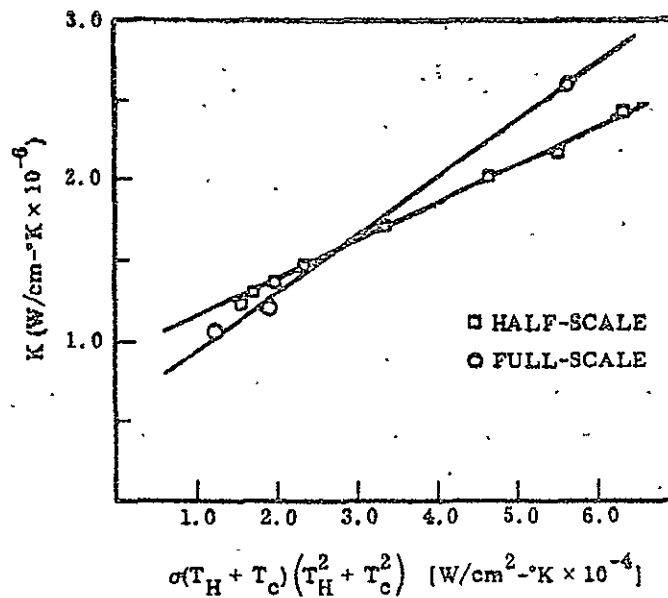


Fig. 26 Insulation Thermal Conductivities for the Full and Half-Scale

occurring in the half-scale insulation apparently results from lessened joint and edge effects. This is an unexpected result as the two-dimensional effects arising from insulation joints should have relatively greater effect on the smaller model, particularly with the high thickness distortion of the insulation. Thus, the inferred reduction in two-dimensional heat flow effects must reflect better quality of joint and edge construction in the half-scale model than in the full-scale model.

A comparison of the interior hot boundary temperature for the half- and full-scale test is made in Fig. 27. The total heat input and temperatures of the half-scale tests have been multiplied by 1/0.63 and 1/1.26, respectively, to produce a direct comparison with the full-scale results. A straight line has been fitted to the three points of the full-scale tests and can be used to estimate the deviations of the half-scale model points. Excellent agreement is achieved, with the modeled temperatures falling slightly below those observed in the full-scale case. If allowance is made for the

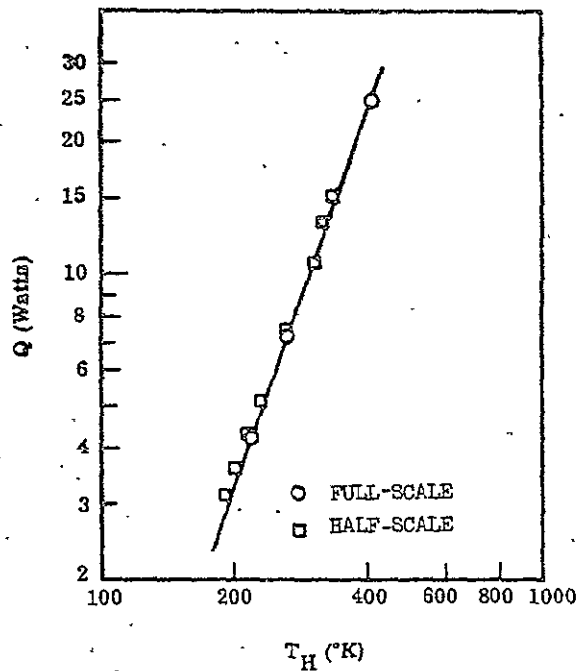


Fig. 27 Correlation of Internal Temperatures for One-Dimensional Heat Flow

5%-over design of the insulation (1.4 layers out of 27 layers), the heat rate of all the points would be reduced. This would result in the higher temperature points modeling to temperatures higher than needed and the lower temperature points still modeling to temperatures lower than desired. Thus, with the correct number of insulation layers, the data of Fig. 27 would reflect essentially the behavior of the conductivity curves and to a lesser extent the effect of nonconstant  $K_I^*$  values for the various temperature conditions.

As an example of the influence of the temperature variation of the conductivity on the insulation distortion, the half-scale data can be used to represent the behavior of a prototype insulation. If these data are used to model the same temperature point (270° K), the calculation used previously with the full-scale insulation data now gives  $K_I^* = 1.25$ . Thus, a prototype of 36 layers would scale to half size with  $t^* = 0.625$  and  $N' = 22.5$  layers. This 15% reduction in the insulation thickness gives a much



smaller distortion of the insulation and shows that insulation with lower temperature dependences are more easily modeled.

Transient tests were performed with the full- and half-scale insulations by modification of the one-dimensional test configuration. The three insulated cylinders were separated to provide thermal isolation with regard to solid conduction in the axial direction. The insulated end plate was removed from Section B and replaced with an uninsulated cylindrical Section A. Variable temperature levels of this section and the top of the insulated cylinders could be maintained by a system of tungsten filament lamps which directly illuminated the outside of these regions. This system was tested with a constant heat flux input to the top of the insulation and a cyclically controlled temperature distribution on Section C.

Representative temperature data for the full-scale insulation system are shown in Fig. 28. These transient data were obtained after numerous heating and cooling cycles had established reproducible temperature behavior. Data for the half-scale system are shown in Fig. 29, where the temperature and time values are scaled by factors of  $1/1.26$  and  $4.0$ , respectively. The tendency of the internal insulation temperatures of the half-scale model to lag behind those of the full-scale model in the cooling portion of the cycle is mainly due to the too-slow cooling rate of Section A of the smaller model. Section A was modeled accurately, however, for the heating portion of the cycle, and here the interior insulation temperatures show a slightly slower transient response. Less than half of this effect arises from the distortion of the  $\rho \cdot V \cdot C$  of the insulation occurring from the thickness distortion and the temperature dependence of the specific heat. The remainder of the effect results from the identical paint thicknesses used on the interior surfaces of both models.

Within the accuracy of the experiment, the relative transient behaviors of the temperatures on the bottom exterior of Section C are identical. Comparison of the absolute value of the minimum temperatures results in considerable error because this area is controlled to a considerable extent by the unscaled cold wall.

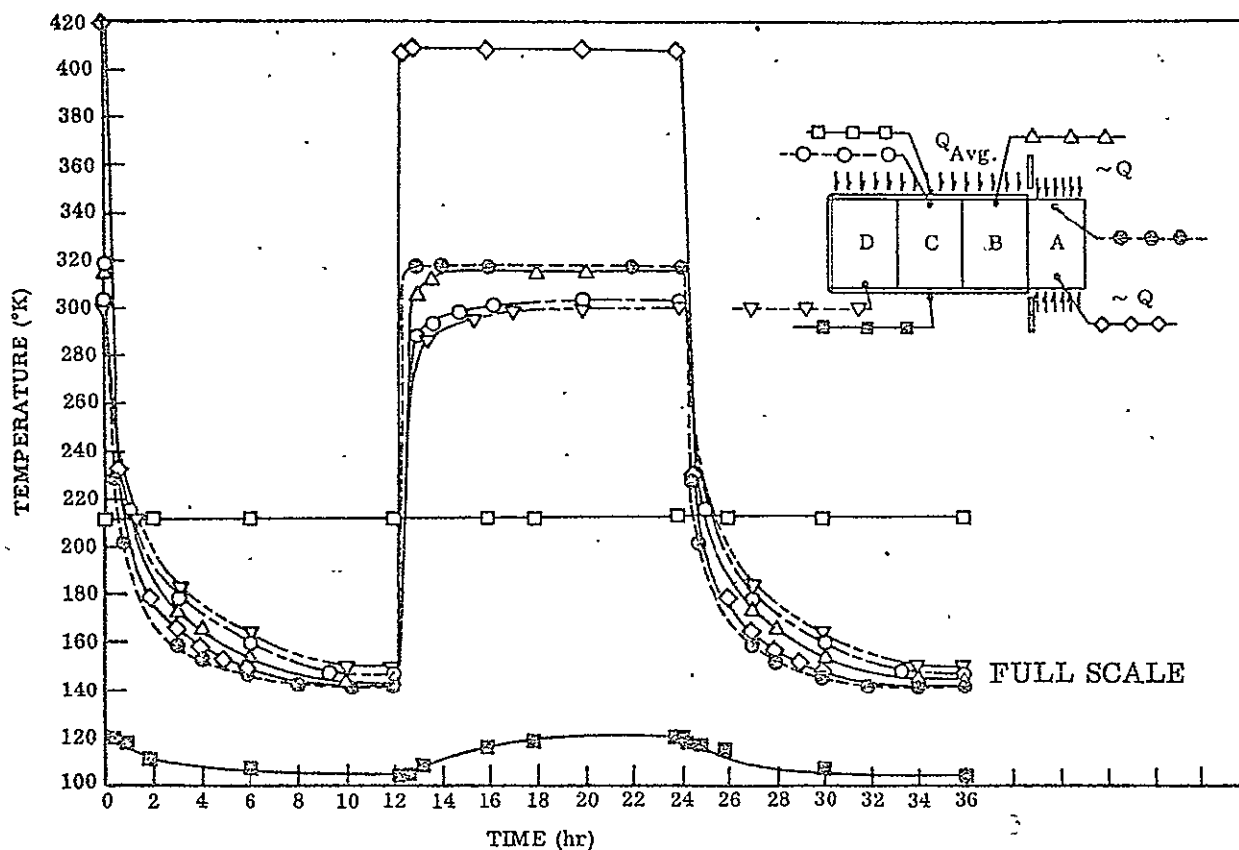


Fig. 28 Transient Temperatures; Section A Cycled and Top Exterior of Sections B, C, and D Subjected to Average Heat Flux

A compilation of the temperatures at the end of the heating and cooling cycles is given in Table 13, along with the errors occurring for comparison of half-scale predictions of full-scale behavior. At the end of the cooling cycle, the interior temperatures are somewhat low owing to the subcooling of Section A by the cold wall. At the end of the heating cycle, the temperatures are in good agreement, with only the previously mentioned discrepancy found for the hollow exterior temperature of Section C.

The good correlation obtained in these transient experiments indicates the adequacy of the one-dimensional heat flow model used for the insulation. This was accomplished in the presence of sizable temperature gradients on the external skin, with the resultant insulation two-dimensional heat flow. These parallel gradients were properly

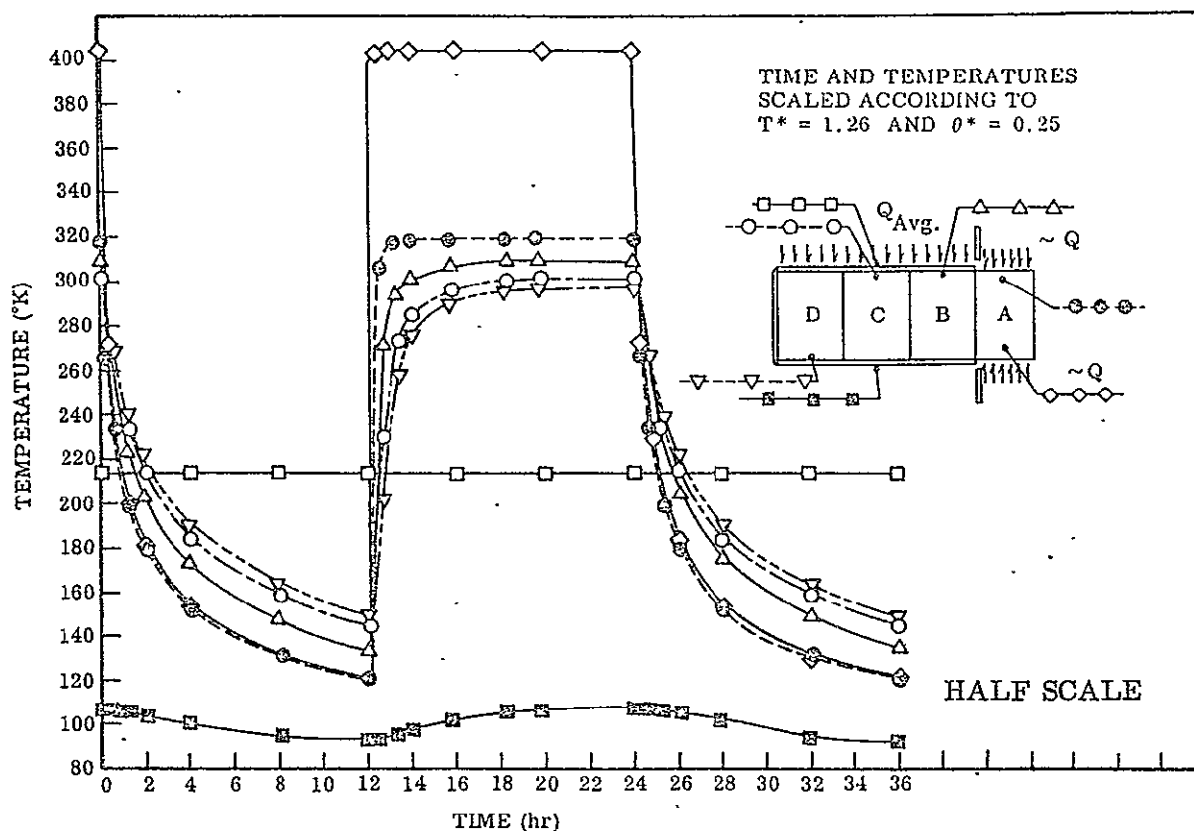


Fig. 29 Transient Temperatures; Section A cycled and Top Exterior of Sections B, C, and D Subjected to Average Heat Flux

modeled by correct modeling of the highly conductive skin, the influence of the insulation on the parallel direction temperature distribution being small.

The larger inaccuracies arose from an unmodeled surrounding temperature and errors in the thermal control of the heat inputs to Section A. The distortion of the transient response attributable to the distorted insulation thickness was minor for this half-scale test.

Table 13  
MODELING RESULTS FOR SECTION A CYCLED AND TOP EXTERIOR  
AT CONSTANT HEAT FLUX  
( $T^* = 1.26$ ; Temperature  $-^{\circ}\text{K}$ )

Location	$T_p$ Full-Scale	$T_m$ Half-Scale	$T_m/T^*$ Predicted	$\Delta T$
End of Cooling Cycle				
Interior B	144	170	135	-9
Interior C	146	180	143	-3
Interior D	149	184	146	-3
Exterior C	210	269	213	3
Exterior C	105	117	93	-12
Top Section A	140	152	121	-19
Bottom Section A	142	155	123	-19
End of Heating Cycle				
Interior B	317	398	316	-1
Interior C	304	381	302	-2
Interior D	302	375	298	-4
Exterior C	213	270	215	2
Exterior C	121	136	108	-13
Top Section A	318	403	319	1
Bottom Section A	409	508	404	-5

The final portion of this program, which involved multilayer insulation modeling, was the testing of a 1/6.43-scale ratio model of a proposed 2-m aperture OTES (Optical Technology Apollo Extension System) telescope. The model geometry for this telescope was presented in section 6 and is shown in Fig. 14. The prototype insulation to be modeled consisted of 36 layers of the previously tested MLI with a nominal 1.27-cm thickness. The performance of the model was compared with the results

obtained from a thermal analyzer network computation used to define prototype behavior.

To provide an insulation which would nominally model the OTES prototype insulation, the data of the preceding MLI experiments were utilized to determine a scaling criterion for specifying the number of layers. The more precisely defined thermal conductivity versus radiative potential curve for the half-scale insulation model was used in characterizing the prototype insulation.

The boundary temperatures calculated for the prototype system were in some cases much lower ( $\sim 60^\circ\text{R}$ ) than could be achieved in the test chamber with a liquid nitrogen cold wall. It was therefore necessary to extrapolate the data of Fig. 26 down to  $P = 0.36 \times 10^{-4}$ . This was accomplished by allowing the linear curve to fall to zero as  $P$  approached zero in the same manner as the calculated curve. For the boundary temperature extreme corresponding to  $P = 1.02 \times 10^{-4}$ ,  $K^*$  remains fairly constant, ranging from 2.35 to 2.56. This behavior is coincidental with the prototype temperatures lying in the region of sharply decreasing  $K$ .

To determine the insulation configuration for the model,  $K^* = 2.36$  was used, giving

$$t^* = k^*L^* = 0.367$$

$$n_m = n_p t^*$$

$$n_m = 36 (0.367)$$

$$n_m = 13.2$$

This value for the number of layers for the model ( $n_m$ ) is further reduced (maximum reduction of 5%), by the  $n/(n-1)$  dependence of the radiative component, so that 13 layers were taken for the model.

The time-scale ratio for one-dimensional heat flow through the insulation is given by Eq. (7.2) as  $K^* C^* L^{*2}$ . For this case,  $C^* = 1.88$  (Ref. 6) results in  $\theta^* = 1/9.35$  compared with  $1/41.3$  for pure materials preservation and with  $\theta^* = 1/26$  desired for the overall telescope system.

The telescope model was tested with precalculated cyclic heat inputs and the data were compared to prototype predictions of a thermal calculation. The trend of the data was for the experimental internal temperatures to be about  $20^\circ\text{K}$  too low. This discrepancy was not associated with the performance of the insulation. However, the exact behavior of the model insulation therefore cannot be assessed from the experiment and, in fact, an accurate evaluation would require an experiment similar to the one-dimensional heat flow experiments used earlier in this work.

#### 7.4 TEMPERATURE PRESERVATION

The problems associated with modeling of MLI using an identical material approach were seen to be associated with obtaining a model wrap thickness with the desired  $K^* = 1$  and the distribution of the two-dimensional field since the required  $t^* \neq L^*$ . These same problems are existent in modeling MLI where a temperature preservation approach is desired. According to the criteria given by Eq. (2.1), the temperature preservation ( $T^* = 1$ ) model must be designed to provide satisfaction of

$$Q^* = \frac{\rho^* V^* C^*}{\theta^*} = \frac{K^* A_n^*}{L^*} = A_i^* \quad (7.30)$$

From this we find that a geometrical similar model,  $A_n^* = A_i^* = L^{*2}$ , must have

$$K^* = L^* \quad (7.31)$$

and

$$\theta^* = \rho^* C^* L^* = \rho^* C^* K^* \quad (7.32)$$

Reduction of model material thermal conductivities in proportion to the length ratio [Eq. (7.31)] is feasible for many of the structural components. However, such a reduction for the MLI insulated regions is frequently not possible since the prototype system has already been designed to have minimum properties at the prototype temperature. In addition, not only would the perpendicular conductivity require reduction, but also the parallel conductivity which, as previously mentioned, is dominated by solid conduction along the layers. Concurrent and controlled reductions of conductivity for both directions through implementation of materials substitution is highly unlikely.

The most practical approach to modeling MLI with  $T^* = 1$  has been found by these investigators to be the use of identical materials with thickness distortion. Once again this leads to considerable distortion of heat transfer in directions parallel to the layers, the influence of which must be assessed for each complete model in terms of overall system thermal performance

Using model criteria derived from Eq. (7.1) with  $T^* = 1$  gives

$$Q^* = \frac{B^* A^*}{t^*} = \frac{C^* A^*}{t^* N^*} \quad (7.33)$$

From Eq. (7.30)  $Q^* = L^{*2}$ , therefore

$$\frac{B^* A^*}{t^*} = \frac{C^* A^*}{t^* N^*} = L^{*2} \quad (7.34)$$

Using an identical wrap results in  $B^* = C^* = N^* = 1$ , and assuming that thickness distortion does not result in surface area distortion (i.e.,  $A^* = L^{*2}$  for insulated inner and outer surfaces) gives

$$t^* = 1 \quad (7.35)$$

Satisfaction of this result means that an identical wrap is used for the model as that for the prototype resulting in complete geometric distortion of the prototype insulation

thickness (i.e.,  $t_m = t_p$  instead of  $t_m = L^* t_p$ ). This procedure results in accurate preservation of  $Q^* = L^{*2}$  for heat transfer perpendicular to the layers. Heat transfer parallel to the layers is obviously increased above that in the prototype.

For the composite system, where one-dimensional heat transfer has been assumed for the model MLI, it is still necessary that all remaining components be modeled in accordance with Eq. (7.30) where strict geometric compliance assures proper simulation of the complete heat transfer system. From that equation with  $T^* = 1$ , we find that the system time response is governed by

$$\theta^* = \rho^* C^* K^* \quad (7.36)$$

If the transient behavior of the MLI regions is an important consideration in setting the time response for the complete system, it is then necessary that the system  $\theta^*$  be the same as the insulation  $\theta^*$ . Since we have selected an identical wrap for the model as that used in the prototype, the relation that must be satisfied for the system is

$$\rho^* C^* K^* = \theta^* = 1 \quad (7.37)$$

The difficulty of applying Eq. (7.37) can be ascertained by referring to the property charts of Section 4. These charts show that there is relatively little variation in  $\rho C$  (about 1:2), and thus Eq. (7.37) will limit  $K^* \approx 1/2$ . This materials limitation sets the scale ratio. As a specific example, the magnesium alloy AZ8C-T5 can be modeled with 410 stainless steel with  $\rho^* C^* K^* = 1.03$  and  $K^* = L^* = 1/1.83$ . The modeling of other components of the system to satisfy the transient condition  $\theta^* = 1$  can, of course, be accomplished with geometric distortion so that the  $K^* = L^*$  requirement can be relaxed. This approach is useful in treating the combination of MLI and supportive skin.

Assuming that the heat flow in the MLI remains one-dimensional, then multidimensional heat flow modeling for other components would still be accomplished according



to the conditions of Eqs. (7.30). Satisfaction of the criteria in the case where a thin skin acts as supporting structure for the MLI and dominates the heat flow processes in the direction parallel to the insulation thickness can frequently be accomplished through thickness distortion.\* In this case the heat transfer area is represented by  $A_n^* = t^* L^*$  and the criteria became

$$\frac{\rho^* C^* L^{*2} t^*}{\theta^*} = K^* t^* = L^{*2} = Q^* \quad (7.38)$$

The steady state conduction parallel to the skin requires that the conductivity be modeled according to

$$K_s^* = \frac{L^{*2}}{t_s^*} \quad (7.39)$$

The modeling of the transient behavior of the skin to match the MLI transient requires that

$$\theta_s^* = \rho_s^* C_s^* t_s^* = 1 \quad (7.40)$$

In many practical cases, the skin may be treated as isothermal in the perpendicular direction. Therefore, Eqs. (7.39) and (7.40) specify the conditions to be satisfied for multidimensional heat flow in a thin skin. (This type of distortion is also applicable to other components where assumption of isothermality along the small dimension is valid, e.g., thin wall tubing.)

---

\*The assumption of one-dimensional flow in the MLI with temperature gradients along the supportive skin can only be approximate. However, because of the large ratio ( $\sim 100:1$ ) of the parallel to perpendicular conductivities of typical MLI, the approximation is a good one for closed insulation systems.

Equations (7.39) and (7.40) may be combined to give criteria for the thermal properties as

$$\frac{\rho_s^* C_s^*}{K_s^*} = \frac{1}{L^{*2}} \quad (7.41)$$

The application of this equation can be made (see Section 4) to model aluminum alloys with stainless steel alloys, giving  $L^* \approx 1/1.4$ . Again, Eq. (7.41) is only necessary in cases for which the transient model response must be mated with that of the insulation. Otherwise, the restriction of Eq. (7.40) is lifted and Eq. (7.39) can then be easily satisfied.

## 7.5 TEMPERATURE PRESERVATION EXPERIMENTS

In this section, the experimental portion of this program involving the application of the criteria developed in section 7.4 will be described. Temperature preservation was chosen as very little modeling has been attempted with this method for which the insulation was a sensitive component of the system. Thus, one of the objectives of this study was to investigate a system in which the characteristics of the MLI dominated the thermal modeling problem. At the same time previous experience has demonstrated the need for careful one-dimensional heat flow characterization of the MLI. For these reasons, the system decided upon consisted of a 36-layer MLI cylinder with closed ends wrapped on a lightweight stainless steel tubular framework. The outer boundary was subjected to a controlled ( $\pm 0.2^\circ\text{K}$ ) room temperature environment and the internal temperature controlled by axial heating wires from which the internal power dissipation was accurately measured. One-dimensional steady state and transient data were taken for a prototype system and 1/2- and 1/4-scale models. Two-dimensional heat flow effects were introduced by cutting a circular hole through the insulation and the steady state and transient measurements repeated. An attempt was made to enhance the sensitivity of this two-dimensional test by constructing a high quality insulation blanket with the minimum number of two-dimensional perturbations from joints and buttons.

### 7.5.1 Multilayer Insulation Test Articles

The insulation used for prototype and scale models consisted of 36 layers of 0.25-mil thick Mylar aluminized on both sides separated by 3-mil thick glass-fibre paper (Dexiglas). This insulation was installed on a lightweight cylindrical framework constructed from thin wall stainless steel tubing. The innermost layer of insulation had a single aluminized surface with the nonaluminized high emissivity surface facing into the cylinder to facilitate isothermal conditions interior to the cylinder.

The insulation was supported from the framework by a number of button attachments. The buttons were made from two 1/2-in. teflon disks held to either side of the insulation by a 0.030-in. Dacron filament which penetrates through the insulation thickness. The prototype and scale model insulation systems are shown in Figs. 30 and 31 mounted to the vacuum chamber door. In this photograph the vertical strips running under the buttons are 1/2-in. Dacron ribbon which serves to distribute the suspension weight throughout the insulation blanket. The entire system is suspended from the door by 10-mil stainless steel wires which attach to the internal tubular framework.

All of the systems tested had three insulation joints. All of these joints were of the staggered overlap variety. In these installations these joints consisted of four nine-layer blankets butted together in a staggered fashion such that no single discontinuity existed through more than 1/4 of the blanket. Two of these joints were used on the top and bottom flat ends where the cylindrical portion of the blanket was folded over the corners to join with end insulation. The third joint was an axial joint where the two sides of the cylinder insulation met. An additional joint was necessary for the larger (178-cm length by 96.5-cm i.d.) prototype system due to the limited available width of insulation materials. This was a circumferential joint located in the central plane of the cylinder.

The insulation test articles were instrumented with 3-mil copper-constantan thermocouples. Ten of these were located on the internal surface and served to define the



Fig. 30 Prototype Insulation Test Article

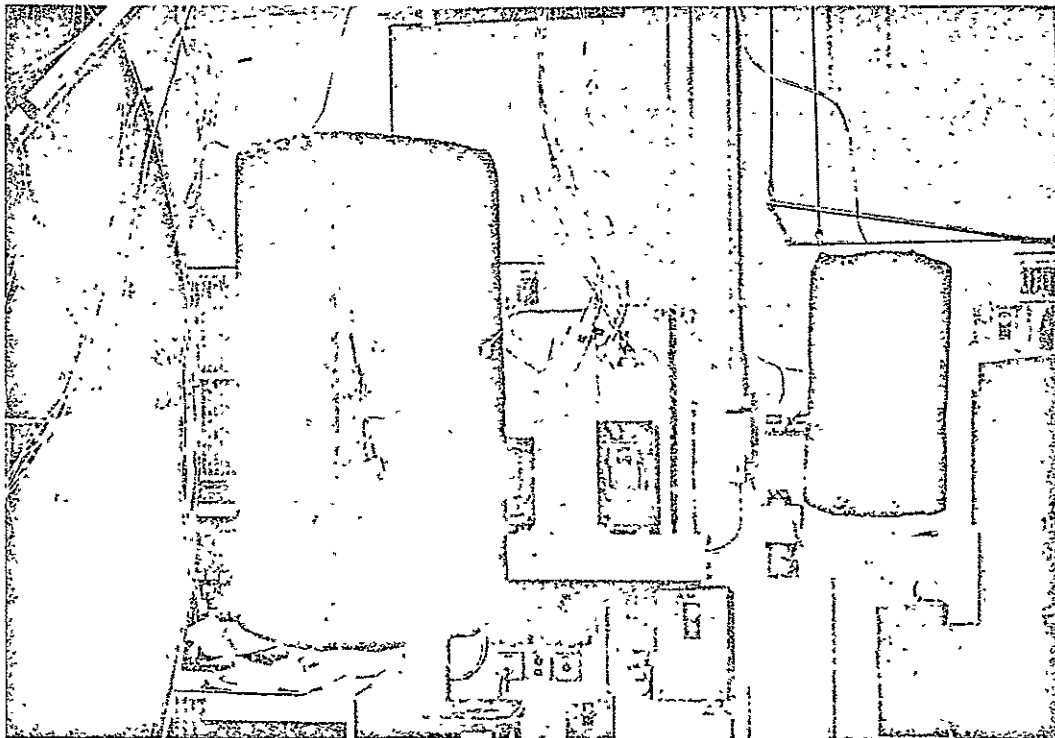


Fig. 31 One-Half and One-Quarter Scale Insulation Test Articles

hot boundary temperature. An additional set of thermocouples was installed on the exterior. This surface was then painted black to provide good thermal coupling with the chamber wall. The internal heaters were made from 10-mil resistance wires positioned near the axis of the cylinder.

#### 7.5.2 Test Procedures

Following the installation of the test articles the vacuum chamber was evacuated to  $1 \times 10^{-5}$  mm Hg and the insulation allowed to pump out for 24 hr. At this time a transient heating cycle was performed in which the interior temperature was raised rapidly to the operating level (420°K) and the decay in heater power monitored. After steady state conditions has been attained, the one-dimensional heat flow data were recorded and the heater shut off. The decay of the internal temperatures was recorded as a cooling transient. The heating transient experiment was essentially a function of the insulation only while the cooling transient depended on the internal framework and heater assembly thermal mass. The steady state data served to define the effective insulation conductivity. Only single temperature points were taken for the scale models whereas three temperature points were obtained for the prototype system. These latter data gave the temperature dependence of the insulation and allowed correlation with other experimental data.

Two-dimensional effects were introduced into the insulation by cutting a hole (approximately 15-cm diameter for the prototype) through the insulation. This hole was then shielded with a single disk of aluminized Mylar at the cold boundary side. The inside surface of this shield was painted black and the outside surface kept as a low emissivity aluminum. With this arrangement, the radiation coupling of the exposed edges to the hot interior was maximized giving a large two-dimensional perturbation of the insulation around the hole. The increase in heat flow via radiation from the low emissivity side of the aluminized Mylar disk was small and calculatable. Additional thermocouples were placed around the hole to measure any radial gradients and one thermocouple placed in the center of the aluminized Mylar shield.

Steady state and transient data were obtained for this configuration in a manner similar to that for the one-dimensional configuration.

### 7.5.3 Test Results

The data acquired for the steady state experiments are presented in Table 14. The heat flow through the insulation is the net heat flow arrived at by subtracting calculated lead wire conduction losses (Ref. 24) from the observed heater power. It should be noted here that the insulation thickness,  $t$ , was not identical for the different test articles. The thicknesses given in the table are approximate thickness measured after testing was completed. This error in insulation thickness is responsible for the inaccuracies in the modeling of  $Q/A$ . The inability to maintain a uniform thickness for the three 36-layer insulation blankets is attributable to the light-weight framework and the fact that a minimum number of constraining button attachments were used. Thus, the larger area specimens were less firmly constrained allowing the insulation to fluff out to much lower densities between buttons.

Table 14  
STEADY STATE DATA

	Prototype				1/2 Scale		1/4 Scale	
	1-D		2-D		1-D	2-D	1-D	2-D
Temp. Internal (°K)	418	368	318	419	420	419	418	419
Temp. External (°K)	302	303	302	302	302	303	302	303
Q Insulation (W)	5.461	2.329	0.456	7.594	1.916	2.579	0.622	0.928
Area Ins. (cm <sup>2</sup> × 10 <sup>4</sup> )	6.90	—	—	—	1.815	—	0.472	—
(A*) <sup>-1</sup>	1.0				3.80		14.63	
Q/A (W/cm <sup>2</sup> × 10 <sup>-5</sup> )	7.9	0.337		0.066	10.56		13.18	
t(cm)	2.54				1.91		1.27	
K <sub>eff</sub> (W/cm-°K × 10 <sup>-7</sup> )	17.32	13.18	10.48		17.06		14.43	

The three temperature points for the prototype configuration are plotted in Fig. 32 against the expected temperature dependency. The agreement with the predictions of Ref. 22 is quite good. This agreement is only possible if the value of  $t = 2.54$  cm is employed. This infers that the insulation was operating with essentially one-dimensional heat flow and that the joints and other instrumental penetrations contributed minor two-dimensional effects.

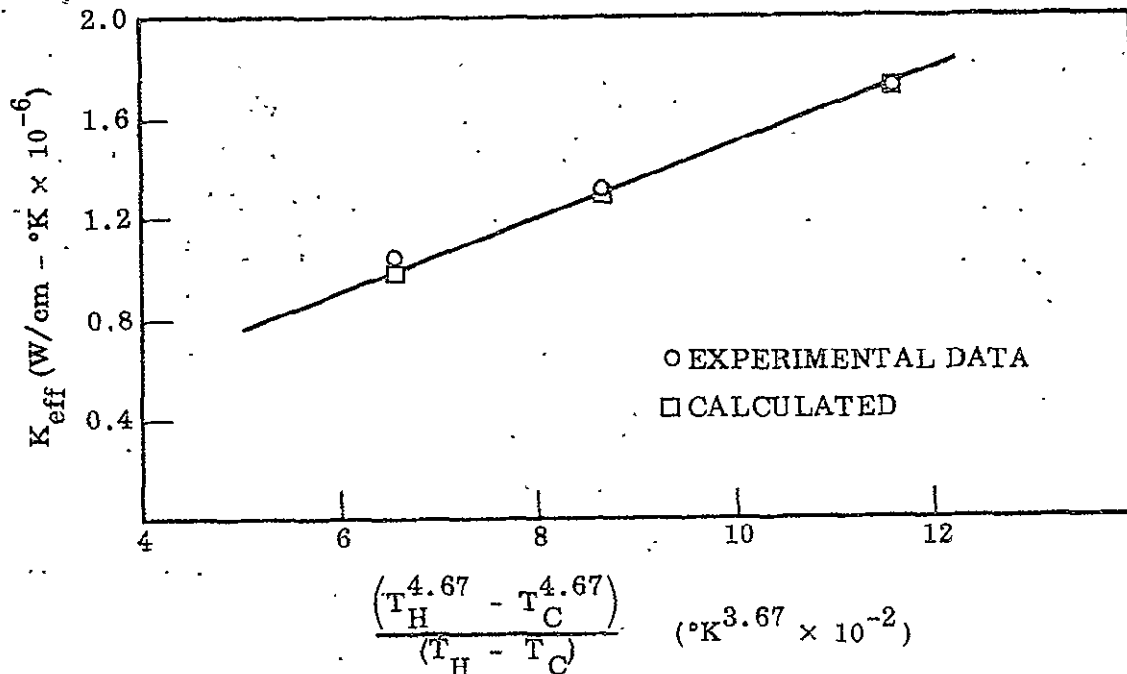


Fig. 32 Insulation Conductivity Variation With Temperature

The two-dimensional steady state data presented in Table 14 was used to determine a  $Q_{2-D}$  for the insulation which represents the increase over and above the insulation one-dimensional heat rate which is induced by the presence of the cut out. To do this a radiative heat balance calculation was performed for the low emissivity shield surface and the chamber wall. This and the original one-dimensional heat rates were subtracted from the total heat rate to obtain  $Q_{2-D}$ . The results are presented in

Table 15. Although the calculation of the shield heat rate cannot be performed accurately, it can be seen that this value is at most 15% of the increase in the one-dimensional heat rate, the remainder arising from the two-dimensional heat transfer occurring in the insulation. The values of  $Q_{2-D}^*$  are plotted in Fig. 33 against  $L_H^*$ , the ratio of the hole diameter. (This diameter could not be exactly controlled to the  $L^*$  ratio of the models.) The data show a behavior which can be described by

$$Q_{2-D}^* = (L_H^*)^{1.51}$$

From the development of section 7.4, the two-dimensional behavior could be expected to be  $(L_H^*)^{2.0}$ . This would assume that the internal walls of the hole were isothermal or nearly so. That this was not the case can be shown by calculation of the interior-to-hole view factors. These view factors are not scaled correctly due to the varying and somewhat uncontrollable insulation thickness. Therefore, it can be said that the data have shown the presence and trend of two-dimensional heat flow effects although the exact magnitude of these effects in a correctly modeled system are not demonstrated.

Table 15

TWO-DIMENSIONAL STEADY STATE DATA

	Prototype	1/2 Scale	1/4 Scale
$Q_{Total}$ (W)	7.594	2.579	0.928
$Q_{Shield}$ (W)	0.737	0.21	0.086
$Q_{1-D}$ (W)	5.461	1.916	0.622
$Q_{2-D}$ (W)	1.39	0.45	0.22
$Q_{2-D}^*$ (W)	1.0	0.346	0.156



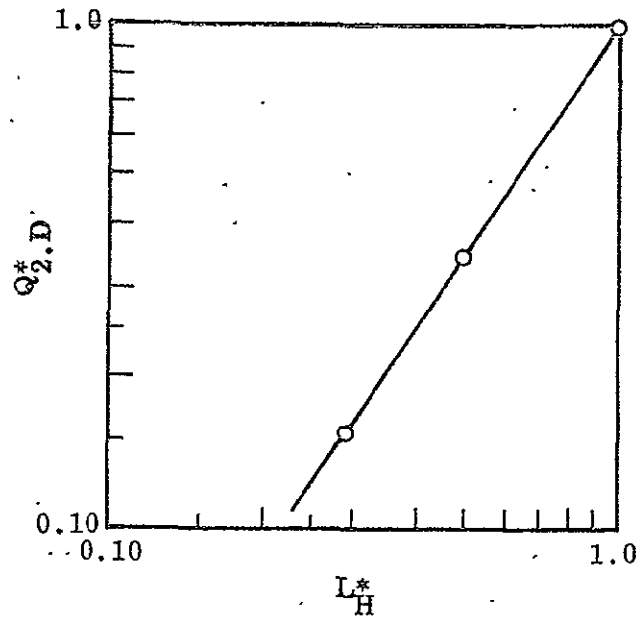


Fig. 33 Two-Dimensional Heat Flow Variation With Scaling Ratio

The transient response of the systems was to be originally determined by observing the decay of heater power after rapidly raising the interior boundary temperature to a fixed value with all initial temperatures at ambient conditions. Since it was difficult to scale the initial fast temperature rise, the experiment depended on observing the power decrease  $Q_i - Q_o$  after the leading term had dominated the process. This procedure proved inaccurate due to the marginal precision of the instantaneous power measurement and the persistence of second-order transient terms associated with the nonideal temperature buildup.

The cooling data for the one-dimensional case are shown in Fig. 34. These data are used to give fairly accurate values of the time constant. The results of these evaluations are given in Table 16 together with the calculated time constant ( $\tau$ ) of the insulation and insulation plus framework thermal mass. The inclusion of the framework improves the absolute correlation of the time constants but has little effect on the time

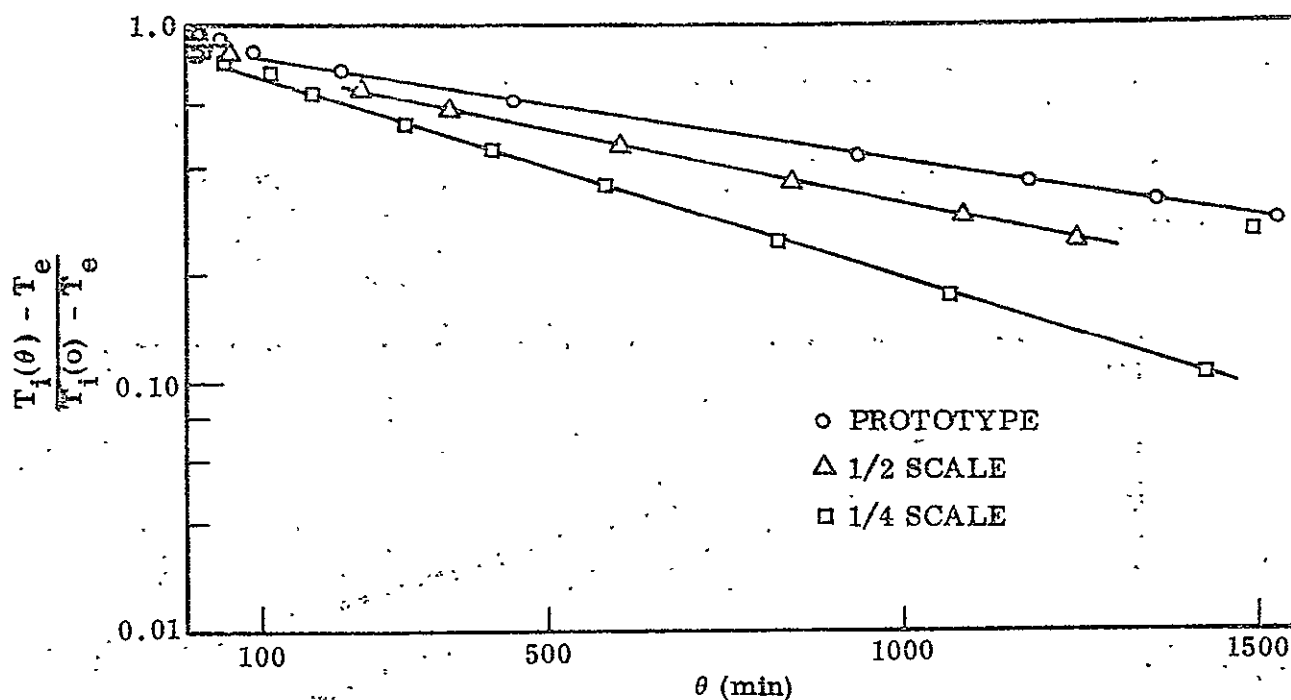


Fig. 34 One-Dimensional Cooling Data

Table 16

ONE-DIMENSIONAL TRANSIENT DATA

	$\tau_{OBS}$ (min)	$\tau_{OBS}^*$	$\tau_{INS}$ (min)	$\tau_{INS}^*$	$\tau_{CALC}$ (min)	$\tau_{CALC}^*$
Prototype	1388		1267		1334	
1/2 Scale	1049	0.756	897	0.708	952	0.714
1/4 Scale	689	0.496	687	0.542	741	0.555

constant ratios. The largest error in  $\tau^*$  is 10% for the 1/4 scale model. No error can be expected from the varying insulation thickness as the time constant is a function of  $k/t = Q/A \Delta T$  which was measured in the steady state experiment.

The transient two-dimensional cooling data is presented in the graph of Fig. 35 and compared to the one-dimensional case in Table 17. The prototype cooling data were lost due to a vacuum chamber malfunction and were not rerun since the heating curve data were assumed to be valid at that time.

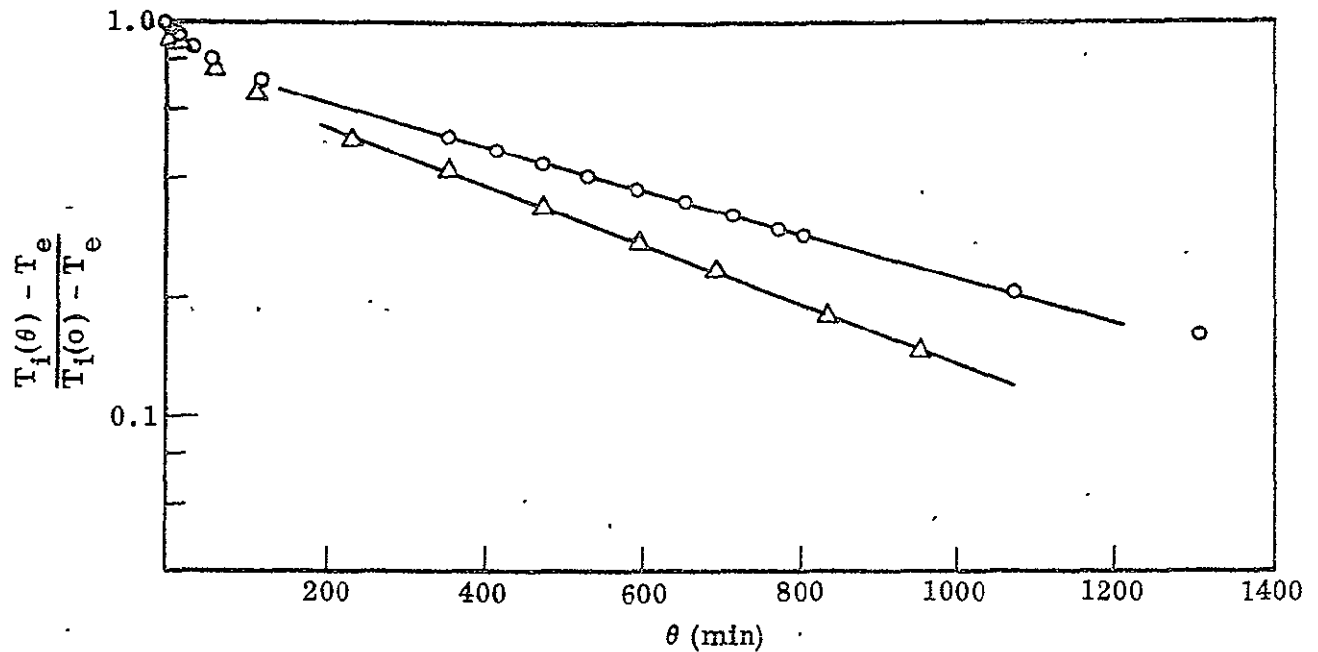


Fig. 35 Two-Dimensional Cooling Data

Table 17

TRANSIENT DATA COMPARISON

	$\tau_{2-D}$	$\tau_{2-D}^*$	$\tau_{1-D}$	$\tau_{1-D}^*$
1/2 Scale	777	—	1050	—
1/4 Scale	576	0.741	690	0.657

## 7.6 CONCLUSIONS

The problems associated with reduced scale modeling of multilayer insulation for space applications are extensive and lead to severe limitations when a precise model of the insulation is necessary. Many of these limitations stem from the difficulty in reproducing the prototype insulation wrap at reduced scale. In many applications the insulation is overdesigned to the point where degradation of its performance has little effect on the overall thermal performance of the system. In these cases, one-dimensional steady state insulation modeling will meet most of the requirements.

The strong temperature dependency of thermal properties makes elevated temperature studies unattractive except when the insulation plays a minor role in the thermal design. Even in the latter cases premodeling insulation tests are advisable except in the simplest of insulation geometries. Temperature preservation modeling eliminates one of the above problems but requires insulation thickness distortions.

The modeling of transient heat flow conditions in multilayer insulation can be accomplished accurately only with severe distortions and material substitutions of other prototype system materials. This procedure is probably not feasible except in simple two-component systems.

When two-dimensional heat flow is present, the modeling is increasingly difficult. Limitations arising from two-dimensional effects are not easy to establish. Where the insulation performance is critical, the evaluation techniques that have been used consist of isolating and testing of the prototype two-dimensional heat flow area. This approach has been used in several cryogenic tank storage tests, in the Lunar Module Vehicle (Ref. 25) and in large spacecraft thermal protection design efforts at Lockheed Missiles and Space Company. In each of these cases the isolation of two-dimensional tests are used as a design aid. A full-scale flight qualification thermal test is generally required for each vehicle.

Although many difficulties are encountered in constructing precise insulation models successful models have been constructed for systems in which extensive use was made of multilayer insulation (see section 6). In these systems the insulation was constructed according to the one-dimensional modeling criteria. Many multilayer insulation thermal design problems of this type can be successfully attacked with thermal modeling.

## Section 8

### SPECIAL COMPONENTS

Special spacecraft components frequently require a unique thermal design to assure maintenance of thermal levels within narrow tolerances. In each of these cases, the model designer is required to furnish a smaller scale system which simulates the prototype behavior. Fortunately, the very fact that a special design has been generated results in a well characterized system whose boundary conditions and design parameters have been specified and tested in detail. The information generated for specification of prototype design then becomes available to the model investigator and special procedures can be implemented to obtain similarity within the constraints of model criteria.

The special components under consideration for present and future use include: extremely high and low conductance joints; resistance heater stabilized components; adiabatic walls using multilayer insulation; phase change thermal sinks; cryogenic refrigerated sensors; high and low temperature emitter panels; heat pipes; and other special thermal components and systems. For each of these special components, the model designer must establish a thermally similar system in the model. It is frequently possible to avoid complete duplication of the component through artificial provision of boundary conditions similar to those of the prototype. For example, the performance of emitter panels may be duplicated through forced cooling loops in cases where panel behavior is in itself not of prime interest. Resistance heater stabilized components can be accurately simulated using temperature monitoring and external control of electrical energy. Adiabatic walls can be provided on the model using methods identical to those of the prototype as long as the mismatch of thermal conductance at very low values is of minor importance. The approaches necessary for modeling of systems using phase change heatsinks, heat pipes, cryogenic refrigerators, and special joints will obviously be unique in terms of each application and will not be covered in detail herein. However, it is of interest to consider the rather formidable problems that arise in connection with thermal modeling of joints.

In cases where a joint has been carefully designed to provide a maximum or minimum resistance, the modeling problem will be amenable to accurate solution since design practices similar to the prototype can be utilized. However, when a common joint assumes an important thermal role, the modeling problem is considerably more complex.

The thermal model criteria for a joint are based upon relations that describe the heat transfer between the opposing surfaces. Considerable work has been done by numerous investigators to establish and confirm the required joint conductance theory.

A coefficient of joint conductance for two mating members in imperfect contact has been defined as

$$h = \frac{q}{A\Delta T} \quad (8.1)$$

where

$q$  = heat flux

$A$  = apparent contact area

$\Delta T$  = temperature drop across the interface

A good deal of experimental data is available on measurements of  $h$  for various materials and methods of contact. However, little success has been achieved in satisfactory correlation of the results with theoretical models.

While advances have been made in predicting joint conductance for carefully controlled joints in laboratory experiment, success in applying these theories to common engineering joints has been limited.

Recent work in this field shows promise for developing an appropriate joint conductance relation. Particularly notable is the work by Clausing and Chap (Ref. 26) and the work by Rice (Ref. 27).

Clausing and Chao have attacked the joint conductance problem assuming that macroscopic effects are dominant which differs from previous assumptions that microscopic effects dominate the conductance.

Clausing and Chao found the joint conductance relation

$$h = \frac{2xk}{b\pi g(x)} \quad (8.2)$$

where

$k$  = thermal conductivity

$b$  = diameter of the apparent contact area

$x$  = constriction coefficient ( $a/b$  Fig. 36)

$g(x)$  = constriction alleviation factor

The value of  $g(x)$  has been determined as

$$g(x) = 1 - 1.40925x + 0.29591x^3 + 0.05254x^5 + 0.02105x^7 + \dots \quad (8.3)$$

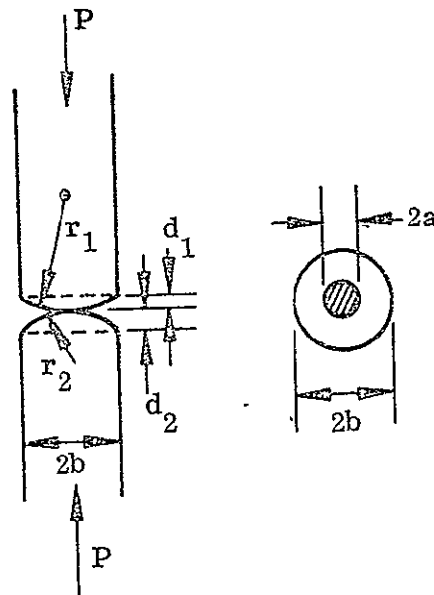


Fig. 36 Geometry for Clausings Relation



Further, for most metals it can be shown that

$$x = 1.285 \left( \frac{Pb}{Ed} \right)^{1/3} \quad (8.4)$$

where

$P$  = contact pressure

$E$  = modulus of elasticity

$d$  = total flatness deviation ( $d = d_1 + d_2$  Fig. 36)

Substituting Eq. (8.4) into Eq. (8.2) gives:

$$h = \frac{2.57 \left( \frac{Pb}{Ed} \right)^{1/3} k}{b\pi g(x)} \quad (8.5)$$

A different approach to determining joint conductance was taken by Rice. Using dimensional analysis and considerations of important parameters, he derived the following relation for a perfectly flat but roughened surface:

$$h = Ck \frac{m}{\sigma} \left( \frac{P}{H} \right)^a \quad (8.6)$$

where

$C$  = a constant

$a$  = a constant

$k$  = thermal conductivity

$m$  = rms value of the slope of the surface roughness

$\sigma$  = rms value of the surface roughness

$p$  = contact pressure

$H$  = microhardness

Rice plotted available experimental data on log-log coordinates and found

$$a = 0.85$$

$$C = 0.55$$

Thus, Eq. (8.6) becomes

$$h = 0.55 k \frac{m}{\sigma} \left( \frac{P}{H} \right)^{0.85} \quad (8.7)$$

### 8.1 JOINT SCALE MODELING CRITERIA

The general modeling criteria for a joint may be derived through equating the relation for heat transfer through a joint to that for conduction and radiation transfer elsewhere in the system. This results in

$$h^* A^* T^* = \frac{K^* A_n^* T^*}{L^*} = A_i^* T^{*4}$$

and for geometrical similarity

$$h^* = \frac{K^*}{L^*} = T^{*3} \quad (8.8)$$

For a material preservation model  $K^* = 1$ ,  $E^* = 1$  and the joint must conform to

$$h^* = L^{*-1} \quad (8.9)$$

Applying this requirement to Calusing and Chao's results, Eq. (8.5), and rearranging gives

$$p^* = \frac{d^*}{b^*} \left( \frac{b^* g(x)^*}{L^*} \right)^3 \quad (8.10)$$

For geometric similarity  $b^* = L^*$  and

$$P^* = \frac{d^*}{L^*} (g(x)^*)^3 \quad (8.11)$$

Using a similar procedure to reduce Rice's result, Eq. (8.7), to materials preservation modeling criteria gives

$$P^* = \left[ \frac{m^*}{L^* \sigma^*} \right]^{1.18}$$

Assuming that identical materials produce the same surface roughness on a macroscopic level, i.e.,  $m^* = 1$  and  $\sigma^* = 1$  results in

$$P^* = L^{*-1.18} \quad (8.12)$$

The difference in results obtained for Eq. (8.11) and (8.12) is due to the inclusion of surface waviness in Clausing's relation [Eq. (8.2)] and the assumption of a perfectly flat surface with microscopic roughness by Rice [Eq. (8.6)]. The inclusion of  $g(x)^*$  in Eq. (8.11) is necessary since it is a function of pressure as well as total flatness deviation. These properties will not be the same in model and prototype even though identical materials are used.

In the case of a temperature preservation model  $T^* = 1$  and Eq. (8.8) becomes

$$h^* = \frac{K^*}{L^*} = 1 \quad (8.13)$$

Using  $h^* = 1$ , and  $b^* = L^*$ , in the Clausing Eq. (8.5) yields

$$P^* = \frac{E^* d^*}{L^*} \left[ g(x)^* \right]^3 \quad (8.14)$$

Likewise, using the same relations in Rice's Eq. (8.7) gives

$$P^* = H^* \left[ \frac{\sigma^*}{m^* L^*} \right] \quad (8.15)$$

Once again the major difference in results is the inclusion of macroscopic waviness in Clausing's relation.

The above results for scaling of  $h$  through control of joint geometry, pressure, roughness, and waviness are indicative of the difficulties to be found in joint modeling. The problems in modeling are essentially the same as those in controlling joint conductance in the prototype.

As has been shown, the joint conductance value for members in contact is extremely sensitive to the surface conditions. Rice's equation presents a reasonable prediction for perfectly flat surfaces. Clausing and Chao's results take into account some surface waviness but depend on an accurate determination of the ratio of total area to actual contact area. This value is difficult to determine for common engineering joints.

Both of the results presented here require uniform pressure at the joint. This generally is not achieved for bolted or riveted joints. Some work has been performed trying to scale bolted joints (Refs. 28 and 29); however, the best scaling achieved was on the order of 30% under very carefully controlled conditions.

The presence of surface films on joined metals has not been included in analytical treatments. Surface films present problems even when using material preservation techniques since the thickness of a film on a given material with similar surface conditions will tend to be constant and uncontrollable. Scaling of the film thickness to conform to model criteria would be most difficult. Duplication of surface film properties for a temperature preservation model would be even more difficult since material substitution would be necessary.

Clausing and Chao have reported that joints made with dissimilar materials frequently exhibited directional effects. That is, a higher temperature drop is measured across a dissimilar metal joint depending upon the direction of heat flow. This phenomena quite obviously introduces a definite limitation in modeling with  $T^* = 1$  since material substitution is necessary. Since the cause of directional effects is not entirely understood, there are as yet no criteria to use as guidelines in model design.

Strain relieving due to changes in temperature and temperature dependent thermal conductivities also change joint conductance. Since in material preservation the temperatures of the model may differ substantially from that of the prototype, these effects must be considered in terms of model thermal performance.

It must be concluded that analytical and experimental results on joint conductance indicate that accurate thermal modeling of common engineering joints is not within the grasp of current technology. Predictable metal-to-metal joints have been manufactured. However, this has been accomplished only for very simple geometries using extreme care in surface preparation and cleanliness. Attempts to predict the thermal conductance of assembly line engineering joints (i. e. , bolted, riveted, spot welded, etc. ) have generally been completely unsuccessful.

In recognition of the wide variations observed in joint conductance, it is becoming standard practice in spacecraft manufacture to design all thermally important joints to have either maximum or minimum achievable conductances. Where this is done through shorting straps, filler compounds, or insulating standoffs, then the model designer can pursue the same solution to eliminate thermal dependence of the component on joint conductance. Where a thermally important joint is found as a result of model tests, then suggestions should be made to the prototype designer to institute procedures to eliminate the thermal sensitivity to joint properties.

## Section 9

### CONCLUSIONS

A discussion of the numerous limitations facing the thermal model designer has been included in each of the major sections of this report. Therefore, only a review of the major conclusions drawn from the study are included in the following paragraphs.

The review of spacecraft geometrical and thermal designs disclosed that all of the vehicles considered were amenable to thermal modeling. Size and geometry of the prototypes are not presently considered as a limitation in thermal modeling studies. The smaller vehicles representative of unmanned satellites can be modeled at between 1/2 and full scale and the larger ones down to 1/7th scale. At the smaller scale ratios, the problems associated with model construction, instrumentation, and materials selection become increasingly difficult. Scale ratios in the range 1/2 to 1/4 are far more convenient in terms of these problem areas.

Model designs based upon either materials preservation or temperature preservation techniques are more difficult to achieve than those requiring neither of these restrictions. Setting a value for  $T^*$ ,  $K^*$ ,  $C_p^*$ , or  $\theta^*$ , restricts the total flexibility available in selection of the most promising property and length ratios for a given model. When all model ratios are left unrestricted, it is possible to pursue several model designs and select the most optimum in terms of closely matching the model criteria with a minimum of distortion. When one of the ratios is initially fixed, the number of possible designs is considerably reduced. Thus, the most desirable model approach is to make no apriori decisions on scaling ratios thereby maintaining maximum flexibility in model design.

Of the two preservation techniques, that of temperature preservation is preferred over materials preservation. Using temperature preservation permits materials

substitution and, through selection of appropriate materials, compliance with model criteria which include the influence of thermally dependent thermophysical properties. Distortion of thicknesses will often be necessary to accomplish the required matching of thermal paths; however, the dependence of the model on material properties can be preserved.

Materials preservation is the least promising model approach since the required change in model temperature (i.e.,  $T^* = L^{*-1/3}$ ) negates satisfaction of  $K^* = C_p^* = 1$ . Most materials experience sufficient changes in  $K$  and  $C_p$  with temperature to significantly alter the assumed preservation of initial properties. It has been suggested by previous investigators that this difficulty can be eliminated through materials preservation with  $T^* = 1$ . Satisfying the model criteria with both restrictions requires geometric distortion of all components which in most complex systems is not possible.

Other difficulties associated with materials preservation when  $T^* \neq 1$  are the need for intense solar simulation and high temperature ratios. Since most present-day solar simulators are limited to  $I^*$  on the order of 2, length ratios on the order of  $1/1.68$  are the smallest available using materials preservation and true solar simulation. Smaller length ratios require higher intensities ( $I^* = L^{*-4/3}$ ) which are provided using infrared simulation and may result in high temperature failure of surface coatings.

Studies of simple shapes such as flat plates, cylinders, and spheres with prescribed boundary conditions are useful in establishing design limits in scale ratios for the complete model. The analyses of a rotating thick plate presented in Section 5 led to the establishment of dimensionless parameters whose values provide ranges within which similarity may be assumed even though the model criteria are not strictly adhered to. For example, when  $(K/\sigma\epsilon T_{avg}^3 L) > 10^2$  for the prototype then a negligible thermal gradient will exist through the thickness of a rotating plate. The model can then be designed with any larger value of  $(K/\sigma\epsilon T_{avg}^3 L)$  as long as other controlling parameters are adhered to. Additional information of this type can easily be obtained through use of Groeber charts for the simple shapes.

Studies of the multilayer insulation systems provided several indications of limitations existent in modeling of this material. For any prototype using multilayer insulation simply as an adiabatic boundary, there exists the possibility of overdesign of the prototype. That is, many such designs suffer negligible changes in temperature of enclosed surfaces for order of magnitude increases in insulation conductance. In these cases, modeling must only accomplish a satisfactory adiabatic condition and accurate modeling of blanket properties is unnecessary. For applications where performance is significantly dependent on the blanket conductivity, the model design is considerably more difficult.

For modeling multilayer insulation with temperature preservation, the best approach appears to be maintenance of  $K^*/t^* = 1$  using the same blanket materials with fewer layers. This corresponds to concurrent preservation of materials and temperature through geometric distortion and allows the designer to use prototype blanket properties. Most important is that the approach avoids temperature dependent properties of alternate materials. Using a distorted thickness results in distortion of the three-dimensional thermal field in the vicinity of penetrations. However, this is generally not of importance for most practical systems.

A materials preservation approach with  $T^* \neq 1$  is most difficult for the multilayer system since the temperature dependence of these insulation systems is quite strong. Performance of the study then requires that a thorough experimental program similar to the one reported in Section 7 be conducted to accurately specify the thermal conductivity of the model. The difficulties associated with laboratory measurements of  $K$  for the material are considerable since the measured wrap must correspond in all details with that to be used on the model. In general, it is undesirable to pursue a design approach of this type due to the need for a sizeable supporting effort on material property measurements with little guarantee that desired thermal properties and temperature coefficients will be achieved.



Modeling of common joints with any degree of acceptable accuracy does not appear to be a possible procedure at the present time. The influences of surface roughness, waviness, and contact pressure are interrelated and sufficiently uncontrollable so that design of prototype joints with prescribed properties is not possible with less than 30% error. A larger error can be anticipated in the model joint in view of size effects, surface preparation difficulties, and other unknowns. Modeling of special joints with designs tailored to circumvent a thermal problem is entirely possible since the influence of surface properties will normally be absent in the prototype.

Section 10  
REFERENCES

1. R. E. Rolling, Thermal Scale Modeling in a Simulated Space Environment, N-05-66-1, Final Report for NASA/MSFC Contract NAS 8-1152, Lockheed Palo Alto Research Laboratory, Palo Alto, Jun 1966
2. B. T. Chao and G. L. Wedekind, "Similarity Criteria for Thermal Modeling of Spacecraft" J. Spacecraft and Rockets, Vol. 2., Mar 1965
3. P. L. Miller and J. A. Wiebelt, "Thermal Modeling in a Simulated Space Environment," Thermophysics of Spacecraft and Planetary Bodies, Progress in Astronautics and Aeronautics, Vol. 20, New York, Academic Press, 1967
4. B. P. Jones, "Thermal Similitude Studies," J. Spacecraft and Rockets, Vol. 1, Jul 1964
5. Handbook of Optical Properties for Thermal Control Surfaces, LMSC-A847882, Vol. III, Final Report for NASA/MSFC under Contract NAS 8-20353, Lockheed Missiles and Space Co., Sunnyvale, Calif., 25 Jun 1967
6. Handbook of Thermal Design Data for Multilayer Insulation Systems, LMSC-A847882, Vol. II, Prepared by Lockheed Missiles and Space Company for NASA/MSFC under Contract NAS 8-20353, Lockheed Missiles and Space Company, Sunnyvale, Ca., Jun 25, 1967
7. S. Katzoff, Similitude in Thermal Models of Spacecraft, NASA TN D-1631, Apr 1963
8. Max Jakob, "Heat Transfer," Vol. 1, John Wiley and Sons, New Yor, 1956
9. Herbert J. Harris, "Steady Periodic Solar Heating of a Rotating Thick Plate in Space," AIAA Fourth Annual Thermophysics Specialists Conference, San Francisco, Ca., Jun 1969

10. F. Gabron, R. W. Johnson, J. M. F. Vickers, and J. W. Lucas, "Thermal Scale Modeling of the Mariner IV Spacecraft," Thermophysics and Temperature Control of Spacecraft and Entry Vehicles, Progress in Astronautics and Aeronautics, Vol. 18, Academic Press, New York, 1966 p. 675-696
11. N. R. Folkman, F. L. Baldwin, and J. B. Wainwright, "Tests on a Thermally Scaled Model Space Station in a Simulated Solar Environment," Thermophysics and Temperature Control of Spacecraft and Entry Vehicles, Progress in Astronautics and Aeronautics, Vol. 18, Academic Press, New York, 1966, p. 607-626
12. R. E. Rolling, "Results of Transient Thermal Modeling in a Simulated Space Environment," Thermophysics and Temperature Control of Spacecraft and Entry Vehicles, Progress in Astronautics and Aeronautics, Vol. 18, Academic Press, New York, pp 627-660
13. R. E. Rolling, and K. N. Marshall, "Thermal Modeling of a Truncated Cone in a Simulated Space Environment," Proc. AIAA/IES/ASTM Space Simulation Conference, Houston, Sep 1966, pp 66-73
14. R. E. Rolling, K. N. Marshall, and J. P. Kirpatrick, "Thermal Testing Techniques at High Solar Intensities," Proc. Second Annual Space Simulation Conf., AIAA/IES/ASTM, Philadelphia, 1967
15. R. E. Rolling, and K. N. Marshall, Thermal and Structural Modeling of a Large Aperture Space Telescope, Final Report NASA/Marshall Space Flight Center, Contract NAS 8-20411, Sep 1968
16. Billy P. Jones, "Theory of Thermal Similitude with Applications to Spacecraft - A Survey," Astronautica Acta, Vol. 12, No. 4 (1966) pp. 258-271
17. J. M. F. Vickers, "Thermal Scale Modeling," Astronautics and Aeronautics, Vol. 3, No. 5, May 1965, pp. 34-39
18. -----, Development of Thermal Testing Techniques at High Solar Intensities, NASA- CR-73098, Final Report for Contract NAS 2-3164, NASA/Ames Research Center, Jun 1967

19. K. N. Marshall and R. E. Rolling, "Scale Modeling of Multilayer Insulated Spacecraft for use in Preliminary Design Studies," AIAA 4th Thermophysics Specialists Conference, San Francisco, Calif., 16-18 Jun 1969, AIAA paper 69-316
20. -----, Performance of Multilayer Insulation Systems for Temperatures to 700°K, NASA CR-907, 1967
21. -----, A Study on High-Performance Insulation Thermal Design Criteria, Final Report Contract NAS 8-20353, Lockheed Missiles and Space Company, Jun 1967
22. G. R. Cunningham and C. L. Tien, "A Study of Heat Transfer Processes in Multilayer Insulations," Progress in Astronautics and Aeronautics (AIAA Series) to be published, Academic Press 1970.
23. G. C. Vliet and R. M. Coston, "Thermal Energy Transport Parallel to the Laminations in Multilayer Insulation," Advances in Cryogenic Engineering, Vol. 13, p. 671.
24. A. R. Shouman, "An Exact General Solution for the Temperature Distribution and the Radiation Heat Transfer Along a Constant Cross-Sectional-Area Fin," Heat Transfer Division ASME, Nov 1967
25. M. N. Tawil and P. Caloger, "The Use of Multilayer Insulation on the LM Vehicle," AIAA 4th Thermophysics Conference, Jun 1969
26. A. M. Clausing and B. T. Chao, "Thermal Contact Resistance in a Vacuum Environment," Transactions of the ASME Series C, Vol. 87, May 1965, pp. 243-251
27. R. E. Rice, Thermal Conductance of Metallic Joints, University of California Mechanical Engineering Department, Berkeley, Ca., May 1966
28. H. C. Hewitt, A. M. Smith, K. W. Nutt, "Thermal Modeling of Bolted Joints," AIAA 3rd Thermophysics Conference, AIAA #68-762, Jun 1968
29. C. Shih, Thermal Scaling of Bolted Joints, Martin Marietta Corp., Denver, Colorado

Appendix A  
SOURCES OF INFORMATION FOR REVIEW OF  
SPACECRAFT DESIGNS

All sources of material used for the review covered in Section 3 are presented in tabular form in this appendix. Readers interested in obtaining the details of a particular spacecraft design are referred to the sources indicated here.

Table A-1

SOURCES OF INFORMATION FOR REVIEW OF SPACECRAFT DESIGNS

Apollo Application Program

1. Final Report for ATM/Rack Thermal Control Study, Augmentation Task No. 7, LMSC-A842255, 7 Jul 1967, prepared by Lockheed Missiles & Space Co. for NASA/Marshall Space Flight Center Apollo Applications Program Office under Contract NAS 8-21003.
2. ATM Thermal Control Study, Augmentation Task No. 32, LMSC-A842323, 5 Sep 1967, prepared by LMSC for NASA/MSFC under Contract NAS 8-21003.
3. Final Report for Multiple Docking Adapter (MDA) Thermal Model, Augmentation Task No. 14, LMSC/HERC-A842023, 6 Jul 1967, prepared by LMSC for NASA/MSFC under Contract NAS 8-21003.
4. Cluster Thermal Model, Final Report, LMSC-A842205, 1 May 1967, prepared by LMSC for NASA/MSFC under Contract NAS 8-21003.
5. Part I, Contract End Item Detail Specification, Performance and Design Requirements CEI 014000A, Multiple Docking Adapter for Apollo Applications Program AAP-2, NASA-CP114A1000026A, 22 May 1967, prepared by Systems Criteria Section, Systems Requirements Branch, Vehicle Systems Division, Propulsion and Vehicle Engineering Laboratory.
6. Cluster A Design Reference Mission (DRM), LMSC-A842147, 11 Mar 1967, prepared by LMSC for NASA/MSFC under Contract NAS 8-21003.
7. Personal Communication with Members of LMSC Orbit Thermodynamic Analysis Group, Oct 1967.

OGO (Orbiting Geophysical Observatory)

1. Final Report, Orbiting Geophysical Observatories I, II, and III, p. 2-1 through 2-77, furnished by W. E. Scull, Project Manager for OGO at NASA/Goddard Space Flight Center.
- 2.\* W. E. Scull, "The Mission of the Orbiting Geophysical Observatories," The Observatory Generation of Satellites, NASA-SP-30, Mar 1963, pp. 1-10, prepared by Goddard Space Flight Center, Greenbelt, Md.
- 3.\* G. E. Gleghorn, "The Engineering Design of the Orbiting Geophysical Observatories," The Observatory Generation of Satellites, NASA SP-30, Mar 1963, pp. 11-24, prepared by Goddard Space Flight Center, Greenbelt, Maryland.

\*Also published in Advances in the Astronautical Sciences: Scientific Satellites, Vol. 12, 27 Dec 1962, edited by Irving E. Jeter, Western Periodicals Co., North Hollywood, Calif.

: Table A-1 (Cont.)

OGO (Cont.)

4. G. J. Gleghorn and W. T. Wiggins, "Design and Development of the Orbiting Geophysical Observatory," Civilian and Military Uses of Aerospace, annals of the New York Academy of Sciences, Vol. 134, Art. 1, pp. 205-233, 22 Nov 1965.
5. J. B. Rittenhouse and J. B. Singletary, Space Materials Handbook, 2nd Edition, Supplement 1, M-54-65-1: ML-TDR-64-40, Dec 1965, Lockheed Missiles & Space Co., Sunnyvale, Calif.
6. J. B. Ritterhouse and J. B. Singletary, Space Materials Handbook, 2nd Edition, Supplement 2, L-58-67-1: AFML-TR-64-40, Mar 1967, Lockheed Missiles & Space Co., Sunnyvale, Calif.

OAO (Orbiting Astronomical Observatory)

- 1.\* R. R. Ziemer and J. E. Kupperian, Jr., "The Mission of the Orbiting Astronomical Observatory," The Observatory Generation of Satellites, NASA SP-30, Mar 1963, pp. 45-52, prepared by Goddard Space Flight Center, Greenbelt, Maryland.
- 2.\* W. H. Scott, "The Engineering Design of the Orbiting Astronomical Observatory," The Observatory Generation of Satellites, Nasa sp-30, Mar 1963, pp. 53-62, prepared by Goddard Space Flight Center, Greenbelt, Maryland.
3. L. H. Hemmerdinger, "Thermal Design of the Orbiting Astronomical Observatory," Journal of Spacecraft and Rockets, Vol. 1, No. 5, Sep-Oct 1964, pp. 477-483.
4. J. Mockovciak, Jr., "Engineering an Earth Satellite," Mechanical Engineering, May 1963, pp 48-51.
5. J. B. Rittenhouse and J. B. Singletary, Space Materials Handbook, 2nd Edition, Supplement 2, L-58-67-1: AFML-TR-64-40, Mar 1967, Lockheed Missiles & Space Co., Sunnyvale, Calif.

AOSO (Advanced Orbiting Solar Observatory)

- 1.\* J. C. Lindsay, "The Mission of the Advanced Orbiting Solar Observatory," The Observatory Generation of Satellites, NASA SP-30, Mar 1963, pp. 25-30, prepared by Goddard Space Flight Center, Greenbelt, Maryland.
- 2.\* A. J. Cervenka, "One Approach to the Engineering Design of the Advanced Orbiting Solar Observatory," The Observatory Generation of Satellites, NASA SP-30, Mar 1963, pp. 31-44, prepared by Goddard Space Flight Center, Greenbelt, Maryland.

\*Also published in Advances in the Astronautical Sciences: Scientific Satellites, Vol. 12, 27 Dec 1962, edited by Irving E. Jeter, Western Periodicals Co., North Hollywood, Calif.

Table A-1 (Cont.)

AOSO (Cont.)

3. AOSO Phase I Final Report, Thermal and Structural Sections, (pp. 1-7 through 1-279), furnished by F. J. Cepollina, NASA Goddard Space Flight Center.

GEOS (Geodetic Satellite)

1. J. E. Phenix, "Structural Design Analysis and Testing of the GEOS Satellite," Technical Memorandum TG-730, Sep 1965, The John Hopkins University - Applied Physics Laboratory, Silver Spring, Maryland.

ATS 4 (Applications Technology Satellite)

1. An Advanced Study of an Application Technology Satellite (ATS-4) Mission, Vol. 1, Book 1, Final Study Report under Contract NASw-1410, General Electric Co., Missiles and Systems Div., Philadelphia, Penn., Nov 1966, (NASA-CR-81767, Doc. 665D4529, Vol. 1, Bk. 2).
2. Final Report ATS-4, Vol 3 of 8, prepared by Fairchild Hiller Space Systems Division for Goddard Space Flight Center, CR-81603, Dec 1966.

P-11 (Orbital-Launched Satellite)

1. Lockheed P-11 Orbital-Launched Satellite (sales brochure), 15 Feb 1964, Lockheed Missiles & Space Co., Sunnyvale, Calif.
2. Personal Communication with Pat Denicore of LMSC P-11 Structural Design Group.

Nimbus

1. R. A. Stampel and H. Press, "The Nimbus Spacecraft System," Aerospace Engineering, Vol. 21, No. 7, Jul 1962, pp. 16-28.
2. Space Materials Handbook, 2nd ed., Supplement 1, op. cit.
3. Drawings containing some information on materials and spacecraft configuration:
  - "Mechanical Interface Design Spec. Control Drawing," General Electric ER475J207702.
  - "Mechanical Interface, Nimbus Altitude Control Subsystem," General Electric 47J207723.
  - "Sensory Ring Configuration," General Electric 47J209953.

Multi-Purpose Communications Satellite

1. Multi-Purpose Communications Satellite Study, Final Report, Vol. II, Satellite Design, LMSC-A881659, 20 Jul 1967, Lockheed Missiles & Space Co., Sunnyvale, Calif., prepared for Communications Satellite Corporation.
2. Personal Communications with LMSC personnel.



Table A-1 (Cont.)

Pioneer VI and VII

1. Space Materials Handbook, 2nd ed., Supplement 2, op. cit.
2. Personal Communication with J. P. Kirkpatrick and J. Frank, NASA Ames Research Center, Moffet Field, Calif.

Mars Orbiter

1. Mariner Mars 1969 Orbiter Study, Final Report M-29-64-1, 4 Oct 1964, prepared by Lockheed Missiles & Space Co., Sunnyvale, Calif., under Contract JPL-950877.
2. "Mariner Mars Orbiter Structural Analysis," Interdepartmental Communication, Lockheed Missiles & Space Co., Sunnyvale, Calif., 11 Aug 1964.

Orbital Tanker

1. Orbital Tanker Design Data Study, Final Report, Vol. II, LMSC-A748410, 30 May 1965, prepared by Lockheed Missiles & Space Co., Sunnyvale, Calif., for NASA/MSFC under Contract NAS 8-11326.

OTES (Optical Technology Experiment System)

1. Optical Technology Experiment System (OTES), LMSC Input to Phase I Final Technical Report, LMSC-A820889, 1 Sep 1966, submitted by Lockheed Missiles & Space Co. to The Perkin-Elmer Corp. in support of Prime Contract NASA 8-20255 (MSFC).
2. Study for an Optical Technology Apollo Extension System, Interim Report, No. 8319, 15 Apr 1966, prepared by The Perkin-Elmer Corp. for NASA/MSFC.
3. Additional information obtained as a result of LMSC activity on research Contract NAS 8-20411 (Thermal Similitude).

Agena

1. Standard Agena Space Vehicle Model SSO1-B, Description Manual, LMSC-A397890, 15 Oct 1967, Lockheed Missiles & Space Co., Sunnyvale, Calif.
2. Personal Communication with C. MacQuiddy of LMSC Agena Engineering.
3. Drawings:
  - Structure - Forward Section, No. 1393253 (LMSC)
  - Structure - Aft Section, No. 1393373 (LMSC)
  - Tube Structure - Forward Section, No. 1395062 (LMSC)
  - Ring Segment - Forward Section Structure, No. 1395156 (LMSC)
  - Beam Assembly - 30, Aft Section, No. 1393214 (LMSC)

Table A-1 (Cont.)

Advanced Multi-Purpose Space Exploration Spacecraft

1. Starlet/Starlite System, Technical Description, LMSC-A847990, 17 Apr 1967, Lockheed Missiles & Space Co., Sunnyvale, Calif. (LMSC Proprietary design).

Surveyor

1. Space Materials Handbook, 2nd ed., Supplement 2, op. cit.
2. Surveyor V, A Preliminary Report, NASA SP-163, Dec 1967, National Aeronautics and Space Administration, Washington, D.C.
3. Personal Communications with J. Fortenberry, J. Smith, and B. C. Jones, Jet Propulsion Laboratory, Pasadena, Calif.
4. Drawings:  
    Surveyor Spacecraft-General Arrangement, 3025125 (Hughes Aircraft Company)  
    Subassembly installation drawings useful for defining details of configuration: Hughes Aircraft Co. Nos. 230084-3, 230093-2, 230108, 230126-3, 230128-3, 230135-2, 230136-1, 230167-3, 261336, 261487, 264238, 264272, 264292, 264449-3, 276167, 276500, 285919-3, 286124-2, 3025733, 286405, 286582-1, 292005, 292130, 3025093, 3025156, 3025188, 3025203, 3025262, 3025288, 3025353, 3025354.

Mariner

1. Space Materials Handbook, 2nd ed., Supplement 1, op. cit.

Voyager (LMSC proposed Configuration)

1. Voyager Spacecraft System Proposal, Vol. 1, 22 Feb 1965, LMSC-A733418, Lockheed Missiles & Space Co., Sunnyvale, Calif.

Explorers

1. Space Materials Handbook, 2nd ed., Supplement 1, op. cit.
2. Space Materials Handbook, 2nd ed., Supplement 2, op. cit.
3. J. M. Madez and R. C. Baumann, Structures for Small Scientific Satellites, NASA-TM-X-55285, Jul 7, 1965.

Lunar Orbiter

1. Space Materials Handbook, 2nd ed., Supplement 2, op. cit.

Ranger

1. Space Materials Handbook, 2nd ed., Supplement 1, op. cit.

Table A-1 (Cont.)

ESRO II (European Space Research Organization)

1. D. M. Squires and C. R. Hume, "Structural Design of the ESRO II Solar Astronomy Satellite," presented at the Colloque Sur Les Structures De Satellites, 8 Jun 1965, copies available through AIAA Technical Information Service.
2. "The Design of ESRO II," Systems In Space: A Regular Survey of Space Engineering Progress, 1965.
3. A. W. Lines, "Design of Spacecraft for Experiments in the ESRO Scientific Program," Journal of the Royal Aeronautical Society, Vol. 69, No. 1965, pp. 759-762.

San Marco (Italy)

1. L. Broglio, The San Marco 1-A Scientific Satellite, XVI International Astronautical Congress, Athens, Greece, 1965.
2. "The Structural Configuration of the San Marco Satellite," Sciences Et Industries Spatiales, 9/10, 1966.

U.K. -3 (England)

1. J. L. Blonstein, Progress with U.K. -3, 1965, British Aircraft

In addition to the references listed above, the following documents were found to contain useful information on spacecraft configurations and/or materials:

1. TRW Space Log, a quarterly publication of TRW Systems Group, Redondo Beach, Calif., (pertinent information on the foregoing spacecraft in: Vol. 4, No. 3, Fall 1964; Vol. 5, No. 2, Summer 1965; Vol. 5, No. 3, Fall 1965; Vol. 6, No. 1, Spring 1966; Vol. 6, No. 2, Summer 1966; Vol. 6, No. 3, Fall 1966; Vol. 6, No. 4, Winter 1966-67; Vol. 7, No. 2, Summer 1967; Vol. 7, No. 4, Winter 1967-68).
2. Review and Evaluation of Recent Structural Development Programs, Vol. 1, 15 Aug 1966, R-ME-IT-10044, Internal Note, NASA, Marshall Space Flight Center.
3. Proceedings of the AIAA/ASME 8th Structures, Structural Dynamics, and Materials Conference, Palm Springs, Calif., Mar 29-31, 1967.
4. Program 461 Spacecraft Materials Handbook, LMSC-A327227, May 1964 Lockheed Missiles & Space Co., Sunnyvale, Calif.
5. Proceedings of the AIAA Fifth Annual Structures and Materials Conference, Palm Springs, Calif., 1-3 Apr 1964, AIAA Publication CP-8.
6. Space Materials Handbook, Second Edition, Jan 1965, edited by C. G. Goetzl, J. B. Rittenhouse, and J. B. Singletary, ML-TDR-64-40, Air Force Materials Laboratory, Wright-Patterson Air Force Base, Ohio.

## Appendix B

### THERMOPHYSICAL PROPERTIES

The table and figures of this appendix contain information on the thermophysical properties of materials in current use on spacecraft. The information may also be used to assist in initiating design of a thermal model.

The data represent best values available at the present time and are not intended as an accurate value for a specific sample. Considerable differences in properties are frequently found on the literature surveyed requiring judgment and averaging to be used to establish values for the following compilation. Therefore, the reader is likely to find numerical differences between the quoted values and those measured for a specific sample. However, the data are considered an excellent indication of variations in  $\rho$  and  $C_p$  for various metal alloys, insulations, and composites, and of considerable aid for initiation of model design.

Following the presentation of data in numerical and graphical form is a listing of references used for preparation of this appendix.

Table B-1

THERMOPHYSICAL PROPERTIES OF TYPICAL SPACECRAFT AND  
MODELING MATERIALS

Material	Density (gm/cm <sup>3</sup> )	Thermal Conductivity (W/cm·K) (at 395°K)	Specific Heat (J/gm·K) (at 295°K)	Thermal Diffusivity (cm <sup>2</sup> /sec) (at 295°K)	Average Coefficient of Thermal Expansion (in./in./°K) (295 to 373°K)
<b>Structural</b>					
<b>Aluminum</b>					
1100-0	2.71	2.22	0.92	0.891	$2.36 \times 10^{-5}$
1100-H14	2.71	2.20	0.92	0.885	$2.36 \times 10^{-5}$
1100-H18	2.71	2.18	0.92	0.876	$2.36 \times 10^{-5}$
2014-T0	2.80	1.93	0.96	0.719	$2.30 \times 10^{-5}$
2014-T4	2.80	1.21	0.96	0.450	$2.30 \times 10^{-5}$
2014-T6	2.80	1.54	0.96	0.573	$2.30 \times 10^{-5}$
2020-T0	2.71	1.05	—	—	$2.28 \times 10^{-5}$
2020-T4, -T6	2.71	0.88	—	—	$2.28 \times 10^{-5}$
2024-T0	2.78	1.93	0.92	0.755	$2.32 \times 10^{-5}$
2024-T3, -T4, -T351	2.78	1.21	0.92	0.473	$2.32 \times 10^{-5}$
2219-T0	2.83	1.71	—	—	$2.32 \times 10^{-5}$
2219-T6	2.83	1.12	—	—	$2.32 \times 10^{-5}$
2219-T87	2.83	1.25	0.96	0.460	$2.23 \times 10^{-5}$
3003-0, -H18	2.74	1.76	0.92	0.699	$2.32 \times 10^{-5}$
5052-T0, -H32, -H34	2.68	1.38	0.92	0.560	$2.38 \times 10^{-5}$
6061-T0	2.70	1.71	0.96	0.660	$2.36 \times 10^{-5}$
6061-T4, -T6	2.70	1.55	0.96	0.599	$2.36 \times 10^{-5}$
7039	2.74	—	—	—	—
7075-T0	2.80	1.71	0.96	0.636	$2.36 \times 10^{-5}$
7075-T6, -T651	2.80	1.30	0.96	0.484	$2.36 \times 10^{-5}$
7079-T6, -T651	2.75	1.25	0.96	0.474	$2.38 \times 10^{-5}$
7178-T6, -T651	2.83	1.25	0.96	0.460	$2.32 \times 10^{-5}$
356-T6	2.68	1.51	0.95	0.595	$2.14 \times 10^{-5}$
<b>Structural Metals</b>					
<b>Magnesium</b>					
Mag. (99.9+% pure)	1.74	1.54	1.03	0.860	$2.61 \times 10^{-5}$
AZ31B-0, H24	1.77	0.76	1.00	0.430	$2.63 \times 10^{-5}$
AZ31B-F	1.77	0.76	1.01	0.425	$2.63 \times 10^{-5}$
A780-T5	1.80	0.502	1.05	0.286	$2.63 \times 10^{-5}$
HK31A-0	1.79	1.06	1.03	0.575	$2.63 \times 10^{-5}$
HK31A-H24	1.79	1.14	1.03	0.619	$2.63 \times 10^{-5}$
HM21A-T8	1.78	1.37	1.05	0.734	$2.63 \times 10^{-5}$
HM31A-T5	1.80	1.05	1.05	0.556	$2.63 \times 10^{-5}$
ZK60A-F	1.83	1.17	1.05	0.610	$2.61 \times 10^{-5}$
ZK60A-T5	1.83	1.21	1.05	0.630	$2.61 \times 10^{-5}$
ZH62A-T5	1.85	1.09	1.03	0.572	$2.63 \times 10^{-5}$
<b>Magnesium-Lithium</b>					
LA141A-T7	1.34	0.44	1.45	0.226	$3.82 \times 10^{-5}$
<b>Stainless Steel</b>					
A-286	7.93	9.237	0.42	0.071	$1.85 \times 10^{-5(a)}$
304	8.05	0.169	0.50	0.042	$1.72 \times 10^{-5}$
321	7.89	0.134	0.50	0.034	$1.68 \times 10^{-5}$
347	8.05	0.161	0.50	0.040	$1.67 \times 10^{-5}$
410	7.75	0.276	0.40	0.077	$0.99 \times 10^{-5}$
18-8	8.05	0.159	0.45	0.044	$1.73 \times 10^{-5}$
Maraging Steel (18 Ni)	8.05	—	—	—	$1.01 \times 10^{-5}$
PH-15-7 Mo	7.85	0.161	—	—	$(0.9 \text{ to } 1.08) \times 10^{-5}$
<b>Beryllium</b>					
Commercially Pure	1.85	1.82	1.89	0.519	$1.15 \times 10^{-5}$
Lockalloy (Commercial)	2.07	2.13	1.69	0.610	$1.66 \times 10^{-5}$
Be-Cu Alloy (Be-1.9%, Co-0.2%)(Cu- bal)	8.30	1.13	0.42	0.324	$1.67 \times 10^{-5}$
<b>Titanium</b>					
Commercially Pure	4.61	0.170	0.52	0.072	$1.045 \times 10^{-5}$
6Al-4V-0	4.47	0.0727	0.53	0.0307	$0.83 \times 10^{-5}$
6Al-1Mo-1V	4.37	0.086	—	—	$0.65 \times 10^{-5}$
5Al-2.6 Sn	4.46	0.094	0.57	0.033	$0.94 \times 10^{-5}$
13V-11Cr-3Al	4.85	0.069	0.54	0.026	$0.97 \times 10^{-5}$

(a) Temperature range 300°K to 1030°K for A286.

Table B-1 (Cont.)

Material	Density (gm/cm <sup>3</sup> )	Thermal Conductivity (J/gm °K) (at 295 °K)	Specific Heat (J/gm °K) (at 295 °K)	Thermal Diffusivity (cm <sup>2</sup> /sec) (at 295 °K)	Average Coefficient of Thermal Expansion (in./in./°K) (295 to 373 °K)
<b>Adhesives</b>					
Silicone (RTV)	1.2- 1.5	0.0017- 0.0031	1.21- 1.55	0.00117 0.00133	$2.92 \times 10^{-4}$ $6.3 \times 10^{-3(b)}$
Epoxy	1.21	0.0019	1.28	0.00125	
Resin Cements	1.3	0.0024	1.45	0.00127	
<b>Optical Materials</b>					
Fused Silica (Corning 7940)	2.2	0.0133	0.73	0.0083	$5.6 \times 10^{-7}$
Fused Quartz	2.2	0.0138	0.89	0.0091	$5.5 \times 10^{-7}$
Microsheet (Corning 0211)	2.5	—	—	—	$72.0 \times 10^{-7}$
<b>Honeycomb</b>					
Ti-(Ti-faces/Ti-rigs)	—	0.017	—	—	—
Ti-(Duplex Core Ti/Glass honeycomb-Ti faces)	—	0.008	—	—	—
Reinforced Plastic Facing & Core (core 1 in. thick)	—	0.00089	—	—	—
Glass fabric-polyester facing/nylon phenolic core, 0.309 in. thick	0.084 <sup>(c)</sup>	0.00071	—	—	—
Glass fabric-polyester facing/glass fabric phenolic core, 0.311 in. thick	0.090 <sup>(c)</sup>	0.00087	—	—	—
Stainless Steel (17-7PH) (face: 0.032 in. thick; core: 0.375 in. cells, 0.625 in. thick)	—	0.00158	0.55	—	$3.6 \times 10^{-5(d,b)}$ $1.06 \times 10^{-5(e,b)}$
Aluminum (2024-T3) Face: 0.02 in. thick; core: 0.25 in. cell size; 0.625 in. thick	—	0.0058	1.07	—	$1.87 \times 10^{-5(d,b)}$ $1.98 \times 10^{-5(e,b)}$
Foam (Polyurethane)	0.16	0.0004	1.47	0.0017	$6.3 \times 10^{-5}$
Mylar (0.006 mm thick)	1.39	0.0015	1.32	0.0008	$1.89 \times 10^{-5(f)}$
Kapton (0.006 mm thick)	1.42	0.0016	1.05	0.001	$2.7 \times 10^{-5(f)}$
Aluminized Kapton (0.025 mm thick)	1.42	0.0018	—	—	—
Nylon	1.14	0.0036	1.55	0.002	$8.1 \times 10^{-5}$
Plexiglass	1.18	0.0015	1.30	0.001	$7.0 \times 10^{-5}$
Teflon - (P+FE)	2.13	0.0017	1.05	0.0008	$10.0 \times 10^{-5(f)}$
Teflon - (FEP)	2.13	0.0021	1.17	0.0008	$8.3 - 10.4 \times 10^{-5(g)}$
Glass Fabric Reinforced Epoxy 181 glass fabric/shell X-131 Epoxy Resin	1.87	0.0017	—	—	—
181 glass fabric/(Epon/plyophen Resin)	1.74	0.0011	—	—	—
Glass Fiber Reinforced Epoxy: YM31A glass fiber/DER 332 Epoxy Resin	1.85	0.0048(t) <sup>(h)</sup> 0.0048(l) 0.0063(  )	0.845	0.0028(t) 0.0031(l) 0.0040(  )	$16.9 \times 10^{-6(t)(f,b)}$ $24.3 \times 10^{-6(l)(f)}$ $5.4 \times 10^{-6}(  )(c)$
<b>Miscellaneous</b>					
Inconel 718	8.21	0.194	—	—	$1.68 \times 10^{-5}$
Mo-0.5 Ti	10.6	1.185	0.251	0.45	$5.35 \times 10^{-6(l)}$
Mo-0.5 Ti - 0.8 Zr	10.22	1.45(l)	0.276(l)	0.52	$5.35 \times 10^{-6(l)}$
Alloy 510 (Phosphor Bronze A)	8.85	0.69	0.377	0.21	$9.9 \times 10^{-6}$

(b) Room temperature value.

(c) Core density.

(d) Across thickness.

(e) Longitudinal.

(f) At room temperature.

(g) At cryogenic temperatures.

(h) (t) = Meas. in thickness direction of material.

(l) = Meas. perpendicular to reinforcement.

(||) = Meas. parallel to reinforcement.

(i) Pure Mo

Table B-2

EFFECTIVE THERMAL CONDUCTIVITY OF MULTILAYER INSULATION AS A FUNCTION  
OF LAYER DENSITY AND BOUNDARY TEMPERATURES

Multilayer Insulation Description <sup>a</sup>	K <sub>eff</sub> (W/cm <sup>2</sup> °K × 10 <sup>5</sup> ) through Multilayer Insulation								Uncompressed Density (g/cm <sup>3</sup> )	Uncompressed Thickness (cm)	No. of Shields	No. of Spacers
	Layer Density (Radiation Shields/in. )											
	10	30	50	70	90	110	130	150				
Single-aluminized crinkled Mylar (0.25 mil NRC-2), Mylar forms integral spacer (300/78°K)	—		0.052	0.045	0.052	0.065	0.080		0.0168	0.56	10	Integral
Same as above (295/21°K)	—	0.056	0.029	0.060	0.081	0.101	0.125	0.152			20	Integral
Double-aluminized Mylar (0.25 mil) with Tissuglas (0.6 mil thick) spacers (300/78°K)	—	—	—	—	0.025	0.026	0.030	0.037	0.0376	0.33	10	11
Double-aluminized Mylar (0.25 mil) with Dexiglas (2.8 mil thick) spacers (300/78°K)	—	—	0.055	0.048	0.050	0.055	0.064	—	0.048	0.509	10	11
Same as above with buttons on 8-in. centers (278/77°K)					0.057 (120 rad. shields/in.)						40	40
Same as above with buttons on 8-in. centers (278/21°K)					0.045 (120 rad. shields/in.)						40	40
Crinkled double-aluminized Mylar (0.25 mil) with Tissuglas (0.6 mil) spacers (300/78°K)	—	0.137	0.085	0.070	0.068	0.073	0.083	0.099	0.0144	0.89	10	11
Crinkled double-aluminized Mylar (0.15 mil) with Tissuglas (0.6 mil) spacers (300/78°K)	—	0.062	0.043	0.038	0.041	0.054	—	—	0.0128	1.018	10	11
Aluminized Polyimide Film with Dexiglas (2.8 mil thick) spacer (600/273°K)	—	0.82	0.37	0.97	1.09	1.23	1.39	—	0.069	1.27	10	11

<sup>a</sup> Hot and cold boundary temperatures given as (xxx/xx°K)

Table B-3

VALUES OF  $\rho C_p$ ,  $\rho C_p/K$ , and  $\rho C_p/K$  FOR VARIOUS  
SPACECRAFT MATERIALS

Material	Temp = 295°K $\rho C_p$ J/gm-°K	Temp = 295°K $\rho C_p/K$ $\frac{1}{\text{cm}^4 \cdot \text{°K}^2}$	Temp = 295°K $\rho C_p/K$ $\frac{1}{\text{sec/cm}^2}$
Aluminum			
1100-0	2.4932	5.5349	1.1231
1100-H14	2.4932	5.4850	1.1333
1100-H18	2.4932	5.4352	1.1437
2014-T0	2.6880	5.1878	1.3927
2014-T4	2.6880	3.2525	2.2215
2014-T6	2.6880	4.1395	1.7455
2020-T0			
2020-T4-T6			
2024-T0	2.5576	4.9362	1.3252
2024-T3-T4	2.5576	3.0947	2.1137
2219-T0			
2219-T6			
2219-T87	2.7168	3.3960	2.1734
3003-0-H18	2.5208	4.4366	1.4323
5052-T0-H32-H34	2.4656	3.4025	1.5158
6061-T0	2.5920	4.4323	1.5158
6061-T4-T6	2.5920	4.0176	1.6723
7075-T0	2.6880	4.5965	1.5719
7075-T6-7651	2.6880	3.4944	2.0677
7079-T6-T651	2.640	3.300	2.1120
7178-T6-T651	2.7168	3.3960	2.1734
356-T6	2.546	3.8445	1.6861
Magnesium			
99.9+ % pure	1.7922	2.7600	1.1638
AZ31B-0, H2Y	1.77	1.3452	2.3289
AZ31B-F	1.7877	1.3587	2.3522
AZ80-T5	1.890	0.9488	3.7649
HK31A-0	1.8437	1.9543	1.7393
HK31A-H24	1.8437	2.1018	1.6173
HM21A-T8	1.869	2.5605	1.3642
HM31A-T5	1.890	1.9845	1.8000
ZK60A-F	1.922	2.2487	1.6427
ZK60A-T5	1.922	2.3256	1.5884
ZK62A-T5	1.9055	2.077	1.7482



Table B-3 (Cont.)

Material	Temp = 295°K $\rho C_p$ J/gm-°K	Temp = 295°K $\frac{\rho C_p}{K}$ cm <sup>4</sup> °K <sup>2</sup>	Temp = 295°K $\frac{\rho C_p}{K}$ 1 sec/cm <sup>2</sup>
Mag-Lithium LA141A-T7	1.943	0.8549	4.4159
Stainless Steel			
A-286	3.3306	0.7894	14.0532
304	4.025	0.6802	23.8166
321	3.945	0.5286	29.4403
347	4.025	0.648	25.0000
410	3.565	0.980	12.9636
18-8	3.623	0.576	22.7862
Beryllium			
Comm. Pure	3.5154	6.3980	1.9315
Lockalloy	4.4091	7.4514	2.6089
Be-Cu	3.4860	3.9392	3.0850
Titanium			
Comm. Pure	2.3452	0.3987	13.7953
6 Al-4V-0	2.3691	0.1722	32.5873
5 Al-2.5 Sn	2.5422	0.2135	30.2643
13 V-11 Cr - 3 Al	2.6190	0.1807	37.9565
Optical Materials			
7940 F.S.	1.606	0.02136	120.75
Fused Quartz	1.518	0.02095	110.00
Pyrex	1.930	0.02181	170.79
Nylon	1.767	0.00636	490.83
Teflon (PTFE)	2.2365	0.00380	1315.59
Teflon (FEP)	2.4921	0.00523	1186.71
Plexiglas	1.534	0.00230	1022.67
Fiberglass			
181 glass/selection	1.9474	0.00253	1498.00
YM31A/DER Eposy	1.563	0.00719	339.78
Mo-015 Ti	2.661	3.180	2.2268
Alloy 510 (Phosphor Bronze)	3.336	2.302	4.8348
Pure Aluminum	2.425	4.947	1.1887

Table B-3 (Cont.)

Material	Temp = 295°K $\rho C_p$ j/gm-°K	Temp = 295°K $\frac{\rho C_p}{K}$ cm <sup>4</sup> °K <sup>2</sup>	Temp = 295°K $\frac{\rho C_p}{K}$ $\frac{1}{\text{sec/cm}^2}$
Pure Copper	3.428	13.232	0.8881
95% Cu 5 Al (Alum Bronze)			
75 Cu, 25 Sn(Bronze)	2.970	0.772	11.423
85 Cu, 9 Sn, 6 Zn (Red Brass)	3.350	2.030	5.5281
Molybdenum	2.560	3.098	2.1157
Pure Nickel	3.969	3.572	4.410
Tungsten	2.586	4.215	1.5865
Silk	0.080	$2.91 \times 10^{-5}$	174.5
Cotton	0.103	$6.077 \times 10^{-5}$	
Honeycomb ASTEC Mat. A Alum/Alum 1/4" th			

174

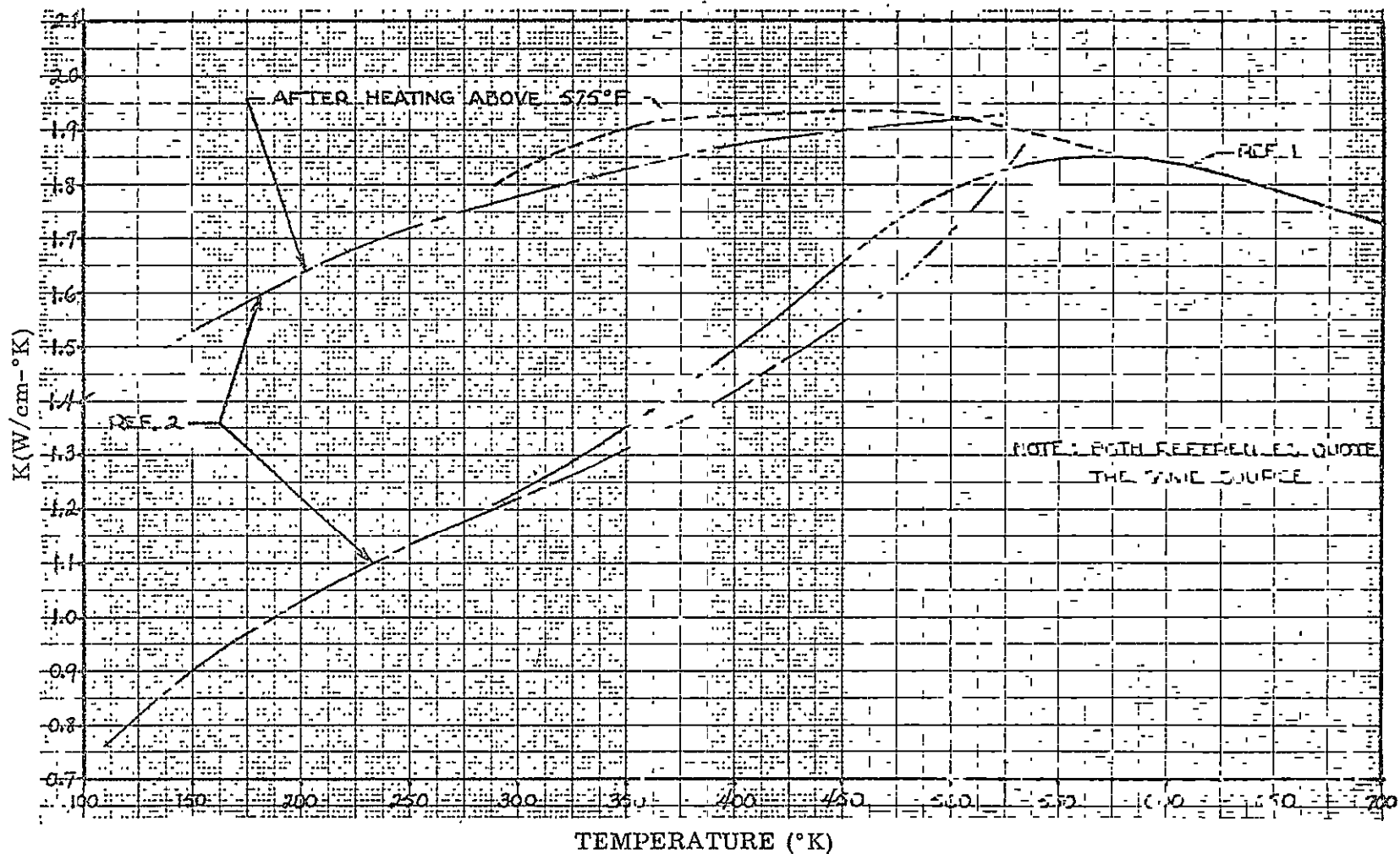


Fig. B-1 Thermal Conductivity of Aluminum 2024-T4

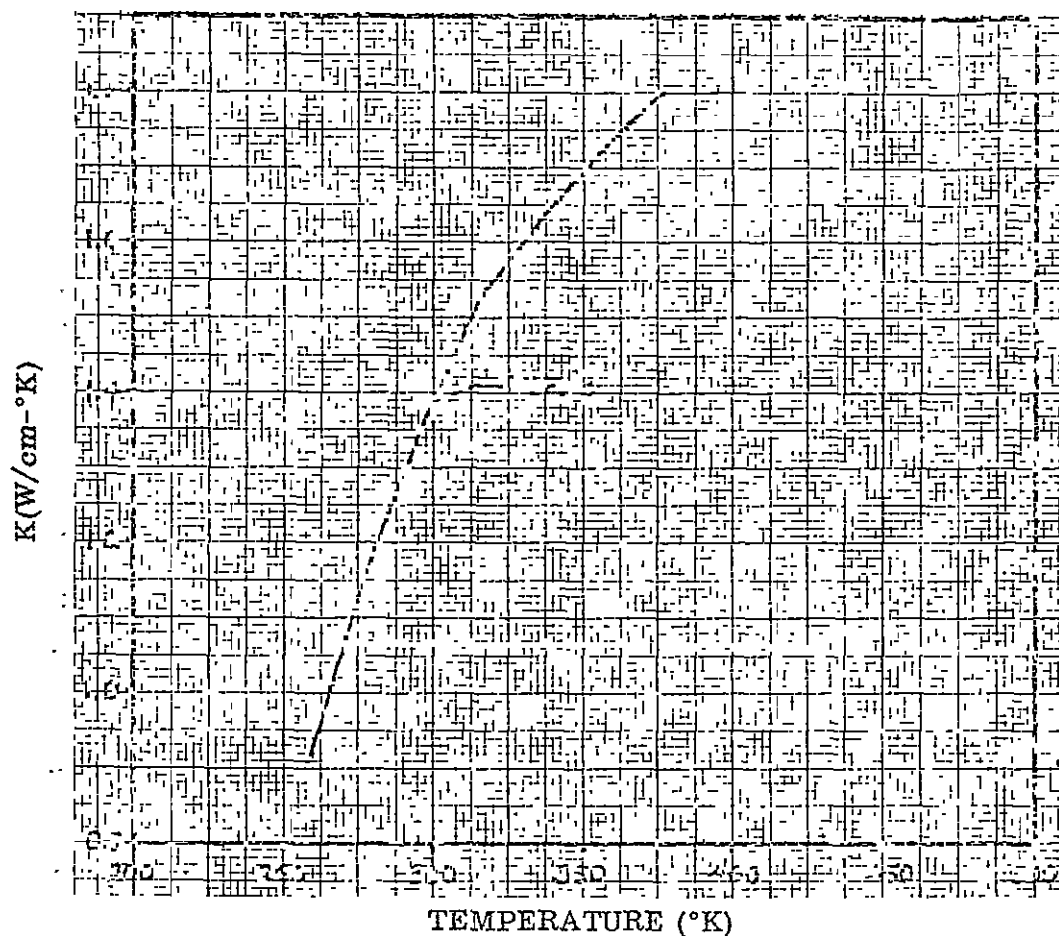


Fig. B-2 Thermal Conductivity of Aluminum 5052-T0

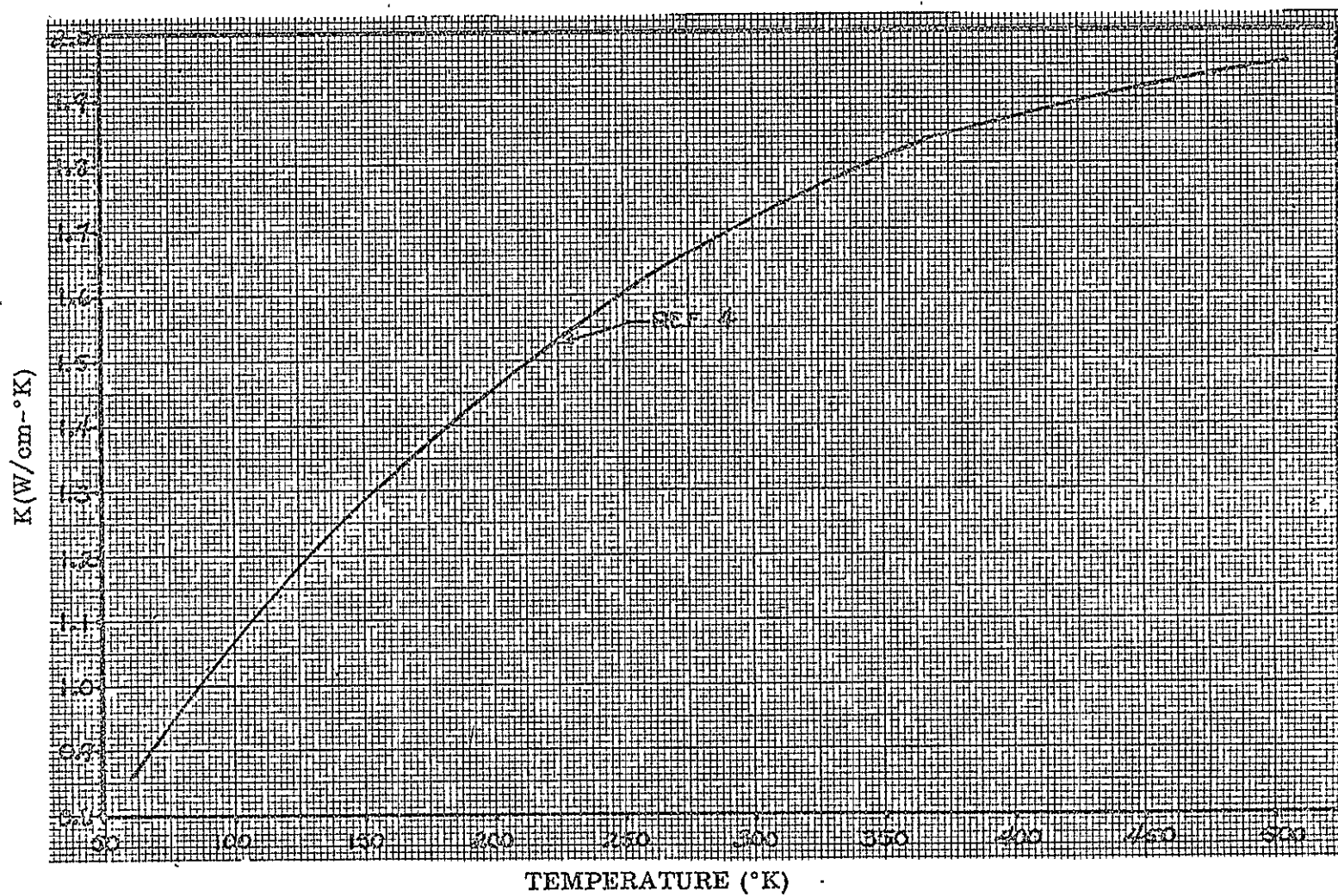


Fig. B-3 Thermal Conductivity of Aluminum 6061-T0

177

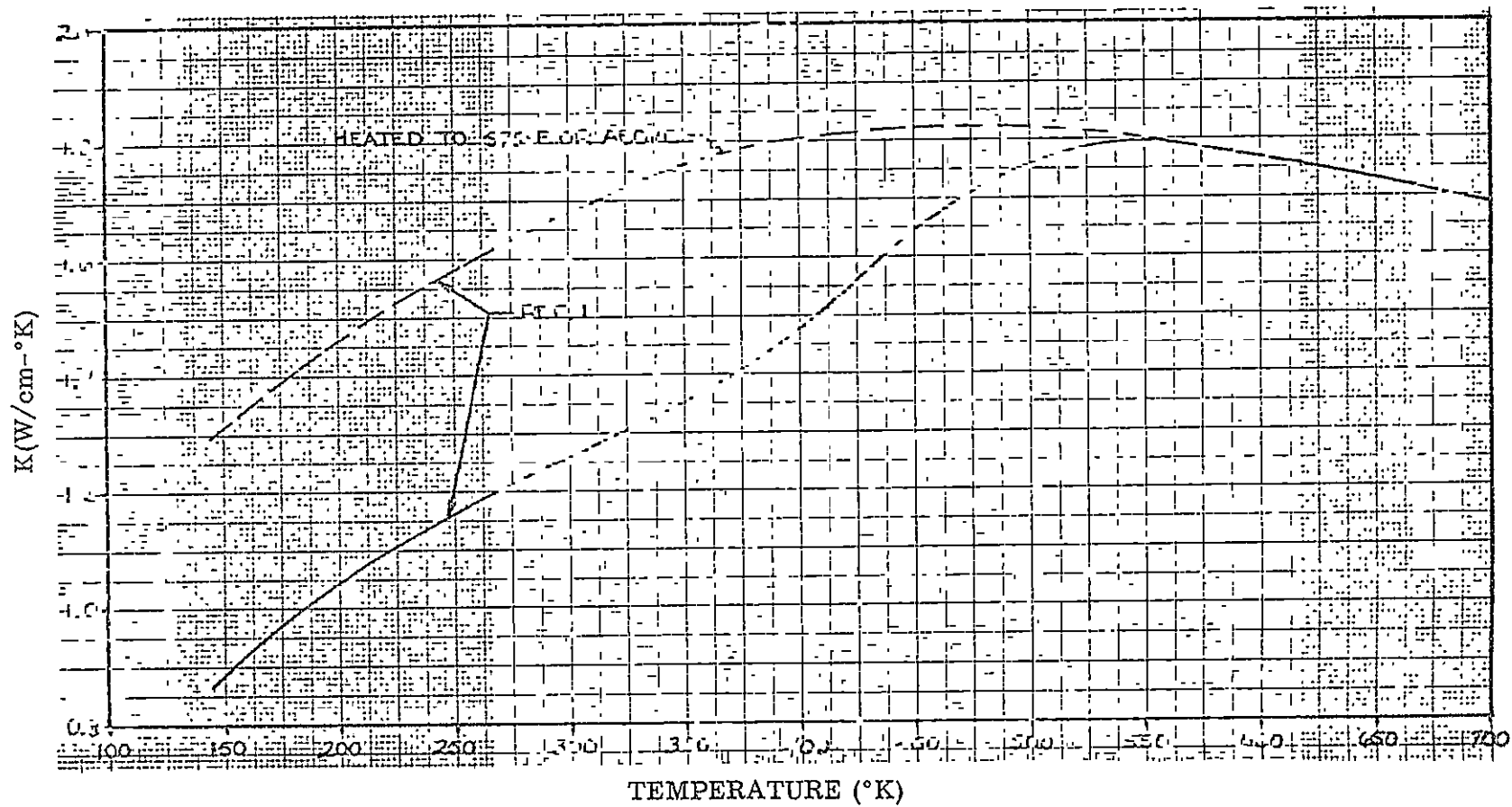


Fig. B-4 Thermal Conductivity of Aluminum 7075-T6

178

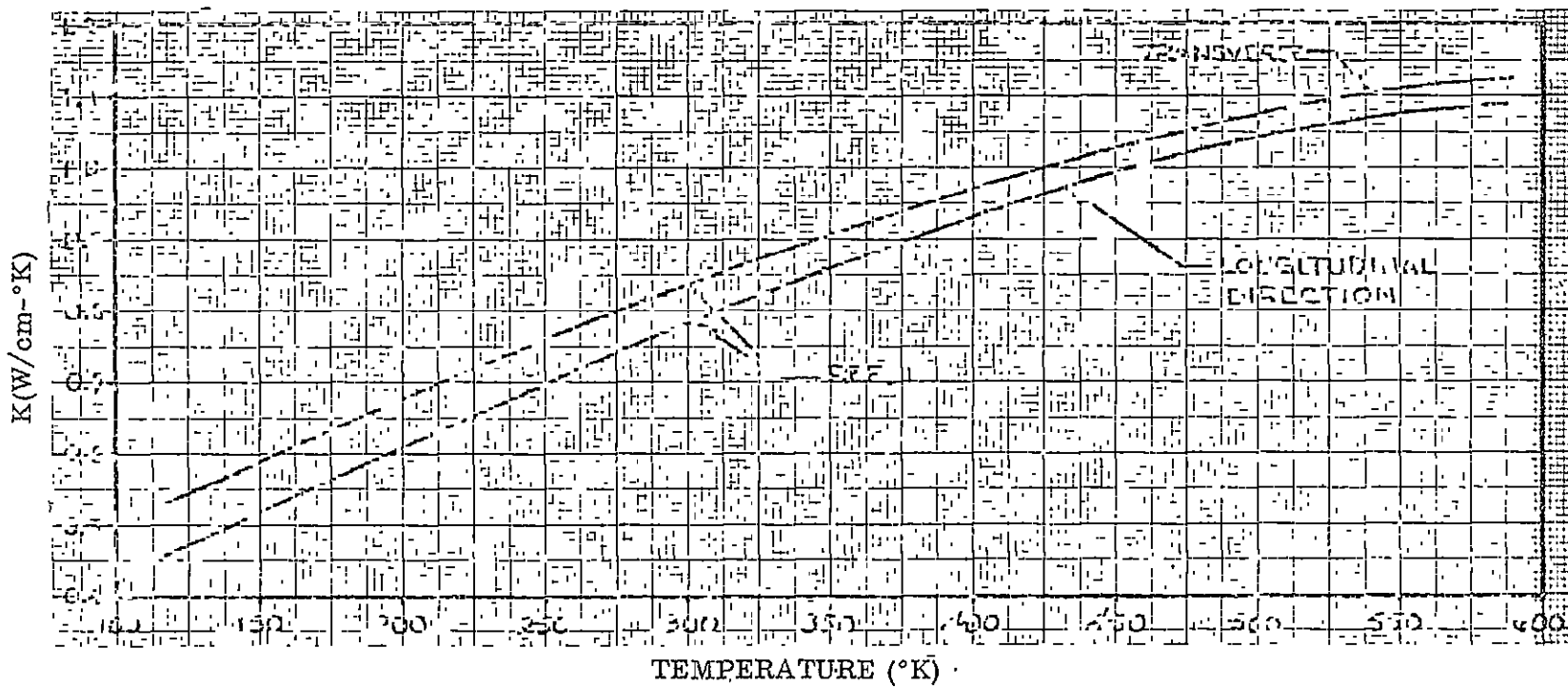


Fig. B-5 Thermal Conductivities of Magnesium AZ-31B-0 and AZ-318-H24

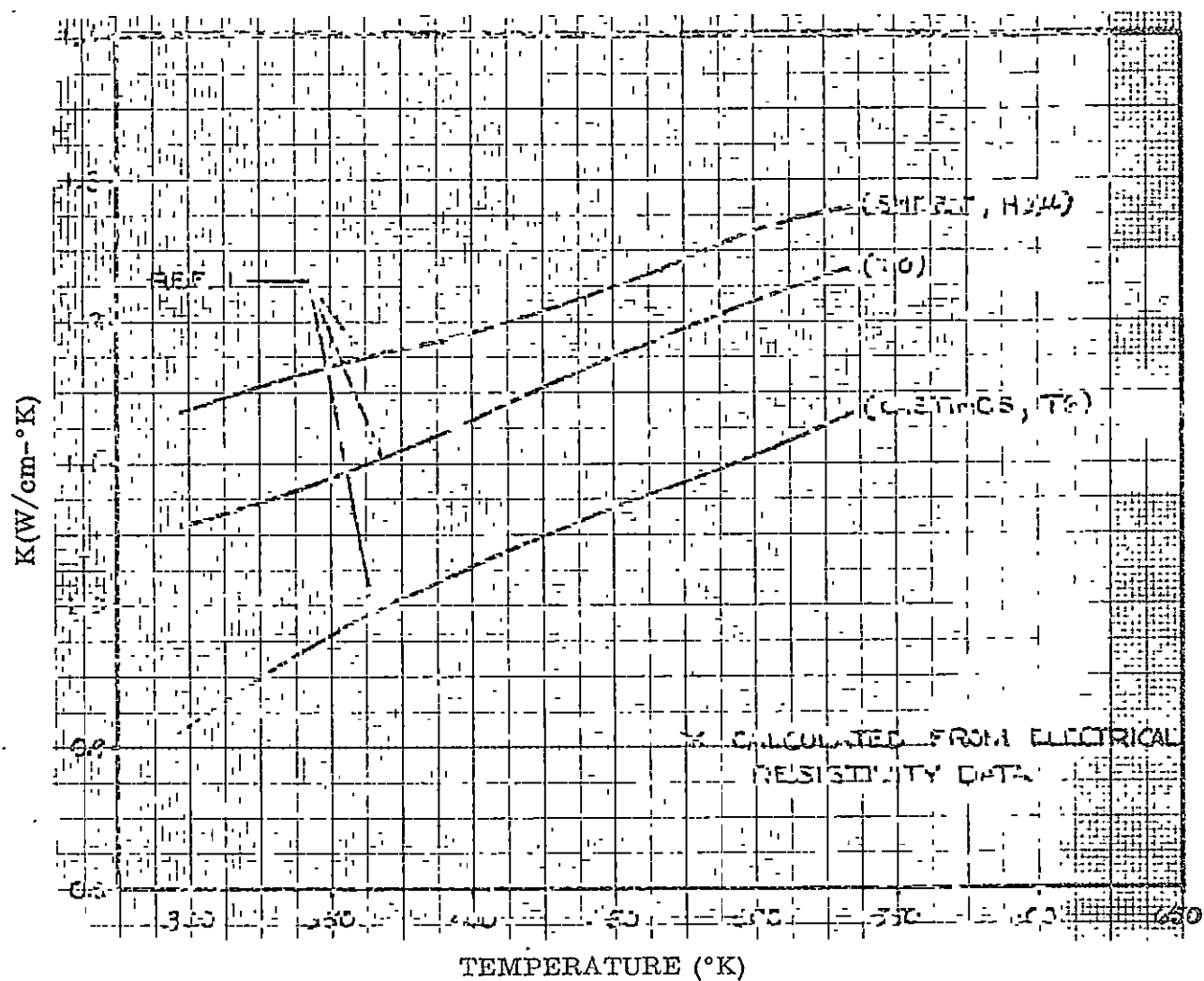


Fig. B-6 Thermal Conductivities\* of Magnesium HK-31A-TO, HK-31A-T6, and HK-31A-H24



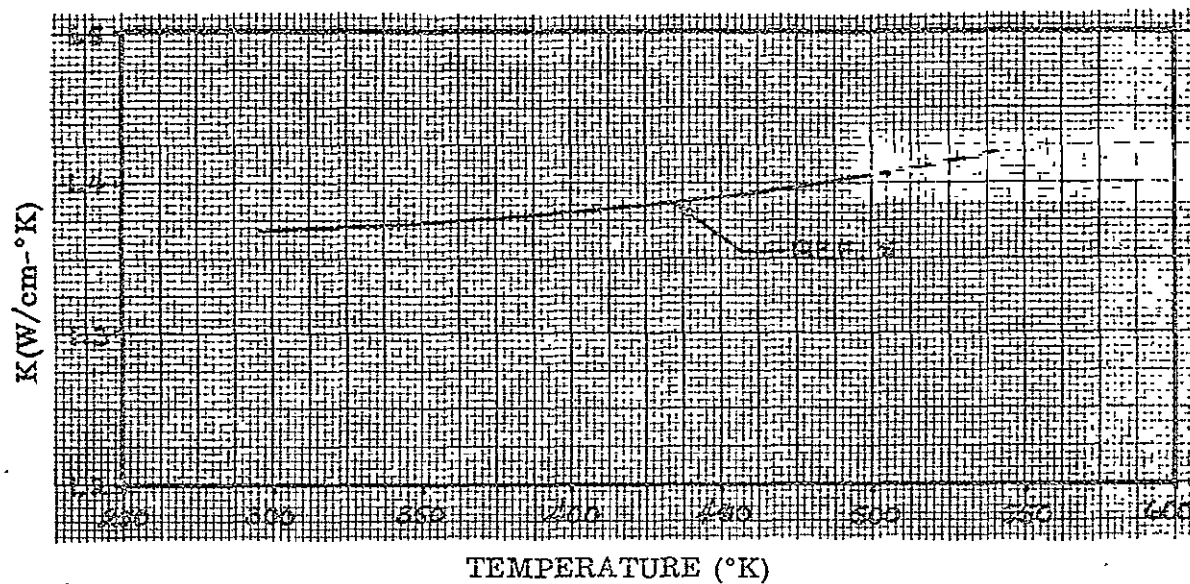


Fig. B-7 Thermal Conductivity of Magnesium HM-21A

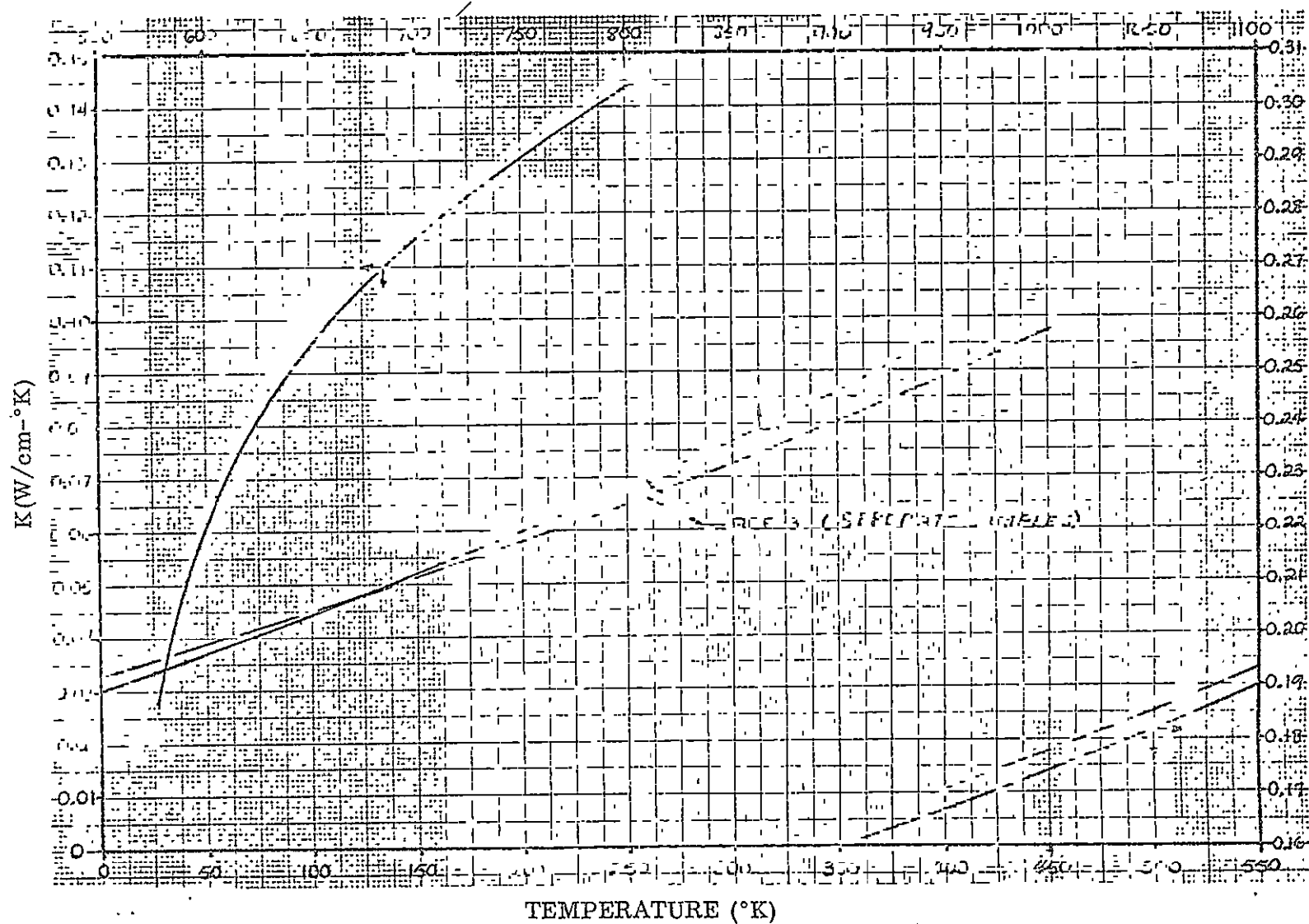


Fig. B-8 Thermal Conductivity of Stainless Steel (304)

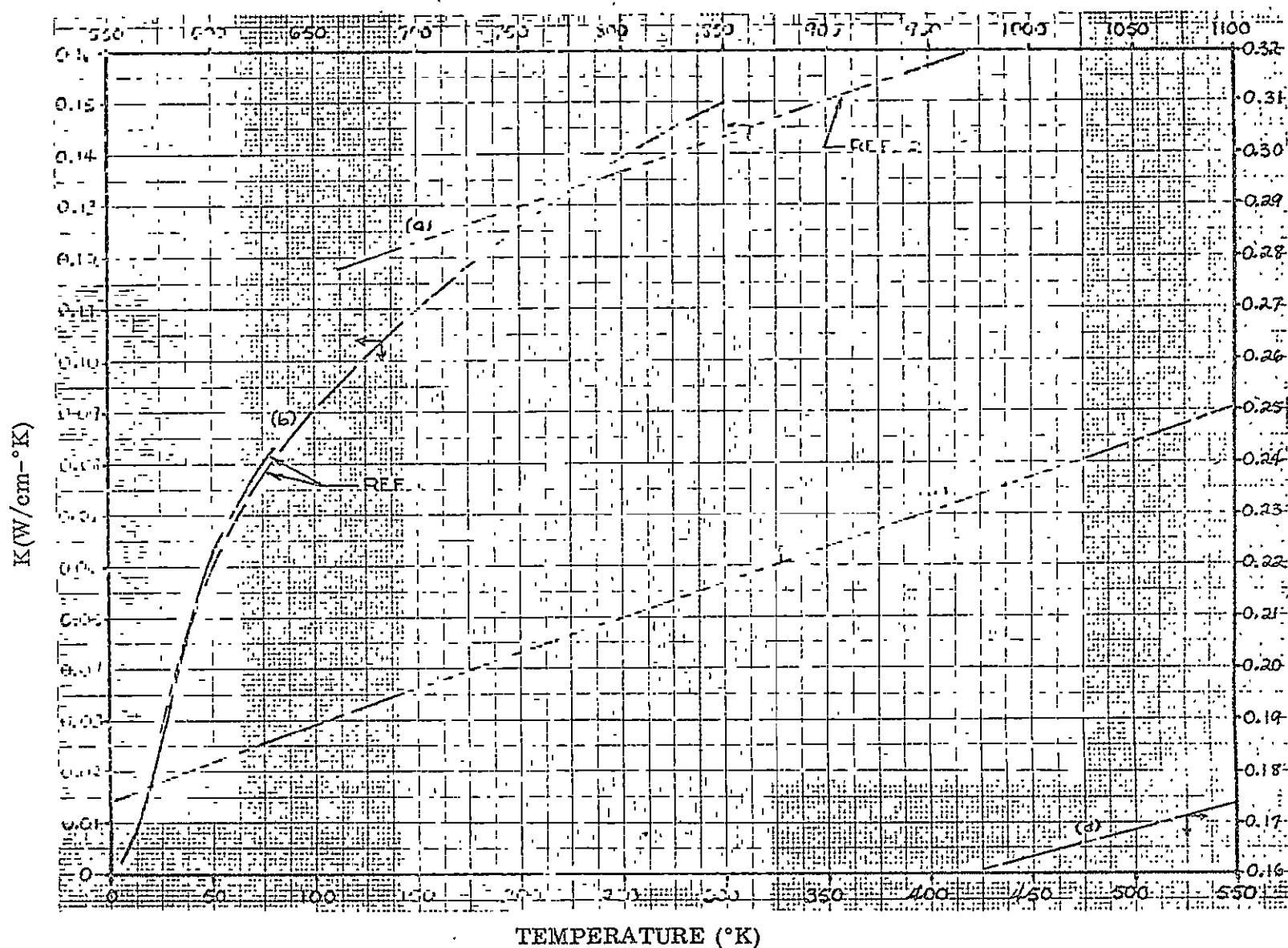


Fig. B-9 Thermal Conductivity of Stainless Steel (347)

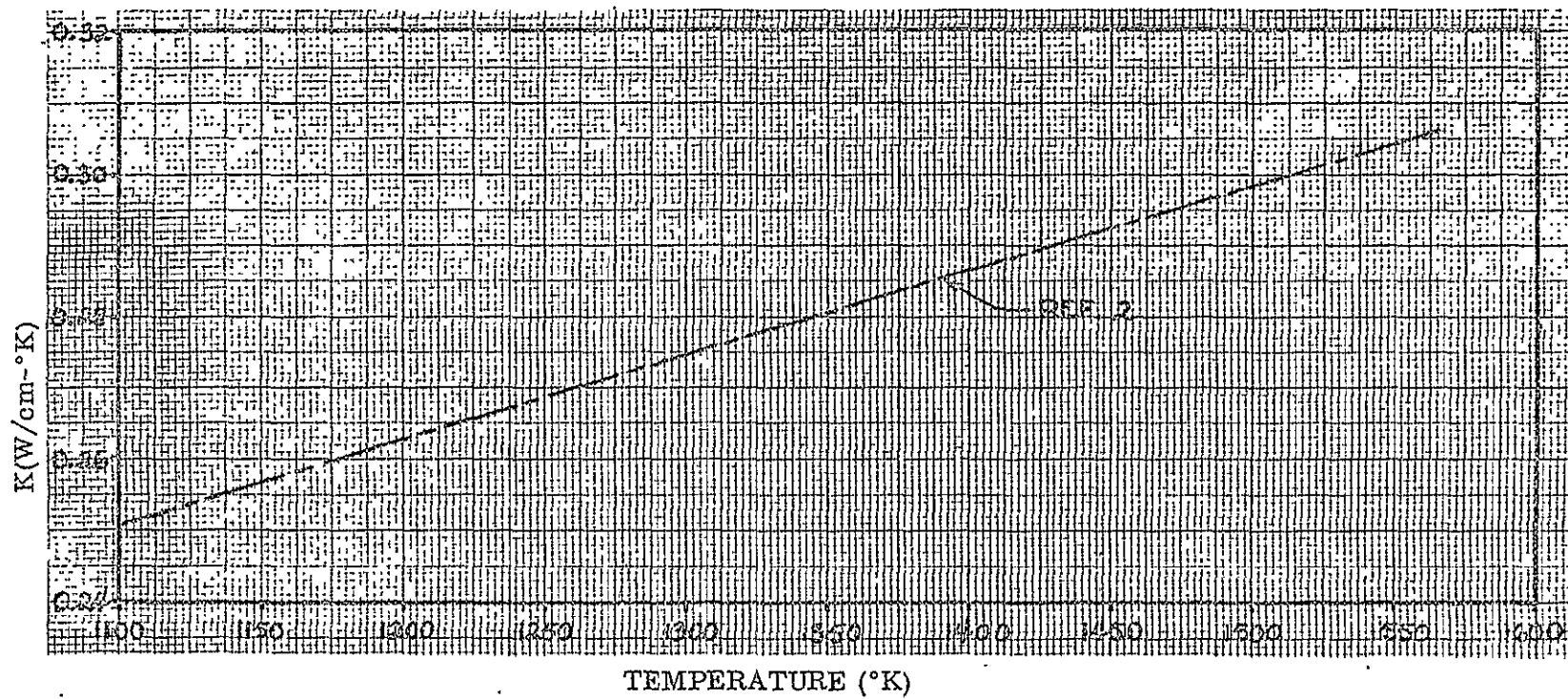


Fig. B-9 (Cont.) Thermal Conductivity of Stainless Steel (347)

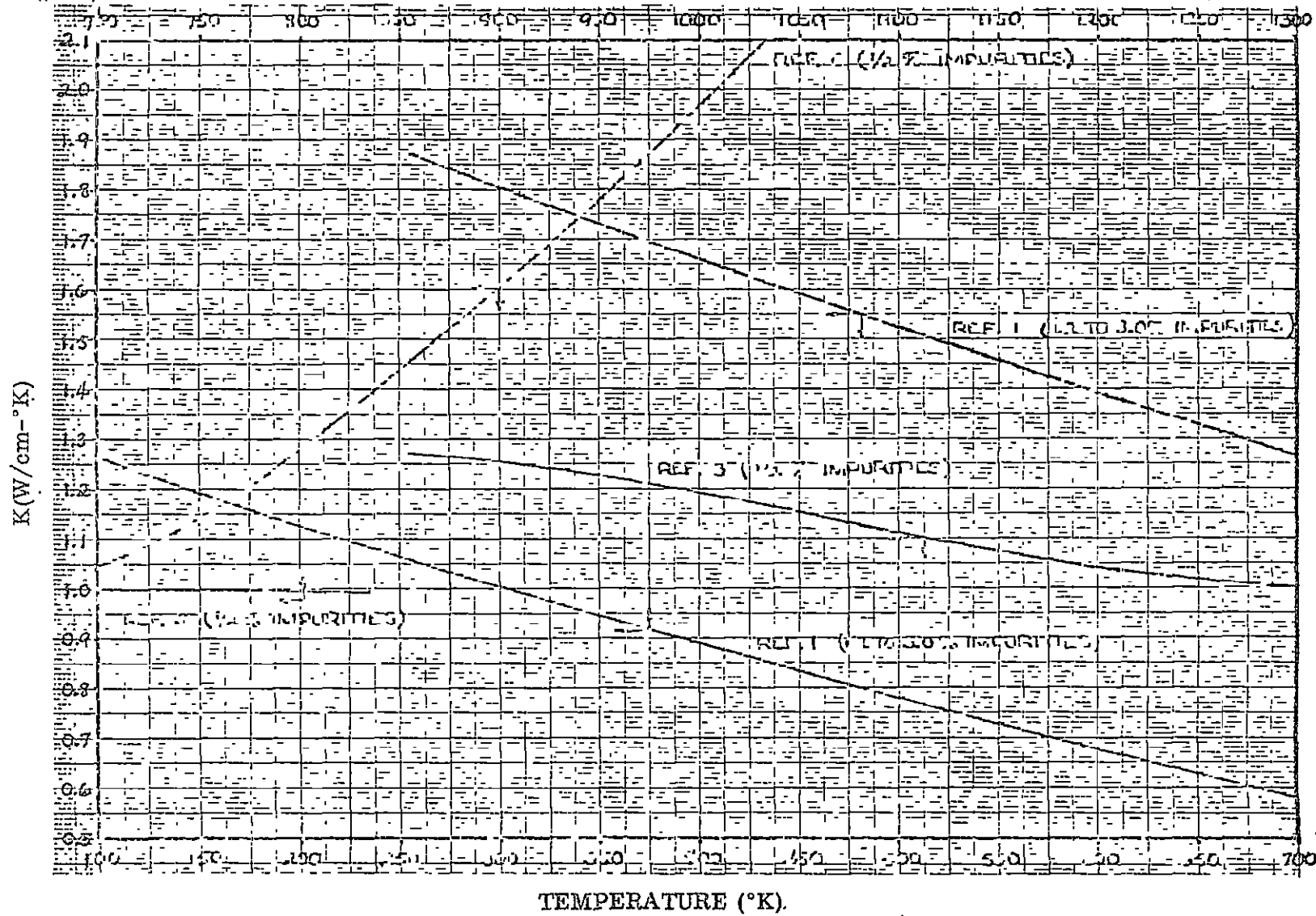


Fig. B-10 Thermal Conductivity of Beryllium (Commercially Pure)

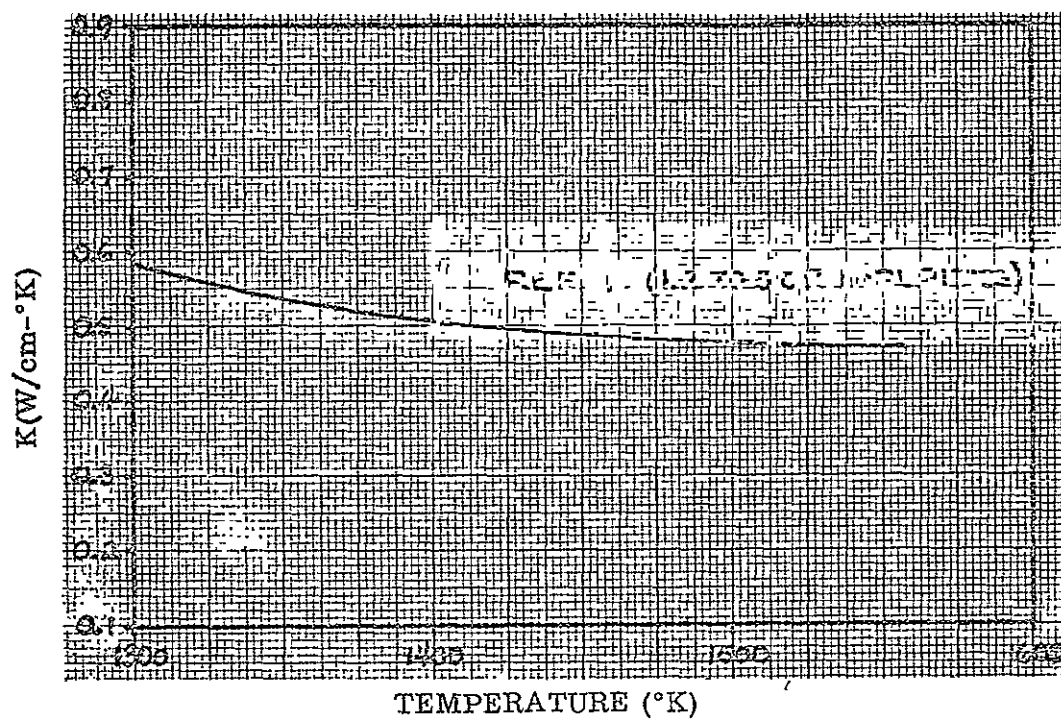


Fig. B-10 (Cont.) Thermal Conductivity of Beryllium  
(Commercially Pure)

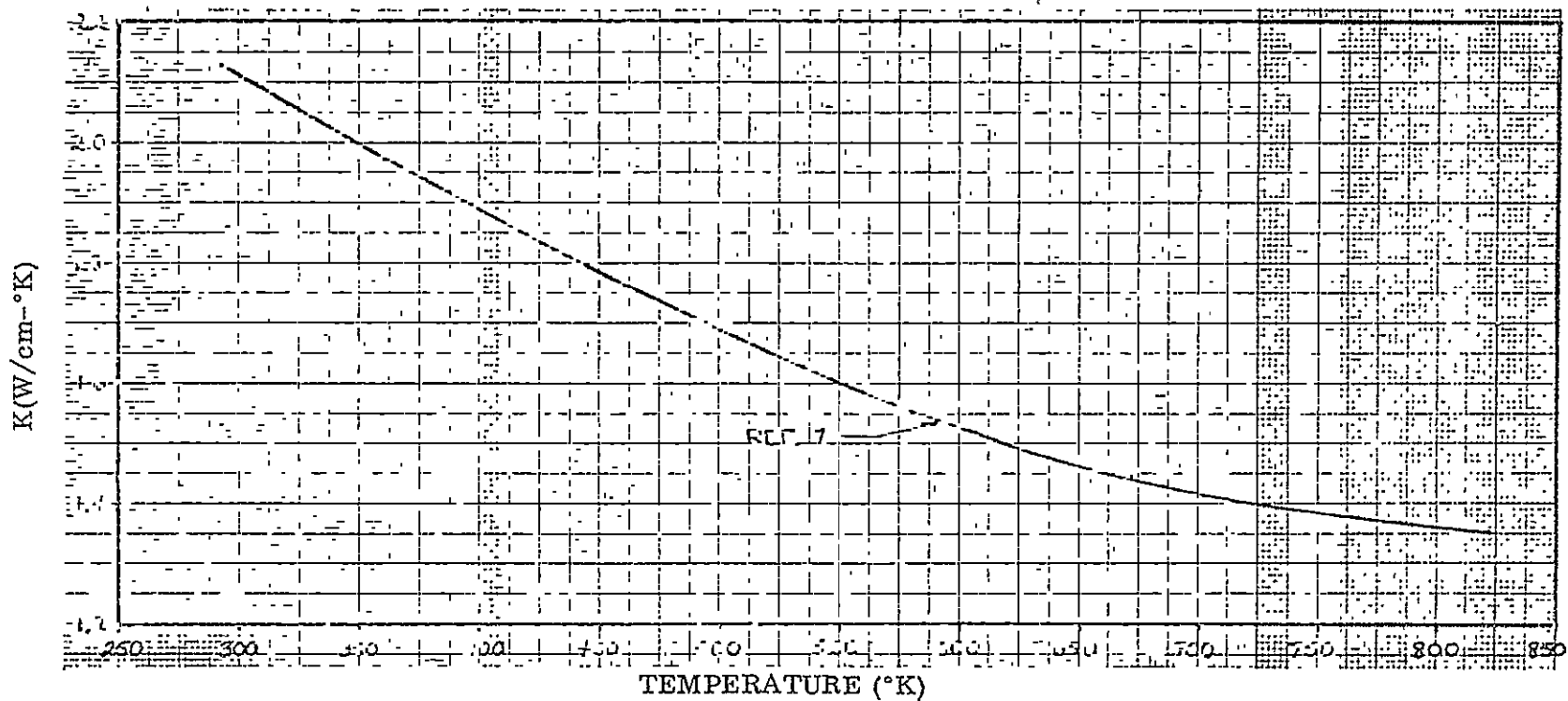


Fig. B-11 Thermal Conductivity of Beryllium - Lockalloy (62% Be, 38% Al)

187

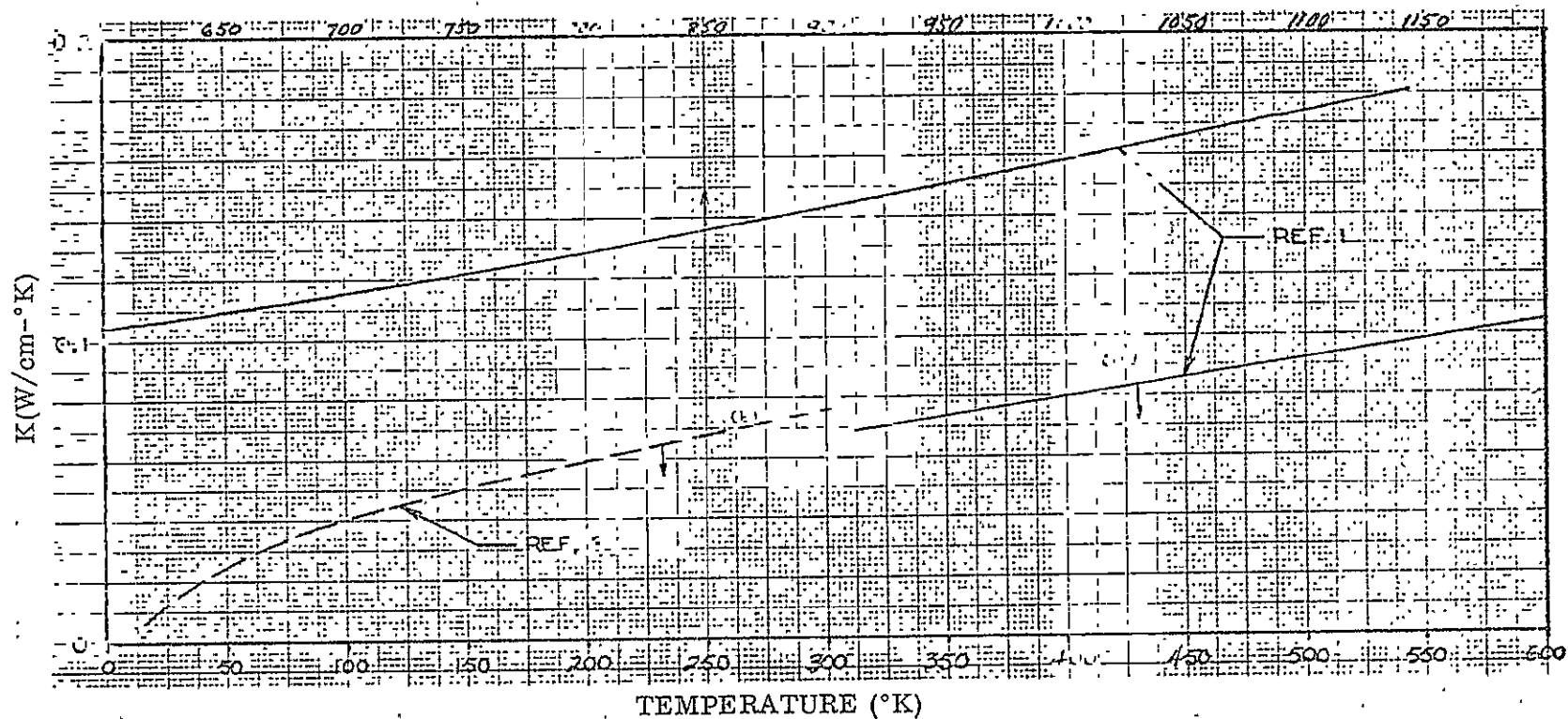


Fig. B-12 Thermal Conductivity of Titanium (6 Al-4V)



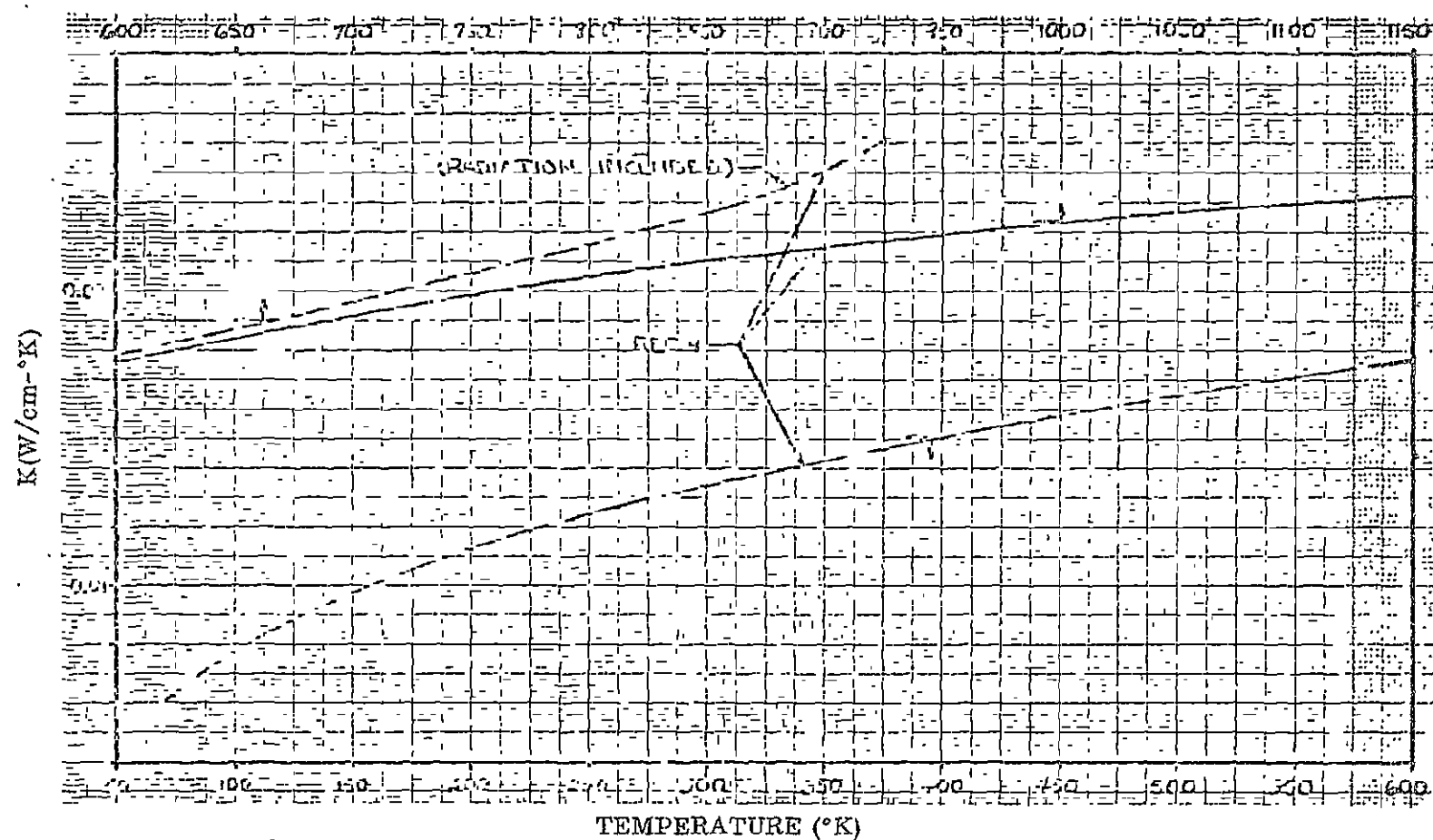


Fig. B-13 Thermal Conductivity of Fused Silica (Corning 7940)

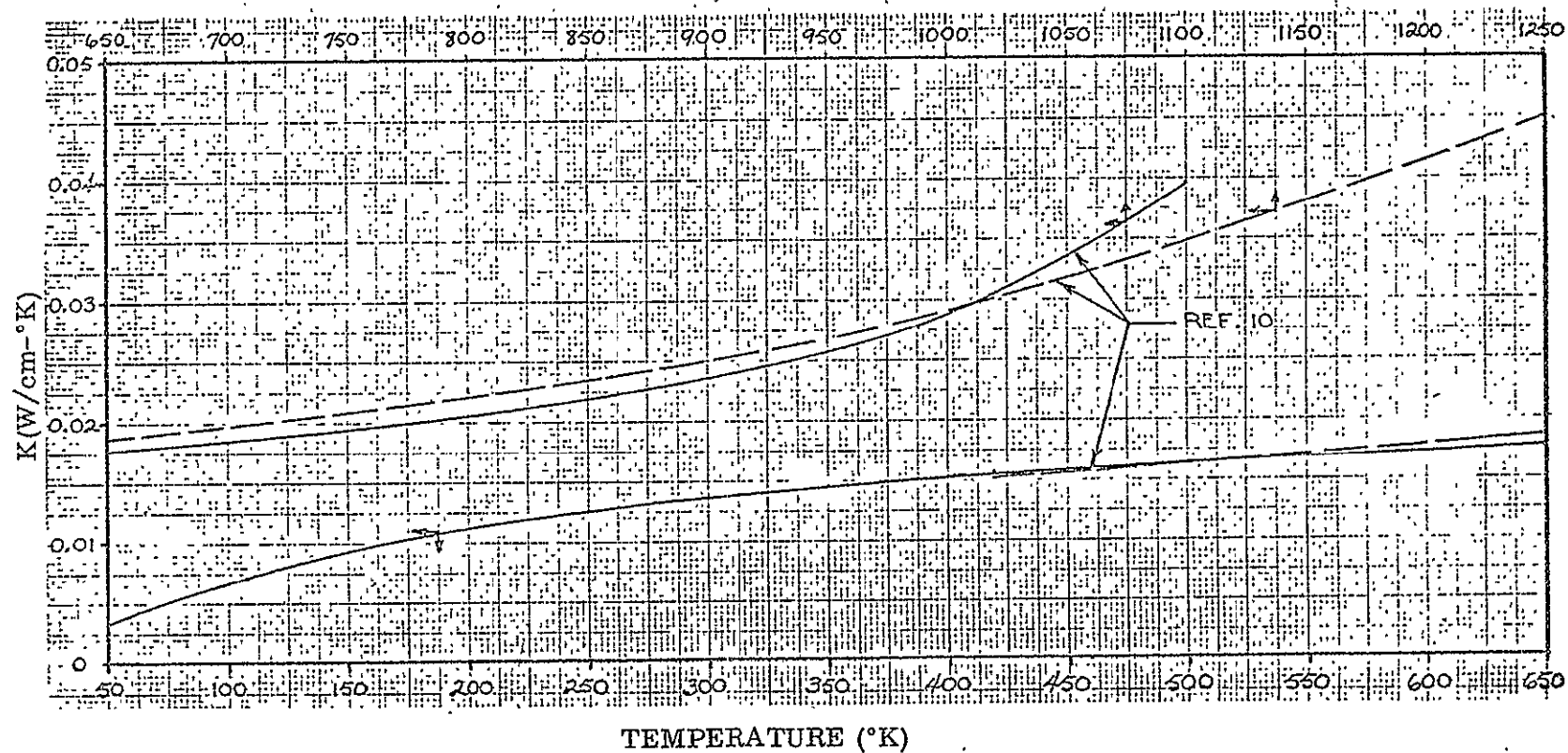


Fig. B-14 Thermal Conductivity of Fused Quartz

190

$K(W/cm^{\circ}K)$

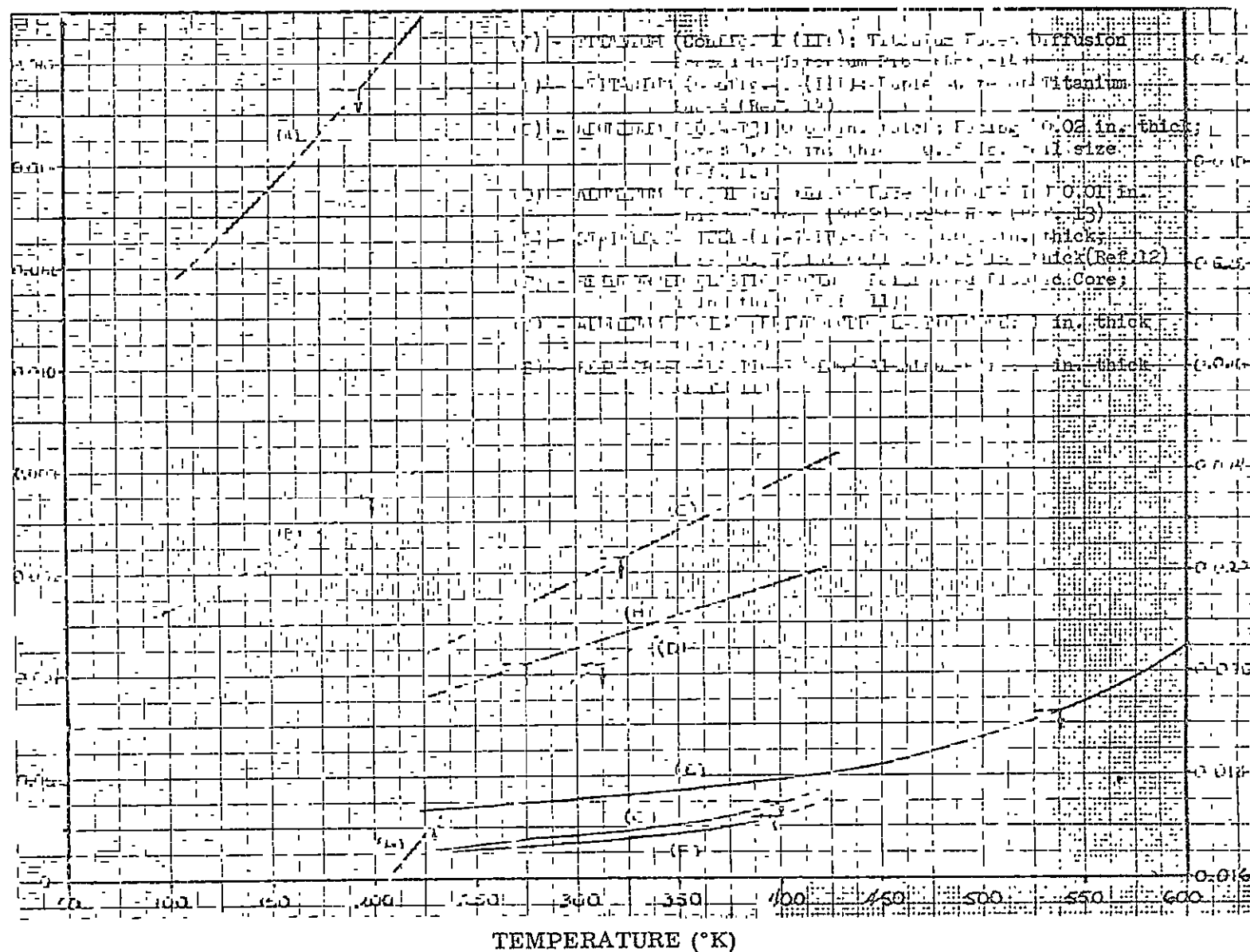


Fig. B-15 Thermal Conductivities of Various Configurations of Honeycomb

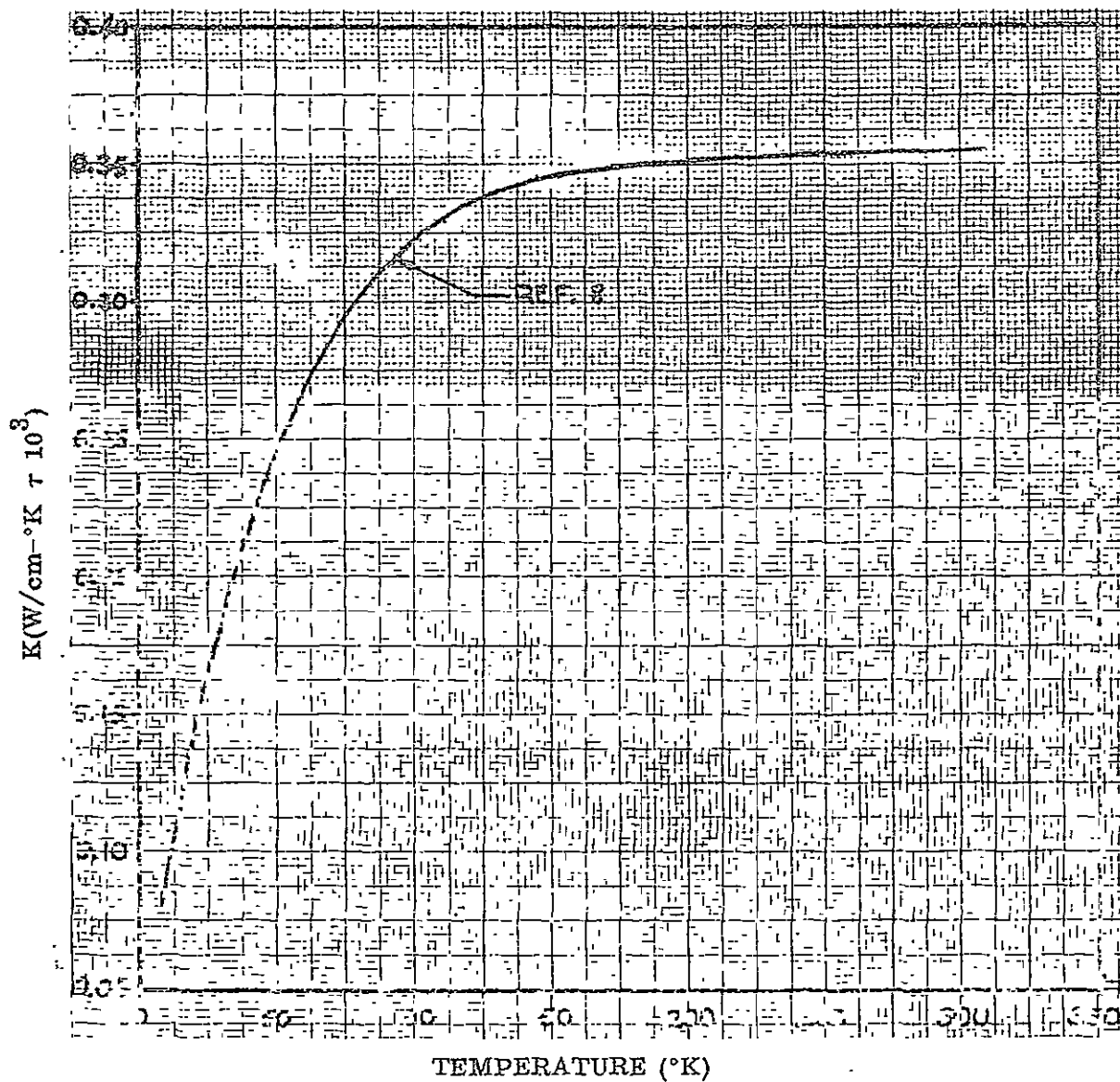


Fig. B-16 Thermal Conductivity of Nylon

192

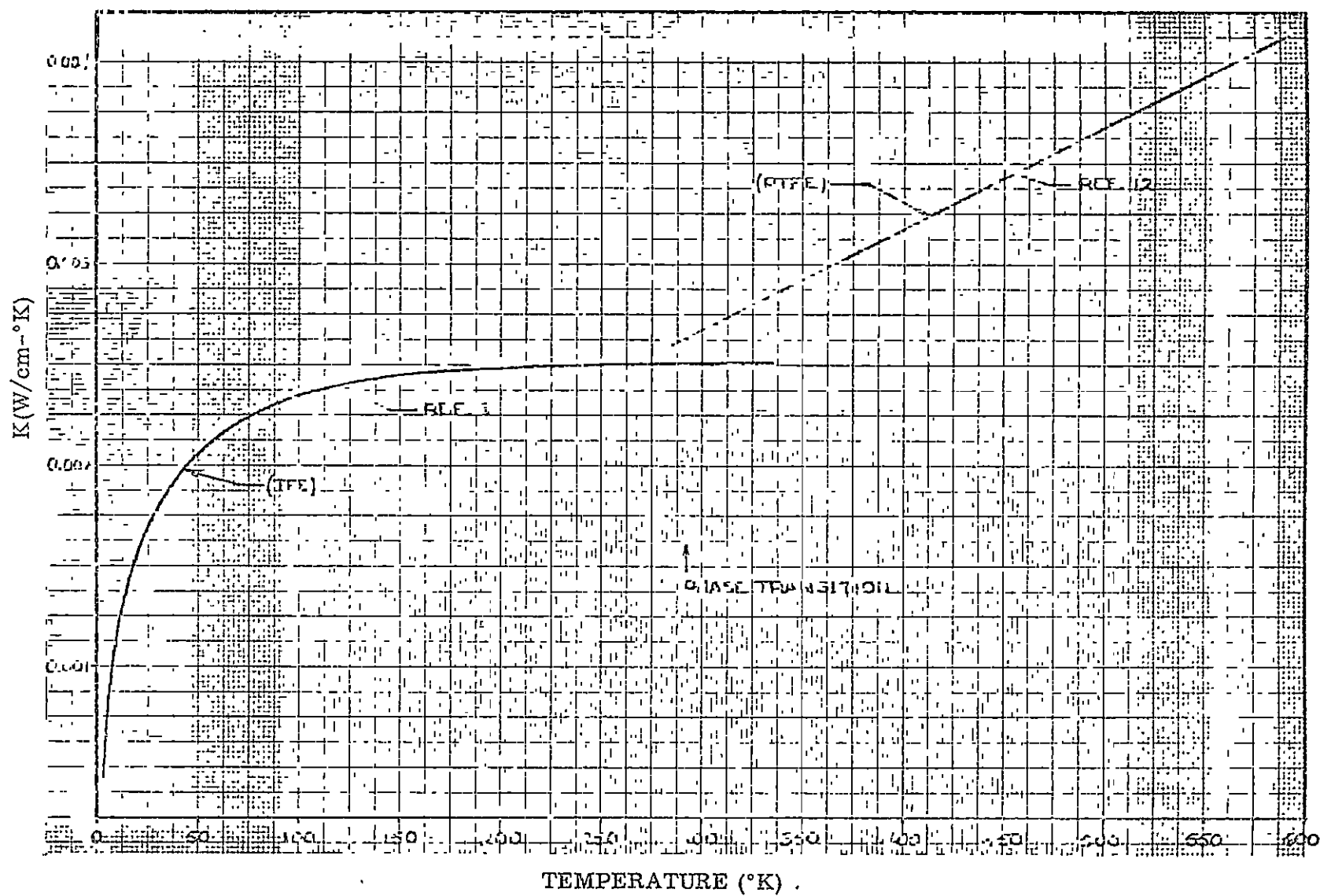


Fig. B-17 Thermal Conductivity of Teflon (PTFE and TFE)

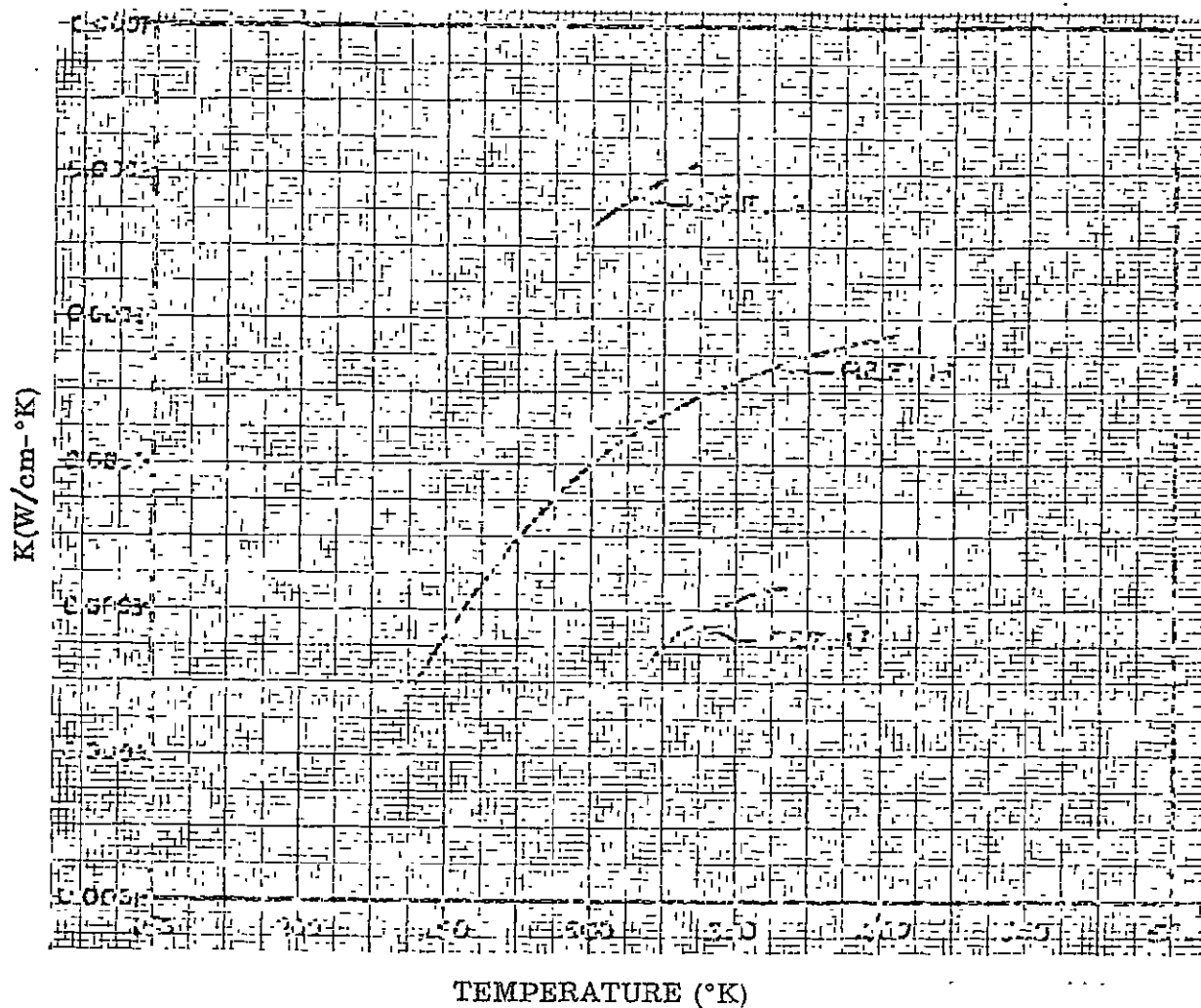


Fig. B-18 Thermal Conductivity of Polyurethane Foam

194

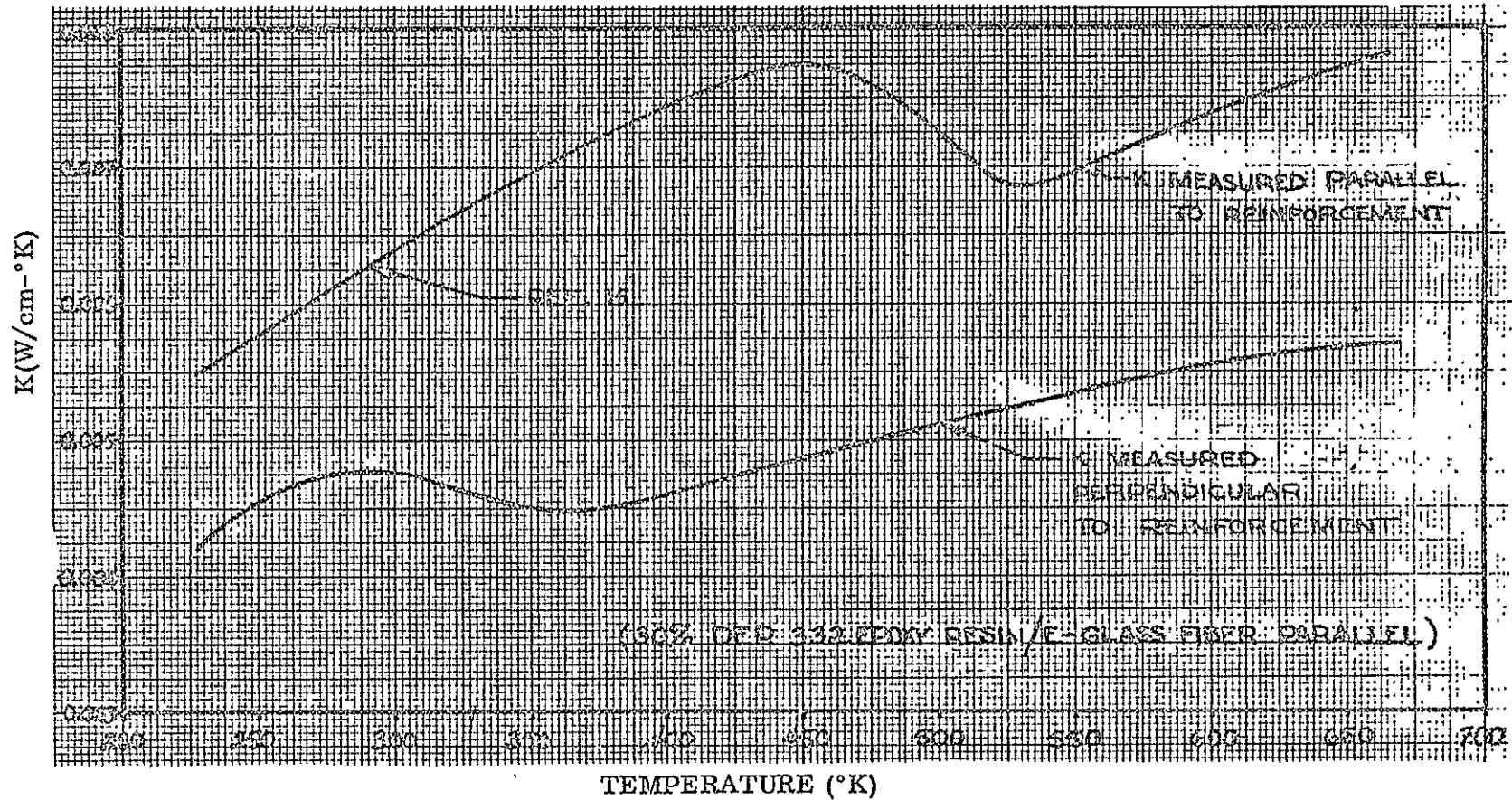


Fig. B-19 Thermal Conductivity of Fiberglass (Glass Fiber Reinforced Epoxy)

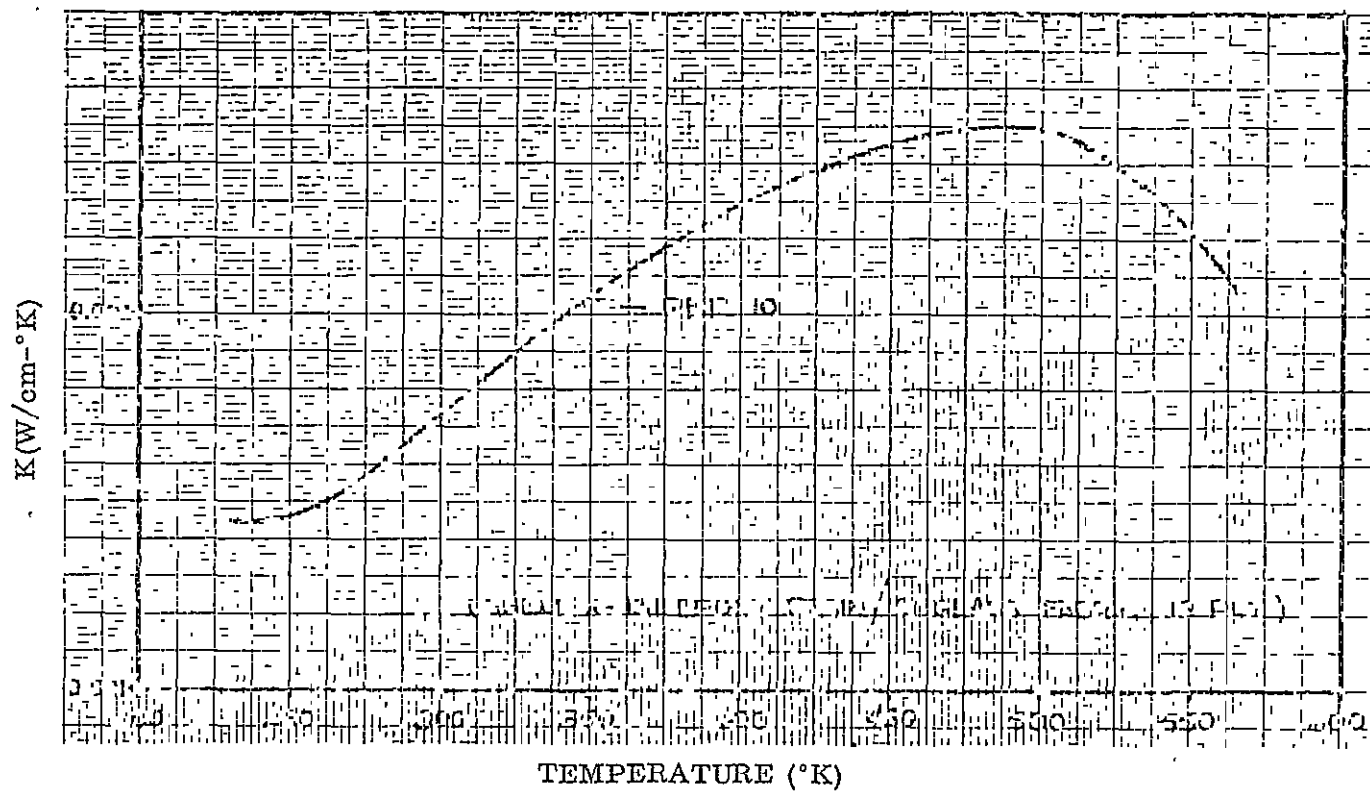


Fig. B-20 Thermal Conductivity of Fiberglass (Glass Fabric Reinforced Epoxy)



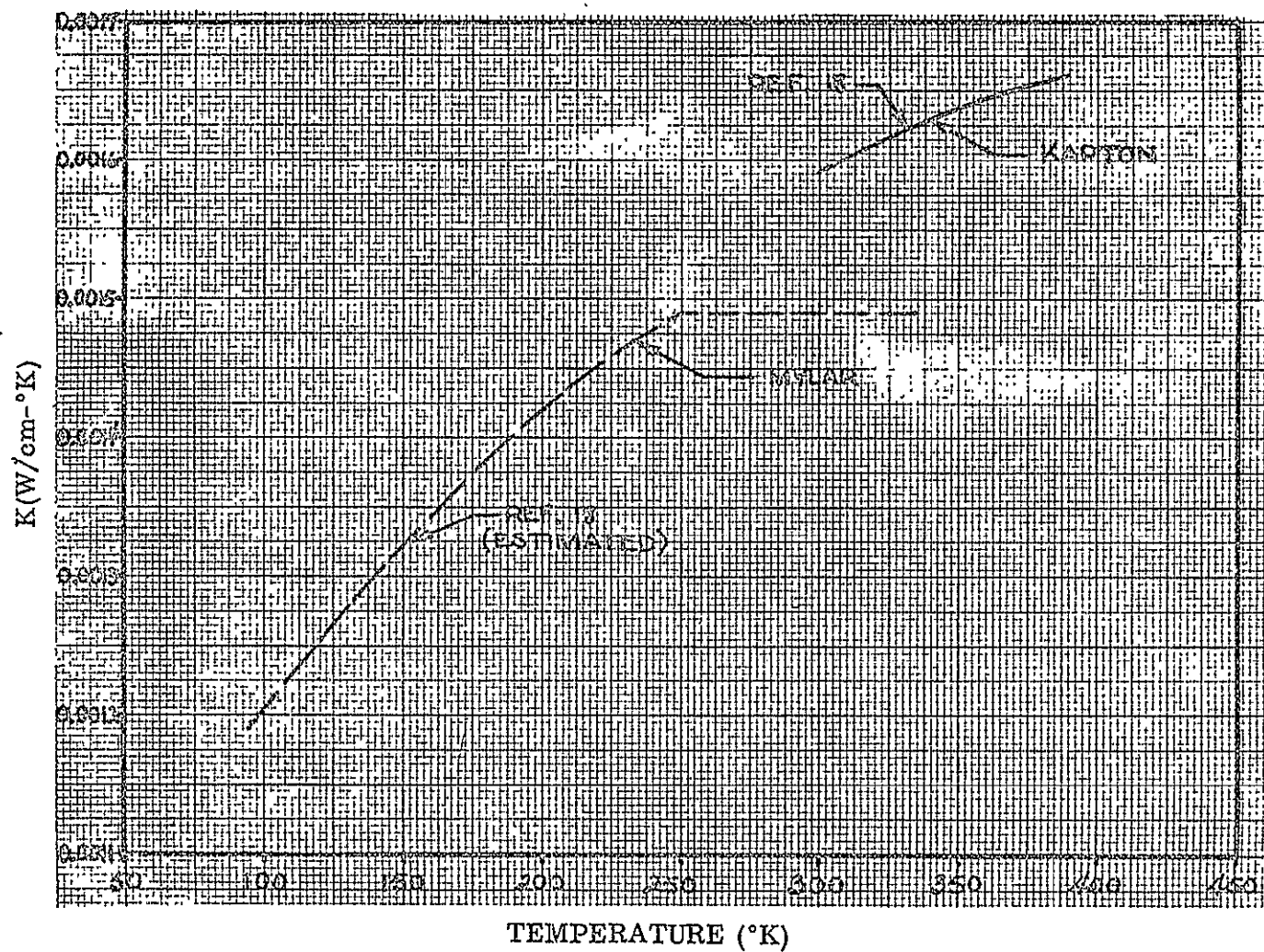


Fig. B-21 Thermal Conductivities of Mylar and Kapton

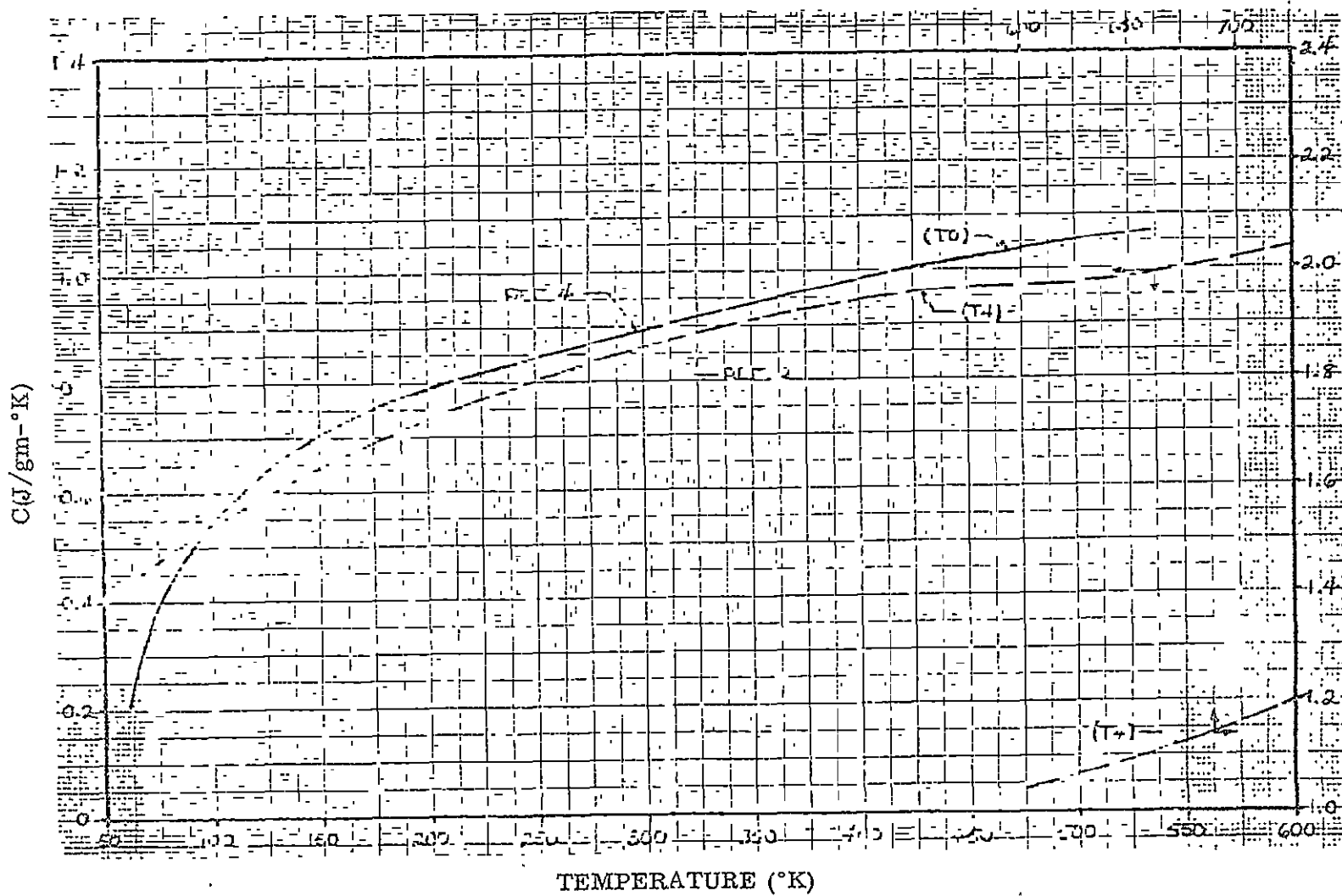


Fig. B-22 Specific Heats of Aluminum 2024-TO and 2024-T4

198

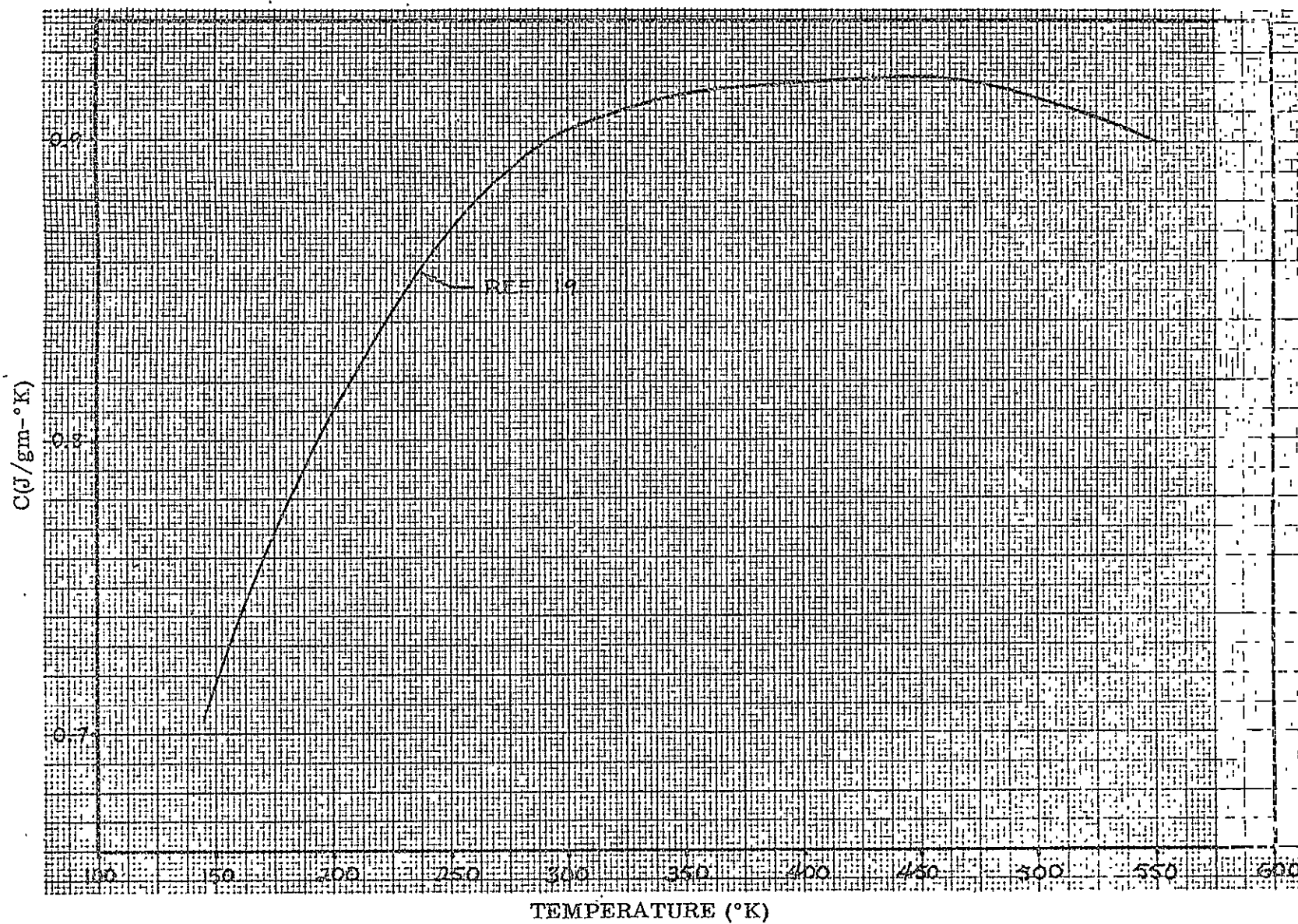


Fig. B-23 Specific Heat of Aluminum 6061-T6

199

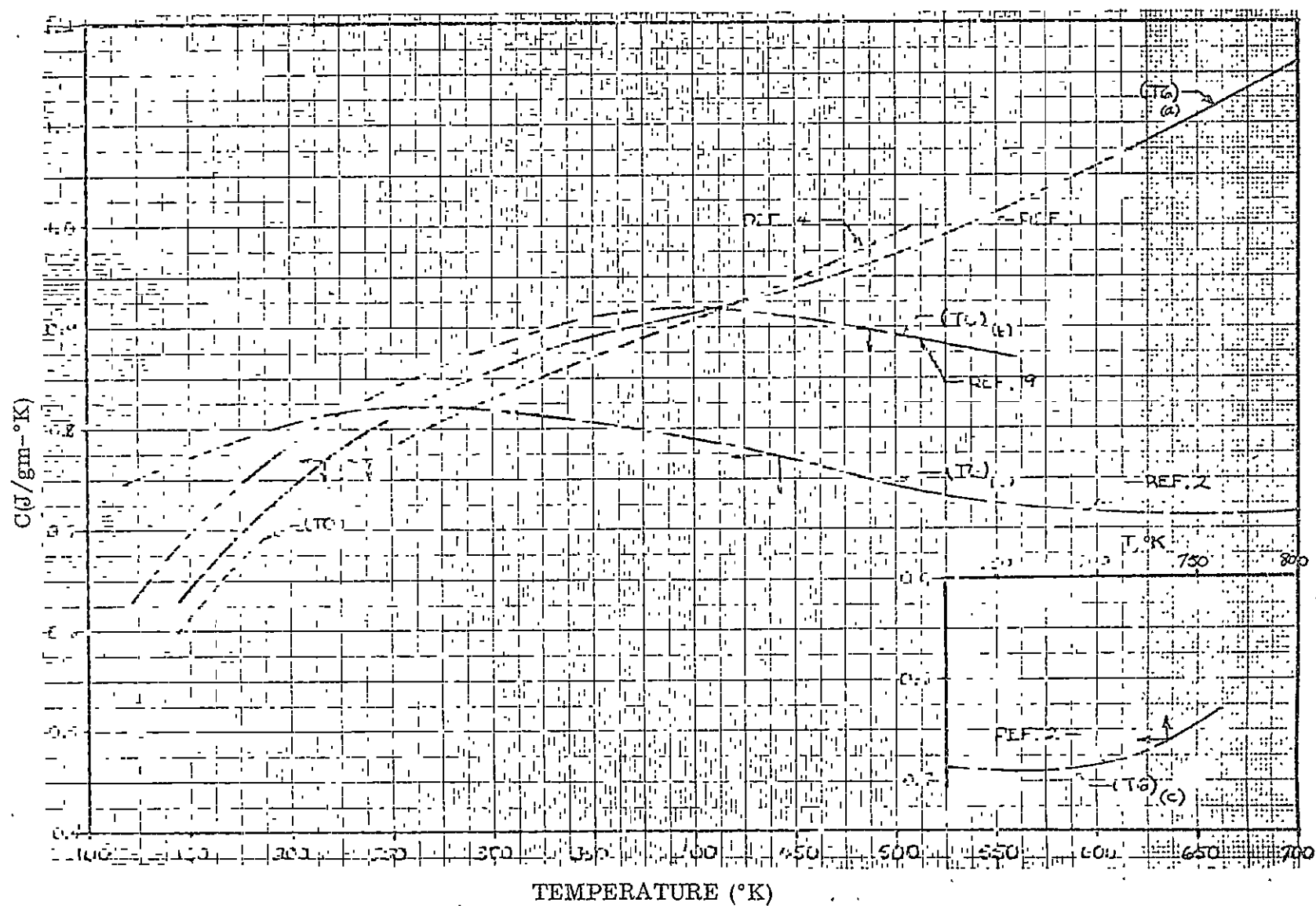
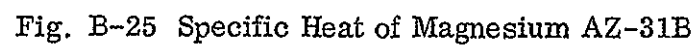


Fig. B-24 Specific Heats of Aluminum 7075-TO and 7075-T6



201

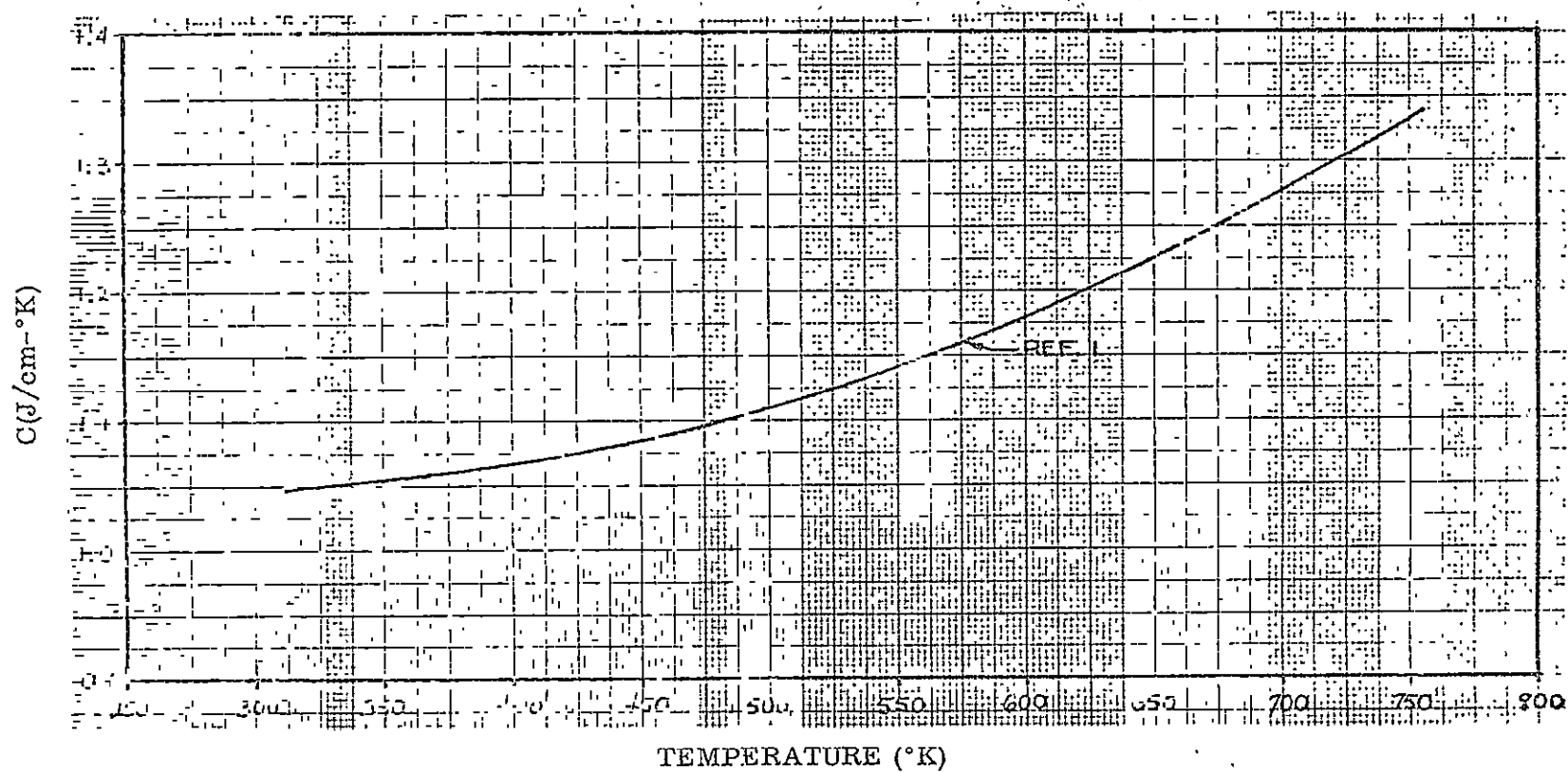


Fig. B-26 Specific Heat of Magnesium HK-31A

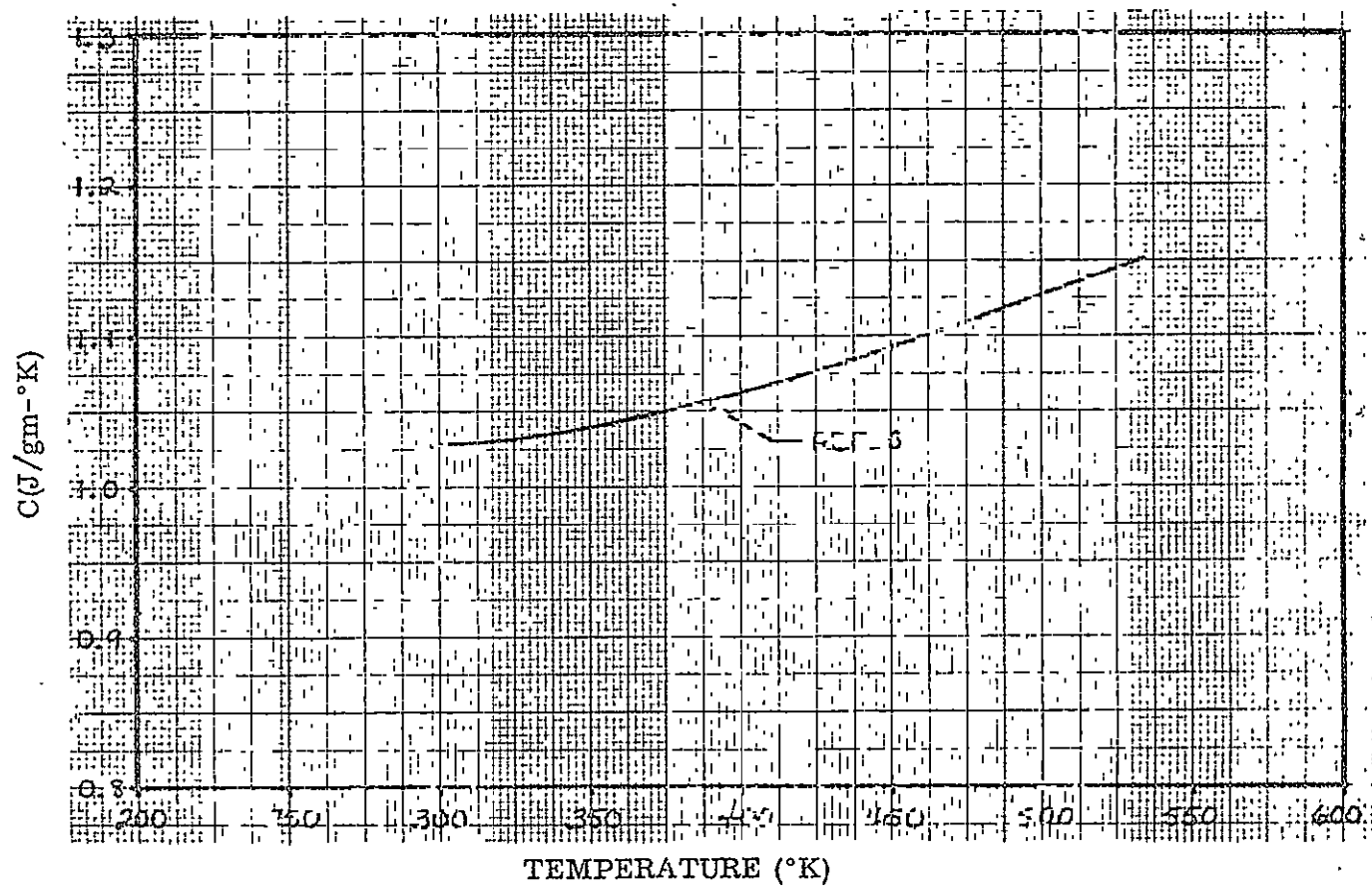


Fig. B-27 Specific Heat of Magnesium HM-21A

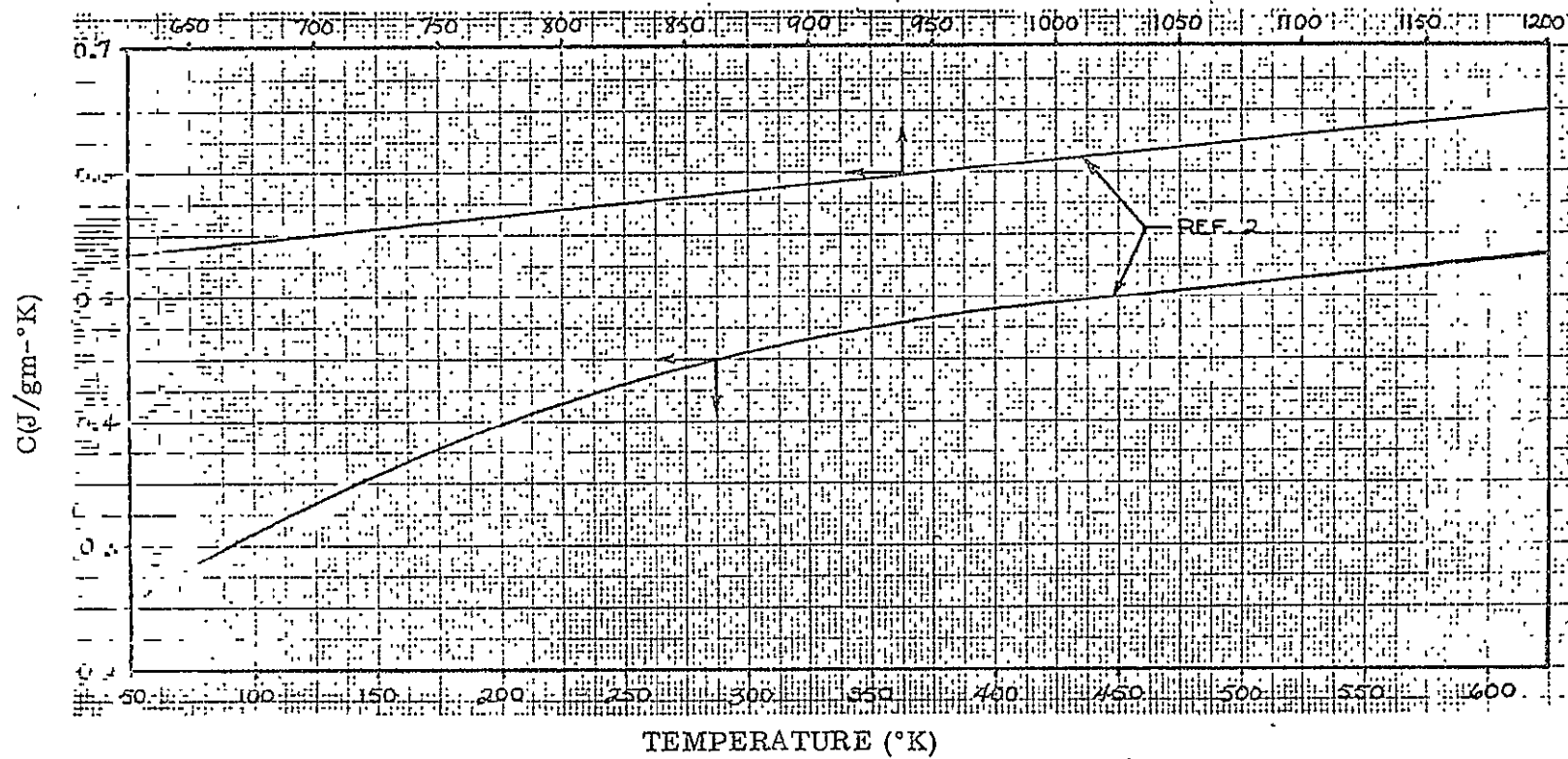


Fig. B-28 Specific Heat of Stainless Steel (347)



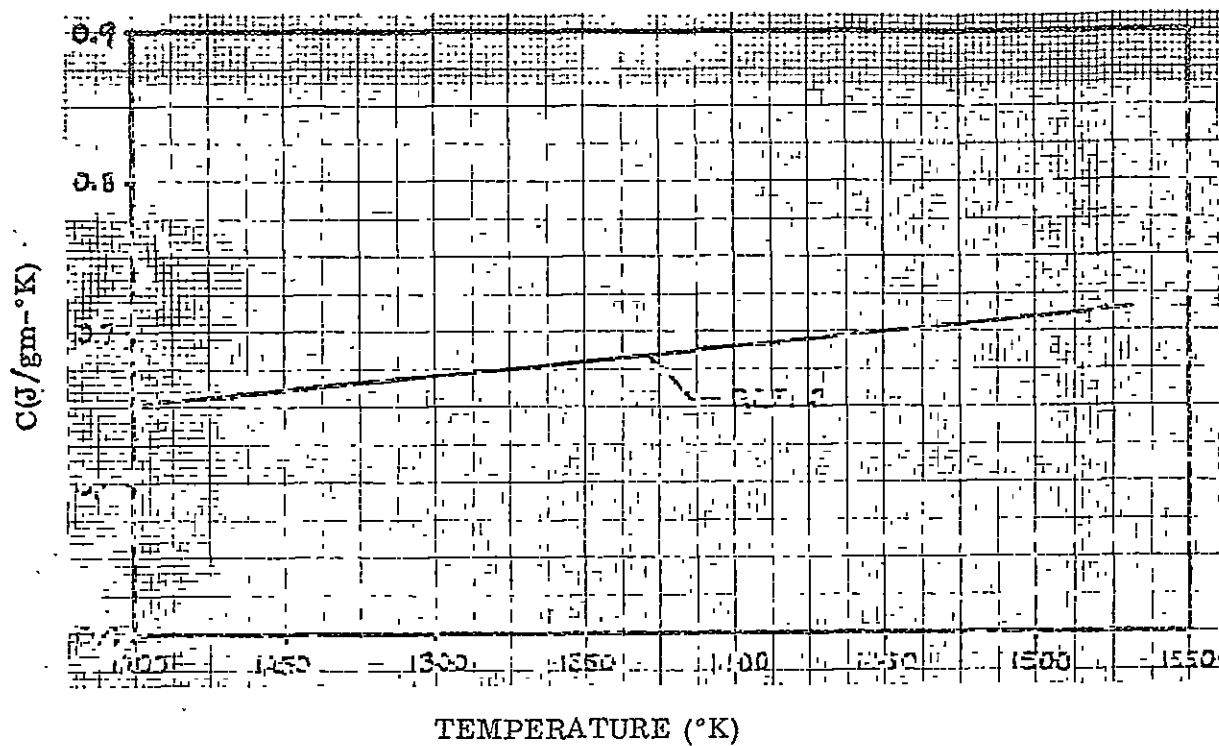


Fig. B-28 (Cont.) Specific Heat of Stainless Steel (347)

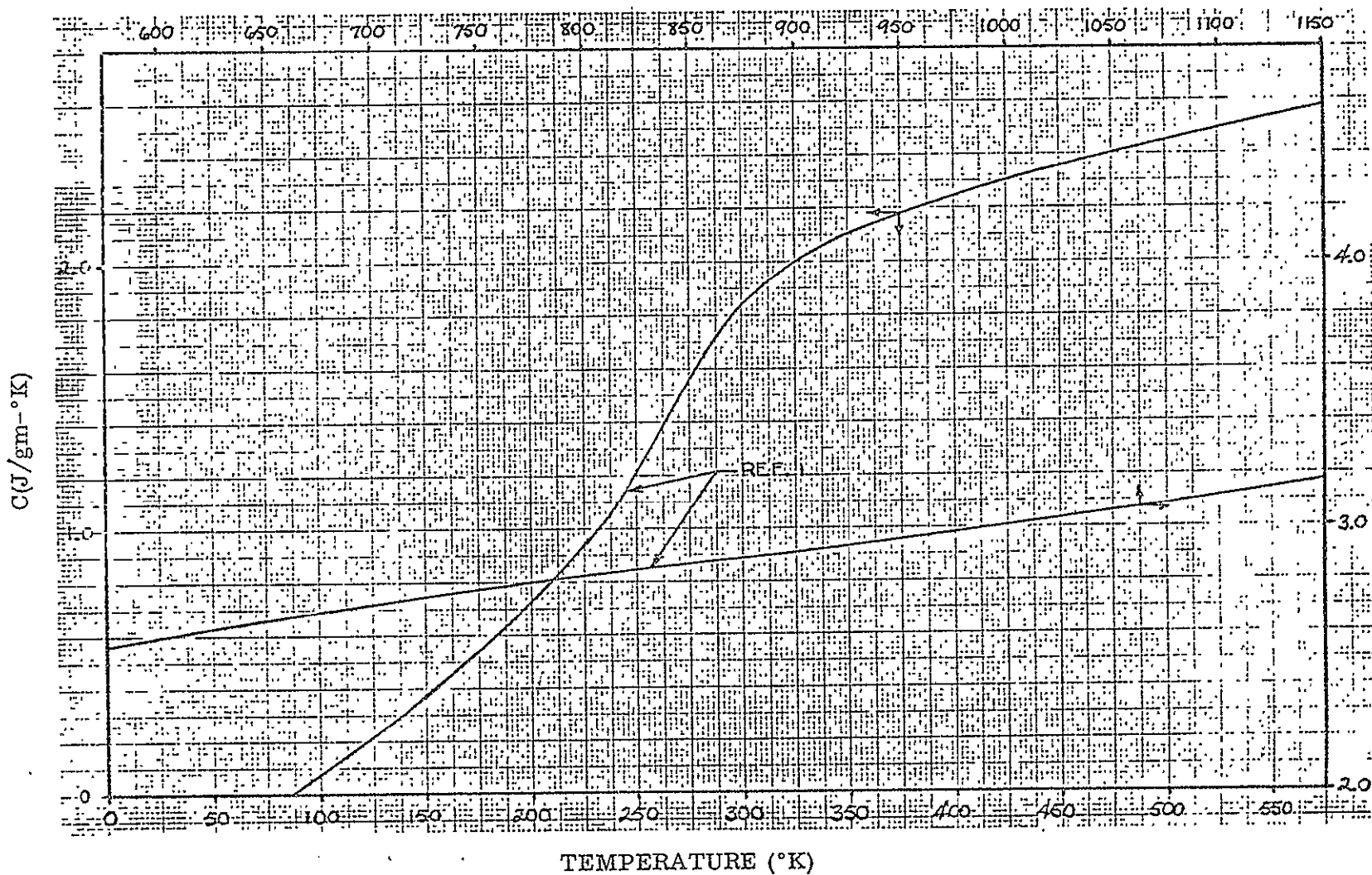


Fig. B-29 Specific Heat of Beryllium

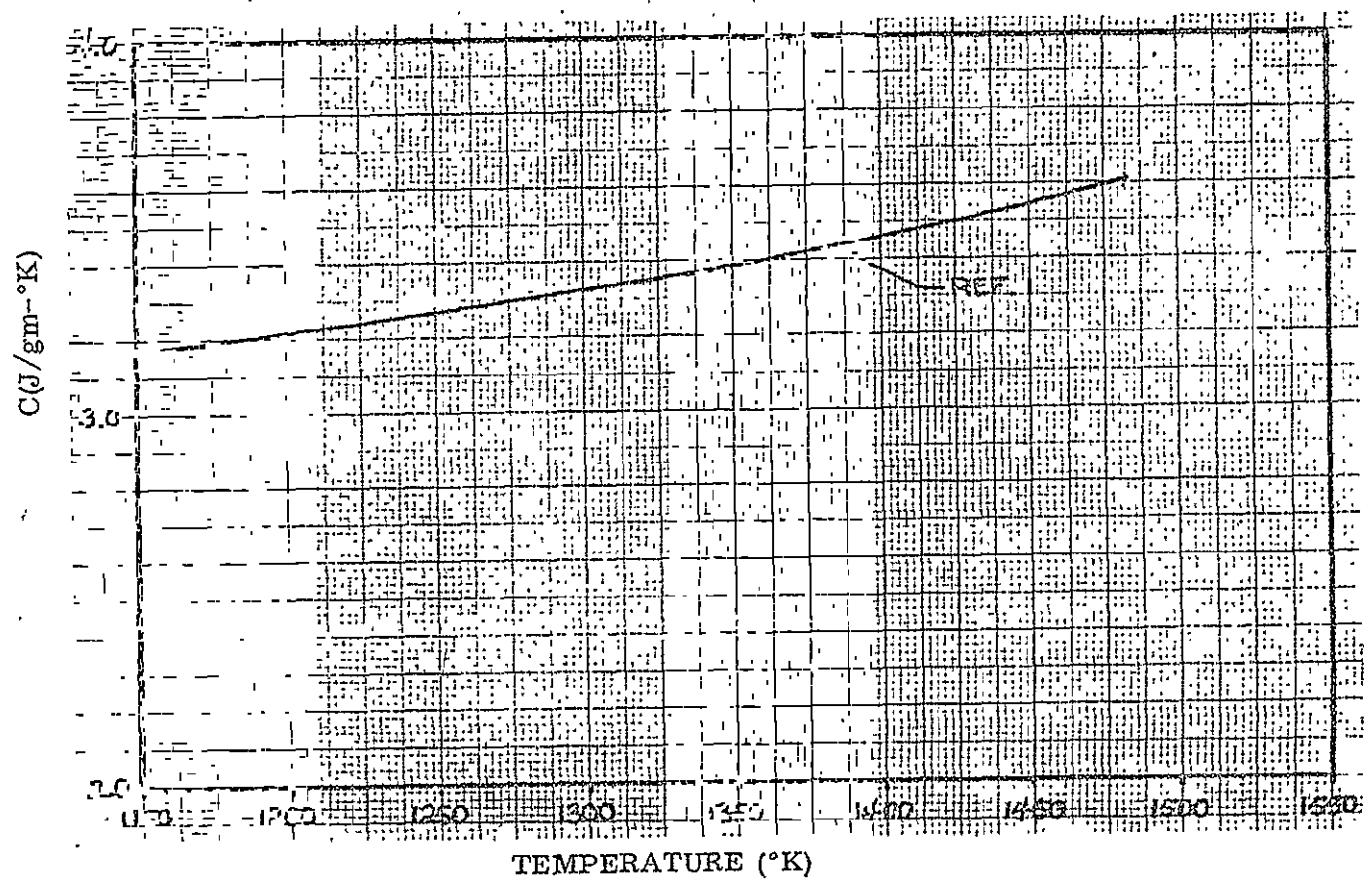


Fig. B-29 (Cont.) Specific Heat of Beryllium

207

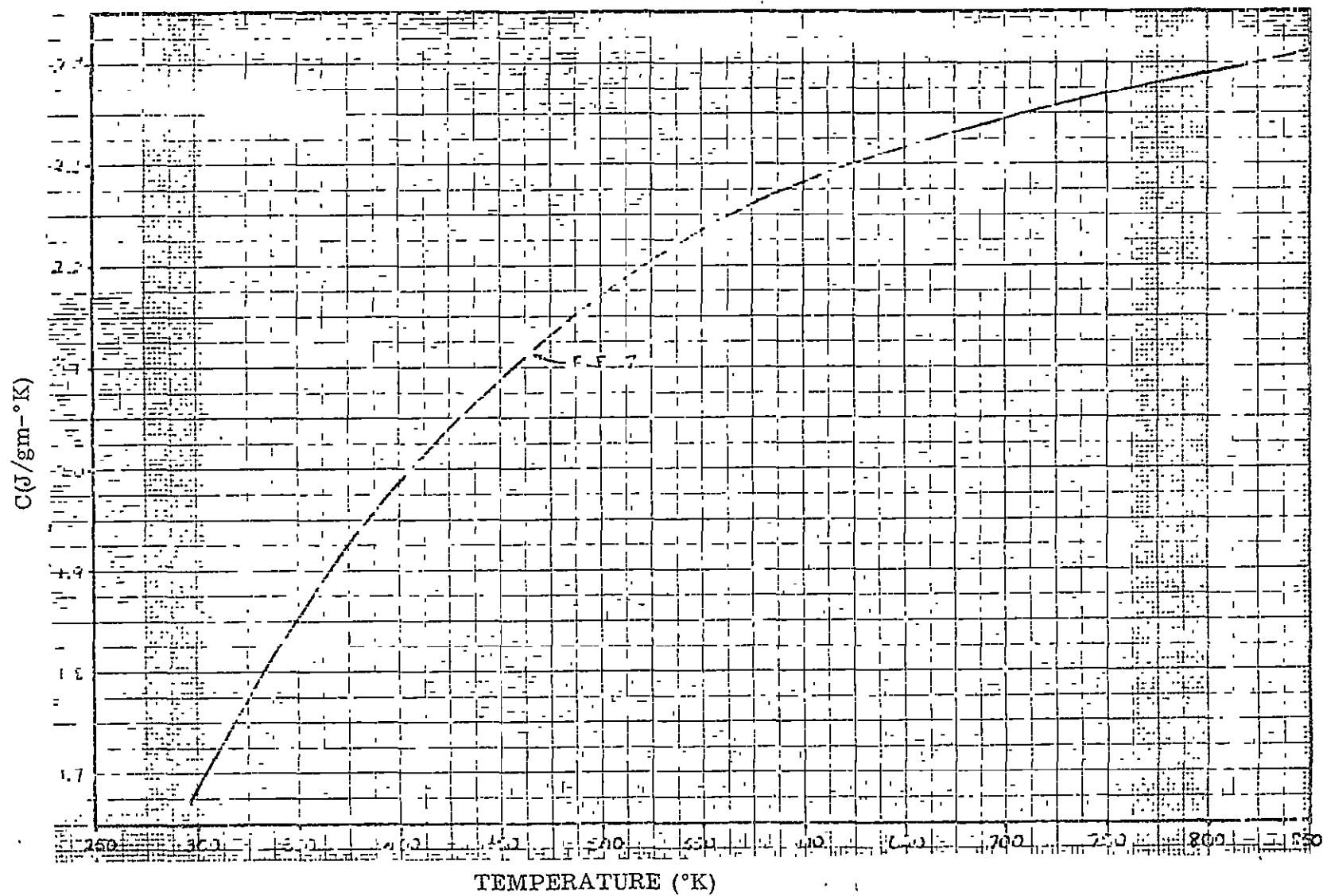


Fig. B-30 Specific Heat of Beryllium - Lockalloy (62% Be, 38% Al)

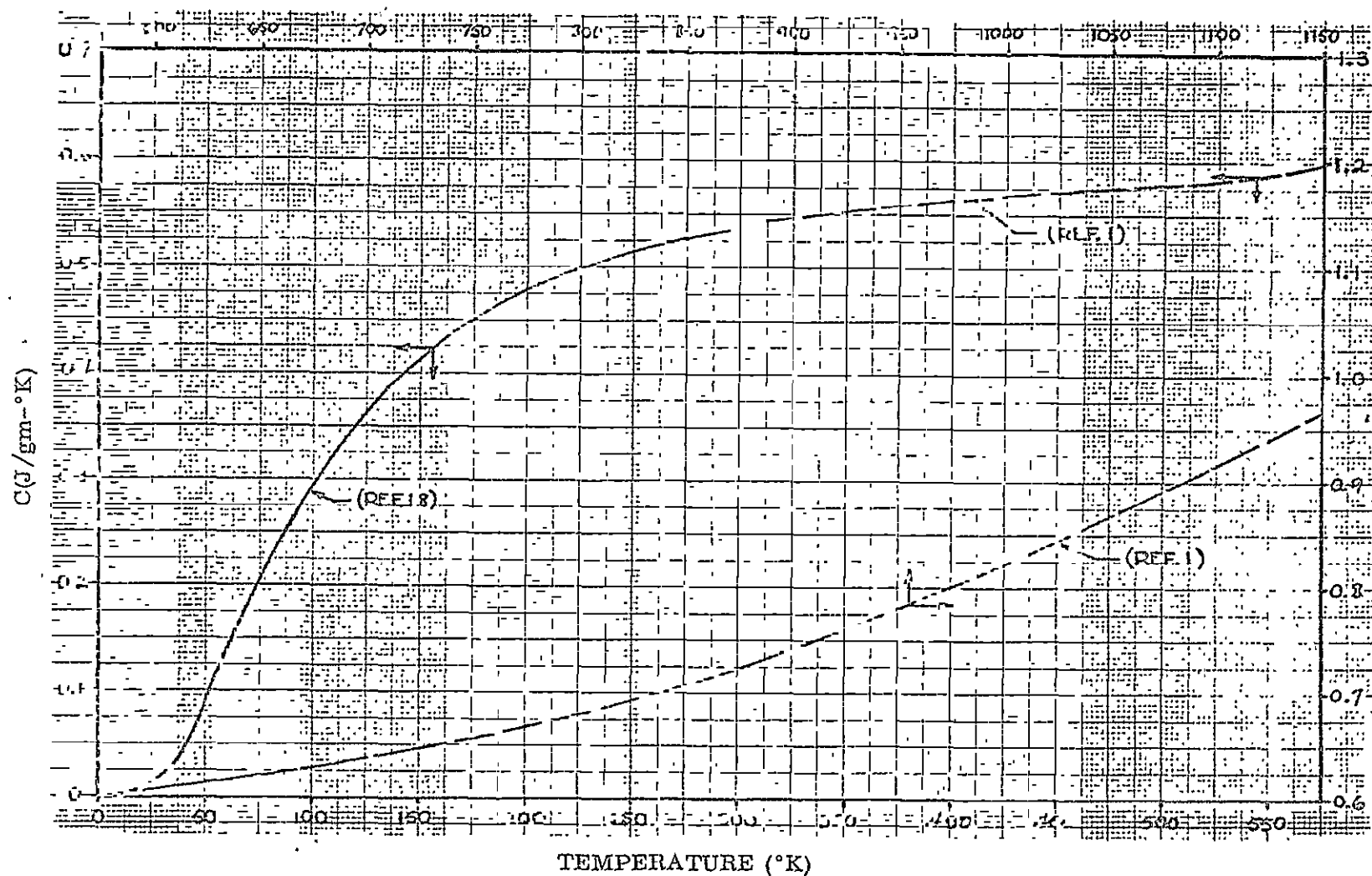


Fig. B-31 Specific Heat of Titanium (6Al-4V-0)

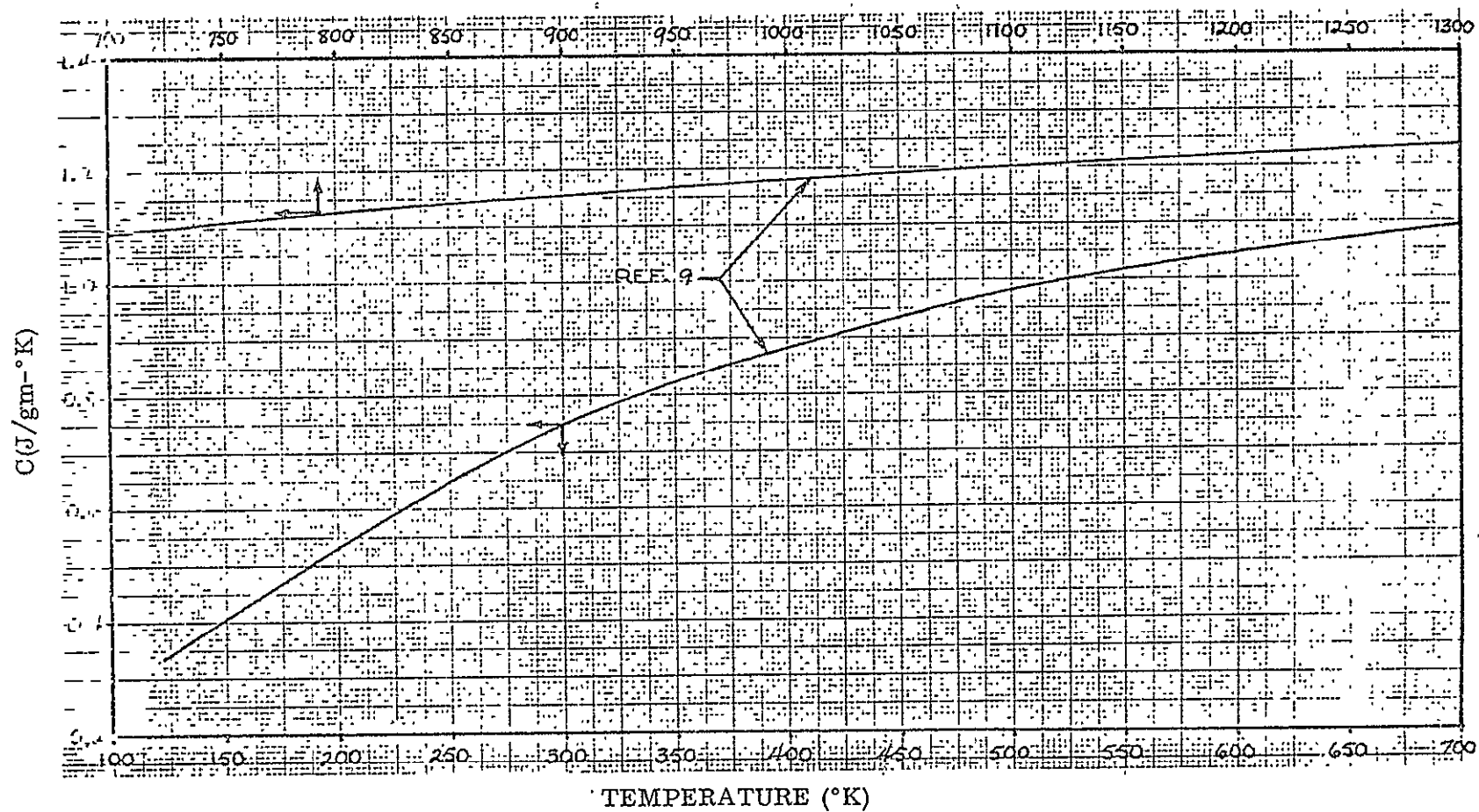


Fig. B-32 Specific Heat of Fused Silica (Corning 7940)

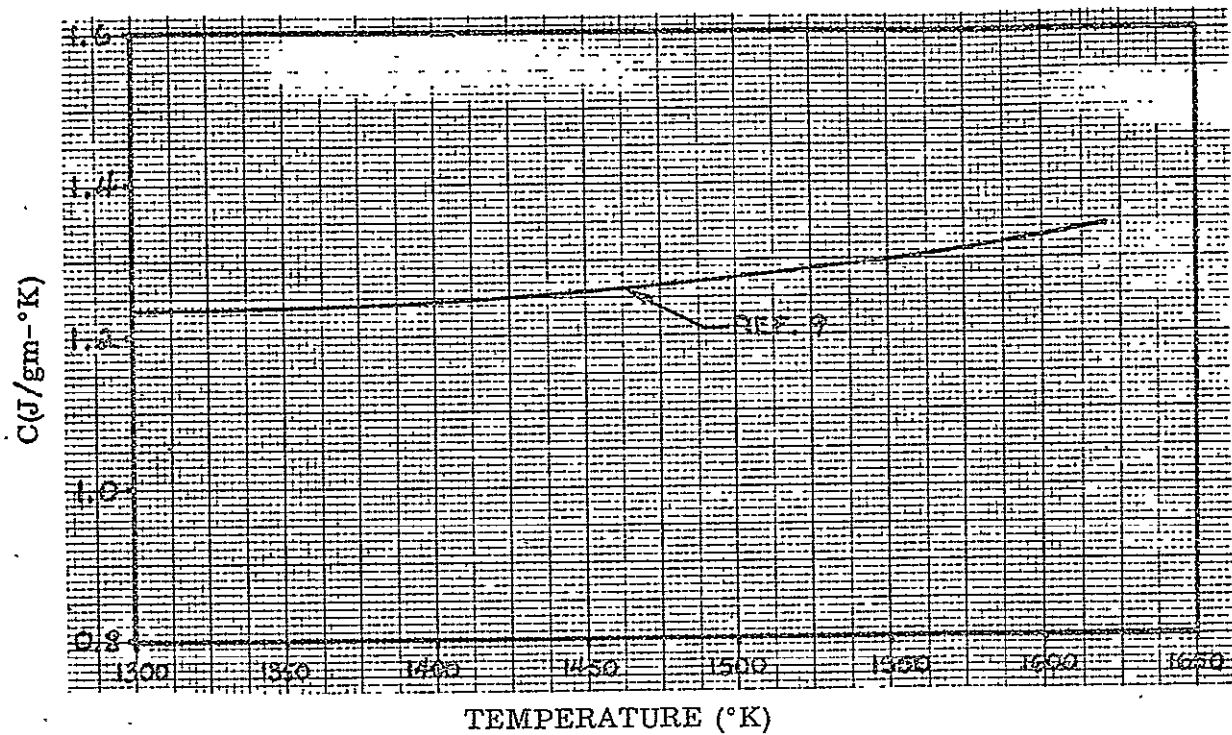


Fig. B-32 (Cont.) Specific Heat of Fused Silica (Corning 7940)

211

$C(J/gm-^{\circ}K)$

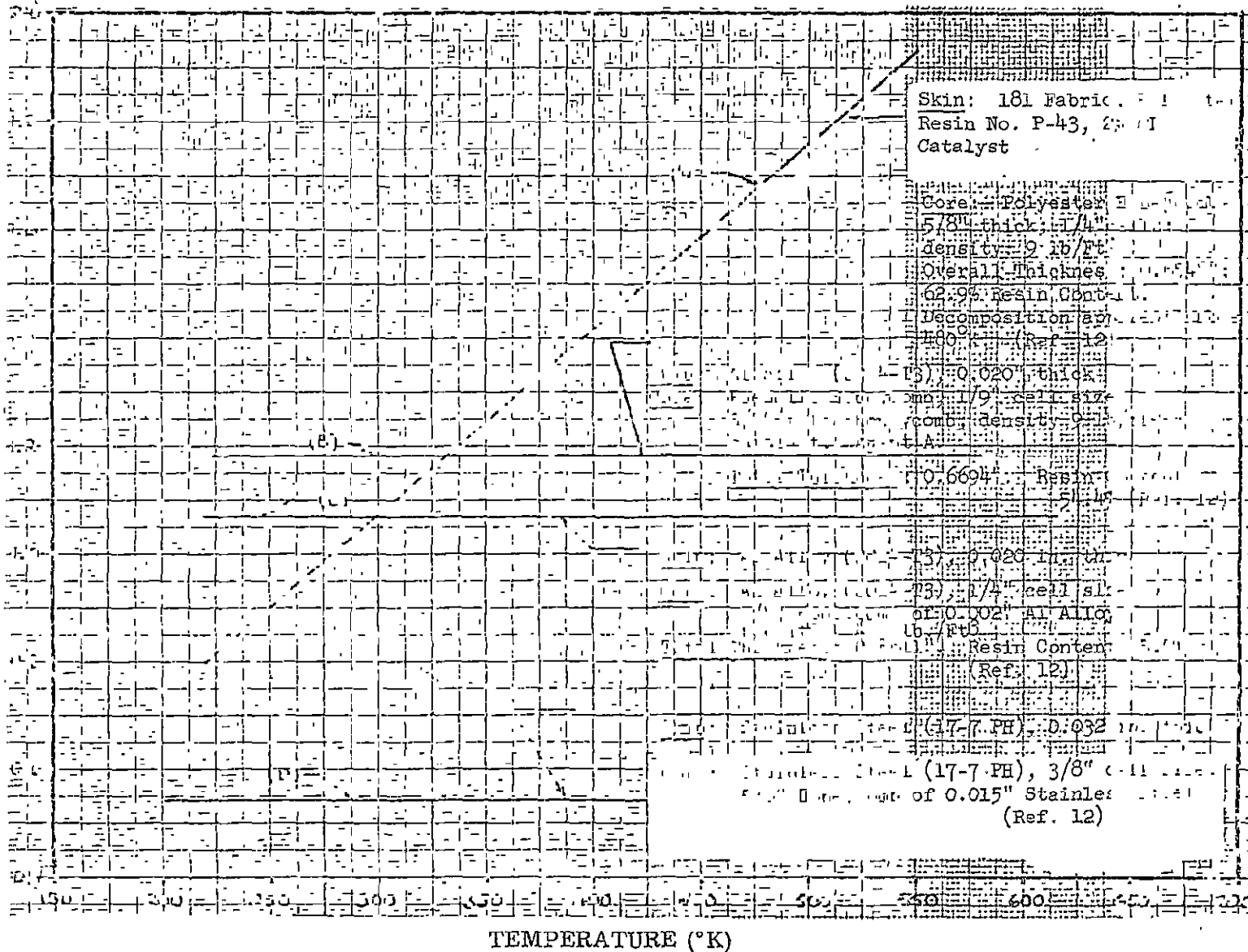


Fig. B-33 Specific Heat of Various Configurations of Honeycomb



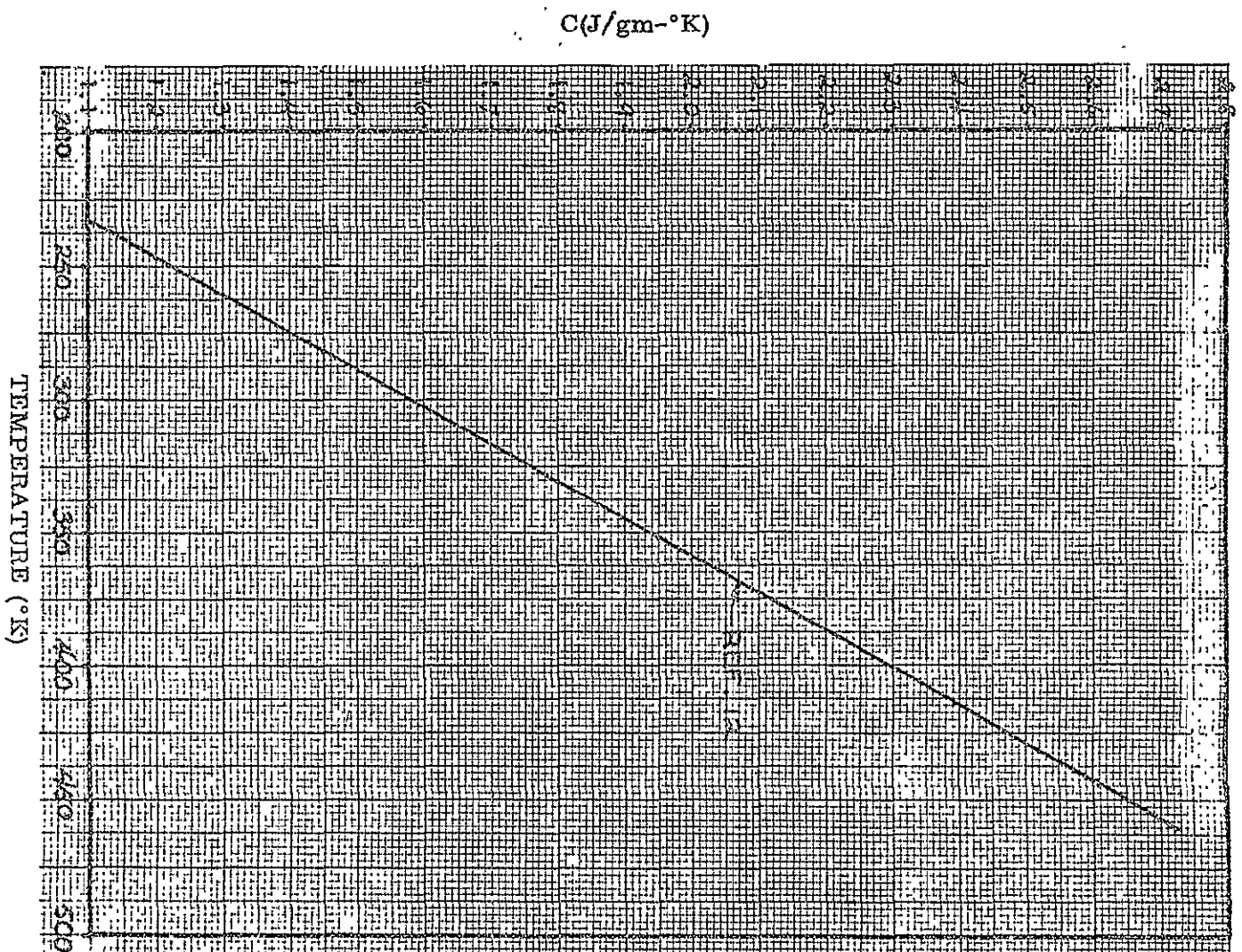


Fig. B-34 Specific Heat of Nylon

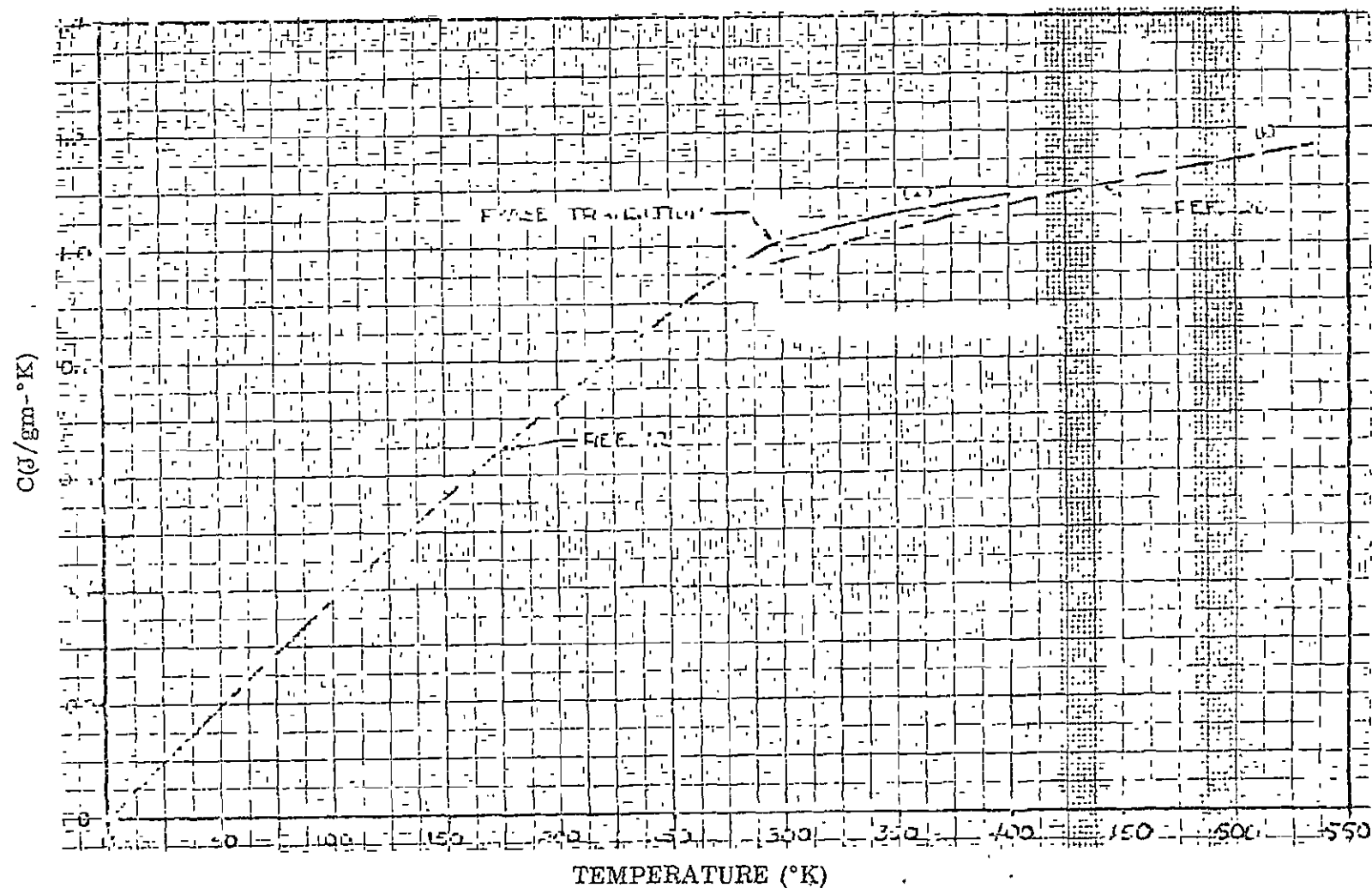


Fig. B-35 Specific Heat of Teflon (TFE)

214

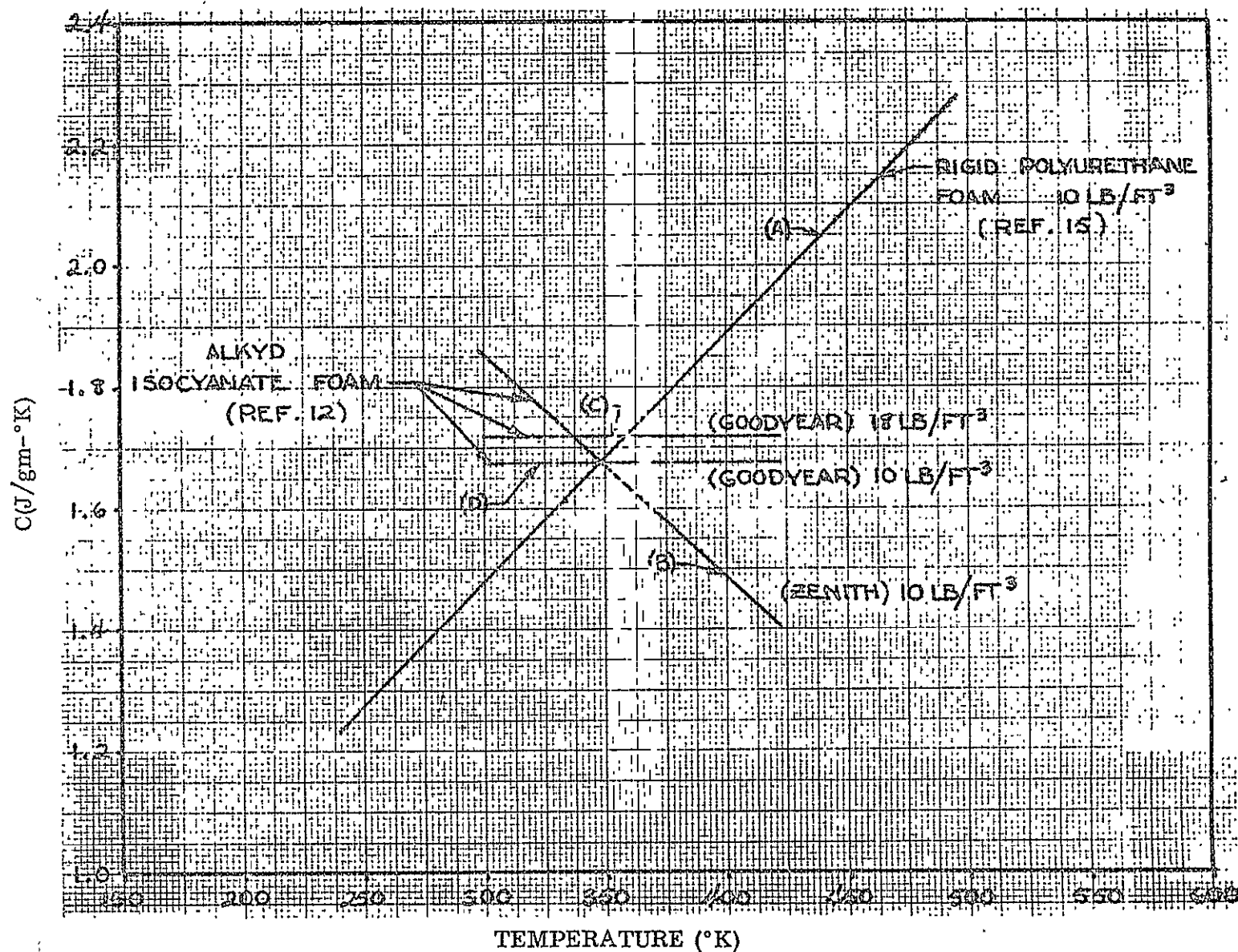


Fig. B-36 Specific Heat of Polyurethane Foam

215

(K<sup>o</sup>-gm/K<sup>o</sup>)

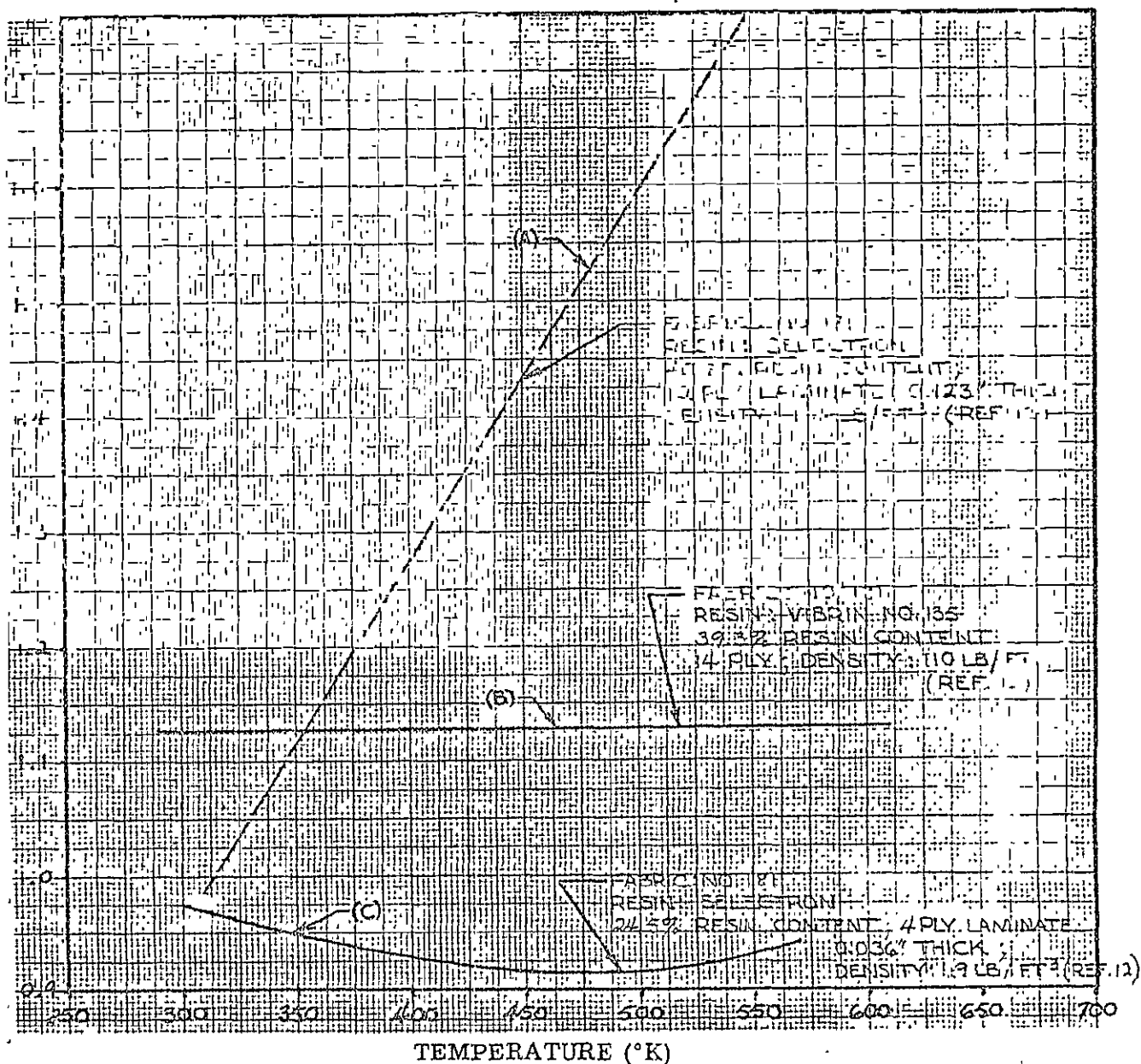


Fig. B-37 Specific Heat of Fiberglass (Glass Fabric Reinforced Polyester)

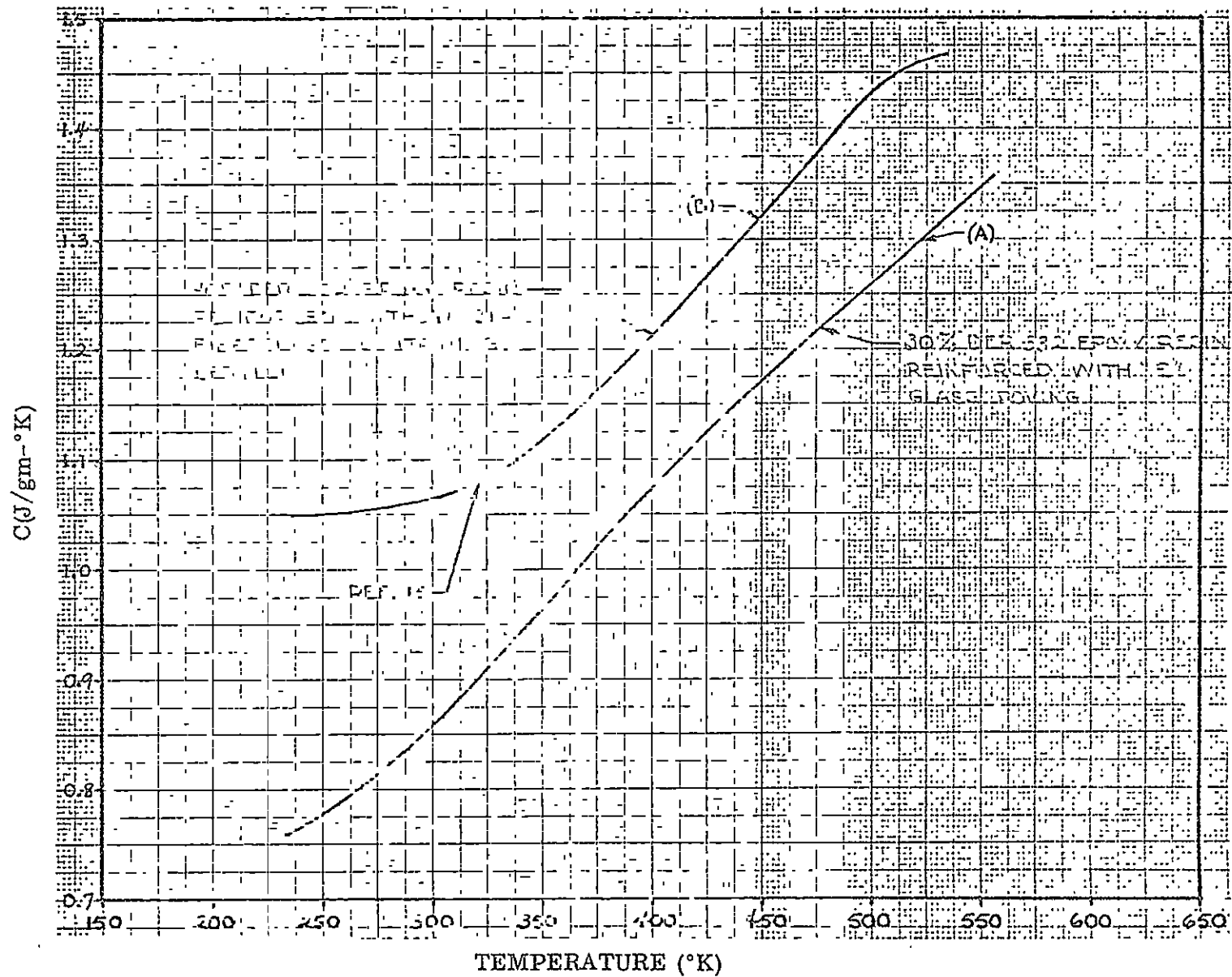


Fig. B-38 Specific Heat of Fiberglass (Glass Fiber Reinforced Epoxy)

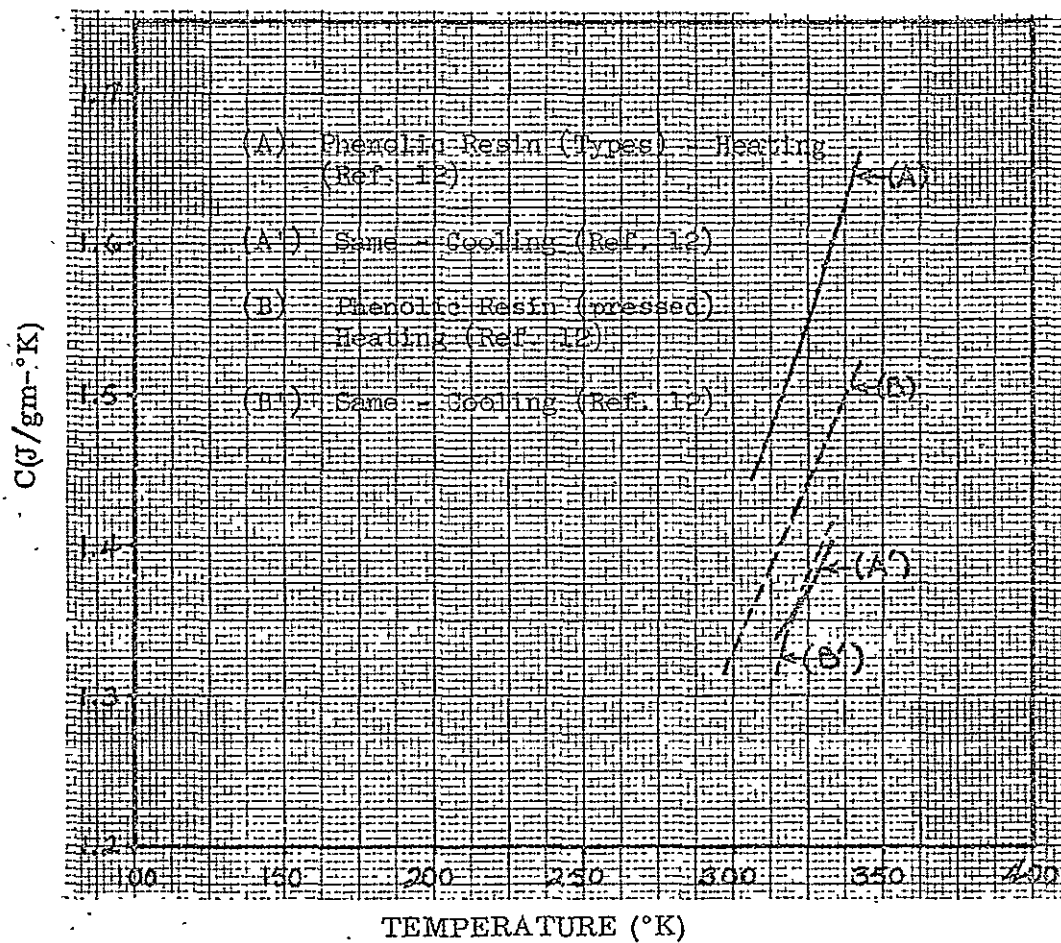


Fig. B-39 Specific Heats of Resin Cements

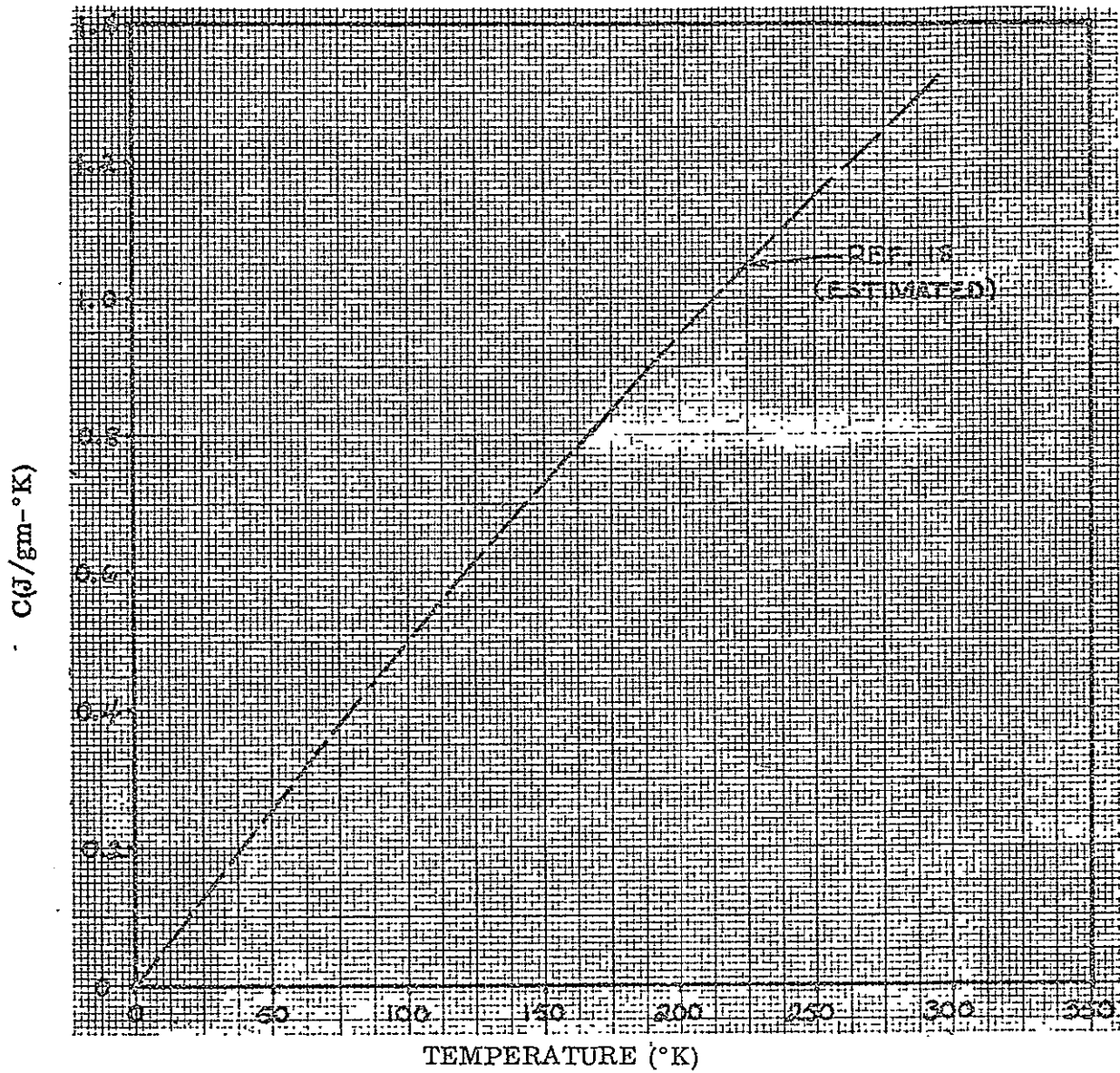


Fig. B-40 Specific Heat of Mylar



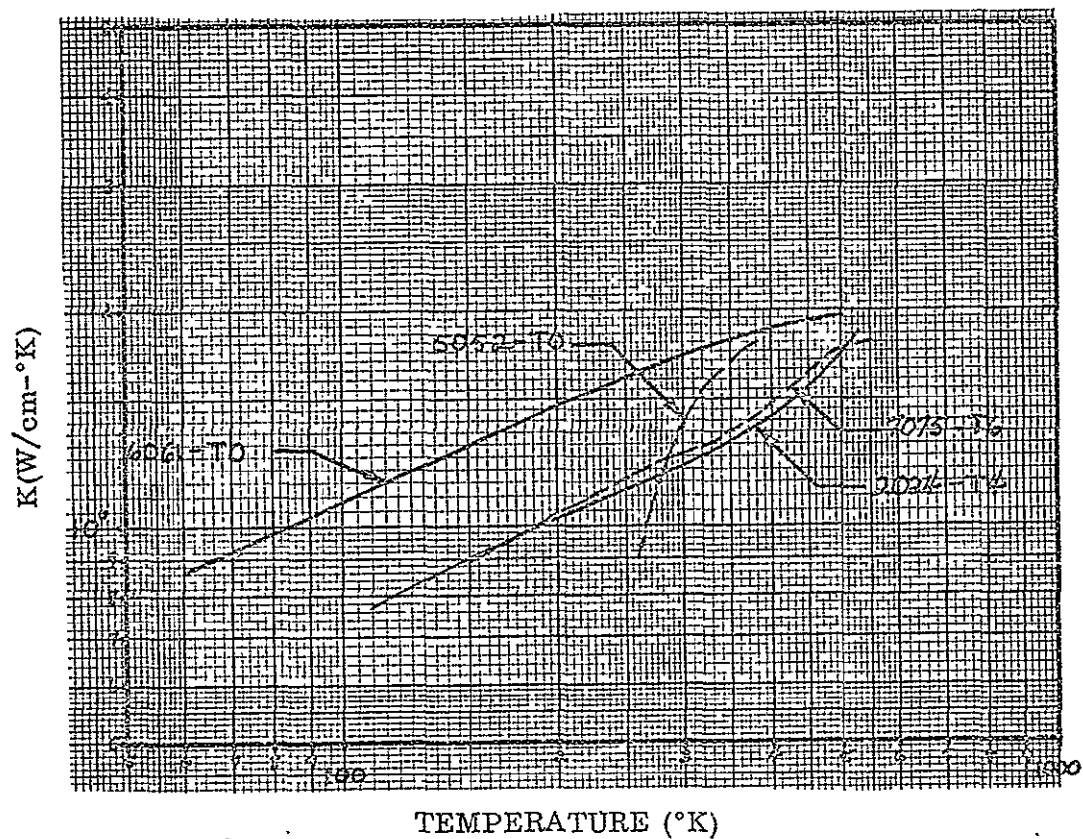


Fig. B-41 . Logarithmic Dependence of the Thermal Conductivities of Various Aluminum Alloys



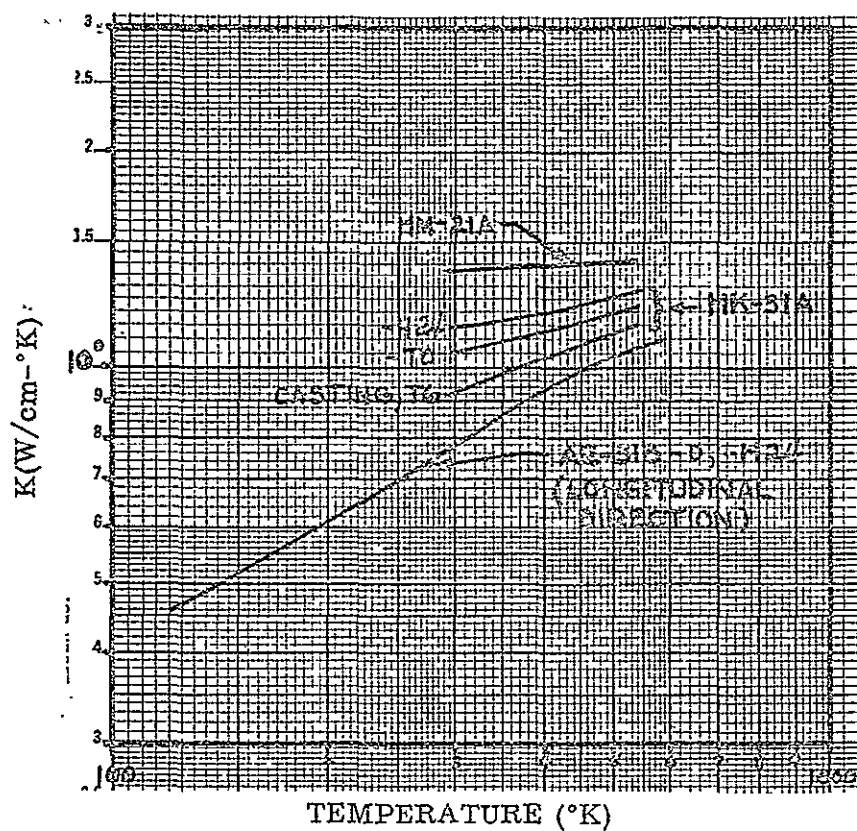


Fig. B-42 Logarithmic Dependence of the Thermal Conductivities of Various Magnesium Alloys

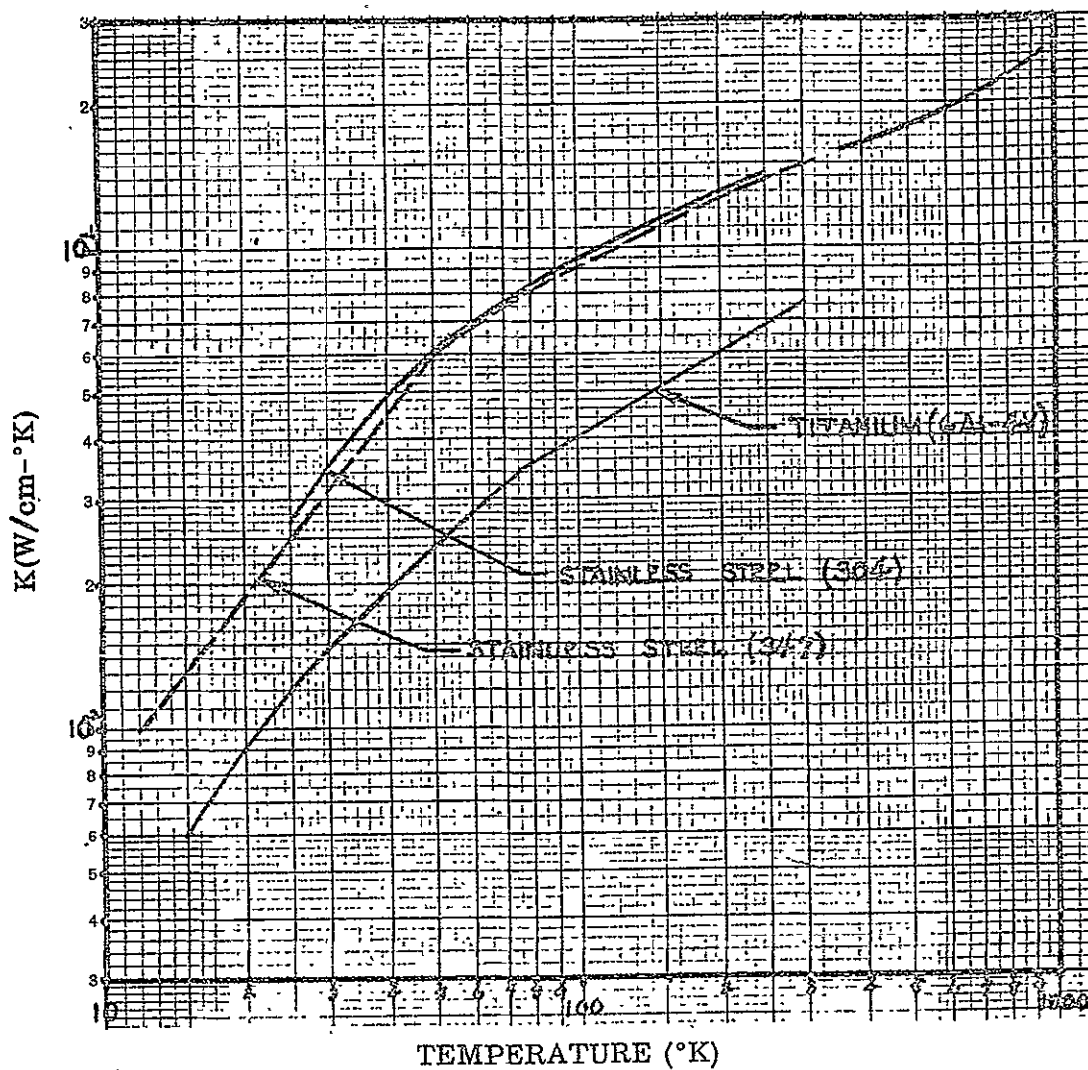


Fig. B-43 Logarithmic Dependence of the Thermal Conductivities of Stainless Steel (304) and (347) and Titanium (6Al-4V)

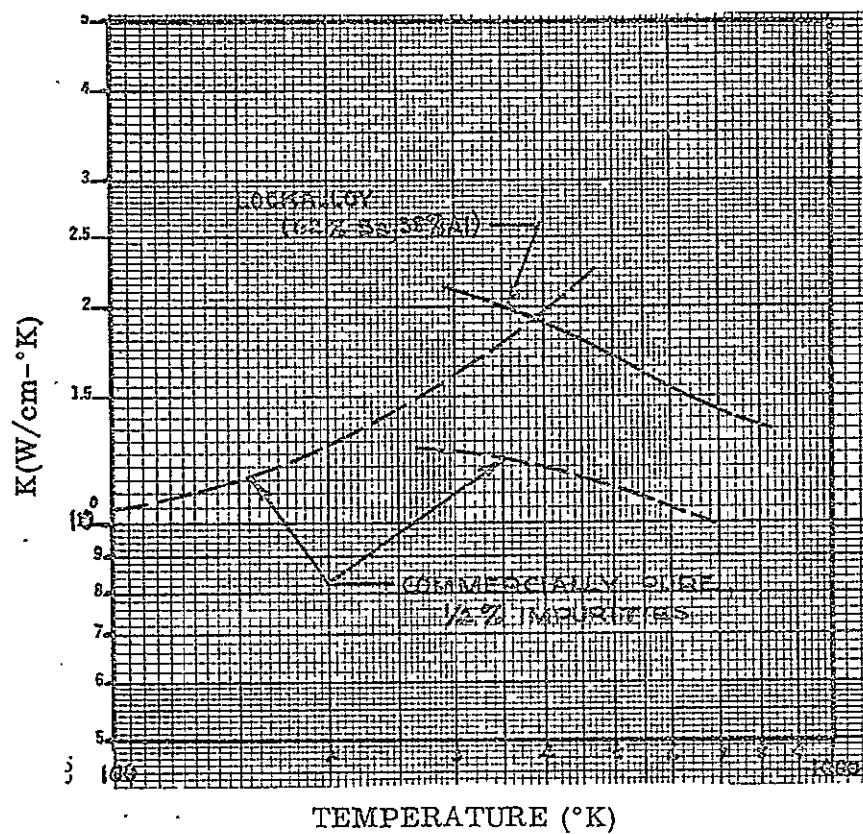


Fig. B-44 Logarithmic Dependence of the Thermal Conductivity of Beryllium (Lockalloy and Commercially Pure)

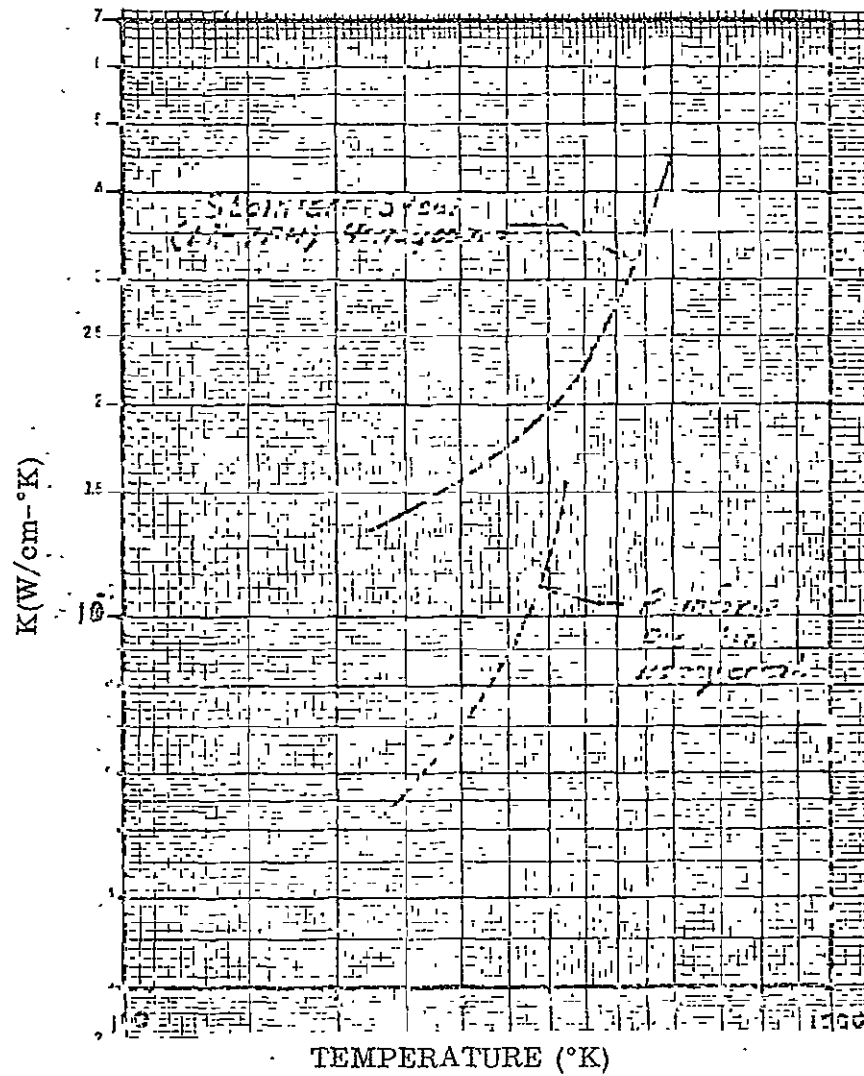


Fig. B-45 Logarithmic Dependence of the Thermal Conductivities of Stainless Steel and Reinforced Plastic Honeycomb

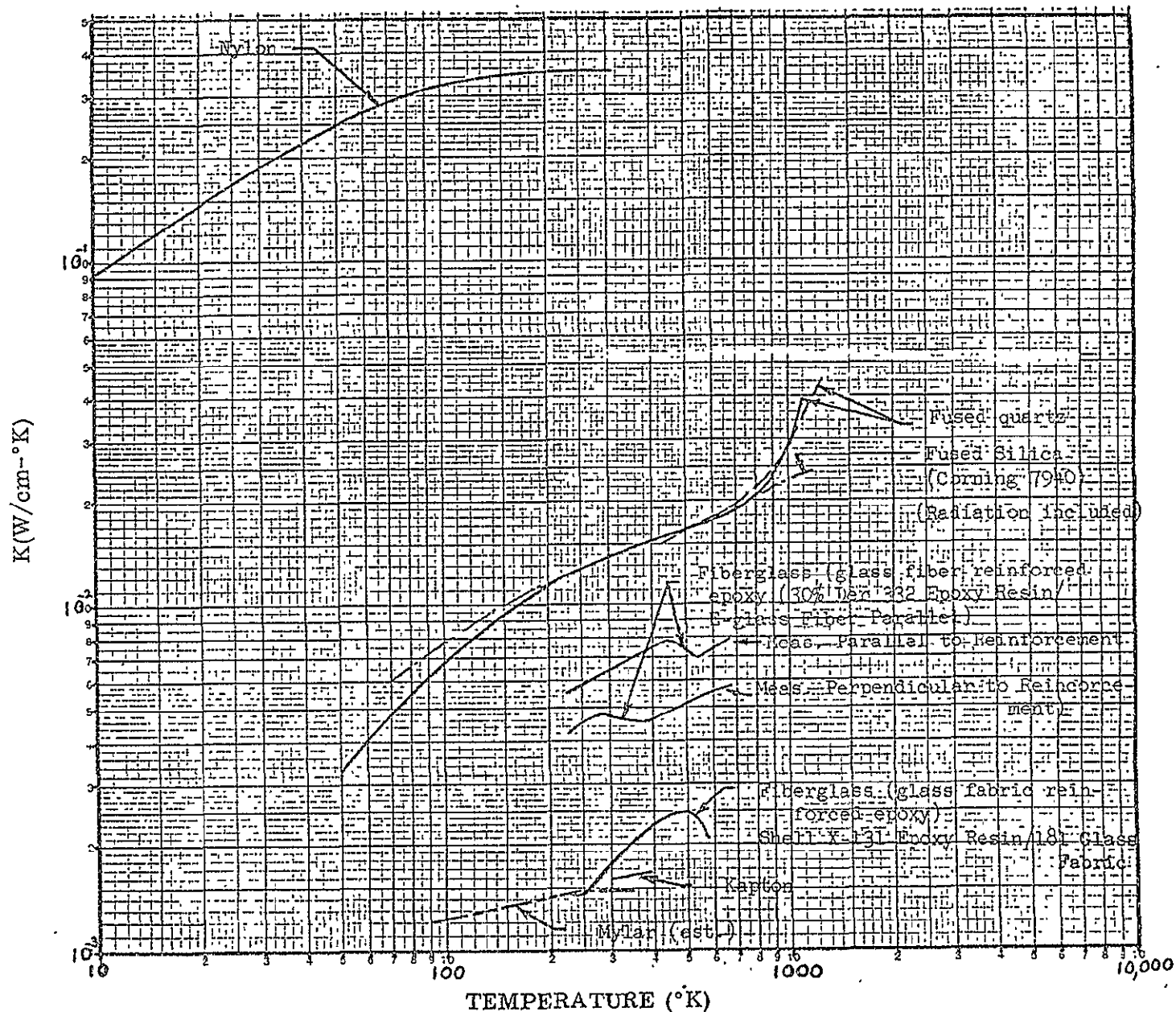


Fig. B-46 Logarithmic Dependence of the Thermal Conductivities of Nylon, Kapton, Mylar, Fiberglass, and Fused Quartz

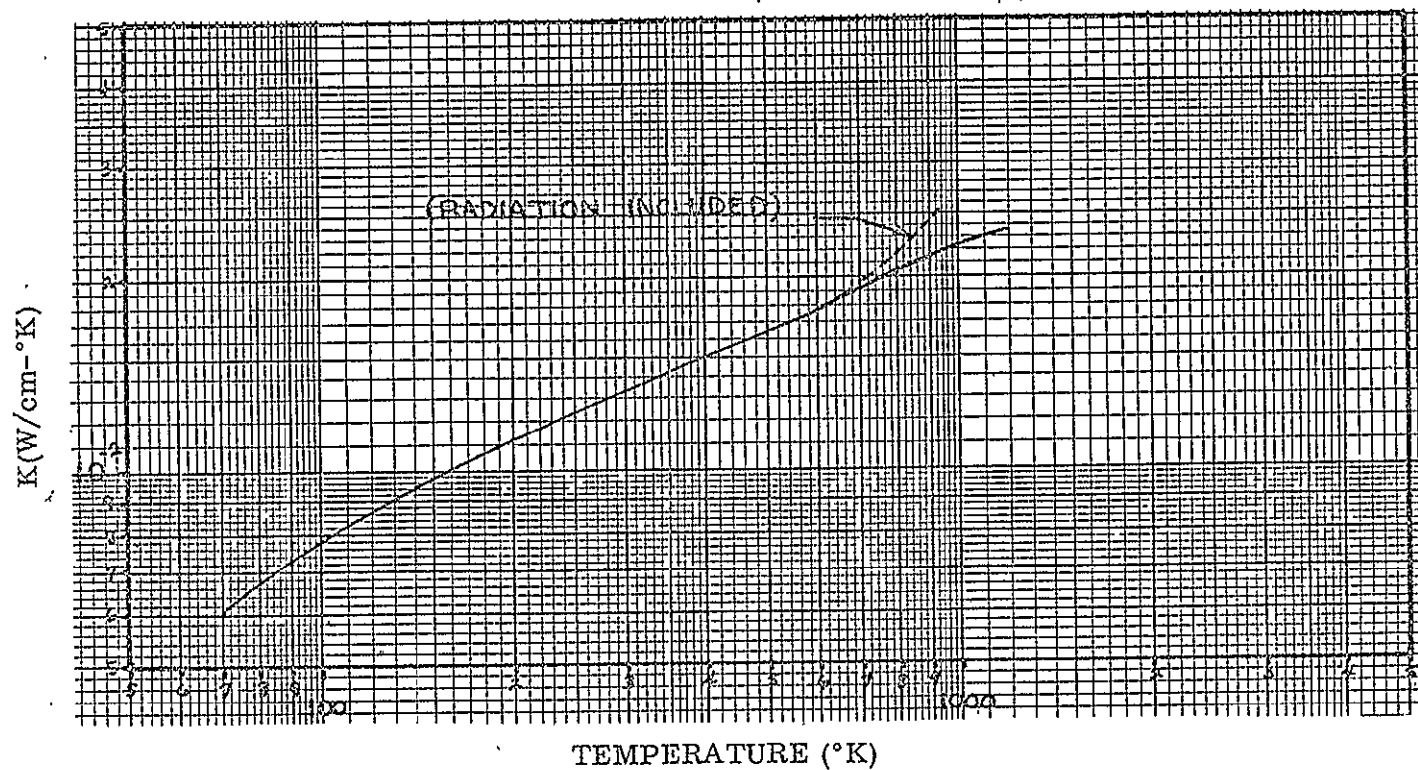


Fig. B-47 Logarithmic Dependence of the Thermal Conductivity of Fused Silica (Corning 7940)

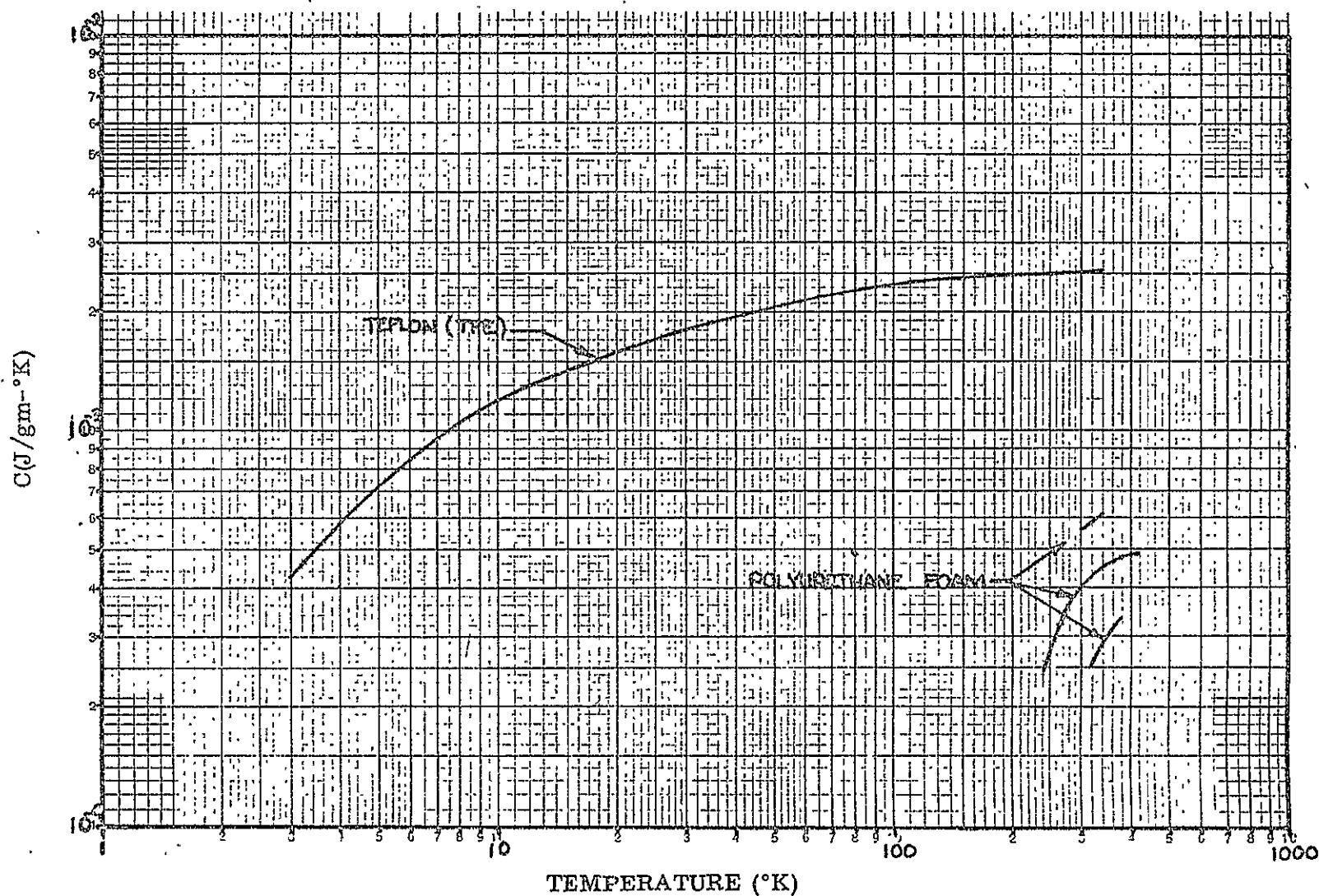


Fig. B-48 Log Plot of Logarithmic Dependence of the Thermal Conductivities of Polyurethane Foam and Teflon (TFE)

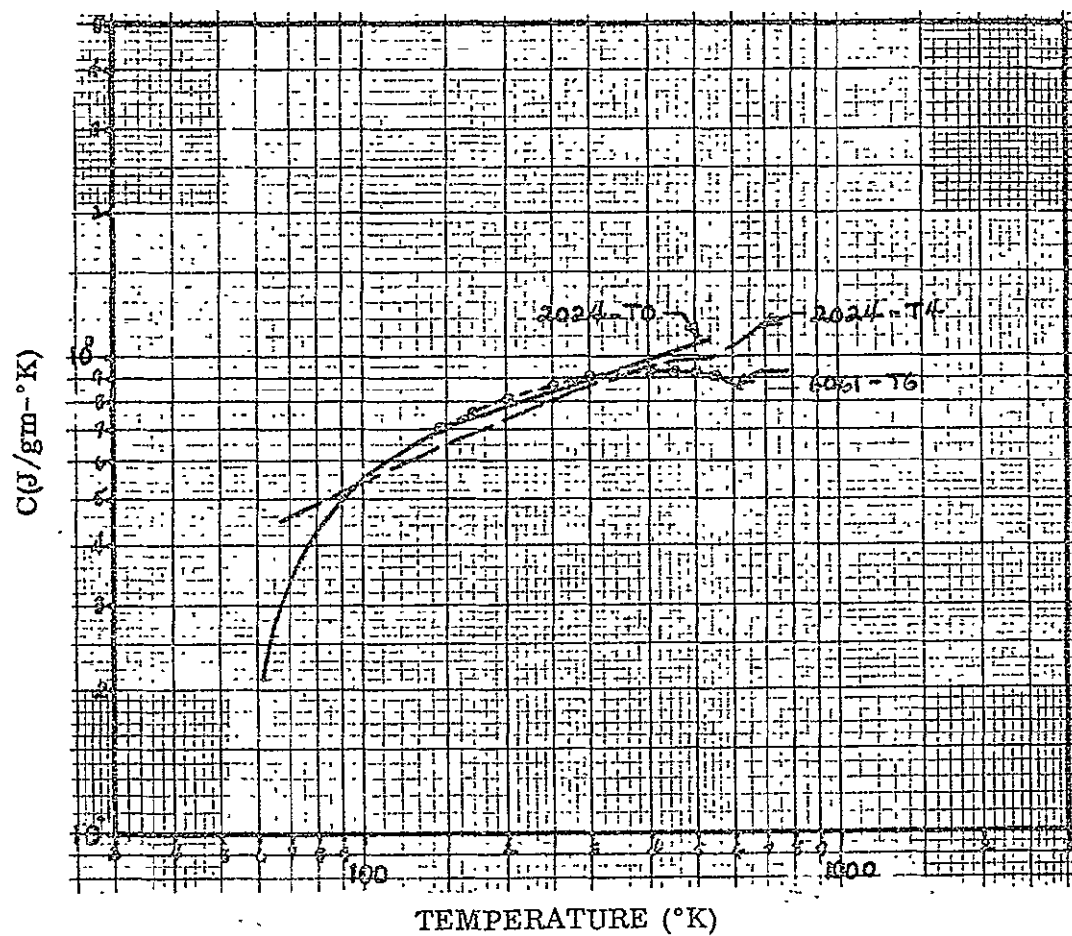


Fig. B-49 Logarithmic Dependence of the Specific Heats of Various Aluminum Alloys



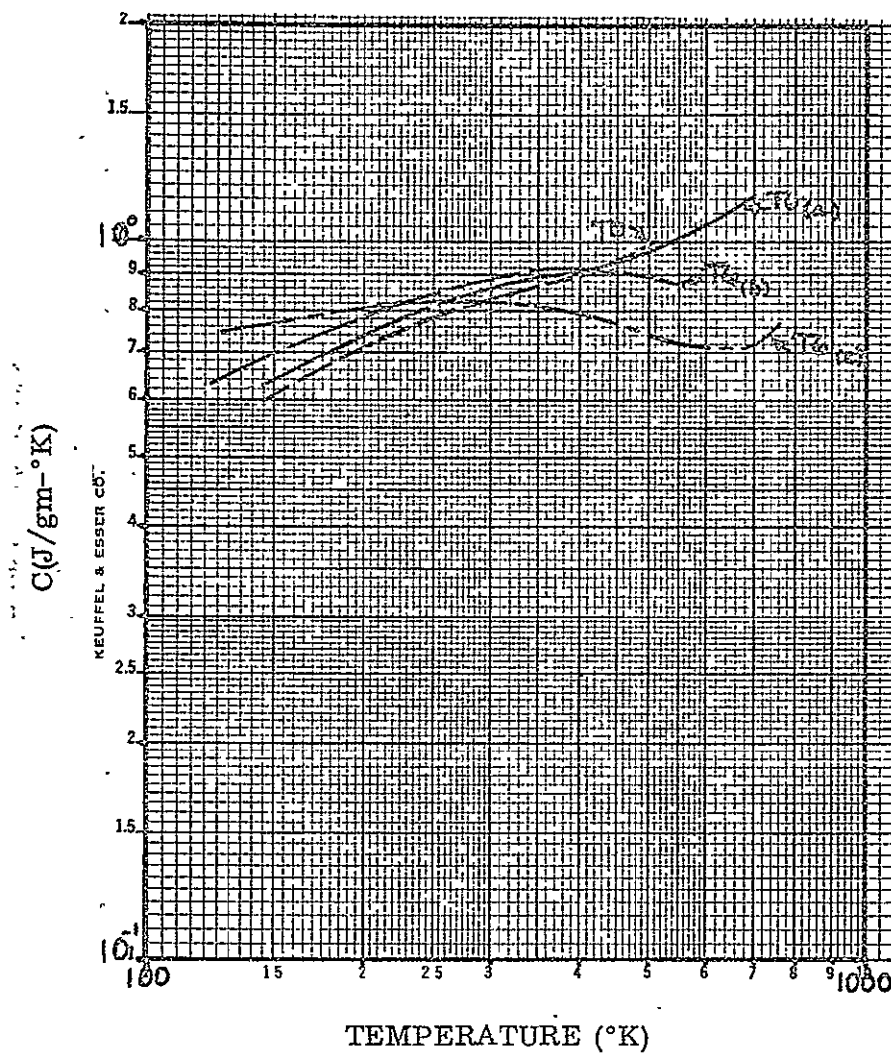


Fig. B-50 Logarithmic Dependence of the Specific Heats of Aluminum Alloys (7075-T0 and 7075-T6)

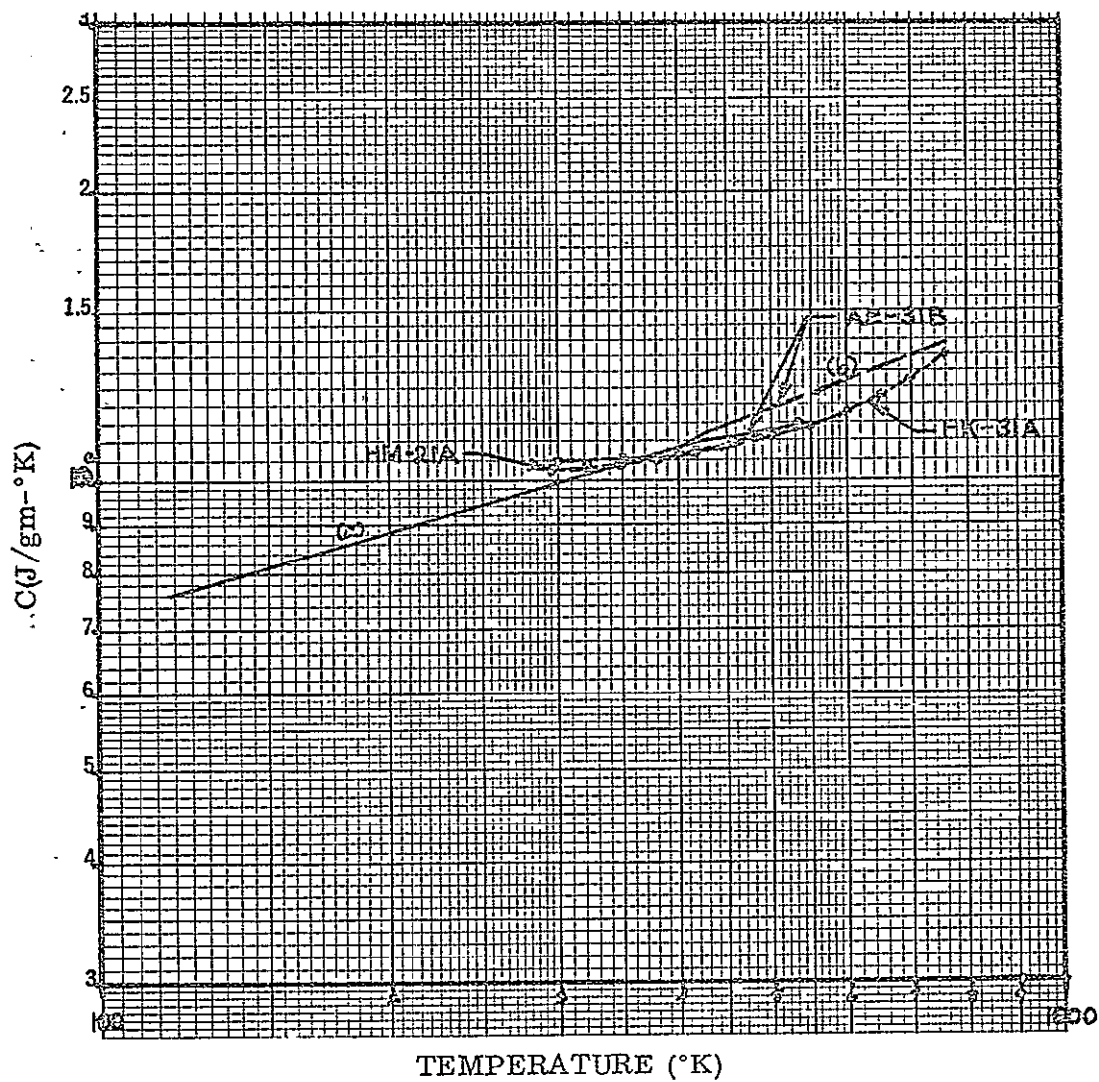


Fig. B-51 Logarithmic Dependence of the Specific Heats of Various Magnesium Alloys

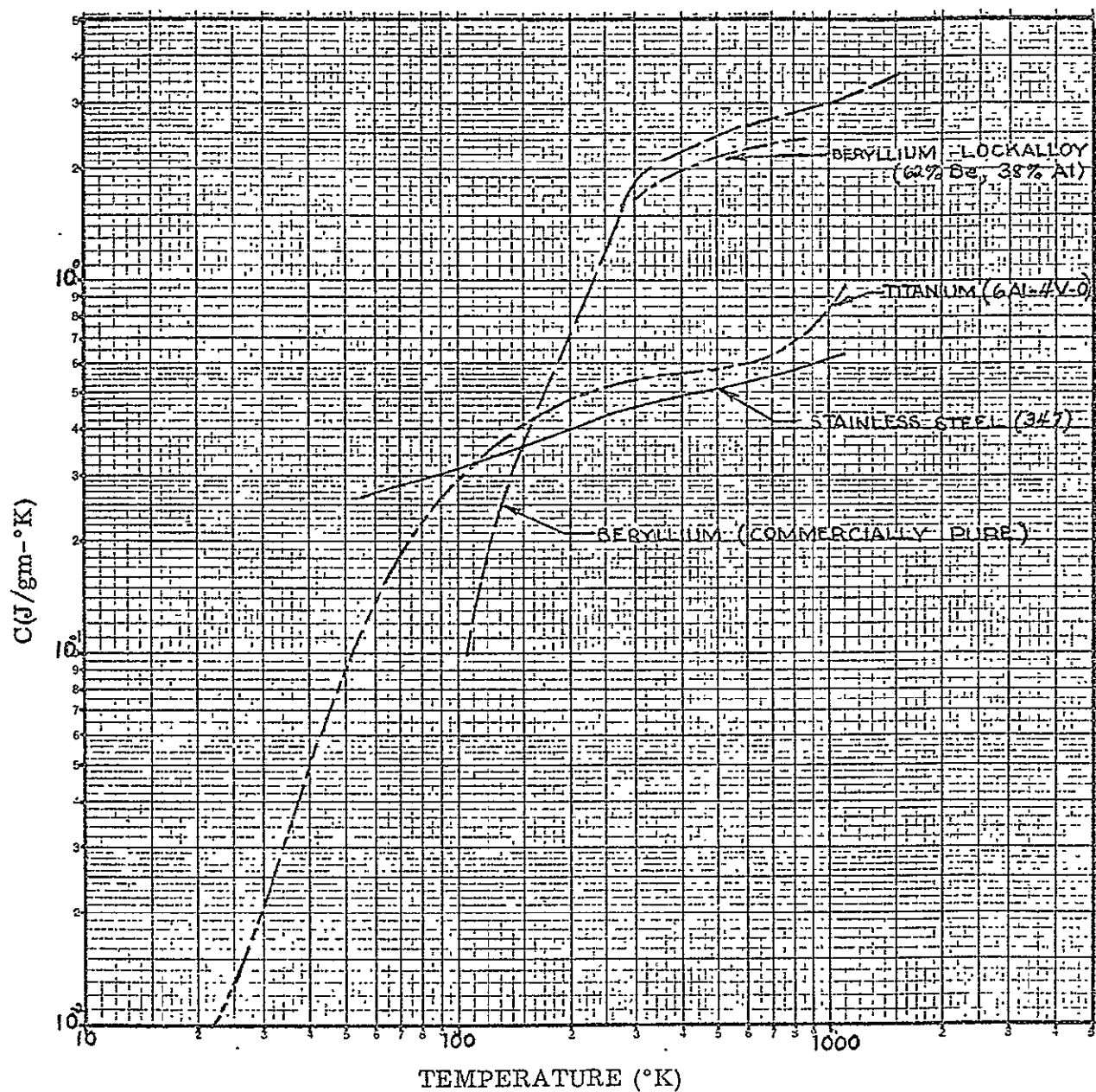


Fig. B-52 Logarithmic Dependence of the Specific Heats of Titanium, Stainless Steel, and Beryllium Alloys

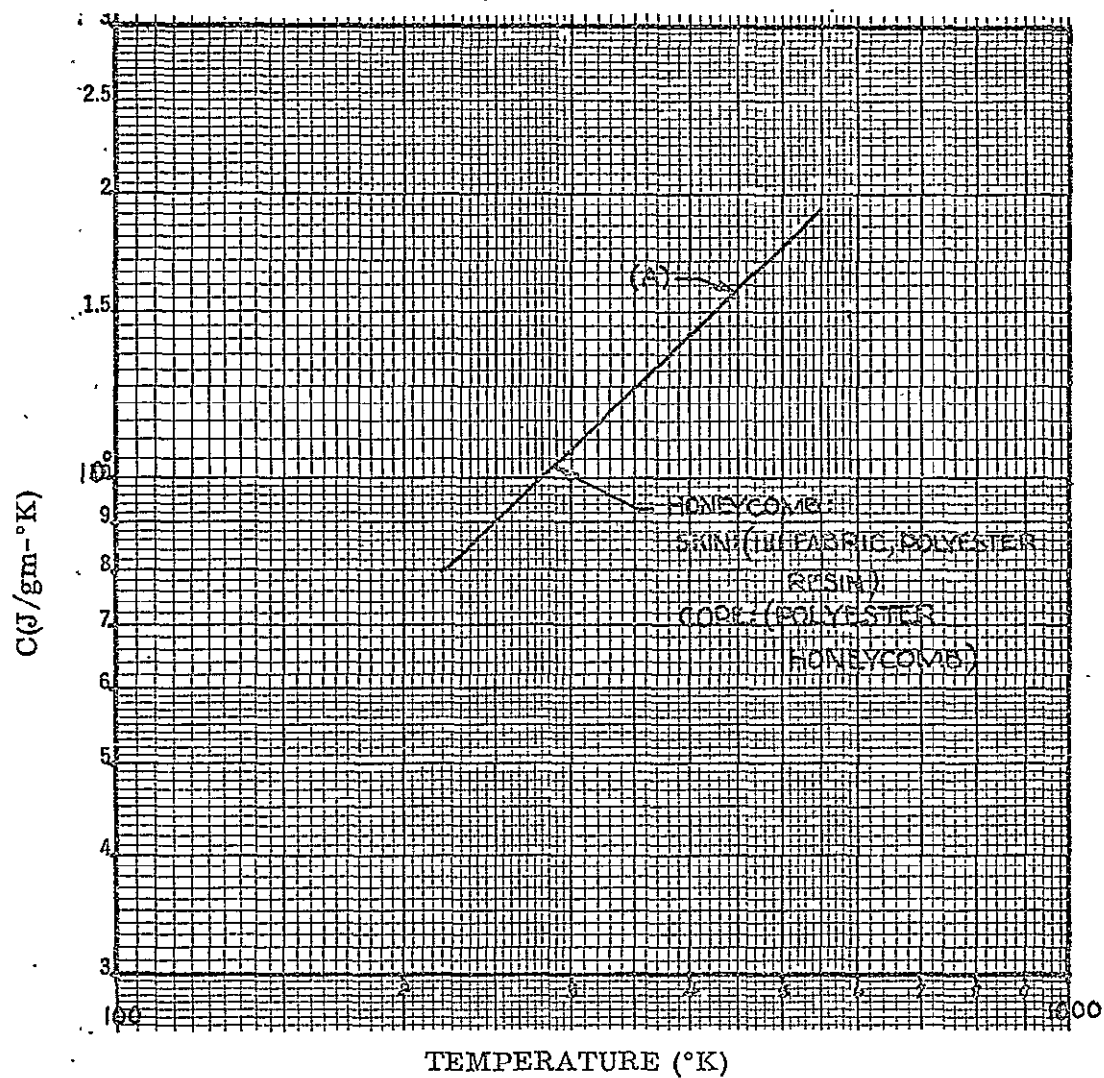


Fig. B-53 Logarithmic Dependence of the Specific Heat of Honeycomb

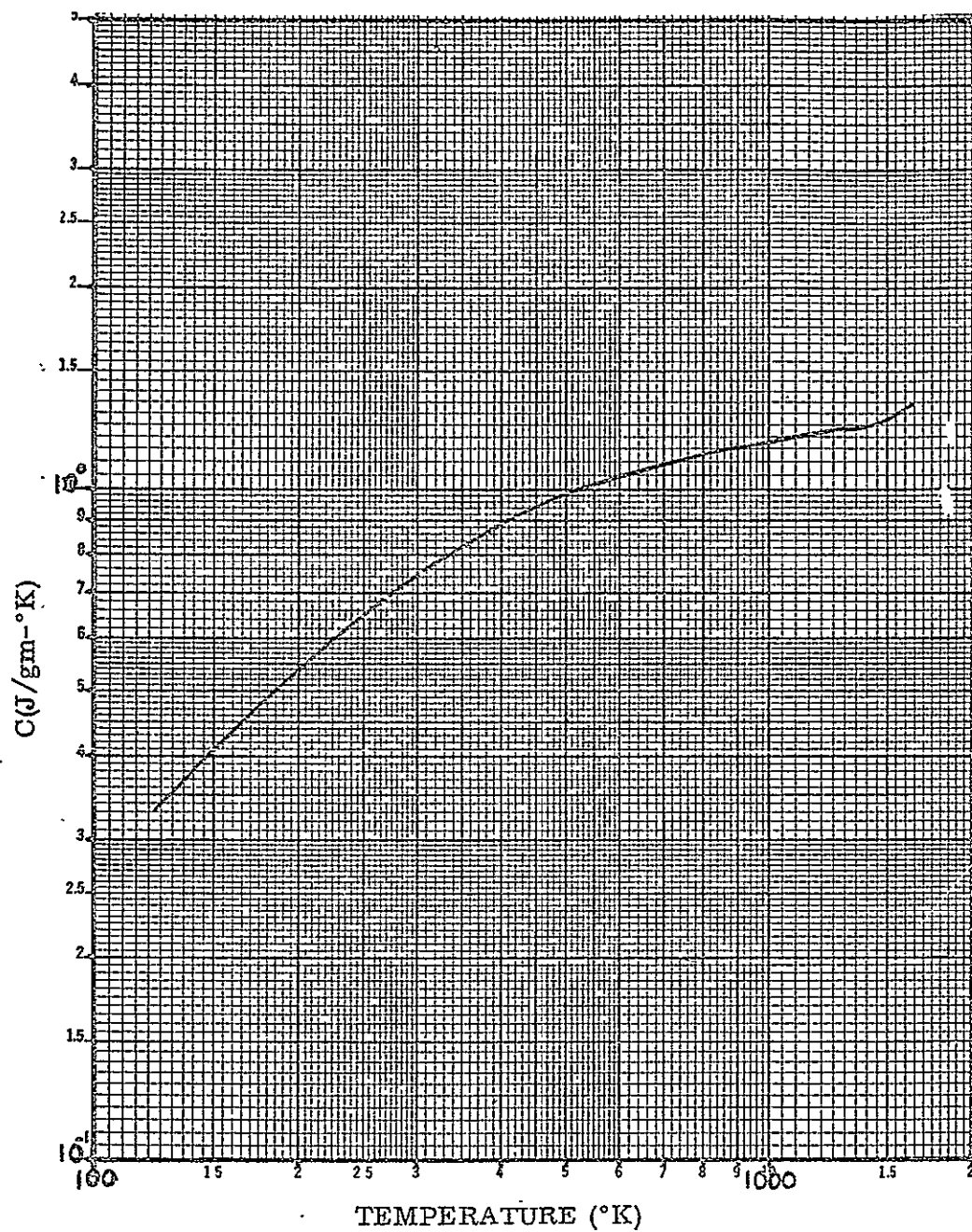


Fig. B-54 Logarithmic Dependence of the Specific Heat of Fused Silica (Corning 7940)

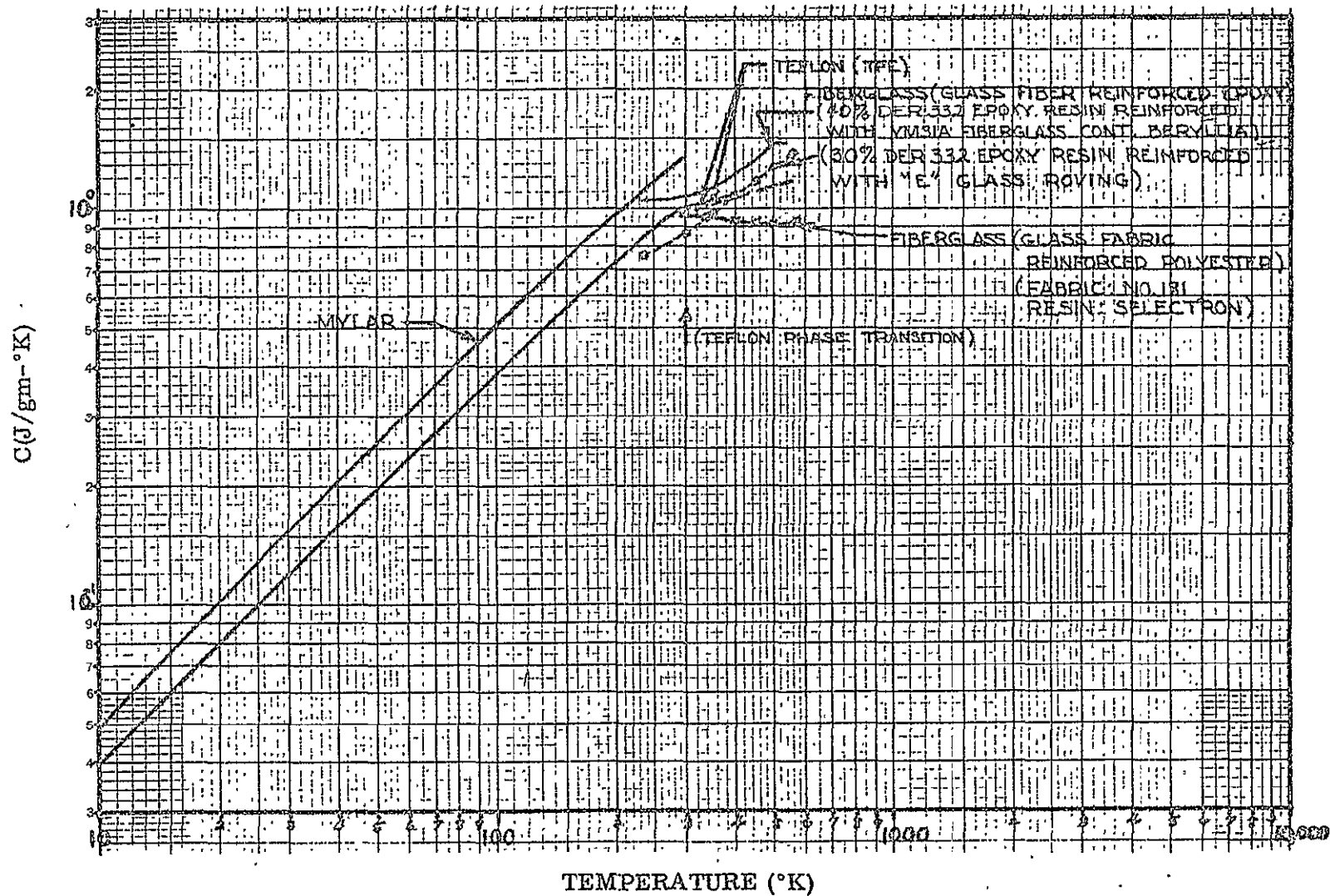


Fig. B-55 Logarithmic Dependence of the Specific Heats of Mylar, Teflon, and Fiberglass

## MATERIALS PROPERTIES REFERENCES

1. Syracuse University Research Institute, Aerospace Structural Metals Handbook, Vol. II - Non-Ferrous Alloys, Mar 1963, ASD-TDR-63-741
2. A. Goldsmith, H. Hirshhorn, T. Waterman, Thermophysical Properties of Solid Materials, Vol. II - Alloys, WADC Technical Report 58-476, Rev. Ed., Nov 1960
3. Purdue University, Thermophysical Properties Research Center, Data Book, Vol. I, Rev. 1960 Ed.
4. "Engineering Data Book," Cryogenic Engineering News, Jan 1968. (Data Book and Buyer's Guide/1968), Vol. 3, No. 1, Business Communications, Inc., Cleveland, Ohio
5. R. Fenn, Jr., et al., "Beryllium-Aluminum-Alloys," AIAA Fifth Annual Structures and Materials Conference, Apr 1964, AIAA Publication CP-8, Amer. Inst. of Aeronautics and Astronautics, New York, N.Y.
6. R. Powell and Wm. Blanpied, Thermal Conductivity of Metals and Alloys at Low Temperatures, 1954, NBS Circular 556. United States Department of Commerce. National Bureau of Standards
7. Lockheed Missiles and Space Company, unpublished data
8. Handbook of Thermal Design Data for Multilayer Insulation Systems, LMSC-A847882, Vol. II, Prepared by Lockheed Missiles and Space Company for NASA/MSFC under Contract NAS 8-20353, Lockheed Missiles and Space Company, Sunnyvale, Ca., Jun 25, 1967
9. Manufacturer's Published Data on Corning Fused Silica Code 7940. Corning Glass Works, Corning, New York, 1962
10. Purdue University, Thermophysical Properties Research Center, Data Book, Vol. III, Rev. 1960 Ed.
11. Manufacturer's Published Data on Honeycomb, Mechanical Properties of Hexcel Honeycomb Materials, Hexcel-TSB-120, Hexcel, Dublin, Ca., Jan 1966

12. A. Goldsmith, H. Hirschhorn, and T. Waterman, Thermophysical Properties of Solid Materials, Vol. IV -- Cermetes, Intermetallics, Polymerics, and Composites; WADC Technical Report 58-476, Rev. Ed., Nov 1960
13. Lockheed Missiles and Space Company unpublished data
14. J. Huffman and F. La Iacona, "Diffusion Bonding of Titanium Sandwich Structure for Saturn Tank Wall Application," AIAA/ASME 8th Structures, Structural Dynamics, and Materials Conference, Mar 1967, American Institute of Aeronautics and Astronautics, New York, N.Y.
15. C. Pears, W. Engelke, J. Thornburgh, The Thermophysical Properties of Plastic Materials from -50°F to Over 700°F, Part I, Technical Documentary Report No. ML-TDR-64-87, Aug 1964
16. Lockheed Missiles and Space Company unpublished data
17. Lockheed Missiles and Space Company unpublished data
18. Handbook of Thermal Design Data for Multilayer Insulation Systems, LMSC-A742953-VI, Prepared by Lockheed Missiles and Space Company for NASA/MSFC Under Contract NAS 8-11347, Lockheed Missiles and Space Company, Sunnyvale, Ca., Aug 11, 1965
19. Lockheed Missiles and Space Company unpublished data
20. J. Milek, Survey of Materials Report on TFE Plastics, Sep 1964, Hughes Aircraft Company



Please leave the  
Protector cover with  
Back of doc.